LAWRENCE
LIVERMORE
NATIONAL
LABORATORY

LLNL-TH-657830

Ligand Exchange Kinetics of Environmentally Relevant Metals

A. F. Panasci

July 28, 2014

Disclaimer

This work performed under the auspices of the U.S. Department of Energy by Lawrence Livermore National Laboratory under Contract DE-AC52-07NA27344.

LIGAND EXCHANGE KINETICS OF ENVIRONMENTALLY RELEVANT METALS

By

ADELE FRANCES PANASCI
B.S. (Saint Mary's College of California, Moraga, CA) 2009

DISSERTATION

Submitted in partial satisfaction of the requirements for the degree of

DOCTOR OF PHILOSOPHY

in

CHEMISTRY

in the

OFFICE OF GRADUATE STUDIES

of the

UNIVERSITY OF CALIFORNIA

DAVIS

Approved:

William H. Casey

Alexandra Navrotsky

Michael D. Toney
Committee in Charge
2014
LLNL-TH-657830

To my supportive family and friends:

Adele Frances Panasci
August 2014
Chemistry

Ligand Exchange Kinetics of
Environmentally Relevant Metals

Abstract

The interactions of ground water with minerals and contaminants are of broad interest for geochemists but are not well understood. Experiments on the molecular scale can determine reaction parameters (i.e. rates of ligand exchange, activation entropy, activation entropy, and activation volume) that can be used in computations to gain insight into reactions that occur in natural groundwaters. Experiments to determine the rate of isotopic ligand exchange for three environmentally relevant metals, rhodium (Rh), iron (Fe), and neptunium (Np), are described. Many environmental transformations of metals (e.g. reduction) in soil occur at trivalent centers, Fe(III) in particular. Contaminant ions absorb to mineral surfaces via ligand exchange, and the reversal of this reaction can be dangerous, releasing contaminants into the environment. Ferric iron is difficult to study spectroscopically because most of its complexes are paramagnetic and are generally reactive toward ligand exchange; therefore, Rh(III), which is diamagnetic and less reactive, was used to study substitution reactions that are analogous to those that occur on mineral oxide surfaces. Studies on both Np(V) and Np(VI) are important in their own right, as ^{237}Np is a radioactive transuranic element with a half-life of 2 million years.

Not only are the reactions that occur at the water-mineral interface difficult to probe *in situ*, but the structure of mineral surfaces are not well understood, making it difficult to study and predict the chemistry of these reactions. Experimentally determined oxygen-isotope exchange rates of small, structurally well-defined molecules provide a foundation for understanding how

structural changes affect reactions at the mineral-water interface, enabling more reliable chemical computations to predict surface interactions. Therefore in Chapter 2, I studied two monomeric rhodium complexes that differ by one ligand using isotopic mass spectrometry to determine how neighboring functional groups affect the rate of water exchange. One rhodium complex containing two adjacent bound waters was found to have a rate of exchange, activation enthalpy, and activation entropy of: $k_0^{298} = (5 \pm 0.5)\cdot 10^{-8}$ s^{-1}, $\Delta H^{\ddagger} = 119 \pm 3$ kJ mol^{-1}, $\Delta S^{\ddagger}$=14 ± 1 J mol^{-1} K^{-1}, for the fully protonated molecule. The second complex containing a single bound water with a neighboring inert chloride, which mimics an isolated exchangeable functional group on a mineral surface, was found to have a rate of $k_0^{298} = (2.5\pm 1)\cdot 10^{-9}$ s^{-1}, an activation enthalpy of $\Delta H^{\ddagger} = 132 \pm 3$ kJ mol^{-1}, and an activation entropy of $\Delta S^{\ddagger}$= 41.5 ± 2 J mol^{-1} K^{-1}. For the complex containing two adjacent waters, the rate for water exchange increased upon deprotonation of one of the bound waters because adjacent bound hydroxyl and water could quickly exchange a proton and the overall charge of the complex is reduced, increasing the reactivity of a bound water. Therefore, neighboring functional groups, especially a ligand that contains an acidic proton, may affect the rate of exchange of an adjacent bound water.

Chapter 3 elaborates on studying the effect structure has on ligand exchange rates by examining the kinetics of oxygen-isotope exchanges in a Fe(III) oligomer, since only a single study has ever been done on water exchange of a multimeric Fe(III) complex. The ultimate goal was to establish a correlation between rates of water exchange and calculable or measureable properties, such as <Fe^{III}-OH_2> bond lengths. ^{17}O nuclear magnetic resonance spectroscopy (NMR) line broadening experiments employing the Swift-Connick formalism were used to compare oxygen exchange rates and activation volumes of a tetrameric iron complex with those of smaller monomeric iron complexes. The fully protonated neutral Fe(III) complex studied was

found to have an average rate of water exchange of $k_{eq}^{298} = (8.3 \pm 0.8)\cdot 10^5$ s^{-1} at pH<5, ~10^4 times faster than the fully aquated Fe(III) monomer. The average activation enthalpy, entropy and volume were determined to be $\Delta H^{\ddagger} = 46 \pm 4.6$ kJ mol^{-1}, $\Delta S^{\ddagger} = 22 \pm 18$ J mol^{-1} K^{-1}, $\Delta V^{\ddagger} = +1.8 \pm 0.2$ cm^3 mol^{-1}. Increasing the number of irons and the complexity of the molecule does not strongly affect the rate of exchange, rather the metal-oxygen bond length and the reactivity of the bound water control the rate. Experimentally derived correlations between structural characteristics and exchange rates lead to better predictions of interactions that occur between water and the surface of minerals.

Finally in Chapters 4 and 5, experiments to determine the reactivity of Np(V) and Np(VI) complexes are described. It is of particular interest to determine the extent to which the chemistry resembles that of the less dangerous uranium systems and the reactivities of the transuranic elements, in general. Monomeric neptunium ions were studied using NMR to determine the rate of carbonate exchange at high pH values and oxygen exchange at low pH values. In alkaline conditions and an abundance of carbonate, the dominant neptunium ion is in the sixth oxidation state and three bidentate carbonate ligands are bound in the equatorial plan to form the $[NpO_2(CO_3)_3]^{4-}$ ion. A ^{13}C NMR saturation-transfer pulse sequence was used to determine the rate of carbonate exchange on the $[NpO_2(CO_3)_3]^{4-}$ ion in the pH range of $8.1 \leq pH \leq 10.5$. In the pH range of $9.3 \leq pH \leq 10.5$, the average rate, activation enthalpy, and activation entropy were found to be: $k_{eq}^{298} = 41 \pm 4$ s^{-1}, $E_a = 45 \pm 4$ kJ mol^{-1}; $\Delta H^{\ddagger} = 43 \pm 4$ kJ mol^{-1}, $\Delta S^{\ddagger} = -72 \pm 13$ J mol^{-1} K^{-1} respectively. Exchange was found to be pH independent above pH 9 and pH dependent below pH 9, where rates increased as the pH value decreased. An increase in the rate, as well as a decrease in activation enthalpy, as the pH decreases from pH 9 to pH 8, show a proton-enhanced pathway for exchange of carbonate. This result is consistent with those

of carbonate exchange for the corresponding carbonate complexes of U(VI) and Pu(VI), but there still is disagreement about the mechanism of the carbonate ligand-exchange reaction, which must be at least a two-step process. It is unclear whether an aquated Np(VI) intermediate state exists between incoming and outgoing carbonates.

In carbonate-free and acidic conditions, the most soluble species is the fully aquated neptunium ion in the fifth oxidation state, NpO_2^+ ion. The Np(V) ion has been shown to be paramagnetic in the solid state and predicted to be paramagnetic in solution as a result of two unpaired *f*-valence electrons ($5f^2$). Thus ^{17}O NMR line-broadening experiments using the Swift-Connick formalism were conducted to determine water exchange rates. We found a lack of measurable broadening which leads us to predict that the rate is slower than can be captured using the NMR methods in this thesis. Simulations of the Block-McConnell equations were performed to predict the width of ^{17}O water signal produced from the NMR experiments to determine whether the experimental approach was feasible. The calculations showed that the rate of exchange is too slow to be measured by our NMR methods, and that a rate of 1.5×10^5 s^{-1} is required to observe measurable broadening at our experimental conditions.

Acknowledgements

I would first and foremost like to thank my advisor, Professor Bill Casey, for his support and advice through my thesis work. During my time in his lab, Bill taught me the importance of asking the right scientific questions, how to approach and overcome obstacles in the lab, and how to better communicate my research. I am extremely grateful for all that Bill has taught me and for all the science he has helped me accomplish.

I would also like to thank Lawrence Livermore National Lab, Dr. Mavrik Zavarin, Dr. Annie Kersting, and Dr. Steve Harley for allowing me to complete research at LLNL and for their guidance and encouragement. Annie and Mavrik helped increase my knowledge of actinide chemistry, and for that, I am extremely grateful. I owe Steve a great deal of gratitude for his help and lessons in NMR. The experience and advice I obtained from LLNL will continue to help me throughout my career.

I would like to thank the rest of my committee members, Professor Alexandra Navrotsky and Professor Michael Toney, for their help.

I also would like to thank Dr. Andy Ohlin, Dr. Rene Johnson, Chris Colla, Dr. Brent Pautler, and the rest of the group for their continued help, support and friendship.

Finally, I would like to thank my dad, mom, and two sisters, Ernie, Nancy, Caitlin, and Carissa Panasci, for all their love and support throughout my life. And to all of my friends who have continuously been there for me.

Thank you so very much!

The author wrote this dissertation in support of requirements for the degree Doctor of Philosophy in Chemistry at University of California, Davis. The research is funded in part by the LLNL Graduate Scholars Program, and is not deliverable for any United States government

agency. The views and opinions expressed are those of the author, and do not state or reflect those of the United States government or Lawrence Livermore National Security, LLC.

Neither the United States government nor Lawrence National Security, LLC, nor any of their employees makes any warranty, expressed, or implied, or assumes any legal liability or responsibility for the accuracy, completeness, or usefulness of any information, apparatus, product, or process trade name, trademark, manufacturer, or otherwise does not necessarily constitute or imply its endorsement, recommendation, or favoring by the United States government or Lawrence Livermore National Security, LLC, and shall not be used for advertising or product endorsement purposes.

This work was performed under the auspices of the U.S. Department of Energy by Lawrence Livermore National Laboratory under Contract DE-AC52-07NA27344.

TABLE OF CONTENTS

Chapter 1:

Introduction

Chapter 1: Introduction

Section 1.1-Preface

The reactions between water, mineral surfaces, metals, and environmentally relevant ligands are important to understand in order to predict the mobility of hazardous contaminants. The reactions in the natural environment are not well understood due to the lack of knowledge about stoichiometry and structure, particularly for those that occur at the mineral-water interface. Small well-defined molecules that share structural similarities to mineral surfaces can be used to establish correlations between exchange parameters and structure, which can help estimate the reactivity at the water-mineral interface where experiments are difficult or impossible to perform. A correlation between reactivity and structure is potentially useful because, although spectroscopy cannot always determine the detailed structure of surface complexes, some of the key parameters, such as bond length between an exchangeable ligand and metal center, can be calculated using methods of computational chemistry. Establishing reactivity trends is most valuable because predictions of environmental interactions can be made with more confidence.

Predicting the reactivity of hazardous metals, especially actinides, is a pressing concern for environmental scientists, yet many basic measurements of reactivity are not established. The determination of physical and chemical properties of actinide complexes provides a basis for understanding their reactivity in different environmental conditions. Experimentally determined values of ligand-exchange rates, activation entropy, activation enthalpy, and activation volume can also be used to establish trends among the actinide group, which hopefully will allow for experimental results with less dangerous elements, such as uranium (U), to be used to predict the reactivity of the more dangerous transuranic elements, like plutonium (Pu) and neptunium (Np).

In this dissertation, the aqueous chemistry of four environmentally relevant systems are probed. In chapter 2, the rates of water exchange on two monomeric rhodium (Rh(III)) species are determined using isotopically labeled ^{18}O water and mass spectrometry. The experiments are intended to determine the effect of neighboring ligands on exchange parameters. This work is followed by ^{17}O nuclear magnetic resonance (NMR) experiments that determined the water-exchange parameters for a tetrameric iron (Fe(III)) complex. The results were compared to rates for other iron complexes to demonstrate a correlation between exchange rates and structure. The goal is to be able to estimate rate parameters from calculated bond lengths alone, which are much easier to acquire than ^{17}O NMR kinetic data. These two projects were undertaken, in part, to refine my experimental techniques in order to undertake experiments on the more dangerous element, Np. The final chapters of the dissertation describe ^{13}C NMR studies on the carbonate ligand exchange on the neptunyl (VI) species (Np(VI)) and ^{17}O NMR studies on the water exchange on another Np(V) complex. The activation parameters of exchange for each of these systems are reported, and the implications are discussed. This work is relevant to two major areas: geochemistry and actinide chemistry.

Section 1.2- Geochemical Implications

The experiments in this thesis were carried out for one of two reasons. The first is to gain insight into the interaction between water and mineral-oxide surfaces at the molecular scale. Determining correlations between exchange parameters and physical properties, such as bond lengths and neighboring functional groups that might lead to a better understanding of reactivity at the mineral surface. The second is to determine ligand-exchange rates for Np to gain insight into its fundamental aqueous chemistry, and in particular, to be able to quantitatively compare its

aqueous chemistry to that of less dangerous uranyl complexes. These reactions are important to the future of the nuclear industry because assessment of the safety of nuclear storage facilities relies heavily on models that predict the migration of actinide species through the storage barriers, soil, and groundwater[1].

The reactivity of bound water on mineral surfaces is affected by the fundamental reactivity of the metal center, the chemical character of neighboring ligands, how the oxygen is bound to the metal, and its local coordination environment. Due to experimental difficulties in characterizing mineral structures and the lack of techniques to determine ligand exchange rates *in situ*, predictions of ligand-exchange rates often rely on computations [2,3] for dangerous or poorly characterized complexes. Water-exchange rates on aqueous metal-oxide ions have been extensively studied since these values can be used to predict the exchange of other ligands, and also give insight into how structural differences affect the reactivity of bound waters[4-13]. The majority of exchange values have been determined for aqueous monomeric species with closely packed exchangeable ligands, and there are few data on multimeric species[6, 14-18]. Our understanding of the interactions between water and mineral surfaces can be advanced by extending the experimentally determined exchange rates to new systems with different features.

The waters bound to mineral oxide surfaces are often attached as the only exchangeable functional group on a surface metal, which is structurally different from the bound waters of octahedral aqueous ions that contain closely packed bound water that have been used to predict geochemical interactions. Aqueous monomeric ions (e.g. $Fe(H_2O)_6^{3+}(aq)$) have been shown to have an enhanced rate of exchange when deprotonation of a bound water occurs, because the overall charge of the molecule is reduced, thereby weakening the metal-water bond, and rapid proton transfer leads to interconversion between a neighboring bound water and a bound

hydroxyl [6, 8, 10, 11]. On the mineral surface where proton-exchanging ligands are separated, the reactivity trends will be different, and few studies have been carried out on such systems [16,17]. Two monomeric Rh(III) species $[Rh(phen)_2(H_2O)_2]^{3+}$ and $[Rh(phen)_2(H_2O)Cl]^{2+}$ (where phen=1,10-phenanthroline) were studied to determine the rates of exchange of bound waters and hydroxyls, and these experiments are described in chapter 2. Rh(III) was chosen as the model system because it is trivalent, similar to the more environmentally relevant Fe(III) and Al(III), but has extremely slow exchange rates compared to Fe(III) and Al(III) due to its low spin t_2g^6 configuration . These slow rates allow for isotopic substitution to be monitored via mass spectrometry rather than a fast-kinetic method. Water exchange rates for $[Rh(phen)_2(H_2O)_2]^{3+}$ and $[Rh(phen)_2(H_2O)Cl]^{2+}$ were determined to be $k_0^{298} = (5 \pm 0.5) \cdot 10^{-8}$ s^{-1} and $k_0^{298} = (2.5 \pm 1) \cdot 10^{-9}$ s^{-1}, respectively. This result demonstrates that proton conversion between a bound water and a neighboring ligand with an acidic proton increases the rate of oxygen exchange, giving insight into how adjacent functional groups can influence the rate of water exchange.

Most common iron minerals in the soil contain oxo- and hydroxo-bridges, and these minerals can absorb environmental contaminants through ligand exchanges on their surfaces. Most experimental water-exchange rate data exist for Fe(III) monomeric ions [12-15], therefore, experimental values on a multimeric Fe(III) molecule with oxide bridges would be beneficial. Chapter 3 extends the work mentioned in chapter 2, by examining oxygen-isotope exchange of a tetra-Fe(III) oligomer that contains both a μ_3-oxo bridge and a μ_2-OH bridge in the inner-coordination sphere of the four Fe(III) centers ($[Fe_4(OH)_2(hpdta)_2(H_2O)_4]^o(aq)$, where hpdta=2-Hydroxypropane-1,3-diamino-N,N,N',N'-tetraacetate), and an isolated water bound to each of the four Fe(III). The water exchange rate for the Fe(III) complex was experimentally determined to be $k_{eq}^{298} = (8.3 \pm 0.8) \cdot 10^5$ s^{-1} at pH<5, which is ~10^4 times faster than the fully aquated Fe(III)

monomer, and has a water-iron bond length 0.08 Å longer than the aquated monomer making it more reactive. This result was used to determine a correlation between water-exchange rates and metal-ligand bond length, which may soon be measurable at aqueous-mineral interface, [19] and which is easily calculable via modern molecular-orbital methods. Thus, the goal is a simple means of estimating the reactivity of complexes to ligand exchange by an empirical correlation and a simple computer simulation rather than a tedious set of experiments.

The future of nuclear energy is threatened by nuclear accidents and waste-storage leaks [20, 21]. In order to safely use nuclear power and store nuclear waste, it is important to understand the fundamental chemistry of actinides in relevant environments [22-25]. It is also important to know how the actinides behave in various geological environments because they have extremely long half-lives, and therefore, pose a long-term health threat. The isotope ^{237}Np, having a half-life of two million years and high toxicity, is of particular concern. The principle mode of migration of these Np species will be through groundwater, and therefore, many chemical processes must be considered when predicting transport, i.e. solubility, redox behavior, complexation, etc.[25] Studying Np is difficult due to multiple oxidation states, its ability to complex with multiple ligands, its potential to form colloids, and their interaction with mineral surfaces.[15] Experimentally determined rates of ligand exchange on Np can be compared to computer simulations to gain confidence in the results of simulations where experiments are impossible. In chapters 4 and 5, ligand-exchange experiments on the environmentally relevant Np(VI) and Np(V) species are described.

There has been an emphasis on studying Np in acidic to neutral conditions, even though nuclear waste is found at more alkaline conditions, because Np(VI) is less soluble at high pH values. Carbonate, which is present in natural groundwater in high concentrations, complexes

strongly with Np(VI) increasing solubility at high pH and potentially facilitating transport. ^{13}C NMR experiments were performed at various pH values to determine carbonate-exchange rates and trends in reactivity as a function of pH. These experiments are an extension of work previously complete by Stout *et al.* who only determined rates at two pH values [26] and reported no pH dependence for the reaction. We, however, experimentally determined the rate of exchange over the pH range of $8.1 \leq pH \leq 10.5$, and found that above $pH \leq 9.3$ the rate is independent of pH. The average rate of exchange in the pH range of $9.3 \leq pH \leq 10.5$ is $k_{eq}^{298} = 41 \pm 4\ s^{-1}$. Below pH 9, exchange was found to be pH independent, hinting at the presence of a proton-enhanced pathway, which is consistent with the results for carbonate exchange in the carbonate complexes of U(VI) and Pu(CI). The reactivity of Np(VI) and carbonate ligands can then be compared to the reactivity of Pu(VI) and U(VI) to understand how actinides are behaving in geologically relevant alkaline conditions.

Finally, rates of water-exchange for the most soluble species, Np(V), have only been reported once via isotope-exchange experiments at a single pH value by Rabideau [27]. ^{17}O NMR experiments on the aqueous Np(V) ion were performed to determine the rate of water exchange at various pH values, which provide insight into the pH dependence of ligand exchange reactivity for Np(V). The hypothesis in these experiments was that the ^{17}O NMR line-broadening methods of Swift and Connick [28] can be adapted to Np(V) hydrolysis complexes, however, an initial lack of measurable line broadening required additional experiments to ensure paramagnetism and to test for concentration dependence. New ^{17}O experiments at high total Np concentrations are coupled to simulations of the Block-McConnell equations to assess whether the experimental approach is even feasible. As shown in chapter 5, the rates of exchange can be bounded, but not measured by our NMR methods (see below).

Section 1.3- Actinide Chemistry

The actinide family consists of the elements located in the 5 f row of the periodic table, with the 5f valence electrons imparting unique metal properties. In aqueous environments, actinides can exist in multiple different oxidation states, form colloids, interact with ligands, and change behavior with the pH of the environment. These interactions leads to complex aqueous chemistry and the possibility for multiple species to be present.[25] Even though there are experimental limitations when working with actinides due to their radioactivity and toxicity, there is great motivation to study the chemical and physical properties of actinides for the future of nuclear energy. In this thesis two chapters present the work done to determine fundamental reaction rates for two Np species.

Ligand-exchange rates on actinides have been studied, with an emphasis on U and Pu [26, 32-41]. The experiments described in chapters 4 and 5 determine the ligand-exchange rates of Np and compare the results to those for U and Pu. (*Appendix A* and *B* are experiments previously done on U that were extended to study Np at the Seaborg Institute at Lawrence Livermore National Lab.)

Np can exist in oxidation states ranging from Np(III) to Np(VII) with Np(V) and (VI) being the most stable. In the (V) and (VI) oxidation state, the ion contains two opposing axial "yl" oxygens with a high bond order and additional ligands in the equatorial position. Chapter 4 describes the study of the Np(VI) species fully complexed with three bidentate carbonate ligands $[NpO_2(CO_3)_3]^{4-}$. In chapter 5, the aqueous Np(V) species NpO_2^+ with five equatorial waters was studied [28-31]. Both structures are similar to those experimentally determined for the U species $[UO_2(CO_3)_3]^{4-}$ and the aqueous U(VI), with the aqueous U(VI) oxygen-metal bond lengths being shorter, however the aqueous Pu(V) ion contains four equatorial bound waters[29]. Experimentally

determined differences in reactivity and structure between actinides leads to fundamental understanding of this group of elements.

Both Np(V) and Np(VI) are paramagnetic species, with Np(V) containing two unpaired *f*-valence electrons ($5f^2$), and Np(VI) containing one valence electron ($5f^1$). As paramagnetic species, Np ions can be used for NMR exchange experiments via the Swift-Connick formalism [42,43], which was used by Stout *et al*. in their study of the $[NpO_2(CO_3)_3]^{4-}$ ion carbonate exchange [26]. ^{13}C NMR of the $[NpO_2(CO_3)_3]^{4-}$ ion in carbonate solution shows two well-separated peaks, one for the bound carbonate and the other for the free carbonate. The presence of two assignable peaks indicates that exchange between the bound and free carbonate is slow on the NMR time scale. Selective-excitation experiments, which directly measure the rates of substitution and is a second mean of estimating rate coefficients that is independent of assumptions of the Swift-Connick formalism, were used in chapter 4 [40]. In chapter 5, the Swift-Connick formalism was used to study the water exchange on the aqueous NpO_2^+ ion. As mentioned above, and shown in chapter 5, the rate of exchange of waters bound to Np(V) can be bounded, but not measured by our NMR methods.

Section 1.4- Publications

The following dissertation is a compilation of the following publications:

Panasci, Adele F.; McAlpin, J. Gregory; Ohlin, C. André; Christensen, Shauna; Fettinger, James C.; Britt, R. Davis; Rustad, James R.; Casey, William H. "Cooperation between water and hydroxyls in controlling isotope-exchange rates", *Geochim. Cosmochim. Acta.* **2012**, *78*, 18-27.

Panasci, Adele F.; Ohlin, C. André; Harley, Stephen J.; Casey, William H. "Rates of water exchange on the $[Fe_4(OH)_2(hpdta)_2(H_2O)_4]^0$ molecule and its implications for geochemistry", *Inorg. Chem.* **2012**, *51*(12), 6731-6738

Panasci, Adele F.; Harley, Stephen J.; Zavarin, Mavrik; Casey, William H. "Kinetic studies of the $[NpO_2(CO_3)_3]^{4-}$ ion at alkaline conditions using ^{13}C NMR", *Inorg. Chem.* **2014**, *53* (8), 4202-4208

Harley, Stephen J.; Ohlin, C. André; Johnson, Rene L.; Panasci, Adele F.; Casey, William H. "The pressure dependence of oxygen isotope exchange rates between solution and apical oxygen atoms on the $[UO_2(OH)_4]^{2-}$ ion", *Angew. Chem. In. Ed.* **2011**, *50*(19), 4467-4469.

Johnson, Rene L.; Harley, Stephen J.; Ohlin, C. André; Panasci, Adele F.; Casey, William H. "Multinuclear NMR study of the pressure dependence for carbonate exchange in the $[UO_2(CO_3)_3]^{4-}$ (aq) ion", *ChemPhysChem*. **2011**, *12*(16), 2903-2906.

Section 1.5- References

[1] Poinssot, C.; Geckeis, H. *Radionuclide Behavior in the Natural Environment; Science, Implications, and Lessons for the Nuclear Industry*; Woodhead Publishing Ltd.; Cambridge, U.K., 2012.

[2] Rustad, J. R., *Adv. Inorg. Chem.* **2010,** *62*, 391-436.

[3] Wang, J.; Rustad, J. R.; Casey, W. H., *Inorg. Chem.* **2007,** *46*, (8), 2962 - 2964.

[4] Burgess, J. *Metal Ions in Solution*; John Wiley: London, 1978

[5] Casey, W.H.; Rustad, J. R.; Spiccia, L., *Chemistry*. **2009**, *15*, (18), 4496-4515

[6] Helm, L. and Merbach, A. E., *Chem. Rev.* **2005,** *105,* (6), 1923-1959.

[7] Dunand, F. A.; Helm, L.; Merbach, A. E,. *Adv. Inorg. Chem*. **2003**, 54, 1-69.

[8] Lincoln S. F., Richens D. T., and Sykes A. G., *Compr. Coord. Chem. II*. **2004**, *1*, 515-555.

[9] Richens D., *Comments Inorg. Chem.* **2005**, *26*, (5-6), 217-232.

[10] Richens D. T., *The Chemistry of Aqua Ions*. John Wiley: London: 1997.

[11] Richens D. T., *Chem. Rev.* **2005**, *105,* (6), 1961-2002.

[12] Grant, M.; Jordan, R. B., *Inorg. Chem.* **1981,** *20*, (1), 55-60.

[13] Swaddle, T. W.; Merbach, A. E., *Inorg. Chem.* **1981,** *20*, (12), 4212-4216.

[14] Mizuno, M.; Funahashi, S.; Nakasuka, N.; Tanaka, M., *Inorg. Chem.* **1991,** *30*, (7), 1550-1553.

[15] Ostrich, I. J.; Liu, G.; Dodgen, H. W.; Hunt, J. P., *Inorg. Chem.* **1980**, *19*, (3), 619-621.

[16] Springborg J., *Adv. Inorg. Chem.* **1988**,*32*, 55-169.

[17] Tagore R., Chen H., Crabtree R. H., and Brudvig G. W., *J. Am. Chem. Soc.* **2006**, *128,* (29), 9457-65.

[18] Balogh, E.; Todea, A. M.; Muller, A.; Casey, W. H., *Inorg. Chem.* **2007,** *46*, (17), 7087-7092.

[19] Catalano, J. G.; Fenter, P.; Park, C. *Geochim. Cosmochim. Acta* **2009,** 73, (8), 2242-2251.

[20] Pearce, J. M., *Sustainability*, **2012**, *4*, 1173-1187.

[21] Burns, P.C.; Ewing, R.C.; Navrotsky, A., *Science*. **2012**, *335*, 1184-1188.

[22] Silva, R. J.; Nitsche, H., *Radiochimica Acta.* **1995**, *70-71*, 377-396.

[23] Dozol, M; Hagemann, R. *Pure Appl. Chem.* **1993**, *65*, 1081.

[24] Maher, K.; Bargar, J. R.; Brown, Jr., G.E., *Inorg. Chem*. **2012**. *52*, 7, 3510-3532

[25] Clark, D. L.; Hobart, D. E.; Neu, M. P., *Chem. Rev.* **1995**, *95*, 25-48

[26] Stout, B. E.; Choppin, G. R.; Sullivan, J. C., The Chemistry of Uranium(VI), Neptunium(VI), and Plutonium(VI) in Aqueous Carbonate Solutions. In *Transuranium elements: a half century*, Morss, L. R.; Fuger, J., Eds. An American Chemical Society Publication: Washington D.C., 1992; pp 225-232.

[27] Rabideau, S. W. *J. Phys. Chem.* **1963***, 67*, 12, 2655-2659.

[28] Swift, T. J.; Connick, R. E., *J. Chem. Phys.* **1962,** 37, 307-20.

[29] Skanthakumar, S.; Antonio, M. R.; Soderholm, L. *Inorg. Chem.* **2008**, *47*(11), 4591-4595.

[30] Combes, J. M.; Chrisholm-Brause, C. J.; Brown, G. E., Jr.; Parks, G. A.; Conradson, S. D.; Eller, P. G.; Triay, I. R.; Hobart, D. E.; Meijer, A. *Environ. Sci. Technol.* **1992**, *26*, 376-382.

[31] Allen, P. G.; Bucher, J. J.; Shuh, D, K.; Edelstein, N. M.; and Reich, T. *Inorg. Chem.* **1997**, *36*(21), 4676-4683.

[32] Ikeda-Ohno, A.; Henning, C.; Rossberg, A.; Funke, H.; Scheinost, A. C.; Bernhard, G.; Yaita, T. *Inorg. Chem.* **2008**. *47*(18), 8294-8305.

[33] Szabó, Z.; Toraishi, T.; Vallet, V.; Grenthe, I., *Coord. Chem. Rev.* **2006,** *250*, 784-815.

[34] Clark, D. L.; Conradson, S. D.; Donohoe, R. J.; Gordon, P. L.; Keogh, W.; Palmer, P. D.; Scott, B. L.; Tait, D. C., *Inorg. Chem*. **2012**, *52*, 7, 3547-3555.

[35] Brucher, E.; Glaser, J.; Toth, I., *Inorg. Chem.* **1991,** *30*, 2239-2241.

[36] Banyai, I.; Glaser, J.; Micskei, K.; Toth, I.; Zekany, L., *Inorg. Chem.* **1995,** *34*, 3785-3796.

[37] Tait, C. D.; Palmer, P. D.; Ekberg, S. A.; Clark, D. L., "Report on Neptunium Speciation by NMR and Optical Spectroscopies", **1995**.

[38] Lincoln, S. F. *Pure Appl. Chem*. **1979**, *51*, 2059.

[39] Szabo´, Z.; Glaser, J.; Grenthe, I. *Inorg. Chem.* **1996**, *35*, 2036.

[40] Szabo´, Z.; Grenthe, I., *Inorg. Chem.* **1998**, *37*, 6214

[41] Johnson, R. L.; Harley, S. J.; Ohlin, C. A.; Panasci, A. F.; Casey, W. H., *Chemphyschem,* **2011,** *12*, 2903-2906.

[42] Harley, S. J.; Ohlin, C. A.; Johnson, R. L.; Panasci, A. F.; Casey, W.H., *Agnew. Chem. Int. Ed.* **2011**, *50*(19), 4467-4469.

[43] Harley, S. J.; Ohlin, C. A.; Casey, W. H., *Angew. Chem., Int. Ed.***2011,** 75, 3711-3725.

Chapter 2:

Cooperation between bound waters and hydroxyls in controlling isotope-exchange rates

Section 2.1- Introduction

How reactive are functional groups on the surfaces of oxide minerals? Answers to simple questions such as these about Earth materials are often difficult. Mineral surface structures are poorly known and often structurally dissimilar to the convenient experimental models. For example, there is a large library of kinetic data about ligand-exchange rates on aqueous monomeric ions [1, 2], but these aqueous monomer ions usually have closely packed exchangeable ligands, such as bound waters. In contrast, minerals often have isolated exchangeable functional groups, as in the simple example shown in **Figure 2.1** where some bound waters on the edges of goethite are not close packed to one another.

Aqueous monomer ions may also be a poor guide to mineral reactions because the effects of deprotonation are different. For an aquo ion (e.g., $Fe(H_2O)_6^{3+}(aq)$), conversion of an inner-sphere bound water to an inner-coordination bound hydroxyl typically leads to enhanced rates of substitution at all other sites in the inner-coordination sphere. The enhancements are typically in the range of 10^2-10^4 [1-4] and arise for two reasons. First, deprotonation reduces the overall charge of the molecule, thereby weakening bonds to oxygens. Secondly, the bound hydroxyls can change into a water molecule by a simple quick proton transfer among inner-sphere ligands.

The case is different when the proton-exchanging ligands are separated from one another, and such arrangements are probably common at oxide surfaces, as for the water molecules attached to adjacent doubly bridged M-(μ_2-OH)$_2$-M metal centers, labeled '**B**' in **Figure 2.1**. For separated waters there are surprisingly few studies in the literature to draw upon. Springborg (1988[5]) reviews some cases of reactions where bound waters are isolated, but his focus is on equilibrium properties, dimerization and cleavage of the oligomers. Tagore et al. [6] showed that

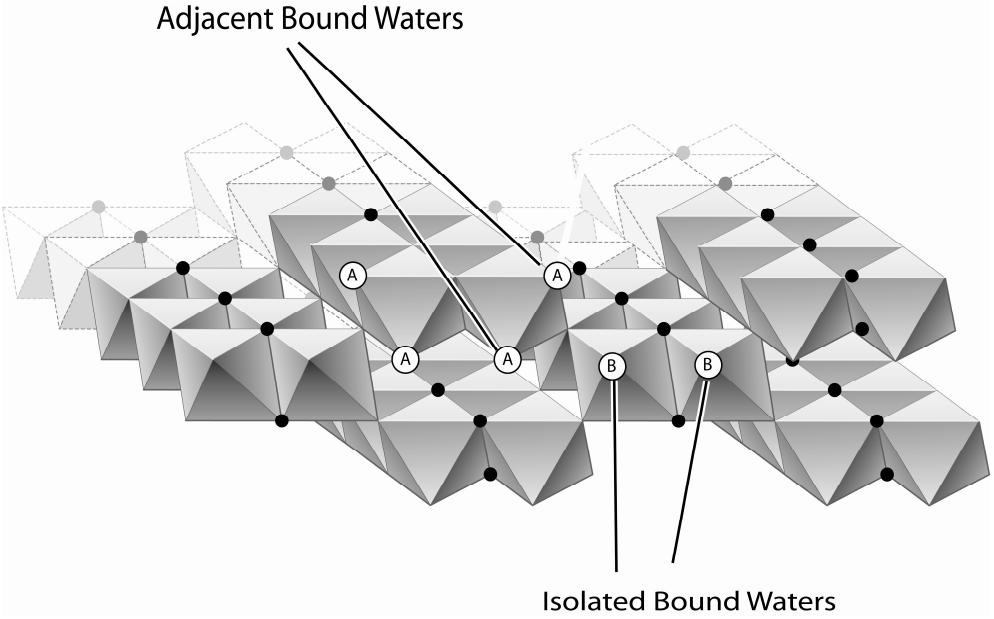

Figure 2.1: A cartoon showing various sites that might have a bound water molecule. At corner sites, denoted '**A**', the metal has more than a single terminal functional group. Thus, '**A**' could signify bound waters, or bound hydroxyls, bonded to a single metal. For sites marked '**B**', the terminal functional groups are on adjacent metals sites and can cooperate via hydrogen bonding. The key point is that these '**B**' functional groups are separated from one another, on different metals, unlike the aquo ions for which much kinetic data exist.

the rates of isotopic exchange of a μ_2-oxo bridge bound to Mn(III) in a dimer complex was much larger if there exists an adjacent bound water.

Here we illustrate the differences by measuring the rates of exchange of waters and hydroxyls in two model complexes. We focus on two distinct Rh(III) species, $[Rh(phen)_2(H_2O)_2]^{3+}$ **[2.1]** and $[Rh(phen)_2(H_2O)Cl]^{2+}$ **[2.2] [Figure 2.2]**. We use Rh(III) because it is a trivalent metal like Fe(III) and Al(III), yet reacts sufficiently slowly that isotope-exchange rates can be easily followed over weeks and because the rates of ligand exchange are much, much slower than the rates of proton transfer, which are usually in the millisecond to microsecond time scales. Our goal is to observe how neighboring functional groups might interact to facilitate, or inhibit, isotope-exchange events. The complexes are similar save for the single replacement of a bound water with an inner-sphere chlorine. The <Rh-OH_2> bond lengths in the crystal structures are nearly identical (2.041±.001, one estimated standard deviation) Ångström in the $[Rh(phen)_2(H_2O)Cl][NO_3]_2$ crystal; 2.036(±.001) and 2.039(±.001) Ångström in the $[Rh(phen)_2(H_2O)_2][NO_3]_3$ crystal).

Section 2.2- Experimental

Section 2.2.1- Syntheses and Characterization

The compounds were made by replacing bound chlorides in two precursor salts. The precursor to both compounds, $[Rh(phen)_2Cl_2]Cl$, was made according to the method established by Gidney et al.[7] where (phen)=1,10-phenanthroline. Compound 2, $[Rh(phen)_2(H_2O)Cl](NO_3)_2$, was synthesized by dissolving $RhCl_2(Phen)_2]Cl$ (642 mg) in hot water (100 ml) to which $AgNO_3$ (570 mg) was added. After two hours of reflux, a pale mixture was obtained, to which concentrated HNO_3 (70%, 8.5 ml) was added. Reflux was continued for another 45 minutes and the mixture was allowed to cool. The precipitated silver chloride was removed on a 0.2 um nitrocellulose filter, and the clear, pale yellow solution concentrated under rotary evaporation at

80 °C to ca 10 ml, and placed in the refrigerator. $Rh(phen)_2(H_2O)Cl](NO_3)_2$ crystals formed after 48 hours of refrigeration.

The $[Rh(phen)_2(H_2O)Cl](NO_3)_2$, containing compound **[2.2]**, was synthesized by chloride abstraction by adding three molar equivalents of $AgNO_3$, followed by addition of a stoichiometric amount of HNO_3 while refluxing. After the solution cleared from milky-white to pale-yellow, a gray AgCl precipitate formed. The mixture was allowed to cool, filtered, and the volume was reduced to one tenth by rotary evaporation. $[Rh(phen)_2(H_2O)Cl](NO_3)_2$ crystals formed after 48 hours of refrigeration. Compound **[2.1]** was synthesized by drop wise addition of 5 ml of KOH (0.1 M) to a 5 mM solution of $[Rh(phen)_2(H_2O)Cl]^{2+}$ to form $[Rh(phen)_2(OH)Cl]^{+}$, followed by heating at 70ºC for 24 hours to form $[Rh(phen)_2(OH)_2]^{+}$. Concentrated nitric acid was then added to reduce the pH ~10 and the solution was refrigerated until crystals formed.

The amount of uncompensated charge in solution was used to estimate pK_a values and was calculated from a charge-balance equation that includes the analyzed concentrations of protons and hydroxide, and the known concentrations of counterions added in the titration **[Figure 2.3]**:

$$Z=\frac{[H^+]+[K^+ \text{or } TMA^+]-[NO_3^-]-[OH]^-}{[\text{Compound}_{Tot}]} \quad (2.1)$$

The counterion concentrations are adjusted for dilution and the Z values were relatively insensitive to values of activity coefficients. The pK_{a1} and pK_{a2} values for **[2.1]** were estimated to be 4.85(±0.03) and 6.9(±0.04), respectively, with the uncertainties reported as the standard

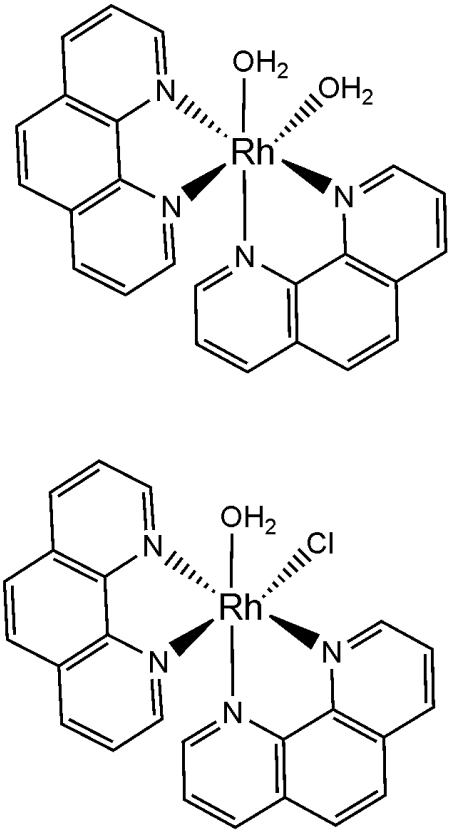

Figure 2.2: (top) Compound **[2.1]** is the $[Rh(phen)_2(H_2O)_2]^{3+}(aq)$ ion with adjacent geminally bound waters, and **(bottom)** Compound **[2.2]** is $[Rh(phen)_2(H_2O)Cl]^{2+}(aq)$ ion with only a single bound water.

error of the regression. To accomplish the titrations, a 5 mM solution of $[Rh(phen)_2(H_2O)_2](NO_3)_3$ was degassed for 1.5 hours and then titrated by 0.1 M KOH addition followed by back-titration using 0.103 M HNO_3. The acid-base chemistry was reversible **[Figure 2.3]**, in the region of the rate experiments.

Potentiometric titrations of solutions in which these crystals had been dissolved identified a pK_a of 6.15 for compound **[2.2]**. In this titration, a 3 mM solution of $[Rh(phen)_2(H_2O)Cl](NO_3)_2$ in 1.1 M TMACl (TMA=tetramethylammonium) background salt was titrated by the addition of 0.050 mM TMAOH. At pH>6.15 the compound decomposes to $[Rh(phen)_2(OH)_2]^{3+}(aq)$ within a day. However, the conversion of **[2.2]** with increased pH is sufficiently slow for us to estimate a $pK_a \approx 6.15$, but makes it difficult to properly assign uncertainties since the titration cannot be reversed. There is a clear inflection in the titration curve.

Section 2.2.2- Structures

A yellow striated plate of $[Rh(phen)_2(H_2O)_2][NO_3]_3$, with approximate orthogonal dimensions 0.37 x 0.33 x 0.14mm^3, was placed and optically centered on the Bruker SMART1000 CCD system at –183°C(90K). The initial unit cell was indexed using a least-squares analysis of a random set of reflections collected from three series of 0.3° wide ω-scans, 10 seconds per frame, and 25 frames per series that were well distributed in reciprocal space. Four ω-scan data frame series were collected [MoKα] with 0.3° wide scans, 25 seconds per frame and 606 frames were collected, at varying phi angles (phi=0°, 90°, 180°, 270°), for each series. The crystal-to-detector distance was 4.29cm, thus providing a complete sphere of data with processing to $2\theta_{max}$=55.08°. Structure of the $[Rh(phen)_2(H_2O)Cl](NO_3)_2$ was collected at

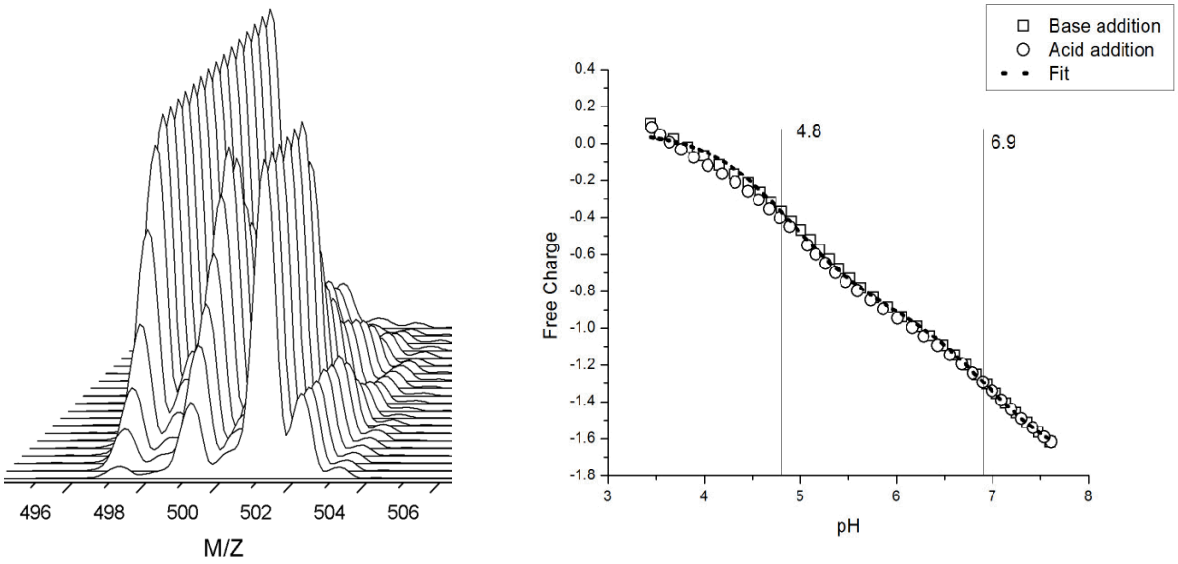

Figure 2.3: (**left**) Stacked plot of the ESI-MS spectra as a function of reaction time showing m/z ratios = 501, 499, and 497, corresponding to: $[Rh(phen)_2(^{18}OH)_2]^+$: $[Rh(phen)_2(^{18}OH)(^{16}OH)]^+$ and $[Rh(phen)_2(^{16}OH)_2]^+$, respectively, as monitored by ESI-MS. Note that the peaks change in intensity with time due to isotope exchange between the ion and the solvent. The solution was reacted at pH=6.3. These peaks vary in relative concentration because of isotopic substitution at the bound waters. (**right**) Titration of compound **[2.1]** to yield pK_{a1} and pK_{a2} at 298 K.

broadly similar conditions and on the same diffractometer only the crystal had approximate orthogonal dimensions 0.15 x 0.23 x 0.39mm^3.

Section 2.2.3- Oxygen-Isotope-Exchange Rates

Rates were estimated by following isotopic substitutions in electrospray-ionization mass spectra (ESI-MS) as a function of time **[Figure 2.3]**. We dissolved $[Rh(phen)_2(H_2O)_2](NO_3)_3$ and $[Rh(phen)_2(H_2O)Cl](NO_3)_2$ crystals that were enriched with $H_2{}^{18}O$ (97% ^{18}O, Isotec) into isotopically normal 0.1 M KNO_3 solution. The solution pH was adjusted to the desired level through the addition of 0.1M KOH and HNO_3 and the solutions placed in a constant-temperature water bath. Periodically, aliquots were taken from these solutions and directly injected into an Agilent 1956b single-quadrupole electrospray mass spectrometer operating with a cone voltage of 20 V in negative mode. Reactions at the Rh(III) center are much, much slower than the handling time. In some experiments with **[2.2]**, experiments were run with, and without, the nitrate background electrolyte; no substantial difference in rates was found.

For **[2.1]**, reaction progress was monitored by observing relative peak intensity of similar ions: $[Rh(phen)_2(^{18}OH)_2]^+$: $[Rh(phen)_2(^{18}OH)(^{16}OH)]^+$: $[Rh(phen)_2(^{16}OH)_2]^+$ as a function of time **[Figure 2.3, left]** and at 298 K. The mass-to-charge (m/z) ratios in the range of 497 to 505 were monitored for isotopic exchanges and the intensities determined by full line-width fitting using a least-squares algorithm that takes into account the full isotopic envelope. The m/z ratios of 501.07, 499.07, and 497.07 correspond to the largest peaks in the doubly enriched, singly enriched, and unenriched species of the $[Rh(phen)_2(OH)_2]^+$ ion, respectively, as $H_2{}^{18}O$ exchanges for $H_2{}^{16}O$. As the rates of protonation/deprotonation are expected to be fast and can occur in the ESI-MS, we expect our chosen set of $[Rh(phen)_2(^{18}OH)_2]^+$: $[Rh(phen)_2(^{18}OH)(^{16}OH)]^+$:

$[Rh(phen)_2(^{16}OH)_2]^+$ to yield accurate rates for the reaction in bulk solution and, because a single set of peaks is followed, the results are insensitive to day-to-day differences in the ESI-MS.

Isotope-exchange rates for **[2.2]** were measured in to the same way as for **[2.1]**, although at 343 K because the reaction was otherwise very slow. The isotopically enriched version of the compound was dissolved into isotopically normal water and exchange of bound $H_2{}^{18}O$ for $H_2{}^{16}O$ was monitored by observing relative peak intensity of $[Rh(phen)_2(^{18}OH)Cl]^+$:$Rh(phen)_2(^{16}OH)Cl]^+$ as a function of time. Activation energies were established by conducting isotope-exchange experiments for compound **[2.1]** at pH=2.9 and temperatures of 338 K, 343 K, 348 K and 353 K, and for compound **[2.2]** at pH=2.1 and 298 K, 311 K, 326 K and 343 K **[Table 2.1]**.

Table 2.1: Compilation of pseudo-first-order rate coefficients, k_{obs} (s^{-1}), corresponding to the characteristic time for isotope-exchange in stable versions of compounds **[2.1]** and **[2.2]**. These rates correspond to isotopic exchange of ^{16}O for ^{18}O bound to functional groups in the compounds.

$[Rh(phen)_2(OH_2)_2]^{3+}$	pH	$\log(k_{obs}/s^{-1})$ in 0.1 M KNO_3
2.5 mM	6.4	-3.6
	6.8	-3.9
	7.2	-4.25
5.0 mM	2.6	-7.33
	2.1	-4.54 (343K)
	2.1	-5.46 (326 K)
	2.1	-6.5 (311 K)
	2.1	-7.3 (298 K)
	3.75	-7.12
	4.83	-4.61
	4.93	-4.7
	5.54	-4.08
	6.71	-3.81
	6.9	-3.55

	6.95	-3.5
	7.26	-3.91
	7.4	-3.99
7.5 mM	5.95	-3.86
	6.32	-3.8
	7.03	-3.75
	7.5	-3.83
	7.8	-4.07
	7.9	-4.22
	8.2	-4.12
$[Rh(phen)_2(H_2O)Cl]^{2+}$		
5.0 mM	2.5	-5.08 (343.15 K)
	3.3	-5.07 (343.15 K)
	4.4	-4.98 (343.15 K)
	5.5	-5.04 (348.15 K)
	6.2	-5.57 (353.15 K)
	6.3	-5.4 (338.15 K)
	6.5	-5.57 (343.15 K)
	6.5	-5.65 (353.15 K)
	6.8	-5.76 (348.15 K)
	7.0	-5.82 (353.15 K)
	2.9	-5.35 (338.15 K)
	2.9	-5.01 (343.15 K)
	2.9	-4.72 (348.15 K)
	2.9	-4.46 (353.15 K)

All isotope-exchange reactions are assumed to satisfy the McKay equations for a pseudo-first-order reaction.[8] Rates were estimated by full line-width fitting of the spectra. The time variation in intensities were fit to an exponential curve: $I(t) = I_0 \cdot e^{-k_{obs} \cdot t}$, where k_{obs} is the observed rate constant, I_0 is the initial relative concentration, I(t) is the relative intensity at time *t*

in seconds. The enthalpy and entropy activation parameters ($\Delta H^{\ddagger}$, $\Delta S^{\ddagger}$) were calculated from this study using Eyring's equation: $k_i = \frac{k_B T}{h} e^{-(\frac{\Delta H^{\ddagger} - T\Delta S^{\ddagger}}{RT})}$, where k_i is the rate constant for water exchange along the '*ith*' pathway in this system, k_B, the Boltzmann constant, *T,* the experimental temperature in Kelvin, *h,* Planck's constant, and *R,* the gas constant. We leave out of the Eyring equation a transmission coefficient, which is essential for simulation but is experimentally inaccessible.[9]

Section 2.3- Results and Discussion

Compounds **[2.1]** and **[2.2]** are structurally similar, yet exhibit profoundly different pH dependencies of reaction, corresponding to different protonation states of the functional groups and the cooperation among them. In **Figure 2.4** we show log(k_{obs}) for both compounds plotted against the acid-base chemistry and speciation. Complex **[2.2]** with a single bound water molecule, shows a familiar reactivity trend where rates increase as pH decreases, corresponding to a proton-enhanced reaction **[Figure 2.4 (top)]**. The rates estimates are limited to pH<pK_{a1} because the compound dissociates slowly to replace the inner-sphere chloride to form $[Rh(phen)_2(H_2O)_2]^{3+}$(aq) above pH=6.15 and we can no longer easily follow the reaction. This hydrolytic loss of the bound chloride ion makes the ion identical to compound **[2.1]**.

Simple rate laws suggest themselves immediately -- for compound **[2.2]**, the observed rate probably has contributions from two pathways: one involving the complex with a bound water ($[Rh(phen)_2Cl(H_2O)]^{2+}$) and the other involves the deprotonated form: ($[Rh(phen)_2Cl(OH)]^{+}$). Recasting the rates to involve contributions from each complex, assuming that the concentration of isotopically distinct water is constant during an experiment:

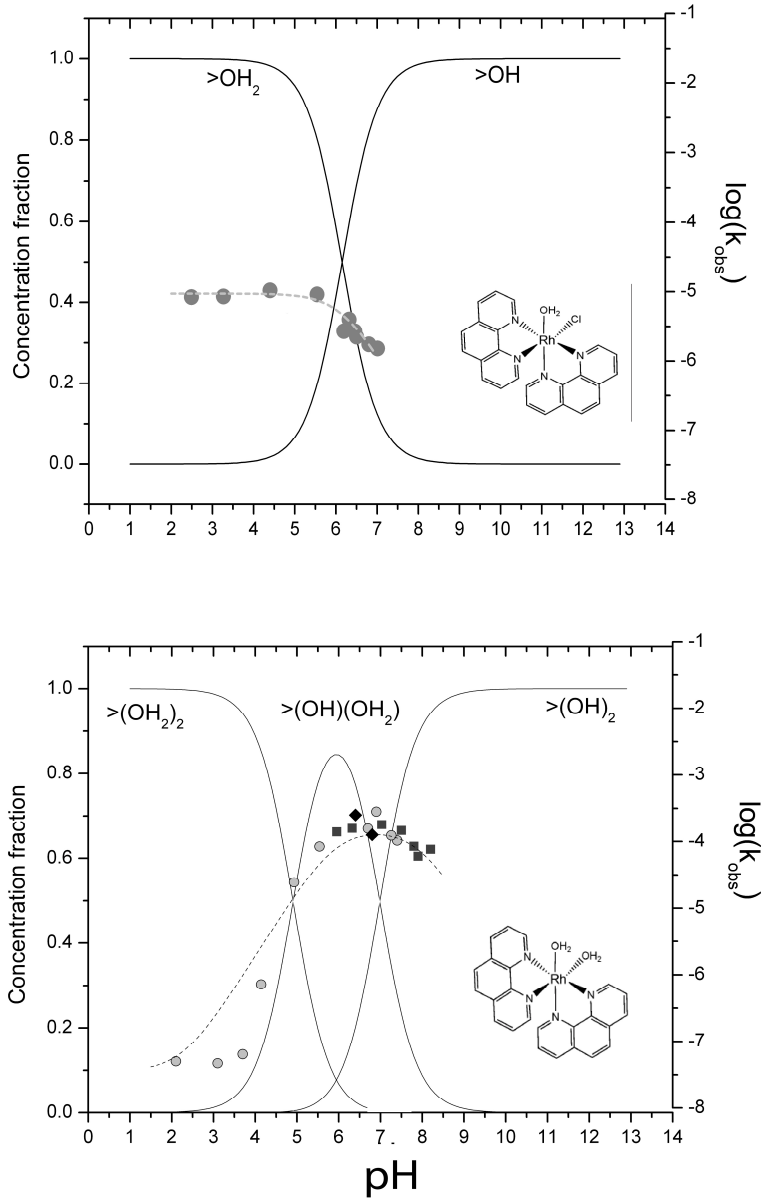

Figure 2.4: Rates of isotope-exchange rates for **[2.2]** (343 K, top) and [1] (298 K, bottom). The symbols are measured k_{obs}, the overall pseudo-first-order rate coefficient for isotope-exchange, including all pathways. The symbols in the bottom figure correspond to experiments at 7.5 (◊), 5.0 (○) and 2.5 (■) mM total metal concentration. Lines show the acid-base speciation from potentiometry and the dashed lines show the fits to rate laws discussed in the text.

$$k_{obs} = \alpha_0 \cdot k_0^{343} + \alpha_1 \cdot k_1^{343} \qquad (2.3)$$

with: $a_0 = \frac{[H^+]}{[H^+] + K_{a1}}$, $a_1 = \frac{K_{a1}}{[H^+] + K_{a1}}$ as the fractions of the molecule **[2.2]** that is fully protonated, and deprotonated, respectively. Fitting the measurements to Eqn. (2.3) assumes a model for the reaction, and independent pathways. Credible fits to the data could be achieved by letting k_1^{343}, but not K_{a1}, freely adjust in a nonlinear regression, yielding: k_0^{343}=8.1·10^{-6} s^{-1} (±2·10^{-6}) with $k_0^{343} \equiv 0$; this assignment of $k_1^{343} \equiv 0$ means that data can be adequately described by assuming that the rate of isotopic exchange of a bulk water for a bound hydroxyl is negligible. The fit to this model is shown in Figure 2.4 as a dashed line through the data at 343 K. Uncertainties were assigned from the standard error of the linear regressions.

We established the activation parameters via experiments at pH=2.9 where the molecule was nearly fully protonated: $\Delta H^{\ddagger}$=132(±3) kJ mol^{-1}, $\Delta S^{\ddagger}$=41.5(±2) J mol^{-1} K^{-1} and k_0^{298}=2.5·10^{-9} s^{-1}(± 1·10^{-9}), respectively. The data may include a small contribution from the enthalpy of protonation because the rates are not fully independent of pH, but such contribution is probably small relative to the bond-rupture enthalpies.

Compound **[2.1]**, with adjacent waters exhibits wide, nonlinear variations in rate **[Figure 2.4, bottom]** and there are three important regions: In Region 1, pH<pK_{a1} and pH<pK_{a2}, the bound waters are fully protonated and rates of isotopic exchange are relatively slow and asymptotically approach a constant value. Correspondingly, this molecule has the highest net charge and the >Rh-OH_2 electrostatic bond strength is also high. The rate parameters, enthalpy and entropy of activation at pH=2.1, when the molecule was near fully protonated, were k_0^{298} =5·10^{-8}(± 0.5·10^{-8}), 119(± 3) kJ mol^{-1}, and 14(±1) J mol^{-1} K^{-1}, respectively, as estimated by application of the Eyring equation to the data.

When fully protonated so as to form an aquo complex, rates of water exchange are expected to asymptotically approach a constant slow rate with decreasing values of pH; this is found in both **[2.1]** and **[2.2]**, and this chemistry is well known from studies of hydrolysable metal ions, such as $Fe(H_2O)_6^{3+}(aq)$, where the rates of exchange are constant as long as the bound waters are fully protonated.

As pH increases to approach the first pK_a value, in **Region 2**, the rates of oxygen-isotope-exchange increase sharply **[Figure 2.4, bottom]** and reach approximately constant values at $pK_{a1}<pH<pK_{a2}$. This pH dependence contrasts markedly between **[2.1]** and **[2.2]** and illustrates the importance of functional-group cooperation in controlling the reactivities. At this condition, the bound H_2O-OH pair can interconvert by proton exchange. The facile interconversion of the bound hydroxyl to a bound water allows for rapid rates of isotopic exchange with an isotopically normal bulk water, as we illustrate as a cartoon in **Figure 2.5**. Such a mechanism was invoked by Rustad et al. [10] to explain oxygen-isotopic exchanges in the $MAlO_4Al_{12}(OH)_{24}(H_2O)_{12}^{7/8+}(aq)$ series of aqueous molecules (M=Al(III), Ga(III) or Ge(IV)) and is well established from structural studies of compounds.[11] Note the scale of the variation--the rates increase by over a factor of $\approx 10^4$ over a small range of pH.

As pH is further increased to above pK_{a2}, the rates decrease sharply, as was observed for when pH increased beyond pK_{a1} for compound **[2.2]**. At this condition, **Region 3**, the exchange rates decrease because the concentration of $[Rh(phen)_2(OH)_2]^+(aq)$ increases with further increases in pH.

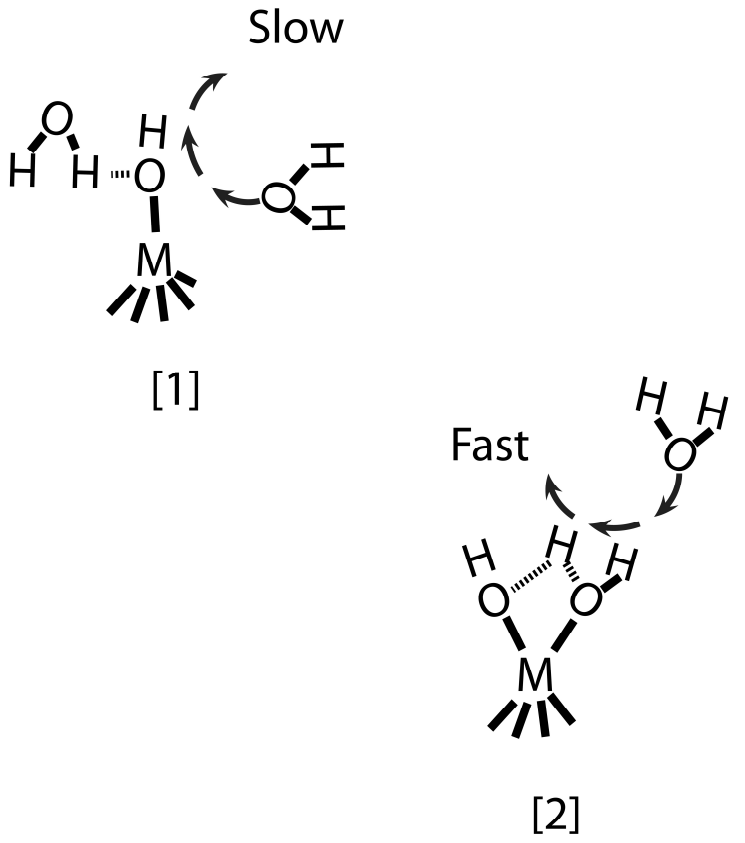

Figure 2.5: Bound waters adjacent to a bound hydroxyl can facilitate rapid isotopic equilibration because they are stronger Brønsted acids than bulk water and the exchanging moiety is an isotopically distinct water molecule and not a hydroxide or hydronium ion. Hydroxide ions are present in such small relative concentrations in near-neutral and slightly basic solutions, where oxides of trivalent metals develop negative charge, that their contribution in negligible. Thus the bound hydroxyl in **[2.1]** reacts slowly and only at rates proportional to the concentration of bound waters. In contrast, **[2.2]** reacts slowly until pH>pK_{a1} when the charge on the compound is reduced by deprotonation, but an adjacent acidic bound water can donate protons via an $H_3O_2^+$ bridge. The rates of exchange of the bound hydroxyl alone are negligible.

As for compound **[2.1]**, we fit the observed rates of isotopic substitution for compound **[2.2]** to a model that assumes that there are three reactive sites that differ in protonation state. Again, expressing a rate law in terms of ionization fractions:

$$k_{obs} = \alpha_0 \cdot k_0^{298} + \alpha_1 \cdot k_1^{298} + \alpha_2 \cdot k_2^{298} \qquad (2.5)$$

where the α_i are:

$$\alpha_0 = \frac{[H^+]^2}{[H^+]^2 + [H^+]K_{a1} + K_{a1}K_{a2}}$$

$$\alpha_1 = \frac{[H^+]K_{a1}}{[H^+]^2 + [H^+]K_{a1} + K_{a1}K_{a2}}$$

$$\alpha_2 = \frac{K_{a1}K_{a2}}{[H^+]^2 + [H^+]K_{a1} + K_{a1}K_{a2}} \qquad (2.6).$$

A nonlinear fit of Eqn. (2.5) to the experimental data employs only the rate coefficients and the K_{ai} values as adjustable parameters. The rates are independent of metal concentration **[Figure 2.4]**, as expected, because these are isotope-exchange reactions with the isotopically distinct solvent in great excess.

Again, the data are adequately described if we assume that $k_2^{298} \equiv 0$ can account for pH variation **[Figure 2.4]**, but the fit is poor unless the pKa_1 value is roughly an order of magnitude higher than indicated by the potentiometry. The pH variation in the rates is controlled by the α_1 values and no addition of second-order terms provides a better fit. The most striking deviation from the experimental data lies in the pH range where rates are increasing; the fits are constrained to have a slope given by α_1, which is more gentle than the experimental data.

The experimental results, overall, are consistent with a simple view of the isotope-exchange reactions: the fastest way for a hydroxyl oxygen to exchange with solution is to

convert it to a water molecule by proton addition from an adjacent, acidic bound water. Bond lengthening contributes as steric packing can lengthen the M-OH_2 bond and shortens the adjacent M-OH bond as protons are transferred. At these conditions of near-neutral pH, the exchanging moieties are water molecules and thus rates of exchange are sensitive to the position and acidity of adjacent functional groups. There may be other processes at work that cause the extraordinarily rapid increase in rates near pK_{a1} for **[2.1]**, but we cannot resolve them. More importantly, for both compounds **[2.1]** and **[2.2]**, we cannot resolve any isotopic exchanges that involve the fully deprotonated complexes at $pH>pK_{a2}$ for compound **[2.1]** or pK_{a1} in the case of compound **[2.2]**. Such rates may proceed at a slow rate, but we cannot resolve them in the presence of the much more rapid rates of isotopic exchange involving the bound waters and, again, we are limited by the rate model to pH dependencies that scale like $\log(\alpha_i)$ in our model for exchange. Although incoming hydroxide ions or water molecules may exchange for an isolated bound hydroxyl, these rates are so small as to be negligible.

Clearly, differences in the cooperation among functional groups exert great control over the pH dependence of these isotope-exchange reactions. There is, at present, poor information about the hydrogen-bonding structure and dynamics at oxide surfaces but one can easily imagine settings where such cooperation plays a role in the surface chemistry. Three conditions are illustrated in **Figure 2.6** where the protonation state of two truncated surfaces, chosen to expose vicinal and geminal bound water functional groups, are compared as a function of pH and the point-of-zero charge (PZC) of the surface. By drawing comparison with these experiments, the key controls are the acid-base chemistry of the bound waters and their proximity to one another. For a material with PZC at near-neutral pH, such as the oxides of trivalent metals, the concentration of $[OH^-]$ will be so low that the direct-exchange pathway is unimportant. Isotope

exchanges involve a water-molecule-for-water-molecule exchange and the rates of reaction of the bound hydroxyls are, in this study, so slow as to be negligible.

However, the rates are fully consistent with those observed for other ions and clusters. In **Figure 2.7** we show how the activation parameters for **[2.1]** and **[2.2]** in their fully protonated form (or close to fully protonated) compare to other ions and clusters.[4, 12] The near-linear correlation derives from the Arrhenius rate law, but it is reassuring to find agreement between the measurements described here and those for other ions and nanoclusters. Low-spin Rh(III) ions with t_2g^6 electronic configurations are expected to be inert with a dissociative (or interchange-dissociative) water exchange pathway.[2, 4, 13, 14] The lack of lability is due to the strong ligand field associated with the t_2g^6 configuration and the relatively high charge of the trivalent metal, creating strong electrostatic metal-ligand attraction. A dissociative mechanism around Rh(III) is favored because it has a small inner-coordination relatively high charge of the trivalent metal, creating strong electrostatic metal-ligand attraction. A dissociative mechanism around Rh(III) is favored because it has a small inner-coordination sphere and high charge density. As a result, outer-sphere solvent molecules must overcome a greater electrostatic repulsion when attempting to insert into the inner-coordination sphere and make a seven-ligand transition state, which is unlikely.[14-19]

However, such arguments about transition states and the classification of mechanisms [20] were developed for octahedral metal ions.[21, 22] The extent to which they apply to polymeric structures remains unclear and only experiments on model systems and simulation can establish the relevance.[23-29] It appears that the general trends in water-exchange rates across the Periodic Table are not fundamentally disrupted for larger, and even nanometer-size, ions, with the exception of the changes in pH dependencies. When fully protonated, these functional groups

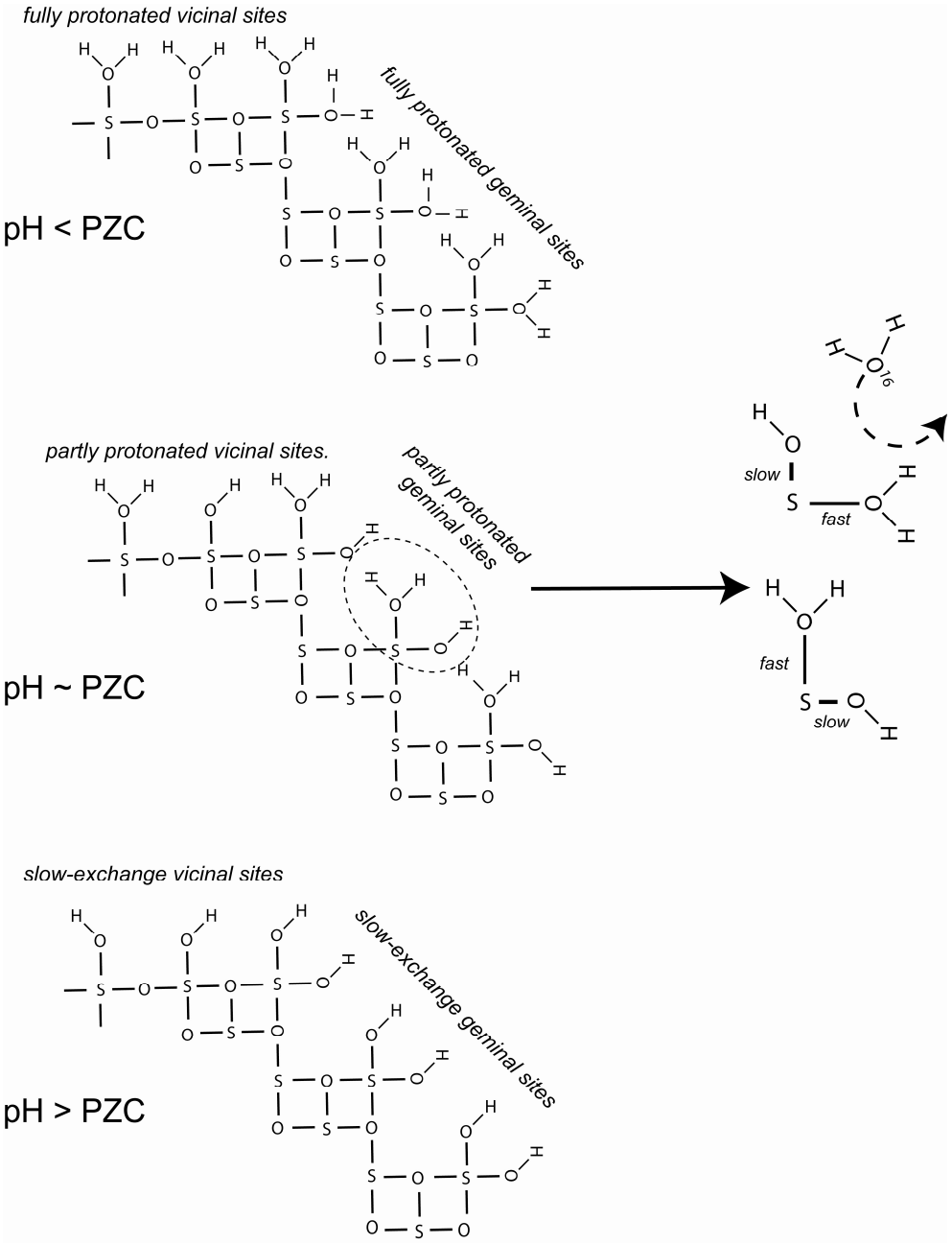

Figure 2.6: Hydrogen-bonded networks affect both rates and pH dependences of isotope- and ligand-exchange reactions. There are two causes: First, the reduction of charge on an individual metal by deprotonation of a bound water weakens bonds to other ligands in the same inner-coordination sphere. Thus bonds to remaining waters are longer. Secondly, proton sharing allows for facile interconversion from a bound hydroxide to a water molecule that can then exchange for bulk waters. Waters are in overwhelming excess relative to bulk hydroxides at the pH condition of most trivalent-metal oxide minerals in water.

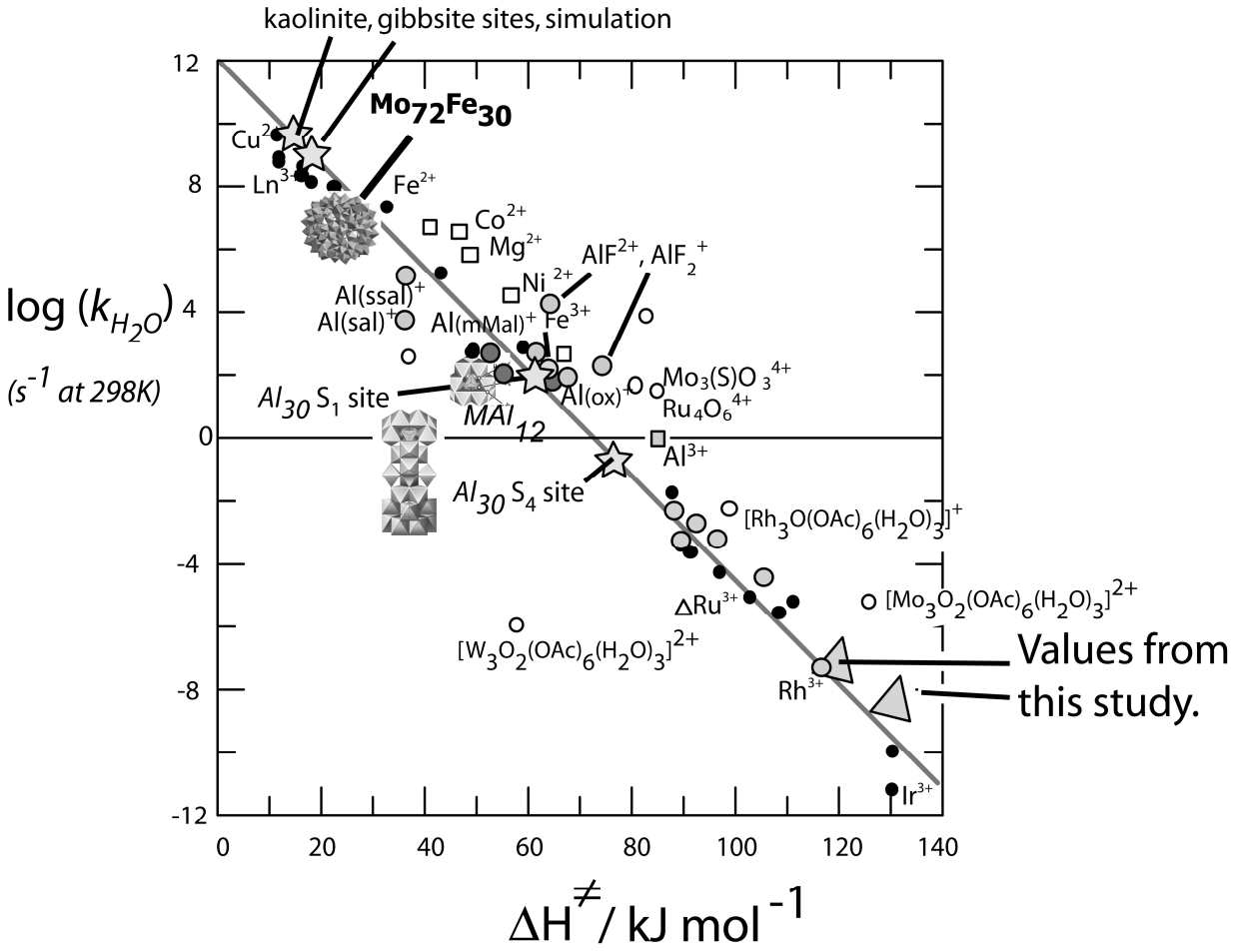

Figure 2.7: Selected values of the rate coefficient for exchange of a bound and bulk water (here denoted $k_{298,}$ which corresponds to k_0^{298} for complexes **[2.1]** and **[2.2]** discussed in the text) compared with the corresponding experimental $\Delta H^{\ddagger}$ values for water exchange rates from fully protonated aqueous complexes and nanometer-size aqueous clusters (adapted from [1,12]and [27]). The large gray triangle symbols correspond to the data presented here. Data in the large stars are from computer simulations.[29]

are relatively insensitive to changes in structure, save for the cooperative effects of having an adjacent, acidic water, such as we detail here.

Section 2.4- Conclusions

These simple Rh(III) molecules illustrate how functional groups can cooperate to influence rates of isotopic substitution. At these conditions, a bound water exchanges most rapidly with bulk solution, much more rapidly than a bound hydroxyl. Thus the pH dependencies of isotope-exchange rates can be inverted and dramatically accelerated, if the two functional groups can shuttle protons. However, we don't want to overemphasize the generalities because single metals with two terminal functional groups, the geminal functional groups, will probably be rare on mineral surfaces and because rates of proton exchanges may approach rates of ligand exchanges for many geochemical metals. Regions where one could imagine such environments might be at corner- or kink-type metal sites, such as '**A**' in **Figure 2.1**, or certain crystallographic faces, such as we show in **Figure 2.6**. Timescales for proton exchanges at mineral surfaces of trivalent metals are poorly known but are probably in the millisecond-to-microsecond time scale.[30] If these timescales are more rapid than ligand exchange, bound waters will interconvert with an adjacent, close-packed bound hydroxyl by rapid proton exchange, relaxing all inner-sphere bonds.

The situation is more subtle, and more uncertain, when metal sites are separated by oxide bridges so that the functional groups are vicinal. In this case deprotonation of a water bound to one metal site also reduces charge, but it will have negligible effect on inner-coordination-sphere bonding in the adjacent metal with the exchangeable water. We don't anticipate the enormous labilization seen in the Rh(III) complexes because differences in charge-induced labilization are

muted. The largest effect will be proton sharing via $H_3O_2^+$ bridges that allows substitution to proceed via a bulk water, which is present in such overwhelming concentration (~55.55 M) relative to hydroxide ion in near-neutral solutions that the pathway is dominant. Hydrogen bonds may also kinetically stabilize a functional group to isotopic exchange, but will only be important in cases where the barrier energy is small relative to the energies of hydrogen bonding. In the case of the Rh(III) complexes, barrier energies are on the order of ~100 kJ mol^{-1}, much larger than the energy of hydrogen bonding. Contributions from hydrogen-bond energy may be important for the ferric-(hydr)oxides where the barrier energies are low (~20-40 kJ mol^{-1}).[2, 4, 31]

Section 2.5- References

[1] Richens, D. T., *Chem. Rev.* 2005, *105*, 1961-2002.

[2] Richens, D. T., *The Chemistry of Aqua Ions*. John Wiley: New York, 1997; p 592 pp.

[3] Lincoln, S. F.; Richens, D. T.; Sykes, A. G., *Compr. Coord. Chem. II* 2004, *1*, 515-555.

[4] Helm, L.; Merbach, A. E., *Chem. Rev.* 2005, *105*, 1923-1959.

[5] Springborg, J., *Adv. Inorg. Chem.* 1988, *32*, 55-169.

[6] Tagore, R.; Chen, H.; Crabtree, R. H.; Brudvig, G. W., *J. Am. Chem. Soc.* 2006, *128*, 9457-65.

[7] Gidney, P. M.; Gillard, R. D.; Heaton, B. T., *J. Chem. Soc., Dalton Trans.* 1972, *1972*, 2621-8.

[8] McKay, H. A. C., *Nature* 1938, *142*, 997-8.

[9] Rustad, J. R.; Stack, A. G., *J. Am. Chem. Soc.* 2006, *128*, 14778-14779.

[10] Rustad, J. R.; Loring, J. S.; Casey, W. H., *Geochim. Cosmochim. Acta* 2004, *68*, 3011-3017.

[11] Ardon, M.; Bino, A., *Struct. Bond.* 1987, *65*, 1-28.

[12] Richens, D., *Comment. Inorg. Chem.* 2005, *26*, 217-232.

[13] Laurenczy, G.; Rapaport, I.; Zbinden, D.; Merbach, A. E., *Magn. Res. Chem.* 1991, *29*, S45-S51. .

[14] Cusanelli, A.; Frey, U.; Richens, D. T.; Merbach, A. E., *J. Am. Chem. Soc.* 1996, *118*, 5265-5271.

[15] Houston, J. R.; Yu, P.; Casey, W. H., *Inorg. Chem.* 2005, *44*, 5176-5182.

[16] Houston, J. R.; Olmstead, M. O.; Casey, W. H., *Inorg. Chem.* 2006, *45*, 7799-7805.

[17] Drljaca, A.; Spiccia, L.; Krouse, H. R.; Swaddle, T. W., *Inorg. Chem.* 1996, *35*, 985-90.

[18] Drljaca, A.; Hubbard, C. D.; Van Eldik, R.; Asano, T.; Basilevsky, M. V.; Le Noble, W. J., *Chem. Rev.* 1998, *98*, 2167-2289.

[19] Drljaca, A.; Zahl, A.; Van Eldik, R., *Inorg. Chem.* 1998, *37*, 3948-3953.

[20] Langford, C. H.; Gray, H. B., *Ligand Substitution Processes. 2nd Ed*. Benjamin: New York, 1974; p 120 pp.

[21] Swaddle, T. W., *Inorg. Chem.* 1980, *19*, 3203-3205.

[22] Swaddle, T. W., *Comment. Inorg. Chem.* 1991, *12*, 237-58.

[23] Swaddle, T. W., Ligand substitution dynamics in metal complexes. In *Physical Inorganic Chemistry: Reactions, Processes and Applications*, Bakac, A., Ed. Wiley: 2010; Vol. 2, pp 339-393.

[24] Spiccia, L.; Casey, W. H., *Geochim. Cosmochim. Acta* 2007, *71*, 5590-5604.

[25] Casey, W. H.; Swaddle, T. W., *Rev. Geophys.* 2003, *41*, 4/1-4/20.

[26] Casey, W. H.; Rustad, J. R.; Spiccia, L., *Chem-Eur. J.* 2009, *15*, 4496-4515.

[27] Ohlin, C. A.; Villa, E. M.; Rustad, J., R.; Casey, W. H., *Nat. Mat.* 2010, *9*, 11-19.

[28] Casey, W. H.; Rustad, J. R., *Annu Rev. Earth Sci.* 2007, *35*, 21-46.

[29] Wang, J.; Rustad, J. R.; Casey, W. H., *Inorg. Chem.* 2007, *46*, 2962 - 2964.

[30] Houston, J. R.; Casey, W. H., *Dalton T.* 2005, 3667-3671.

[31] Balogh, E.; Todea, A. M.; Muller, A.; Casey, W. H., *Inorg. Chem.* 2007, *46*, 7087-7092.

Chapter 3

Rates of water exchange on the $[Fe_4(OH)_2(hpdta)_2(H_2O)_4]^o$ molecule and its implications for geochemistry

Section 3.1- Introduction

Soil eliminates harmful contaminants from water and this purifying action originates largely from ligand- and electron-exchange reactions at the surface of iron-hydroxide and manganese-oxide minerals. In aerobic environments, the iron minerals have high-spin ferric irons separated by oxo- or hydroxo-bridges; these include goethite (α-FeOOH), hematite (α-Fe_2O_3) and lepidocrocite (γ-FeOOH). The minerals adsorb contaminant ions via ligand exchange at their surfaces, sometimes transforming them, and thus prevent the toxicants from entering drinking water and the biosphere. The reversal of these reactions can be profoundly dangerous--reductive dissolution of arsenic-rich ferric-hydroxide minerals, for example, may be the cause of mass arsenic poisonings in south Asia[1] where tens of millions of people are suffering from arsenic-related conditions. In this case, arsenic is released to groundwater when the ferric-hydroxide surface is reduced and the solid corrodes. This water is used for drinking.

Environmental scientists would like to be able to know and predict rates of ligand- and electron exchanges at the functional groups on these mineral surfaces. This work is challenging because the surface structures are not well known, nor easily characterized. No spectrometric methods are yet able to easily measure the ligand-exchange rates *in situ* and predictions often rely heavily on computer simulations.[2,3] Ideally these simulations would be tested using experiments on small oxide-bridged molecules for which the solution structures are confidently known and for which spectroscopic characterization is easy. Yet, there are surprisingly few experimental data describing elementary water-exchange reactions on Fe(III) complexes and virtually all of these are on monomeric complexes. Data exist for the $[Fe(H_2O)_6]^{3+}$ ion, the first hydrolysis complex, $[FeOH(H_2O)_5]^{2+}$ [4,5], and for aminocarboxylate monomer ions [6], but most of these have seven-coordinated Fe(III) **[**see **Table 3.1]**. Rate information also exists for a small set

of Fe(III)-porphyrin complexes that have six-coordinated Fe(III)[11,14] and two axially opposed bound waters. Data on multimeric Fe(III) molecules with oxide bridges and isolated waters would, of course, be most relevant to geochemistry because these can be used to better approximate the oxo- and hydroxo-bridged surface metals. However, save for the data of Balogh *et al.*[15] on a Keplerate ion, there are no measurements for water-exchange rates on multinuclear iron complexes **[Table 3.1]**.

Table 3.1: Rate data for exchange of bound and bulk waters for various aqueous iron complexes (see [7,8]).

Complex	k^{298}	$\Delta H^{\ddagger}$	$\Delta S^{\ddagger}$	$\Delta V^{\ddagger}$	Reference
		Fe(II)			
$[Fe(H_2O)_6]^{2+}$	$4.39\cdot10^6$	41.4	+21.2	+3.8	9
$[Fe(EDTA)(H_2O)]^{2-}$	$2.7\cdot10^6$	43.2	+23	+8.6	10
		Fe(III)			
$[Fe(H_2O)_6]^{3+}$	$1.6\cdot10^2$	64.0	+12.1	-5.4	4
$[Fe(OH_2)OH]^{2+}$	$1.2\cdot10^5$	42.4	+5.3	+7.0	4,11,12
$[Fe(CDTA)(H_2O)]^{-}$	$1.3\cdot10^7$	27	-18	+4.0	13
$[Fe(EDTA)(H_2O)]^{-}$	$7.2\cdot10^7$	24.3	-13	+2.2	13
$[Fe(HEDTA)(H_2O)]^{o}$	$7.8\cdot10^7$	22	-20	+2.1	13
$[Fe(EDDS)(H_2O)]^{-}$	$4.3\cdot10^5$	48	+24	-14.4	13
$[Fe(PhDTA)(H_2O)]^{-}$	$1.2\cdot10^7$	26	-22	+4.6	6
$[Fe(\alpha\text{-EDDADP})(H_2O)]^{-b}$	$2.3\cdot10^8$	36	+36	+3.0	13
	$2.5\cdot10^6$	24	-42		
$[Fe(TPPS)(H_2O)_2]^{3-}$	$2.0\cdot10^6$	67	+99	+7.9	11
	$1.4\cdot10^7$	57.3	+84.5		14
$[Fe(TMPyP)(H_2O)_2]^{5+}$	$4.5\cdot10^5$	71	+100	+7.4	11
	$7.8\cdot10^5$	57.7	+67.5		14
$[Fe(TMPS)(H_2O)_2]^{3-}$	$2.1\cdot10^7$	61	+100	+11.9	11
$[Fe_4(OH)_2(hpdta)(H_2O)_4]^{o}$	$8.1\cdot10^5$	46	+22	+1.85	this paper
$Mo_{72}Fe_{30}$ *	$6.7\cdot10^6$	26.3	-26		15

CDTA = cyclohexanediaminetetraacetic acid; EDTA=ethylenediaminetetraacetate, CDTA= *trans*-1,2-diaminocyclohexanetetraacetate, HEDTA=monoprotonated form of EDTA, EDDS=*s*,*s*-ethylenediaminedisuccinate, PhDTA=*o*-phenylenediamine-*N*,*N*,*N'*,*N'*,-tetraacetato, EDDADP=ethylenediaminediacetatedipropionate, H_2TPPS=*meso*-tetrakis(*p*-sulfonateophynyl)porphine, H_2TMPyP= *meso*-tetrakis(*N*-methyl-4-pyridyl)porphine, H_2TMPS=*meso*-tetrakis(sulfonatomesityl)porphine

*Stoichiometry for this molecule is:
$[Mo_{72}Fe_{30}O_{252}(CH_3COO)_{12}[Mo_2O_7(H_2O)]_2[H_2Mo_2O_8(H_2O)](H_20)_{91}]\bullet\sim150\ H_2O$

In this paper we describe water-exchange rates for a tetra-Fe(III) molecule, which has both a μ_3-oxo bridging two Fe(III) and a carbon, and a μ_2-OH bridge in the inner-coordination sphere of each of the four Fe(III) centers. This molecule is one of a class of potential molecular magnets[16-21] and we selected the $[Fe_4(OH)_2(hpdta)_2(H_2O)_4]^o(aq)$ molecule (hpdta= 2-Hydroxypropane-1,3-diamino-N,N,N',N'-tetraacetate) for detailed study among these multinuclear complexes because of its aqueous stability and solubility. In solution this molecule presents an isolated Fe-bound water in a well-constrained structure and adjacent to oxo bridges. This molecule has two sets of iron-bound bridging oxygens in the inner-coordination sphere of each of the four Fe(III) **[Figure 3.1]** and the bound waters are isolated from one another.[22] Our ultimate goal is to establish a firm correlation between experimental rates of water exchange with some simple easily calculable or measurable property, such as $<Fe^{III}\text{-}OH_2>$ bond lengths. New experimental developments, such as crystal-truncation-rod X-ray-scattering experiments [23], indicate that $<Fe^{III}\text{-}OH_2>$ bond lengths may be soon measureable at the aqueous-mineral interface and they can certainly be calculated using *ab initio* methods. Thus, such a correlation for high-spin oxo Fe(III) complexes would be a useful advance.

Section 3.2- Experimental Methods

Section 3.2.1- Synthesis and Characterization

$[Fe_4O(OH)(hpdta)_2(H_2O)_4](NH_4)\bullet 9\ H_2O$ **[3.1]** (hpdta= 2-Hydroxypropane-1,3-diamino-N,N,N',N'-tetraacetate) was made according to Schmitt *et al.* [25] **[Figure 3.1]** NH_3(aq) (2 M, 84 ml) was added to an aqueous suspension of H_5hpdta (5.18 g, 64 ml). The resulting solution was added drop wise to a stirred solution of $Fe(NO_3)_3\cdot 9H_2O$(aq, 0.34 M, 80 ml), leading to a change in color from yellow to dark red.

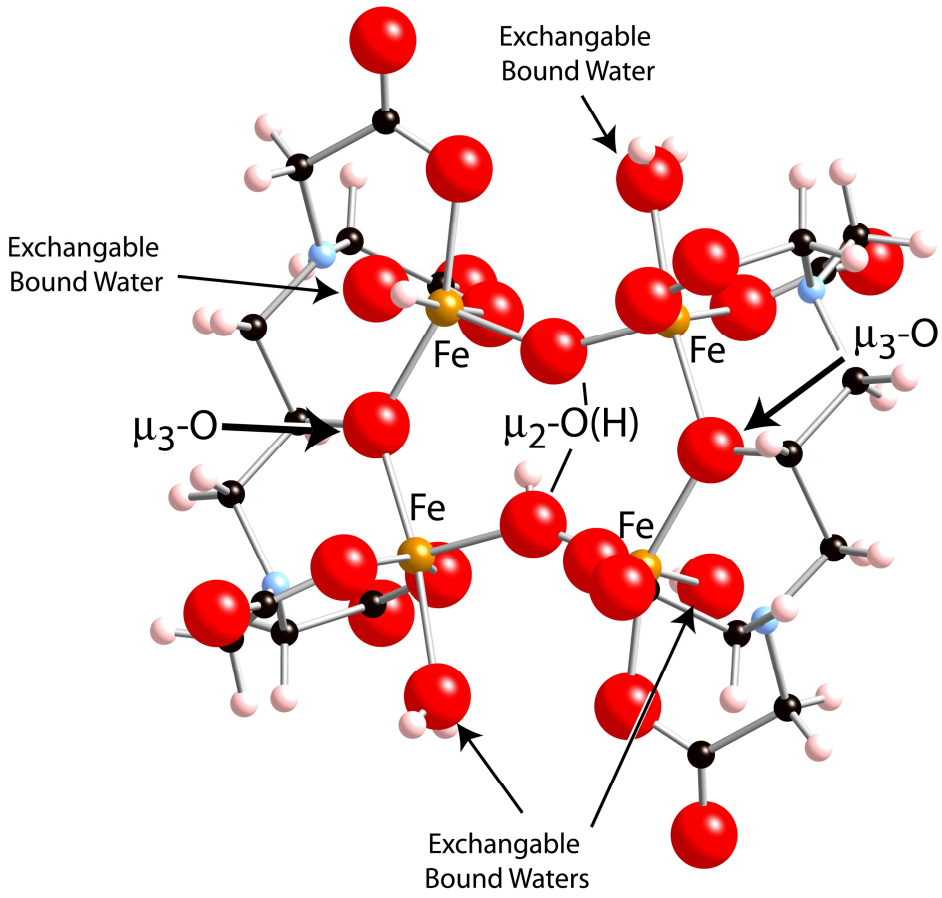

Figure 3.1: The $[Fe_4O(OH)(hpdta)_2(H_2O)_4]^-$ ion in crystals of $[Fe_4O(OH)(hpdta)_2(H_2O)_4](NH_4)\bullet 9\ H_2O$ [24]. The site labeled μ_2-O(H) indicates a proton disordered between the two equivalent μ_2-oxo bridges in the solid state. Both of these bridges are fully protonated at pH<pKa_1 in solution. The inner-coordination-sphere of each Fe(III) has a single bound water, one μ_2-OH bridge, one μ_3-oxo bridge, a bound amine nitrogen and two carboxylate oxygens.

Dimethyl acetamide (64 ml) was added to the solution and slow evaporation over several days yielded brick-red plate-like crystals with a yield of 37% based on $Fe(NO_3)_3$•9 H_2O. The crystals were collected by filtration, air dried and ground to afford a homogeneous powder. Elemental analysis by Galbraith Laboratories of $C_{22}Fe_4H_{57}N_5O_{33}$ found (calculated): C 22.8 (23.12), H 5.56 (5.03), N 8.42 (6.13), Fe 16.50 (19.54), O 46.72 (46.19) % w/w. The crystallographic cell parameters are consistent with those reported by Schmitt *et al.*[24]

Aqueous solutions of the compound at the self-buffering pH were characterized by ESI-MS at a cone voltage of -20V using an HP Agilent MSD G1956b single-quadrupole electrospray-ionisation mass spectrometer, equipped with a syringe pump for direct injection of solutions into the spray chamber at 30 □l min^{-1}. Signals corresponding to $[Fe_4O(OH)(hpdta)_2]^-$ (890.9 m/z), $[Fe_4O_2(hpdta)_2]^{2-}$ (444.9 m/z) and $[Fe_4(hpdta)O_3]^{3-}$ (302.3 m/z) were observed. Assignments were confirmed by comparing the peak shapes with theoretical isotopic envelopes **[Figure 3.2]**.

Section 3.3.2- Solution Chemistry

Evidence for two pKa values was found in the pH region 4<pH<8 both by acid-base potentiometry and by modeling UV-VIS spectra as a function of pH. Potentiometric titrations were performed using a Metrohm 718 STAT Titrino auto-titrator and a 5mM solution of **[3.1]** with 0.1 M KNO_3 background salt. Titration was done by addition of 0.1 M KOH followed by back titration using 0.1 M HNO_3. The titration over the region 4<pH<8 was reversible **[Figure 3.3]**. Plots of uncompensated charge (Z) versus pH were consistent with a single protonation reaction when pH~pK_{a1}:

$$Z=\frac{[H^+]+[K^+]-[NO_3^-]-[OH^-]}{[FeO(OH)(hpdta)_2(H_2O)_4]_{total}} \quad (3.1)$$

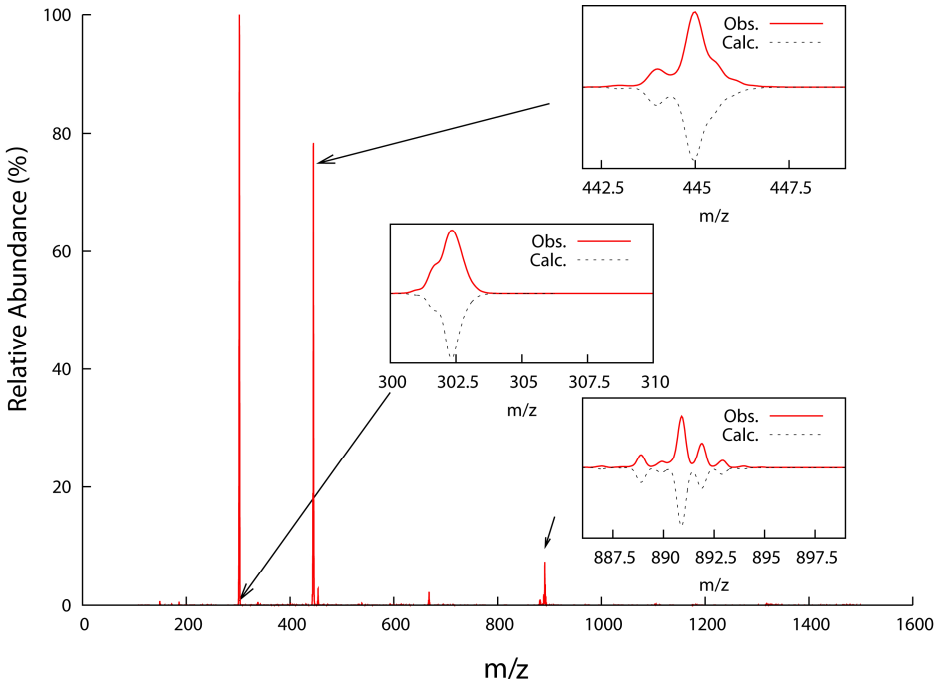

Figure 3.2: A plot of a negative-ion ESI-MS spectra of **[3.1]** taken at pH~6, corresponding to the natural pH upon dissolution of the crystals into water. The three inset plots show the observed and calculated spectra for the most-abundant peaks: 302.3 m/z corresponding to $[Fe_4(hpdta)_2O_3]^{3-}$, 444.9 m/z corresponding to $[Fe_4(hpdta)_2O_2]^{2-}$, and 890.9 m/z corresponding to $[Fe_4(hpdta)_2O(OH)]^{-}$.

UV-VIS titrations were carried out using a Cary 300 UV-VIS spectrometer. 3 ml samples of 0.222mM $[Fe_4O(OH)(hpdta)_2(H_2O)_4](NH_4)\bullet 9H_2O$ with 13.1 mM $TMAClO_4$ (TMA= Tetramethylammonium) background salt were made with varying amounts of $HClO_4$ and TMAOH to create a series of samples with pH values that ranged from 3.7 to 10.2. For each sample, the absorbance for $200<\lambda<800$ nm was recorded.

Section 3.2.3- NMR Spectroscopy

Nuclear magnetic resonance (NMR) measurements were carried out on the solutions using a Bruker Avance DRX 500 MHz (11.75 T, ^{17}O:67.8 MHz; ^{31}P:202.4 MHz) spectrometer equipped with a 5-mm broad-band probe. The ^{17}O spectra were acquired using single-pulse excitations using 10.5 μs $\pi/2$ pulses with 0.6 s recycle delay. The sweep width was set to 2042.48 Hz. The samples were also enriched in ^{17}O; to a 3-ml sample was added 10 μl of 40% $H_2{}^{17}O$ (Isotec Laboratories) so that eight acquisitions could establish adequate signal-to-noise ratio in the spectrum. Temperature was controlled using the Bruker Avance system temperature controller, which is precise and accurate to ±0.5˚C. An acidified 0.05 M $NaClO_4$ solution was used as the diamagnetic standard.

Rate experiments were initiated by dissolving varying amounts, but typically 0.012 g, of **[3.1]** in 463 μL of 0.108 M sodium perchlorate solution. Microliter amounts of perchloric acid were added to lower the pH and then the solutions were brought up to a volume of 1.00 ml. In these experiments, the final $[Fe_4O(OH)(hpdta)_2(H_2O)_4](NH_4)\bullet 9\ H_2O$ concentration was 10 mM and the sodium perchlorate concentrations was 0.05 M. Although the molecule is persistent for days in the pH range $4.0<pH<8.5$, and detectable as an intact molecule in ESI-MS spectra, it dissociates in strongly acidic solutions to form Fe(III) monomers and ultimately iron-hydroxide

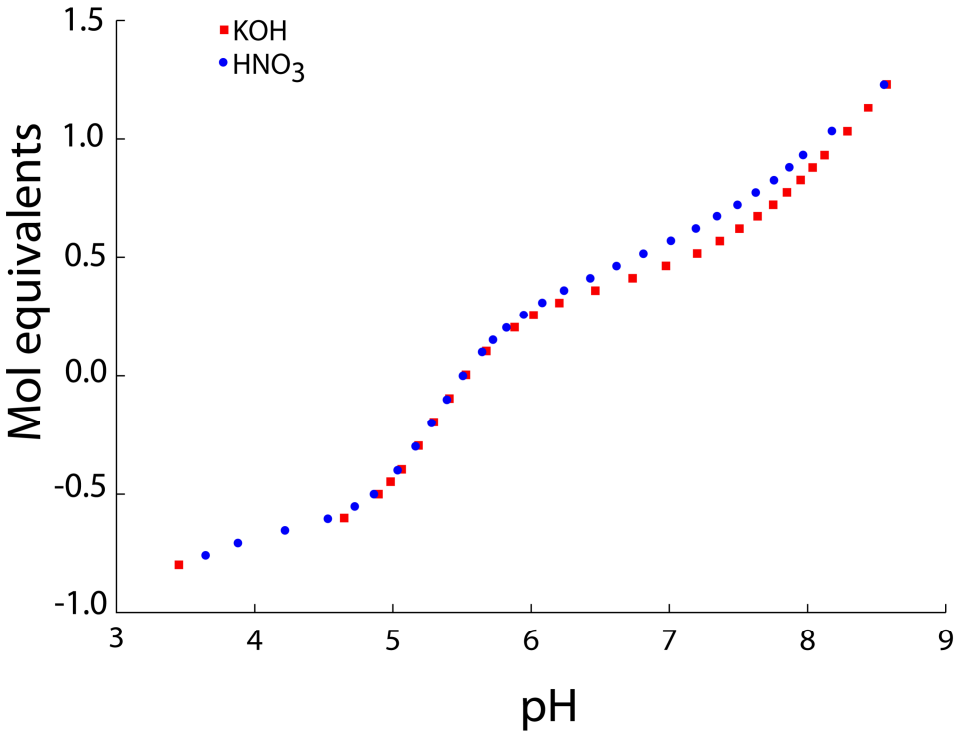

Figure 3.3: Titration of $[Fe_4O(OH)(hpdta)_2(H_2O)_4](NH_4)\bullet 9H_2O$ (5.04 mM, 5 ml volume) in 0.1 M KNO_3 using 0.100 M HNO_3 and 0.105 M KOH. See *Appendix D*.

colloids. At pH>9, there is evidence for some irreversible change in structure, such as formation of higher-nuclear complexes, as has been suspected.[26]

High-pressure NMR experiments were performed in a wide-bore Bruker Avance 400 MHz (9.4 T) spectrometer using a home-built high-pressure probe [27] similar to that used in previous experiments.[28-30] The sample was sealed in a custom high-pressure quartz NMR tube with a dual Viton o-ring plunger and the probe pressure was set with a high-pressure syringe pump in combination with a valve system. *iso*-Hexane was used as the pressure-conduit fluid; pressures were continuously monitored and never allowed to fluctuate more than 0.5% during data acquisition. The temperature was kept constant via a circulating water bath and was monitored with a type-T thermocouple situated in the probe body near the probe head and at pressure. Thermal equilibrium was established after each pressure increase before data were acquired. We used a calibrated 45 μs $\pi/2$ pulse with a 0.4 s relaxation delay.

Rates were estimated via a Swift-Connick formalism.[28,29] Briefly, a two-site exchange mechanism in the dilute-solution limit allows for the peak widths to be interpreted using a simplified form of the steady-state Bloch-McConnell equations.[29] The experimental line widths are first adjusted for the presence of the diamagnetic standard: $\frac{1}{T_{2r}} = \frac{\pi}{P_m}(\Delta\upsilon_{obs} - \Delta\upsilon_{solvent})$. The equation:

$$\frac{1}{T_{sr}} = \frac{1}{\tau_m}\left[\frac{T_{2m}^{-2} + (T_{2m}\tau_m)^{-1} + \Delta\omega_m^2}{(T_{2m}^{-1} + \tau_m^{-1})^2 + \Delta\omega_m^2}\right] \qquad (3.2)$$

derived from Swift-Connick line-broadening analysis[28,29] where P_m is the mole fraction of bound waters (here four) divided by the mole fraction of solvent water and τ_m is the exchange time, which relates directly to the rate coefficient, $\tau_m = \frac{1}{k_{ex}}$. The temperature variation of the

exchange time was described using the Eyring-Polanyi equation: $\frac{1}{\tau_m} = (\frac{k_B T}{h}) e^{(\frac{\Delta S^{\ddagger}}{T} - \frac{\Delta H^{\ddagger}}{RT})}$. The temperature variations of $\frac{1}{T_{2m}}$ is exponential with $\frac{1}{T}$ and $\Delta\omega_{\mathrm{m}}$ is linear with the inverse temperature (see description in Harley *et al.* [29]). The result was a system of nonlinear equations in $\frac{1}{T_{2r}}$ that could be minimized using a *Levenberg*–Marquardt algorithm with data collected over a wide range of temperatures and P_m values. The temperature variation of the experimental data **[Figure 3.4]** has enough curvature to require fitting $\frac{1}{T_{2r}}$ to a form of Eqn. (3.2) that includes paramagnetic contributions to chemical-shift variations; these were used as adjustable parameters. Uncertainties are standard deviations calculated from the covariance matrix obtained from the regression **[Table 3.2]**.

The pressure dependence of k_{ex} at a temperature where $T_{2m}^{-1} >> \Delta\omega^2$, $\square_{\mathrm{m}}^{-1}$ yields the activation volume, $\Delta V^{\ddagger}: \ln[k(p)] = -\frac{\Delta V^{\ddagger}}{RT} P - \ln[k^0]$, where *k(P)* is the pressure-dependent rate constant, P is pressure, R is the gas constant, k^o is the pressure at near-ambient conditions, and T the temperature **[Figure 3.5].**

Section 3.2.4- Magnetic Susceptibility Measurements

Magnetic susceptibility measurements of **[3.1]** were made using a Quantum Design SQUID Magnetometer MPMS-2 and obtained results identical to those of Schmitt *et al.*[20] and are included in the Supplemental Information (*Appendix C*). Schmitt *et al.* studied the magnetism of **[3.1]** extensively and showed that the susceptibility increases with increasing temperature, which is typical behavior of an antiferromagnetic system with a ground state S=0. The magnetic

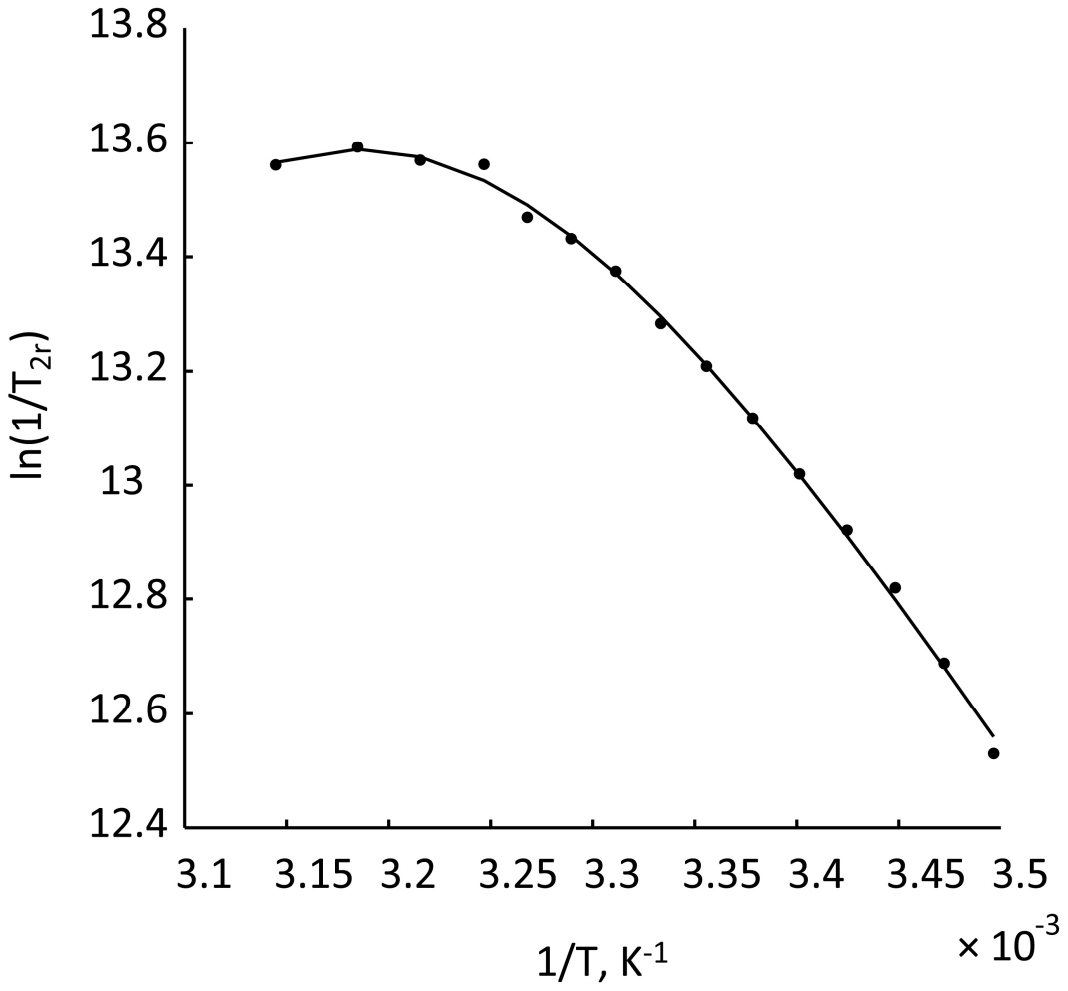

Figure 3.4: ^{17}O-NMR linewidth information as a function of temperature for a 10 mM solution of the $[Fe_4(OH)_2(hpdta)_2(H_2O)_4]^o(aq)$ molecule at pH=4.95. The line corresponds to the nonlinear fit obtained by minimizing a system of nonlinear equations using Levenberg-Marquardt algorithm. Minimized parameters were used to estimate rate coefficients for exchange of bound and bulk waters.

Table 3.2: Rate parameters for rates of exchange of waters bound to compound **[3.1]** derived from ^{17}O-NMR line widths and assuming that there are four exchangeable waters bound to each molecule.

pH	concentration	k^{298} (10^5 s^{-1})[a]	$\Delta H^{\ddagger}$ (kJ mol^{-1})[a]	$\Delta S^{\ddagger}$ (J mol^{-1} K^{-1})[a]
3.8	12.7 mM	9.7±1.2	49.2±0.2	+34.6±4.2
4.5	11.6 mM	12.0±3.0	52.7±0.4	+48.3±12.
4.7	12.6 mM	6.4±1.5	43.4±0.8	+11.8±2.7
4.9	11.7 mM	6.9±3.0	42.9±0.2	+10.8±5.8
4.95	10.5 mM	5.9±1.8	42.3±0.1	+7.8±2.3
5.2	12.1 mM	6.6±6.5	38.6±0.1	-4.0±3.9
5.2	7.3 mM	6.3±1.9	34.4±0.15	-18.4±5.4
5.2	11.7 mM	4.5±3.0	36.5±0.35	-14.2±9.6
5.2	14.1 mM	6.05±1.1	37.8±0.4	-7.4±14
5.2	19.2 mM	5.3±1.4	36.0±0.2	-14.5±4
5.4	10.0 mM	4.5±1.8	34.2±0.3	-22.3±11
5.5	11.5 mM	1.7±0.1	25.0±1.3	-60.9±4.4
5.8	10.0 mM	1.9±0.2	18.9±2.0	-80±7

[a]Uncertainties in $\Delta H^{\ddagger}$ and $\Delta S^{\ddagger}$ are reported as single standard deviation in the regression. Uncertainties in values of k^{298} are also reported as the standard error of the regression, but this uncertainty is probably too small. A more conservative estimate of uncertainty is a factor of ~2 in k^{298} and can be estimated by propagating errors of $\Delta H^{\ddagger}$ and $\Delta S^{\ddagger}$ through $k(T) = (\frac{k_B T}{h}) e^{\left(\frac{\Delta S^{\ddagger}}{R} - \frac{\Delta H^{\ddagger}}{RT}\right)}$ via Monte-Carlo methods; the resulting uncertainty in $\log(k^{298})$ is ±0.3 or less.

susceptibility of **[3.1]** did not reach a maximum in the temperature range 5-300 K, so the Néel point could not be calculated (*Appendix C)*.

Section 3.3- Results

To be useful as a model, the molecule: (i) must remain intact at conditions of the NMR experiments, (ii) the protonation state must be known, and (iii) the rate parameters must be well defined at the experimental pH. Three independent lines of evidence indicate that the molecule is stable in solution with the $[Fe_4(OH)_2(hpdta)_2(H_2O)_4]^o(aq)$ stoichiometry. Firstly, the acid-base chemistry, as inferred from both the UV-Vis data and the potentiometry, indicates that the

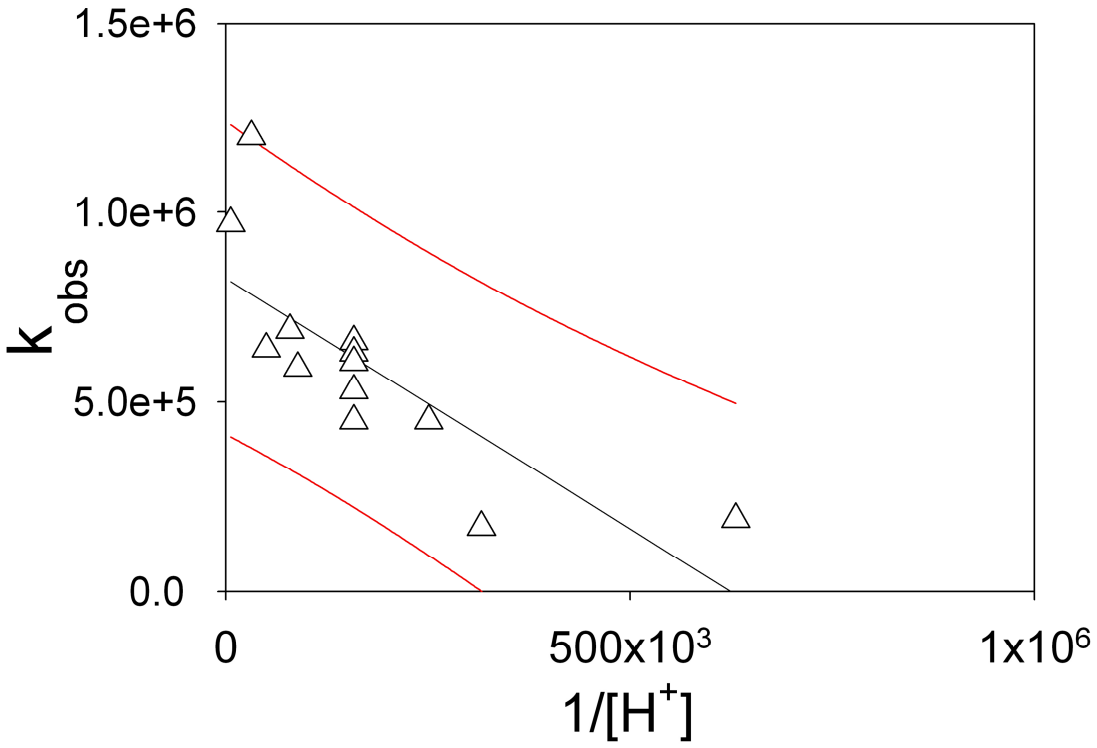
1.5e+6
1.0e+6
5.0e+5
0.0
k obs
0
500x10^3
1x10^6
1/[H+]

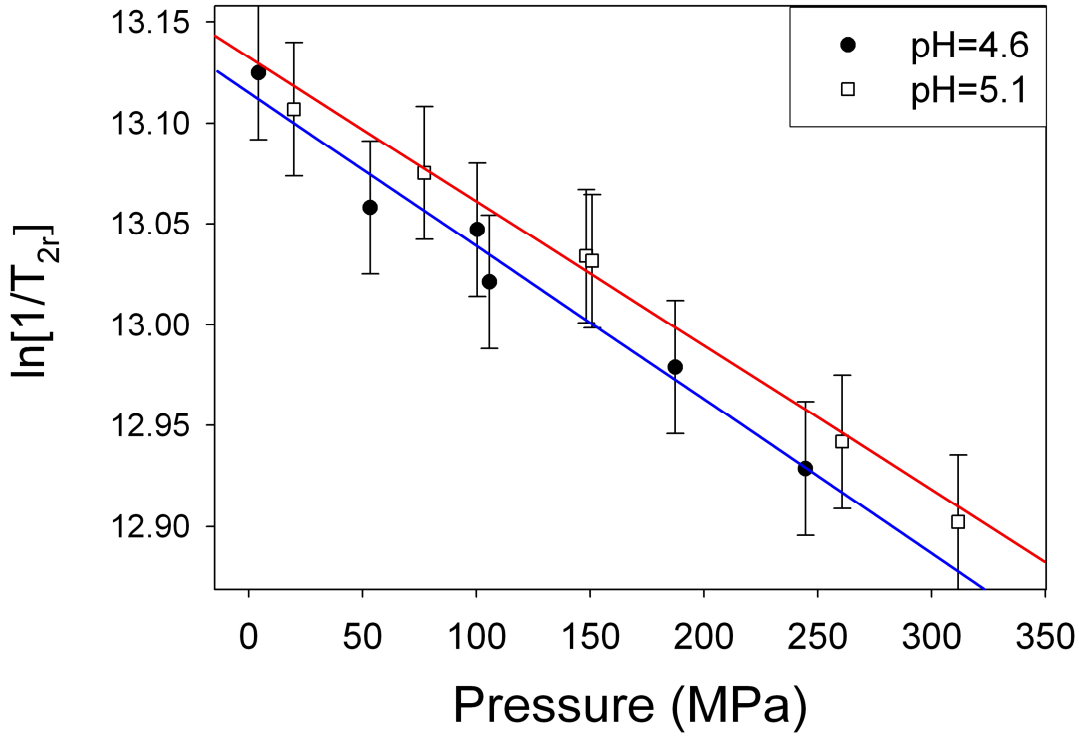
13.15
13.10
13.05
13.00
12.95
12.90
ln[1/T2r]
pH=4.6
pH=5.1
0
50
100
150
200
250
300
350
Pressure (MPa)

Figure 3.5: **(Top)** A regression of the average rate coefficient extracted from the experiments, here defined as k_{obs}, against $1/[H^+]$. The 95% prediction intervals are shown in red. **(Bottom)** ^{17}O-NMR relaxation information yielding ligand-exchange rates for the $[Fe_4(OH)_2(hpdta)_2(H_2O)_4]^o(aq)$ molecule as a function of pressure. The filled circles indicate experiments conducted at 18^{o}C, pH=4.6 and a concentration of **[1]** of 15 mM. The red line corresponds to a linear regressions through the data to yield $\Delta V^{\ddagger} = 1.9(\pm 0.2)$ cm^3 mol^{-1}. The unfilled squares indicate data from experiments at pH=5.1 at 25^{o}C at 14 mM total concentration of **[3.1].** The blue line indicates the regression that yields: $\Delta V^{\ddagger} = 1.8(\pm 0.1)$ cm^3 mol^{-1}. Uncertainties were estimated at ±4 Hz and were determined from replicated measurements.

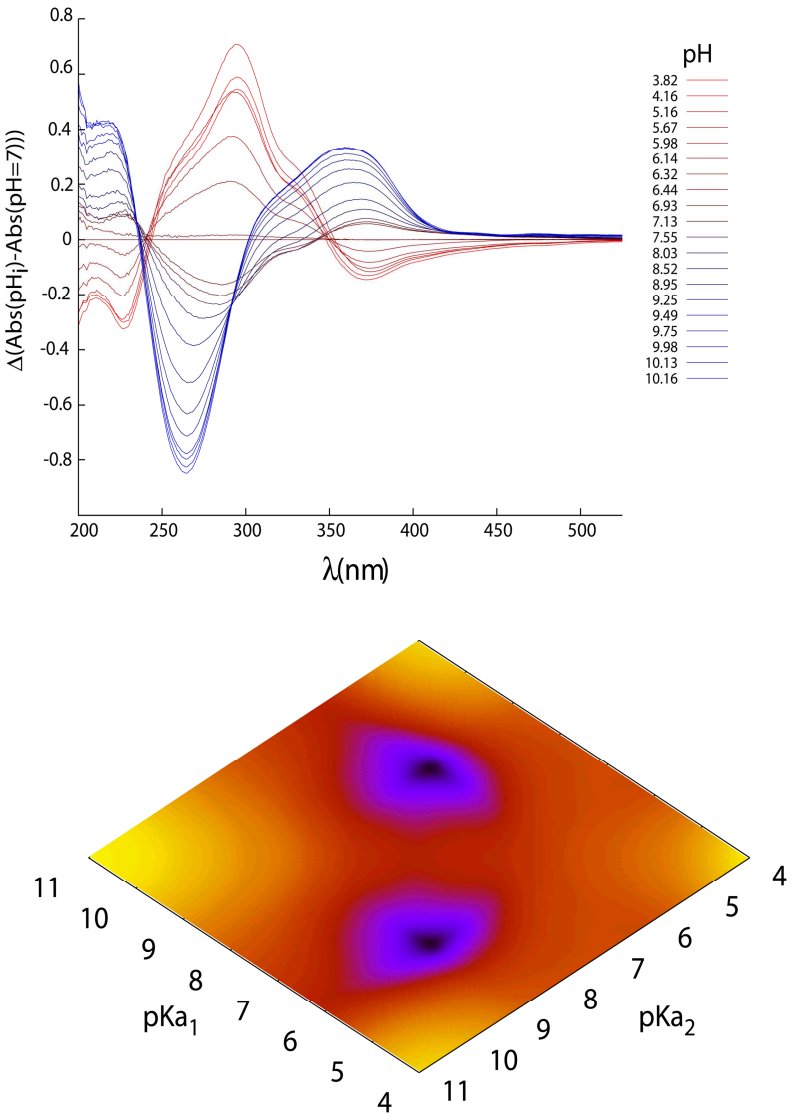

Figure 3.6: (Top) UV-Vis difference spectra of **[1]** as a function of solution pH. The difference spectra were calculated by subtracting the absorbance at a given wavelength at pH=6.44 from that of the absorbance at a given pH at the same wavelength. Two isosbestic points are evident and interpreted to indicate protonation of the complex. **(Bottom)** Least-squares fitting of the UV-VIS titrations detected two significant pKa values at pKa_1 = 5.9(±0.1) and pKa_2 = 8.8(±0.1). Plotted is the variable $\ln\left[\frac{\sum(Abs(\lambda_j)_{obs} - Abs(\lambda_i)_{obs})^2}{Z}\right]$ as a function of pKa_1 and pKa_2, where Z is a scaling factor based on the maximum residual.

molecule undergoes a reversible deprotonation near pH~5.7(±0.2, see below). Secondly, these data are consistent with the ESI-MS data which indicate that the core of the molecule remains intact during analysis. Thirdly, the ^{17}O-NMR data indicate that rates vary slowly with pH at pH<5 [**Table 3.2]**, suggestive of a conjugate base with a different reactivity than the fully protonated $[Fe_4(OH)_2(hpdta)_2(H_2O)_4]^o$(aq) molecule.

Figure 3.3 shows the acid base titration of **[3.1]** and **Figure 3.6** shows the UV-Vis titration data between 4<pH<10. There are two isosbestic points clearly evident in **Figure 3.6 (top)**, consistent with the presence of two pK_a values in the pH range **[Figure 3.6, bottom]**. We applied a numerical method to fit the spectra using a nonlinear least-squares analysis (see [30]), resulting in pKa_1 and pKa_2 values of 5.9(±0.1) and 8.8(±0.1), respectively, which compare well with the potentiometry. The potentiometry indicated two clear inflection points with: pKa_1 = 5.5(±0.15) and pKa_2 = 8.9(±0.2). Whereas the potentiometry could be affected by protonation of NH_3 near pKa_2, the UV-Vis data are not and clearly indicate that these pKa values correspond to protonation on the iron complex. We average these two values of pK_{a1} and assign pKa_1 = 5.7(±0.2), which we use for subsequent discussion. Potentiometric titrations as a function of temperature yielded the enthalpy of the first deprotonation reaction via the Van't Hoff equation with ΔH_{rxn} = 63.3(±5.9) kJ mol^{-1} (*Appendix C*).

At pH<3, the molecule dissociates and releases monomeric Fe(III) to solution, which is easily detectable in the UV-Vis spectra and, over several days, ferric-hydroxide colloids could be detected in these acidic solutions by light-scattering methods. The potentiometry becomes irreversible if extended to pH>9, indicating a change in structure beyond pKa_2.

The acidic protons are probably on the μ_2-oxo bridges and not on the bound waters. X-ray structure of the $[Fe_4O(OH)(hpdta)_2(H_2O)_4](NH_4)\bullet 9\ H_2O$ salt indicates a single proton

disordered between the two μ_2-oxo bridges **[Figure 3.1]**. Dissolution of this molecule into the degassed water results in a mildly acidic solution (pH~6) consistent with $pKa_1 = 5.7(\pm 0.2)$.

The most reasonable interpretation is that one of the μ_2-OH bridges deprotonates as solids precipitate at near-neutral pH, making the ionic crystal. This result may be surprising given the strong acidity of waters in the $[Fe(H_2O)_6]^{3+}$ ion (pKa_1~2.4 [31]) at this ionic strength, however, the hpdta molecule is an aminocarboxylate and withdraws enough charge from the metal centers to dramatically decrease the acidity of the bound waters to Fe(III) centers. The bound water in the Fe(III)-PhDTA complex (PhDTA=*o*-phenylenediamine-*N*,*N*,*N'*,*N'*,-tetraacetato), for example, dissociates at pH>8 (pK_a = 8.71(±0.02) at 298 K and I=1.00 M $NaClO_4$ [6]). In this case the Fe(III) is coordinated to seven ligand atoms, not six as in our molecule **[3.1]**, but the reduced acidity for Fe(III)-bound waters is consistent. The acid-base titration data for **[3.1]** are reproducible at pH<pKa_1 where the complex has the stoichiometry $[Fe_4(OH)_2(hpdta)_2(H_2O)_4]^o(aq)$.

Averaging the data in **Table 3.2** for pH<5 we estimate: k_{ex}^{298} = 8.1(±2.6)·10^5 s^{-1}, $\Delta H^{\ddagger}$ = 46.(±4.6) kJ mol^{-1}, $\Delta S^{\ddagger}$ = 22(±18) J mol^{-1} K^{-1} for the fully protonated, neutral molecule, $[Fe_4(OH)_2(hpdta)_2(H_2O)_4]^o(aq)$. The fraction of the conjugate base at pH<5 is 17% or less. Supporting the assignment of these rate data to the fully protonated molecule is the well known empirical relation between $\Delta H^{\ddagger}$ and $\ln(k_{ex}^{298})$ for water-exchange reactions (see Figure 3 in [32] and Figure 5 in [12]) and the values reported here for the $[Fe_4(OH)_2(hpdta)_2(H_2O)_4]^o(aq)$ ($\Delta H^{\ddagger}$ = 46.(±4.6) kJ mol^{-1} and k_{ex}^{298} = 8.1(±2.6)·10^5 s^{-1}) fall well on this correlation.

Causes of the compensatory pH variation of rate data, however, are unclear. The pH variation can be seen by regressing values of the observed rate coefficient as a function of: $\frac{1}{[H^+]}$ **[Figure 3.6, top]** assuming that there are two pathways, with one corresponding to the fully

protonated $[Fe_4(OH)_2(hpdta)_2(H_2O)_4]^o(aq)$ molecule, which reacts independent of pH, and a second assumed pathway that is proportional to the concentration of the conjugate base, $[Fe_4O(OH)(hpdta)_2(H_2O)_4]^{-1}(aq)$, and thus depends on pH. Assigning $k_{ex}^{298}=k_{obs}$, the empirical rate coefficients for two pathways can be resolved via a linear regression of: $k_{obs} = k_1 + \frac{k_{a1} + k_2}{[H^+]}$.

The linear-least squares intercept is $k_1 = k_{ex}^{298} = 8.3(\pm 0.75)\cdot 10^5\ s^{-1}$, close to the average of values at pH<5, above.

We have no confidence in assigning rate coefficients to the conjugate base $[Fe_4O(OH)(hpdta)_2(H_2O)_4]^{-1}$ (aq) because of uncertainty in the regressed data. The regression slope in **Figure 3.6 (top)**, -1.32(±0.3), when multiplied by the estimate of K_{a1} (pK_{a1}=5.7(±0.2)), yields an estimate of $k_2=2.6(\pm 0.6)\cdot 10^5\ s^{-1}$ for $[Fe_4O(OH)(hpdta)_2(H_2O)_4]^{-1}(aq)$ **[Figure 3.6, top].** This estimate of the rate coefficient unsurprisingly indicates a lower reactivity than for the fully protonated $[Fe_4(OH)_2(hpdta)_2(H_2O)_4]^o(aq)$ form.

The pressure dependencies of the reduced ^{17}O-NMR linewidths were determined at two conditions (pH=4.6, 291 K; pH=5.1, 298 K) and the results are shown in **Figure 3.6 (bottom).** Values of $\Delta V^{\ddagger}$ were estimated by linear-least-squares fits of the pressure variation of the reduced linewidths and the resulting values were virtually indistinguishable: $\Delta V^{\ddagger}=1.9(\pm 0.2)\ cm^3\ mol^{-1}$ at pH=4.6 and $\Delta V^{\ddagger} = 1.8(\pm 0.2)\ cm^3\ mol^{-1}$ at pH=5.1, indicating an exchange pathway that does not strongly depend on pH at these conditions.

Section 3.4- Discussion

The reactivity of bound waters in the $[Fe_4(OH)_2(hpdta)_2(H_2O)_4]^o(aq)$ molecule are broadly similar to those bound to other Fe(III)-aminocarboxylate ions and are more labile than waters in the $[Fe(H_2O)_6]^{3+}$ ion **[Table 3.1]** by a factor of $\sim 10^4$. To a first approximation, we

interpret these differences in labilities to reflect changes in charge on the Fe(III) metal centers and thus should also correlate with bond lengths, although a more sophisticated view of electronic structure may ultimately be necessary.[33] The <Fe^{III}-OH_2> bond length in crystals of $[Fe_4O(OH)(hpdta)_2(H_2O)_4](NH_4)$•9 H_2O, <2.07 Å>, is considerably longer than that of $[Fe(H_2O)_6]^{3+}$, which is <1.986 Å>.[7,17] We add these data to the figure of Balogh *et al.*[15] correlating reactivity with <Fe^{III}-OH_2> bond lengths **[Figure 3.7]**.

The correlation **[Figure 3.7]** is sparse because there is a relatively small set of Fe(III) complexes where both bond lengths in the solid state and rate coefficients are known. Furthermore, among the data, the aminocarboxylate complexes have seven-coordinated iron. Also included in this cohort is a complex where one of the acetate groups on the [EDTA] ligand is protonated **[**indicated as HEDTA in **Table 3.1]** so that the complex has no net charge in solution. This datum shows that neutralization of charge on the molecule caused only a minor increase in lability of the bound water, from k_{ex}^{298}= $7.2 \cdot 10^7$ s^{-1} to $7.8 \cdot 10^7$ s^{-1}. Similarly, the Fe(III)-PhDTA complex is also a seven-coordinated aminocarboxylate with no net charge at the pH conditions where rates were measured.[6] Our datum here for $[Fe_4(OH)_2(hpdta)_2(H_2O)_4]^o$(aq) molecule is for a structure with six-coordinated iron that is neutral in solution.

The correlation shown in **Figure 3.7** is also heavily influenced by two values. The value of k_{ex}^{298}= 160 s^{-1} is the smallest and experimentally best-constrained number, from multiple experiments.[4,5,8] The value assigned to functional groups on the large Keplerate molecule, labeled $Mo_{72}Fe_{30}$ are much less certain. Balogh *et al.*[15] derived the relaxation, but unlike all other data shown in **Table 3.1**, they found no clear area of activation similar to the data shown in **Figure 3.5**. They instead estimated the rate coefficients in a nonlinear least-squares analysis, in a manner analogous to work on gadolinium imaging agents.[31]

The activation volume for the iron complex $[Fe_4(OH)_2(hpdta)_2(H_2O)_4]^o(aq)$ is a small positive value ($\Delta V^{\ddagger}$ = +1.85 cm^3 mol^{-1}), also consistent with other values in large aminocarboxylate complexes **[Table 3.1],** and which indicates a dissociative interchange mechanism, $\mathbf{I_D}$, if interpreted using the traditional formalism derived for octahedral metal ions.[34,35] Within this formalism, the majority of the ferric iron complexes in **Table 3.1** also would be classified as exhibiting $\mathbf{I_D}$ mechanism for water exchange, meaning a slightly positive, but small, $\Delta V^{\ddagger}$ value. One interpretation is that donation of electron density to Fe(III) from nitrogens in the ligand leads to increased $<Fe^{III}\text{-}OH_2>$ bond lengths that favor a dissociative exchange mechanism.[36] A simple example is in the octahedral hydrolysis complexes of Fe(III). For $[Fe(OH_2)_6]^{3+}$, k_{ex}^{298}= 160 s^{-1} and $\Delta V^{\ddagger}$ = -5.4 $cm^3 \cdot mol^{-1}$. Upon hydrolysis to form $[FeOH(OH_2)_5]^{2+}$, the values increase to $k_{ex}^{298}= 1.2 \cdot 10^5$ s^{-1} and $\Delta V^{\ddagger}$= +7.0 $cm^3 \cdot$ mol^{-1}. Hydrolysis causes lengthening of $<Fe^{III}\text{-}OH_2>$ bonds because the overall charge of the complex is reduced from +3 to +2 and protons interconvert the bound hydroxyl to a bound water at rates much more rapid than the water exchanges. Thus, there is a correlation between complex lability and $\Delta V^{\ddagger}$ in these cases.

A conspicuous exception is the $[Fe(EDDS)(H_2O)]^-$ complex **[Table 3.1]**, which has $\Delta V^{\ddagger}$ = -14.4 cm^3 mol^{-1}, near the extreme limit of pathways that would be considered associative, or **A**. These are uncommon and the authors interpreted their result to indicate a profound change in coordination, and also cautioned about breakdown of the complex at temperatures greater than 310 K.[7,8] The complex has no bound waters in the solid state but the authors suggest that one bonded carboxylate group releases in solution to allow a water to bind. This change in structure facilitates associative ligand exchanges, the authors argue.[13] Other six-coordinated iron complexes in **Table 3.1** do not exhibit evidence for an associative pathway and this may be due

to the large bulky ligand around the iron center that blocks addition of a seventh coordinating atom.

Cause of the covariation in fitted $\Delta H^{\ddagger}$ and $\Delta S^{\ddagger}$ cannot be attributed to contribution of enthalpy from a deprotonation reaction, since it has an endothermic enthalpy of reaction (ΔH_{rxn} = 63.3(±5.9) kJ mol^{-1}, *Appendix C*), as one expects for separation of charge. This enthalpy would *add* to the barrier for ligand exchange if a less-reactive complex dominated at high pH, not subtract. We do not understand and cannot evaluate the striking compensatory relation between fitted values of $\Delta H^{\ddagger}$ and $\Delta S^{\ddagger}$ indicating ligand dynamics at pH~pK_{a1}.

We are aware that small concentrations of highly reactive, and undetected, monomer ions could invalidate our interpretation. All studies that employ the Swift-Connick method for establishing rates are so vulnerable because only changes in the linewidth of the bulk-water peak are measured. However, we see no evidence for dissociation of the molecule. Furthermore, increased reactivity of the conjugate base of the $[Fe_4(OH)_2(hpdta)_2(H_2O)_4]^o(aq)$ molecule probably is not affecting the results, unlike the case for the octahedral monomer ions, such as $[Fe(OH_2)_6]^{3+}(aq)$. Upon deprotonation of $[Fe(OH_2)_6]^{3+}(aq)$ to form $[FeOH(OH_2)_5]^{2+}(aq)$, rates of exchange of bound waters increase by ~10^2 times[8] and the $\Delta V^{\ddagger}$ values indicate a clear change in reaction mechanism toward a more dissociative pathway **(I_d)**. This chemistry is in sharp contrast with the case here, where reactivity decreases as pH approaches pK_{a1} and there is no measurable change in $\Delta V^{\ddagger}$ values.

It is not surprising that the conjugate base would be less reactive than $[Fe_4(OH)_2(hpdta)_2(H_2O)_4]^o(aq)$ molecule. In $[Fe(OH_2)_6]^{3+}(aq)$ and $[FeOH(OH_2)_5]^{2+}(aq)$, bound waters and bound

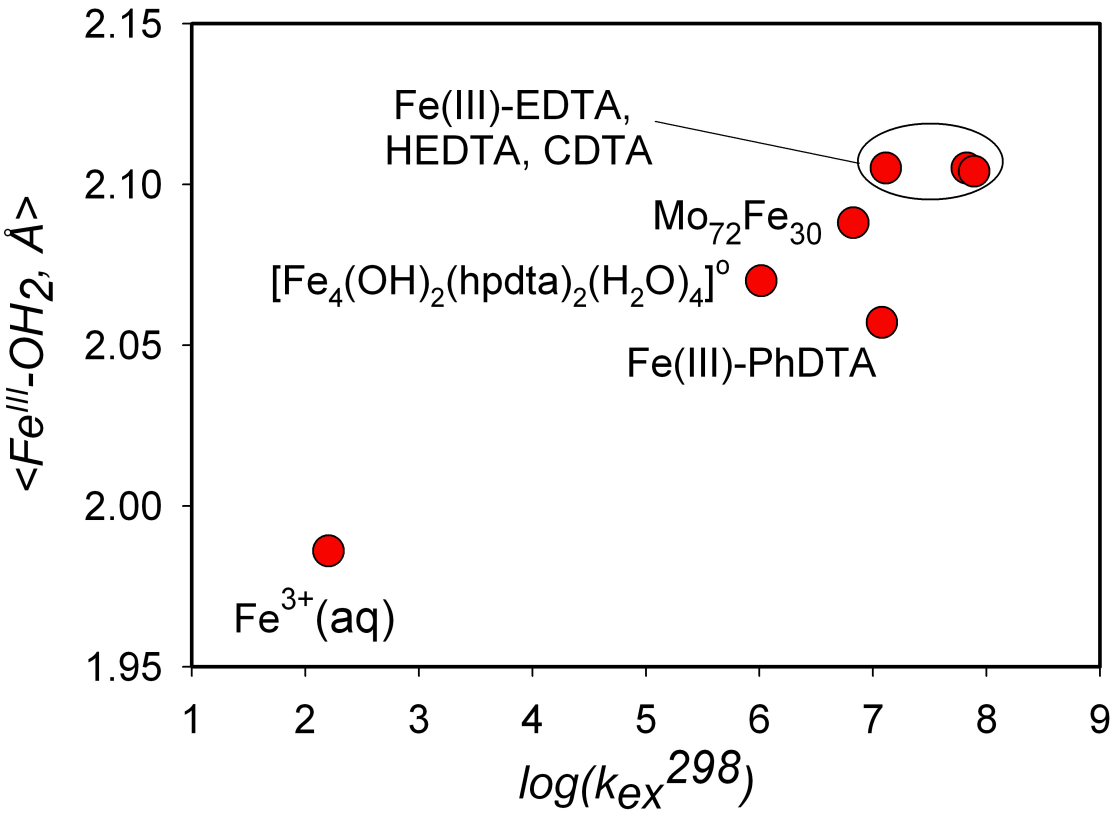

Figure 3.7: A correlation between the $log(k_{ex}^{298})$ and the <Fe^{III}-OH_2> bond length in the corresponding solid. The EDTA and CDTA complexes are monoanionic, the HEDTA complex is neutral and the EDTA, CDTA and HEDTA complexes correspond to seven-coordinated, high-spin Fe(III). The datum for the $Mo_{72}Fe_{30}$ is from Balogh et al.[15] and corresponds to >Fe-OH_2 functional groups exposed on a ~1500 atom, nanometer-size Keplerate molecule. The value for the $[Fe_4(OH)_2(hpdta)_2(H_2O)_4]^o$(aq) molecule is described in this paper and has four hexacoordinated Fe(III) centers, an isolated bound water and sets of μ_2-OH and three-coordinated oxo in the inner-coordination-sphere of each metal. The Fe(III)-PhDTA complex has a single bound water [6] and also has a seven-coordinated Fe(III) center.

hydroxide are close packed and interconvert rapidly by simple proton shuttling among nearby functional groups. The reduced charge as $[Fe(OH_2)_6]^{3+}$(aq) converts to $[FeOH(OH_2)_5]^{2+}$(aq) is also averaged over a relatively small volume of ~111 cm^3/mol (calculated using density functional theory at the B3LYP/dgdzvp/PCM level of theory, this work). However, similar processes do not affect water-exchange rates in the $[Fe_4(OH)_2(hpdta)_2(H_2O)_4]^o$(aq) molecule, where the bound waters remain fully protonated over the entire pH range of this study ($pH<pK_{a1}$) and the Brønsted reaction affects the bridging oxygen in the center of the molecule. Furthermore, the bound waters are separated from one another by ~5.2 Å and the molecule is five times larger than the aqua ion (~520 cm^3/mol; B3LYP/dgdzvp/ PCM level of theory; this work). Thus, it is not unreasonable to expect that deprotonation of the $[Fe_4(OH)_2(hpdta)_2(H_2O)_4]^o$(aq) molecule would reduce the lability of bound waters.

Section 3.5- Conclusions

Rates of water exchange on the $[Fe_4(OH)_2(hpdta)_2(H_2O)_4]^o$(aq) molecule fall into the same range as for other Fe(III) molecules, suggesting that rates of ligand exchange at bound-water sites are not dramatically affected by subtle details of structure. Rates trend with $<Fe^{III}$-$OH_2>$ bond lengths and this variable alone seems to capture variations in lability due to small changes in average charge of the complex and structure, to at least within the small set of structures studied. A similar conclusion was derived from rare-events simulation of mineral-bound waters and experiments on aluminum aqueous complexes.[7] Wang *et al*.[7] used these data to show a correlation with bond lengths, and predicted surprisingly rapid rates in most cases. Unless there were steric hindrances to exchange, the logarithm of rates scaled well with <Al-

OH_2> bond length and were many orders of magnitude more rapid than for the fully protonated monomer ion, $[Al(OH_2)_6]^{3+}$. The data in **Figure 3.7** suggests that rates of exchange of bound and bulk waters are probably in the 10^6-10^7 s^{-1} scale at high-spin iron-oxide surface sites. The rates could be dramatically affected by steric influence and changes in electronic structure, of course, such as by partial reduction of the metal centers. If electron exchange between metal sites has a low barrier energy, the rates of exchange of all surface-bound waters will be dramatically affected by injection of an electron (see [9] for an example) into the extended structure.

Section 3.6- References

[1] Kumar, P.; Kumar, M.; Ramanathan, A.; Tsujimura, M., *Environ. Geochem. Hlth* **2010,** 32, (2), 129-146.

[2] Rustad, J. R., *Adv. Inorg. Chem.* **2010,** 62, 391-436.

[3] Wang, J.; Rustad, J. R.; Casey, W. H., *Inorg. Chem.* **2007,** 46, (8), 2962 - 2964.

[4] Grant, M.; Jordan, R. B., *Inorg. Chem.* **1981,** 20, (1), 55-60.

[5] Swaddle, T. W.; Merbach, A. E., *Inorg. Chem.* **1981,** 20, (12), 4212-4216.

[6] Mizuno, M.; Funahashi, S.; Nakasuka, N.; Tanaka, M., *Inorg. Chem.* **1991,** 30, (7), 1550-1553.

[7] Richens, D. T., *The Chemistry of Aqua Ions*. John Wiley: New York, 1997; p 592 pp.

[8] Helm, L.; Merbach, A. E., *Chem. Rev.* **2005,** 105, (6), 1923-1959.

[9] Ducommun, Y.; Newman, K. E.; Merbach, A. E., *Inorg. Chem.* **1980,** 19, 3696-3703.

[10] Maigut, J.; Meier, R.; Zahl, A.; van Eldik, R., *Inorg. Chem.* **2007,** 46, (13), 5361-5371.

[11] Schneppensieper, T.; Zahl, A.; van Eldik, R., *Angew. Chem., Int. Ed.* **2001,** 40, (9), 1678-1680

[12] Richens, D., *Comment Inorg. Chem.* **2005,** 26, (5-6), 217-232.

[13] Schneppensieper, T.; Seibig, S.; Zahl, A.; Tregloan, P.; van Eldik, R., *Inorg. Chem.* **2001,** 40, (15), 3670-3676.

[14] Ostrich, I. J.; Liu, G.; Dodgen, H. W.; Hunt, J. P., *Inorg. Chem.* **1980,** 19, (3), 619-621.

[15] Balogh, E.; Todea, A. M.; Muller, A.; Casey, W. H., *Inorg. Chem.* **2007,** 46, (17), 7087-7092.

[16] Ako, A. M.; Waldmann, O.; Mereacre, V.; Kloewer, F.; Hewitt, I. J.; Anson, C. E.; Guedel, H. U.; Powell, A. K., *Inorg. Chem.* **2007,** 46, (3), 756-766.

[17] Schmitt, W.; Hill, J. P.; Juanico, M. P.; Caneschi, A.; Costantino, F.; Anson, C. E.; Powell, A. K., *Angew. Chem., Int. Ed.* **2005,** 44, (27), 4187-4192.

[18] Murugesu, M.; Clerac, R.; Wernsdorfer, W.; Anson, C. E.; Powell, A. K., *Angew. Chem., Int. Ed.* **2005,** 44, (41), 6678-6682.

[19] Powell, G., W.; Lancashire, H., N.; Brechin, E., K.; Collison, D.; Heath, S., L.; Mallah, T.; Wernsdorfer, W., *Angew. Chem., Int. Ed.* **2004,** 43, (43), 5772-5.

[20] Schmitt, W.; Anson, C. E.; Pilawa, B.; Powell, A. K., *Z. Anorg. Allg. Chem.* **2002,** 628, (11), 2443-2457.

[21] Schmitt, W.; Murugesu, M.; Goodwin, J. C.; Hill, J. P.; Mandel, A.; Bhalla, R.; Anson, C. E.; Heath, S. L.; Powell, A. K., *Polyhedron* **2001,** 20, (11-14), 1687-1697.

[22] Panasci, A. F.; McAlpin, J. G.; Ohlin, C. A.; Christensen, S.; Fettinger, J. C.; Britt, R. D.; Rustad, J. R.; Casey, W. H., *Angew. Chem., Int. Ed.***2012,** 78, (1), 18-27.

[23] Catalano, J. G.; Fenter, P.; Park, C., *Geochim. Cosmochim. Acta* **2009,** 73, (8), 2242-2251.

[24] Schmitt, W.; Anson, C. E.; Sessoli, R.; van Veen, M.; Powell, A. K.,*J. Inorg. Biochem.* **2002,** 91, (1), 173-189.

[25] Schmitt, W.; Jordan, P. A.; Henderson, R. K.; Moore, G. R.; Anson, C. E.; Powell, A. K., *Coordin. Chem. Rev.* **2002,** 228, (2), 115-126.

[26] Schmitt, W.; Anson, C. E.; Pilawa, B.; Powell, A. K., *Z. Anorg. Allg. Chem.* **2002,** 628, (11), 2443-2457.

[27] Ballard, L.; Reiner, C.; Jonas, J.,*J. Magn. Reson. Ser. A* **1996,** 123, (1), 81-86.

[28] Swift, T. J.; Connick, R. E.,*J.Chem. Phys.* **1962,** 37, 307-20.

[29] Harley, S. J.; Ohlin, C. A.; Casey, W. H., *Angew. Chem., Int. Ed.***2011,** 75, 3711-3725.

[30] Frans, S. D.; Harris, J. M., *Anal. Chem.* **1984,** 56, 466-470.

[32] Ohlin, C. A.; Villa, E. M.; Rustad, J., R.; Casey, W. H., *Nat. Mater.* **2010,** 9, 11-19

[33] Gorun, S. M.; Lippard, S. J., *Inorg. Chem* **1991,** 30, (1625-1630).

[34] Swaddle, T. W., *Inorg. Chem.* **1980,** 19, (10), 3203-3205.

[35] Swaddle, T. W., *Comment. Inorg. Chem.* **1991,** 12, (4), 237-58.

[36] Hubbard, C. D.; Van Eldik, R., *Inorg. Chim. Acta* **2010,** 363, 2357-2374.

Chapter 4

Kinetic studies of the $[NpO_2(CO_3)_3]^{4-}$ ion at alkaline conditions using ^{13}C NMR

Section 4.1- Introduction

The future of the nuclear industry depends on a defendable understanding of environmental risks associated with nuclear accidents and nuclear waste storage. Assessing the safety of storage facilities relies on accurate models that predict how actinide species migrate through engineered barriers, soil, and groundwater.[1] However, modeling the transport of these species, particularly the actinide elements, is difficult due to multiple oxidation states that may be present in natural waters, the presence of complexing ligands, their potential to form colloids, and their interactions with mineral surfaces.[2] Reactive-transport models rely on data from experiments to accurately address these many interactions, but the lack of such data remains a barrier to building effective actinide reactive-transport models. Particularly valuable are the highly constrained experiments that describe simple molecular processes, like ligand-exchanges, where the reaction scale can be compared directly with *ab initio* and molecular-dynamic simulations.

The neptunium actinide is particularly troublesome due to its long half-life, 2.14×10^6 years for the ^{237}Np isotope, its high solubility at conditions typical of natural groundwaters, and its high toxicity.[3-6] Neptunium in water can exist in oxidation states ranging from (III) to (VII), with the pentavalent state being the most stable. While in the pentavalent and hexavalent states, neptunium exists with opposing axial 'yl' oxygens having a high bond order and equatorial bound waters, as NpO_2^+ and NpO_2^{2+}, respectively. There has been an emphasis on studying the chemical behavior of neptunium in acidic to neutral conditions even though nuclear waste is likely to be stored in an alkaline environment.[6-13] Although the hydrated neptunium species are less soluble at high pH values, common ligands in the environment, such as carbonate, can bind to neptunium under these conditions and substantially increase its solubility.[14]

Previous thermodynamic studies showed that, in the presence of carbonate and bicarbonate, Np(VI) dominantly exists as the monomeric species $[NpO_2(CO_3)]^0$, $[NpO_2(CO_3)_2]^{2-}$, and $[NpO_2(CO_3)_3]^{4-}$, or as the trimeric species $[(NpO_2)_3(CO_3)_6]^{6-}$. [15-21] Even at pH values where bicarbonate is at higher concentration than carbonate, monodentate bicarbonate complexes are not found.[16] At high ionic strength and pH less than 7.7, the trimeric species, $[(NpO_2)_3(CO_3)_6]^{6-}$, dominates, while at higher pH conditions and ratios of NpO_2^{2+}:CO_3^{2-} of 1:3 or greater, the monomeric $[NpO_2(CO_3)_3]^{4-}$ species **[Figure 4.1]** dominates.

Tait et al. used ^{13}C NMR spectroscopy to determine the speciation of the Np(VI)-carbonate solutions.[22] The monomeric $[NpO_2(CO_3)_3]^{4-}$ species exhibits a single ^{13}C-NMR peak attributable to bound carbonate with a chemical shift around ~80 ppm **[Figure 4.2]**, while the trimeric species exhibits two peaks at approximately 8 and -89 ppm, again corresponding to bound ligands.

In this paper we extend the work by Stout et al.[23] by revisiting the kinetic behavior of carbonate ligand exchange on the $[NpO_2(CO_3)_3]^{4-}$ ion. Stout et al. reported activation parameters for two pH conditions. These parameters are listed in **Table 4.1**. They report the rate of ligand exchange of k_{ex}^{298} = 143(±1.0) s^{-1} and 64.7(± 3.3) s^{-1} at a pH values of 9.4 and 10.0, respectively.[23] They employed relatively high concentrations of metal: [Total Np(VI) =0.10 M] and ligand [Total carbonate = 0.70 M] and ionic strength of 1.0 M.

Table 4.1: Activation parameters reported by Stout et al. [23] at 25 °C.

pH	E_a (kJ mol^{-1})	k_{ex}^{298} (s^{-1})	$\Delta H^{\ddagger}$ (kJ mol^{-1})	$\Delta S^{\ddagger}$ (J mol^{-1} K^{-1})
9.4	43.8 ± 6.3	143 ± 1.0	41.8 ± 6.3	-65 ± 21
10.0	43.8 ± 6.7	64.7 ± 3.3	41.8 ± 6.6	-71 ± 22

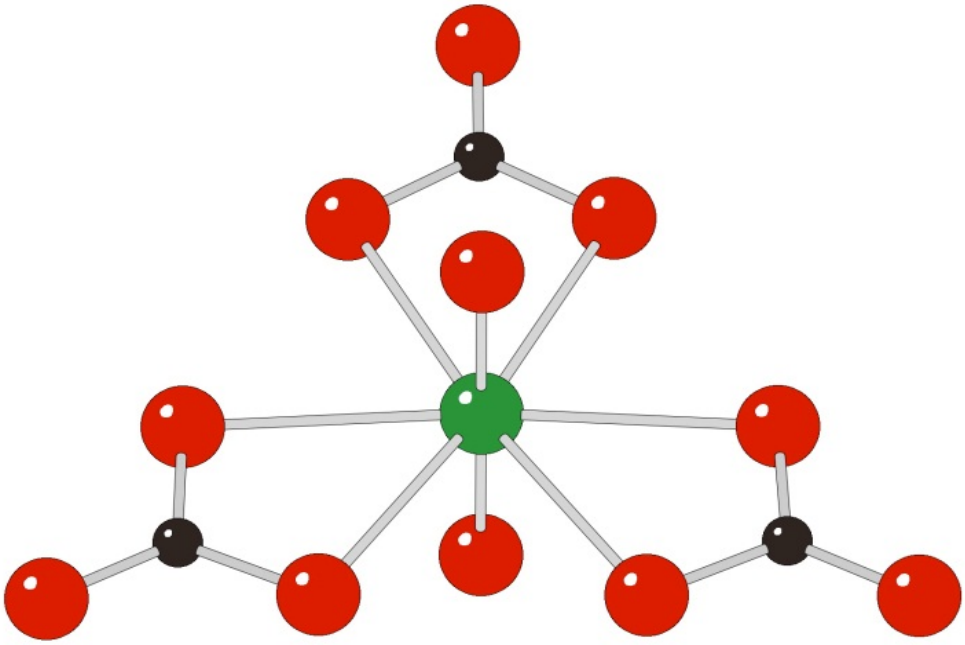

Figure 4.1: The $[NpO_2(CO_3)_3]^{4-}$ ion. Np(VI) is green, oxygen red, and carbon black. The two opposing "yl" oxygens are in the axial positions, while the three, bidentate carbonate ligands are in the equatorial plane.

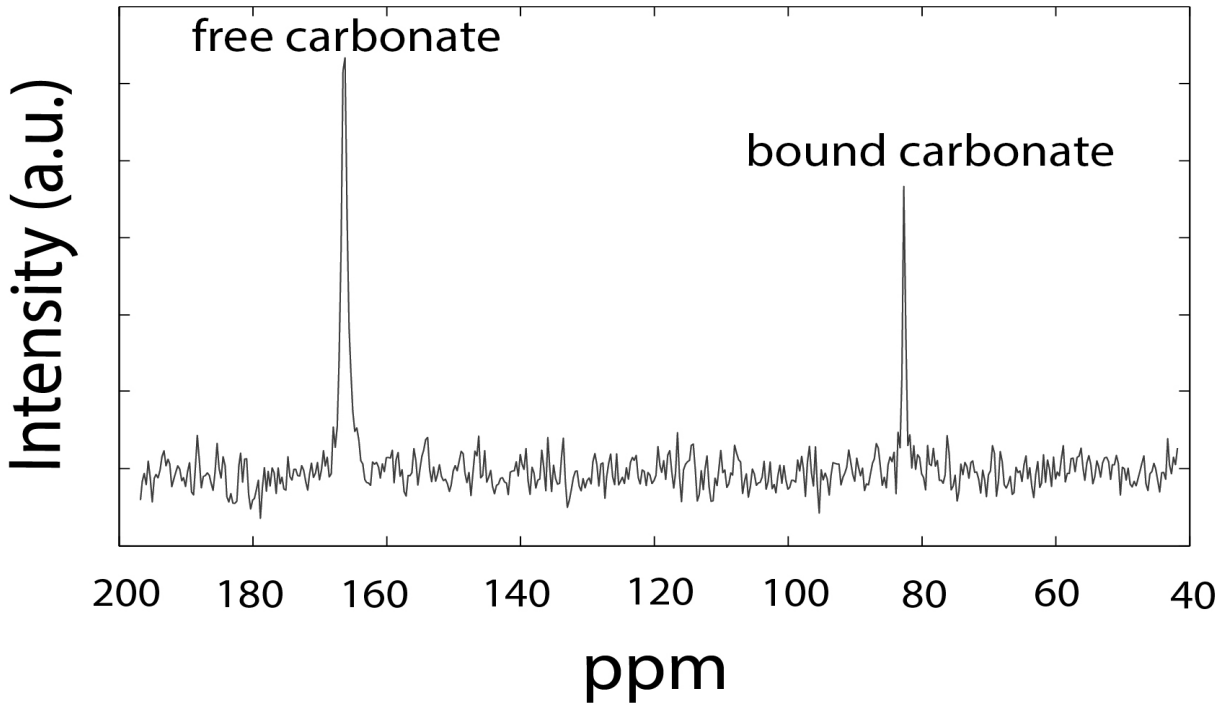

Figure 4.2: ^{13}C NMR spectra of Sample 5 (See **Table 4.2**). The peaks are well separated, indicating slow exchange on the NMR time scale.

With these solutions, they used the line-broadening method described by Swift and Connick[24] in which NMR peak width and chemical shift differences are assigned to the free carbonate ion with, and without, the paramagnetic metal, in this case Np(VI). This method is most commonly used when the signal for the reactive species is unobservable due to paramagnetic broadening and fast exchange, such as when ^{17}O exists in the hydration shell of paramagnetic monomer ions (eg. $[Fe(OH_2)_6]^{3+}$,[17, 25, 26]) and exchanges with bulk water. The rate of exchange from the solvation shell is inferred from the effect on the bulk solution ^{17}O peak. The ^{13}C NMR spectra for the $[NpO_2(CO_3)_3]^{4-}$ ion carbonate solution contain two well-separated peaks, one for the free carbonate (166 ppm) and one for the bound carbonate (84 ppm), which is consistent with the spectra reported by Stout et al. and Tait et al [22, 23] **[Figure 4.2]**. The presence of two individual signals, one assignable to the bound-carbonate ligand and one assignable to free carbonate, indicate that ligand exchange between bound and free carbonate is slow on the NMR time scale.

We found the free- and bound-carbonate peaks to be sufficiently well separated to permit selective-excitation experiments that yield kinetic information about the rates of substitution directly, which is a second means of estimating rate coefficients that is independent of assumptions of the Swift-Connick method. This method also allows us to conduct experiments at total Np(VI) and carbonate concentrations that are lower than those of Stout et al., thus complementing their work. The chemical-shift difference, however, is small enough (~12 kHz) that we could not selectively excite a peak using a conventional 180° long pulse. Instead, we adapted an approach we previously employed to study the $[UO_2(CO_3)_3]^{4-}$ species, which also has close chemical shifts.[27] We conducted ^{13}C NMR saturation-transfer experiments on the $[NpO_2(CO_3)_3]^{4-}$ ion, which is isoelectronic to the $[UO_2(CO_3)_3]^{4-}$ species, and determined

carbonate ligand-exchange parameters at a larger pH range than the experiments described in Stout's paper.

Section 4.2- Experimental

Caution. ^{237}Np is a radioactive isotope and an α-emitter. It should be handled in dedicated facilities with appropriate equipment for radioactive materials to avoid health risks caused by radiation exposure.

Section 4.2.1- Sample Preparation

A stock solution of Np(V) was prepared using the ^{237}Np column purification method of Snow et al.[28] The solution was washed and dried until the solid would not dissolve in water, heated to full dryness, and redissolved into a solution prepared from water of 18-Megaohm resistance that was made slightly acidic with dilute perchloric acid, such that perchlorate would be the counterion. The neptunium concentration of the solution was established by liquid-scintillation counting. The resulting solution was a mix of oxidation states, which we adjusted using a Wavenow USB potentiostat. The potentiostat had a three-electrode array with a Pt-wire working electrode that was separated from a Pt-wire counter electrode by a Vycor frit. The reference electrode was an Ag/AgCl microelectrode.

The solutions were kept under electrolysis at +1.35 V[29-31] until the characteristic UV-Vis-NIR peaks of Np(IV) and Np(V) at 960 and 980 nm, respectively, disappeared and the characteristic peak for Np(VI), 1230 nm, became prominent **[Figure 4.3]**. Once the solution was electrochemically treated to convert neptunium to Np(VI), the solvent was evaporated away and the solid was then redissolved in sodium-carbonate solution that had been enriched with ^{13}C (98%). Aliquots of this stock solution were used to make subsamples for experiment containing 5-15 mM Np(VI) and 20-60 mM carbonate, ensuring that the carbonate concentration was at

least four times that of the Np(VI) and that the tris-carbonato species formed. The pH was measured using an Ingold microelectrode, and was adjusted using dilute perchloric acid or sodium hydroxide. Once the sodium carbonate was added, the UV-Vis-NIR of the solution was taken again, **Figure 4.4**, to confirm the formation of monomeric $[NpO_2(CO_3)_3]^4$; these results were consistent with the spectra reported by Ikeda-Ohno et al.[15] The solution compositions that were employed in experiments are reported in **Table 4.2**.

Table 4.2: Composition of aqueous solutions used for saturation-transfer experiments.

	[Neptunium] (mM)	[Carbonate] (mM)	pH	Ionic Strength (M)
Sample 4.1	12	54.5	10.5	0.21
Sample 4.2	12	54.5	8.8	0.21
Sample 4.3	10	52	9.3	0.21
Sample 4.4	8	32	10.1	0.15
Sample 4.5	7.2	50	10.1	0.20
Sample 4.6	10	50	8.1	0.18
Sample 4.7	10	50	8.55	0.18

All experiments were performed within one week of solution preparation and we found no evidence of sample degradation during this time. No precipitate formed in any samples for which rate data are reported, although samples at pH≥10.6 formed a precipitate within two hours of preparation. The pH values of the samples were measured before and after the NMR experiments to verify that changes in temperature did not alter the pH of the solution via hydrolysis; in all cases the pH varied no more than 0.1 pH units. The pH of the sample solutions were prevented from dropping to pH<8 to ensure that no trimeric species formed. Similarly, NMR spectra were collected on each sample to confirm that no trimeric complex formed, which

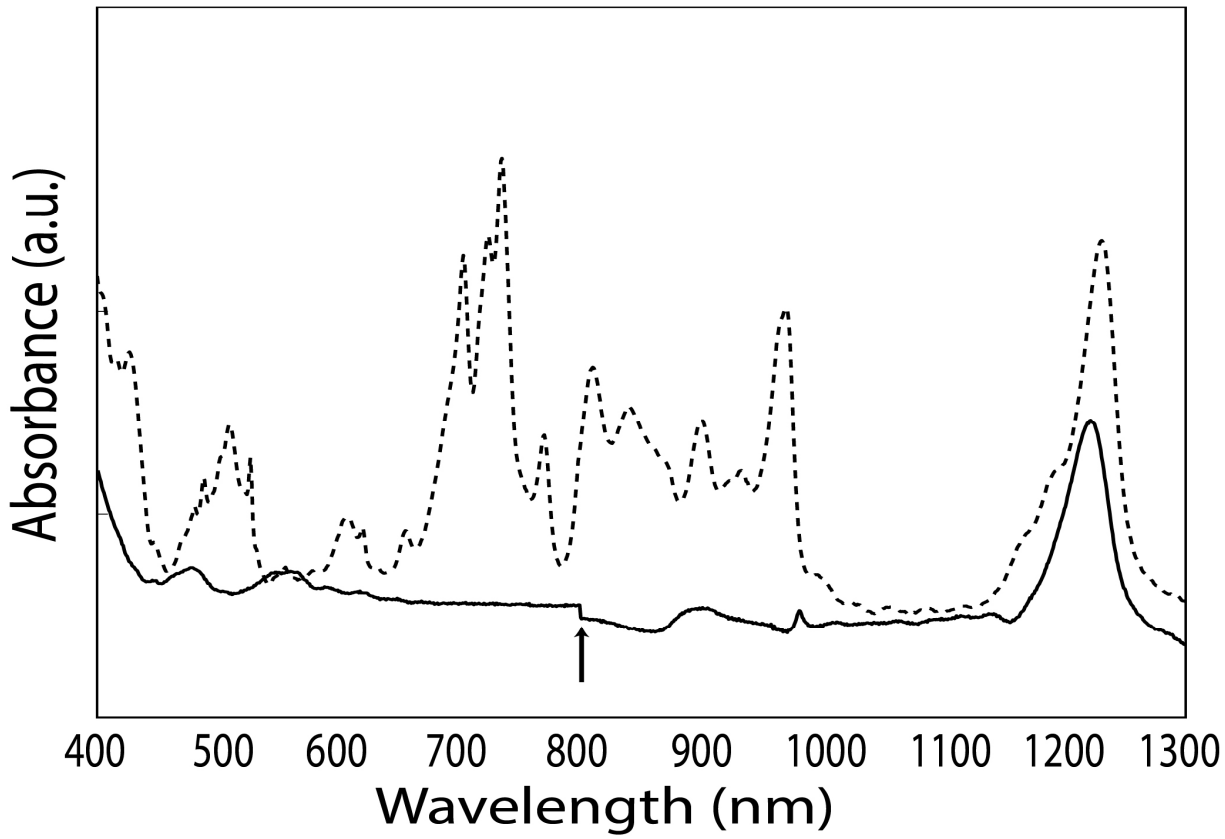

Figure 4.3: UV-Vis-NIR spectra of 10 mM neptunium stock solution before and after electrochemistry. The peak characteristic for Np(VI) is at 1230 nm. The dashed line shows the UV-Vis-NIR spectrum before electrolysis when Np(IV), Np(V), and Np(VI) are present. The solid line is after electrolysis when the solution is nearly pure in Np(VI). The discontinuity in adsorption at 800 nm, indicated by the vertical arrow, is caused by mechanical changes in the light source in the instrument and does not indicate a real chemical change.

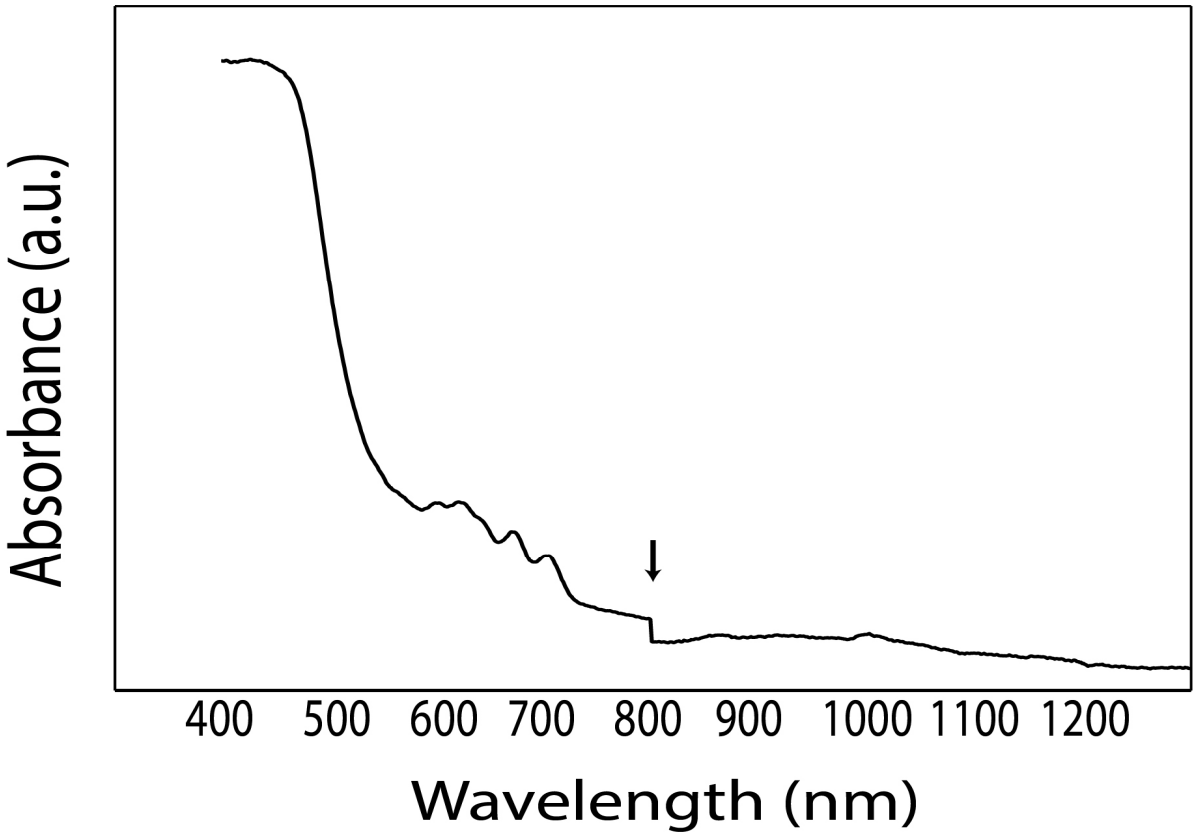

Figure 4.4: UV-Vis-NIR of a solution after purification and after sodium carbonate had been added (Sample 5; see Table 4.2). The absorption between 400-700 nm, and the minor peaks at 550-750 nm, are characteristic of Np(VI). The lack of absorption around 800 nm indicates the absence of Np(V)-carbonate species. The discontinuity in adsorption at 800 nm, indicated by the vertical arrow, is caused by mechanical changes in the light source.

would have been evident as ^{13}C NMR peaks at 8 and -89 ppm. The only Np(VI) species detectable in our solutions was the monomeric $[NpO_2(CO_3)_3]^{4-}$ complex.

Section 4.2.2- NMR Spectroscopy

Nuclear magnetic resonance (NMR) measurements were carried out using a Bruker Avance DRX 600 MHz (14.1 T, ^{13}C: 151.01 MHz) spectrometer equipped with a 5-mm broadband probe. Because of the inherent danger using Np, the sample was doubly contained in the NMR using Wilmad-Labglass Pyrex coaxial system for toxic samples. The ^{13}C spectra were acquired using the previously described pulse sequence[27] consisting of three 90° hard-pulse excitations using 11.26 μs 90° pulse with a recycle delay of 0.5 s to ensure complete relaxation. A schematic of the pulse sequence and magnetization movement is shown in **Figure 4.5**.

For our experiments, the sweep width was set to 1000 ppm (150.8 kHz) and we collected between 100-200 scans, depending on the particular solution, in order to establish an adequate signal-to-noise ratio. Temperature was controlled using the Bruker Avance temperature controller, and experiments were collected over the temperature rand of 293-340 K. The variation in the temperature reported by the Bruker system and the temperature inside the NMR sample tube was calibrated using neat ethylene glycol[32, 33], and the uncertainty in the temperature was determined to be ±0.2 K.

In this pulse program, the magnetization of both sites is initially tipped into the *xy*-plane using a hard 90° pulse on the x-axis. A calculated delay time, τ_{Prec}, is allowed to pass so magnetization that is not on resonance will rotate in the *xy*-plane until the two signals are exactly 180° out of phase. Then, a hard 90° pulse is then reapplied along the *x*-axis to flip both signals, but one is inverted. A variable-time delay is then applied to allow mixing of the two magnetizations until a third hard 90° pulse is applied along the *x*-axis to tip both magnetizations

into the *xy*-plane for detection. As the magnetization is transferred between the two sites, the intensity of the inverted peak will increase and that of the positive site will decrease **[Figure 4.6]** because of chemical exchange.

The system is modeled using the Bloch equations with the McConnell formalism for exchange (Eqn 4.1 and 4.2).

$$\frac{dM_{z,free}(t)}{dt} = \frac{[M_{z,free(t)} - M^{eq}_{z,free}]}{T_{1,free}} k_{bound} M_{z,bound} - k_{free} M_{z,free} \qquad (4.1)$$

$$\frac{dM_{z,bound}(t)}{dt} = \frac{[M_{z,bound(t)} - M^{eq}_{z,bound}]}{T_{1,bound}} k_{free} M_{z,free} - k_{bound} M_{z,bound} \qquad (4.2)$$

where: $M_{z,i}(t)$ and $M^{eq}_{z,i}$ is the magnitude of the z-magnetization for species *i* as a function of time and equilibration, respectively, $T_{1,i}$ is the longitudinal relaxation rate of species *i*, and k_i is the rate constant for the ligand exchange between the bound and free state. Due to the Law of Detailed Balance, $X_{free}k_{free} = X_{bound}k_{bound}$, where X_{free} and X_{bound} are the concentrations of the free and bound carbonate respectively. Each peak was phased independently and then fit to a Lorenzian function and the amplitude value for each peak was organized according to mixing time. The rate of exchange for the bound species, k_{bound}, was obtained by analytically solving the coupled differential equations above **[Figure 4.7**, see also *Appendix D***]** and then fitting the solutions via least-squares minimization using a Levenberg-Marquardt algorithm. The T_1 values for the free and bound carbonate were also allowed to adjust in the optimization algorithm, but the resulting rate coefficients are insensitive to these values. Nevertheless, these optimized T_1 values for the free carbonate, and the fitting uncertainties, are reported in the *Appendix D*.

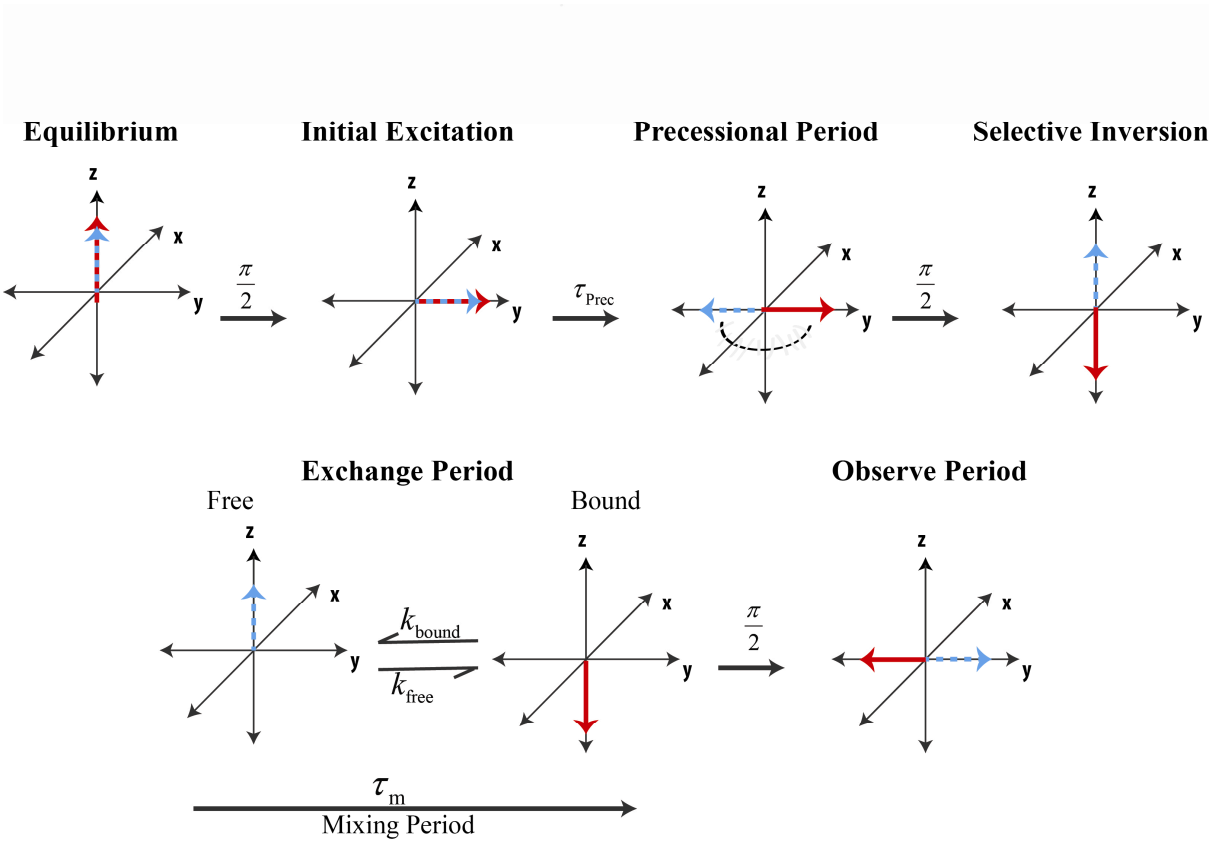

Figure 4.5: The saturation-transfer pulse sequence used to separate the signals from two closely spaced complexes. The solid arrow represents the magnetization of the species that is put on resonance, and the dotted arrow represents the magnetization of the species not on resonance.[28]

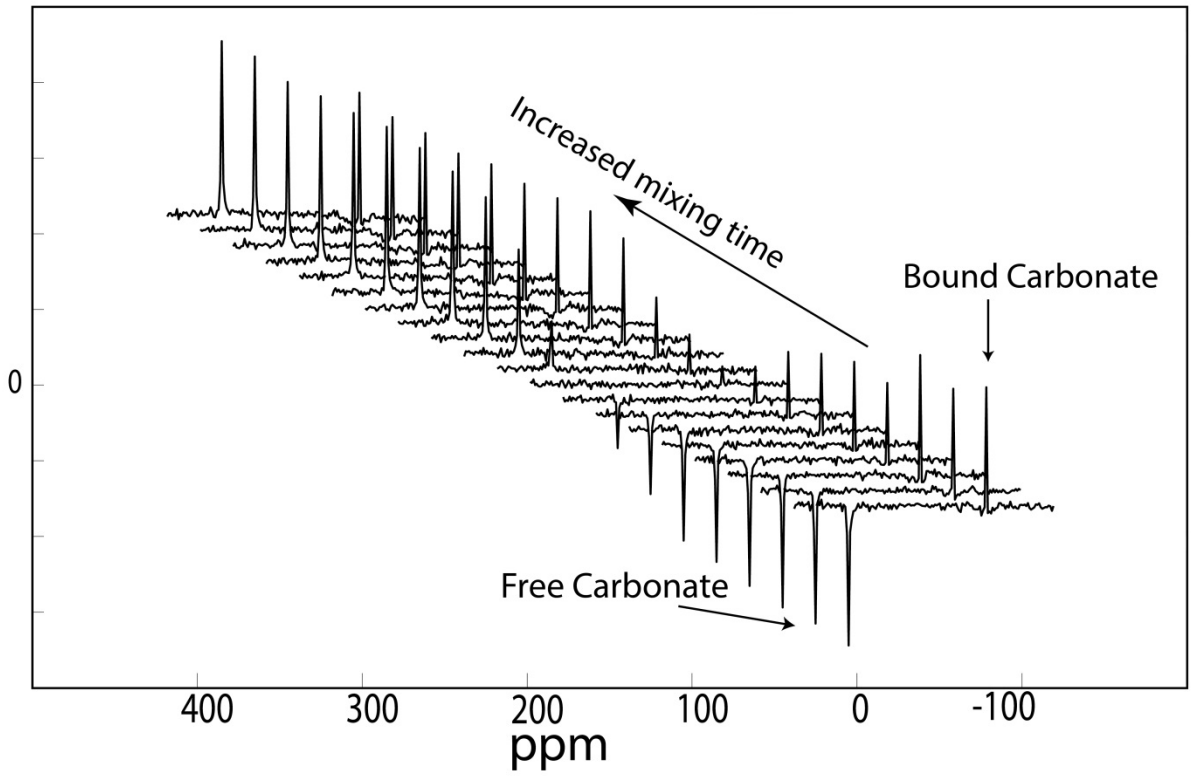

Figure 4.6: ^{13}C NMR spectra of a saturation-transfer experiment Sample 4.5 (see **Table 4.1**). The free carbonate peak is inverted and the magnetization relaxes back along the z-axis after an adjustable mixing time.

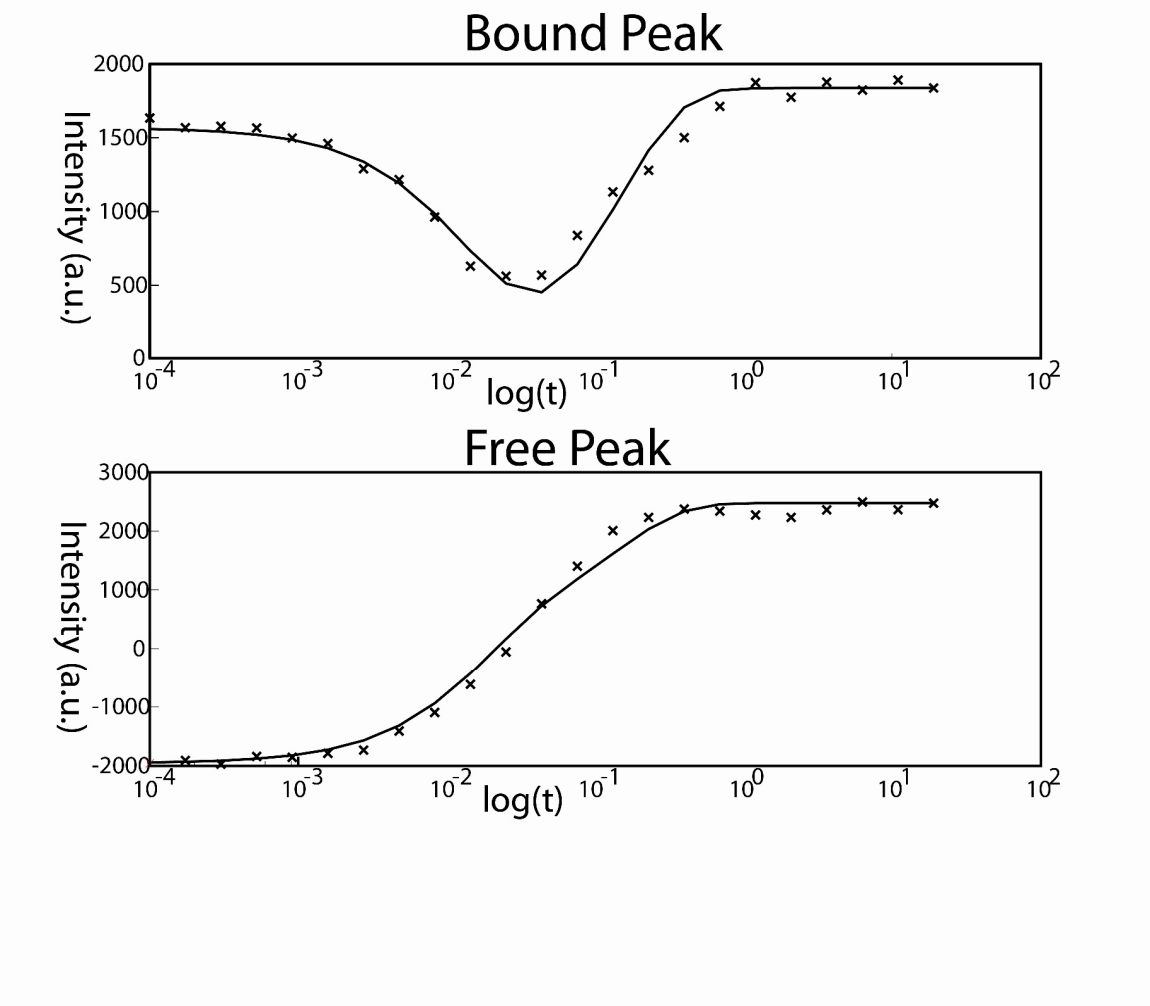

Figure 4.7: Magnetization-transfer experiment of $[NpO_2(CO_3)_3]^{4-}$ (aq) for Sample 4.5 (7.2 mM neptunyl at 10.1 pH). The x's represent measurements and the solid line is the best fit to these data.

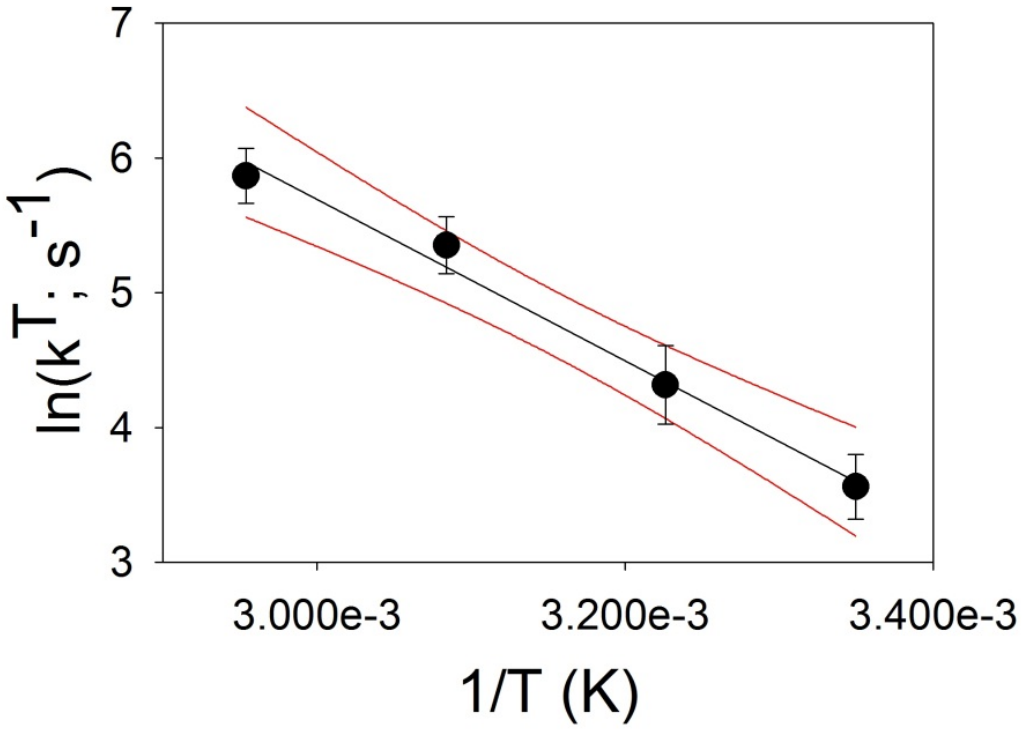

Figure 4.8: Plot of ln(k) vs. 1/T for the exchange of carbonate in $[NpO_2(CO_3)_3]^{4-}$ for Sample 4.1 (12mM $[NpO_2(CO)_3]^{4-}$ solution at pH 10.5). Experimental results are shown by the dots and the solid line is the best fit. The red lines indicate the 95% confidence interval.

The rates thus determined were plotted as a function of 1/T in order to derive activation parameters (k_{ex}^{298}, $\Delta H^{\ddagger}$, and $\Delta S^{\ddagger}$) via Arrhenius equation **[Figure 4.8**, see also *Appendix D*]. A Monte Carlo algorithm was used to assign uncertainties to the activation parameters. We created an array of 1000 randomly generated numbers having a mean value of the regressed rate and a standard deviation of the regression standard deviation for each temperature. A single point of each temperature array was randomly chosen and linearly regressed to calculate the slope and intercept. This single-point process was repeated 1000 times. The mean and standard deviation of these aggregated slopes and intercept values were then used to estimate the uncertainties in all activation parameters. We report these uncertainties in **Table 4.3**.

Banyai et al. extended the study of Brucher et al. who reported a first-order exchange reaction for the $[UO_2(CO_3)_3]^{4-}$ ion.[34, 35] First-order kinetics were also reported for carbonate exchange of $[UO_2(CO_3)_3]^{5-}$ and $[PuO_2(CO_3)_3]^{4-}$ in solutions at high pH.[17,36] As we show (below), the first-order model adequately accounts for the experimental results[1] and is implicit in Eqns. (4.1) and (4.2).

Section 4.3- Results

Our data **[Table 4.3]** agree well with Stout et al. [23], who reported rates for only two samples at pH 9.4 and 10.0 and at different solution conditions. A proton-enhanced pathway at pH<9 is apparently present (see below), making the results consistent with previous work on the isoelectronic and isostructural $[UO_2(CO_3)_3]^{4-}$ molecule. For samples between $9.3 \leq pH \leq 10.5$, there appears to be no strong correlation between the exchange rates and activation enthalpy, pH,or the concentration of Np(VI). If we reject the idea of a pH dependence of the rate for these samples, the average activation parameters at $9.3 \leq pH \leq 10.5$ are found to be: $k_{ex}^{298} = 40.6(\pm 4.3)$

s^{-1}, E_a = 45.1(±3.8) kJ mol^{-1}, $\Delta H^{\ddagger}$ = 42.6(±3.8) kJ mol^{-1}, $\Delta S^{\ddagger}$ = -72 (±13) J mol^{-1} K^{-1}. The precision of the measurements can be gauged by comparing the results for Sample 4 and 5, which have similar concentrations and pH values. The difference in the k_{ex}^{298} is ~7 s^{-1}, and the difference in the enthalpy is ~7 kJ mol^{-1}, which is close to the estimated uncertainties for a single measurement. These are also similar to the uncertainty values reported by Stout et al[1] of ± 3.3 s^{-1} and 6.7 kJ mol^{-1} for rate and enthalpy, respectively. Buffers were avoided in our study because of the possibility that they alter the speciation or kinetics. The similarity of our data to Stout et al.[23] indicates that the effects are negligible.

Section 4.4- Discussion

In the pH range 9.3<pH<10.5, where there is no evident proton enhancement, our data for carbonate exchange, expressed as k_{ex}^{298}, are consistent with, but lower than, those proposed by Stout et al[1] by about a factor of 1.5-3.5. They reported rates of 143(±1.0) s^{-1} and 64.7(±3.3) s^{-1} for pH 9.4 and 10.0, respectively. We determined an average ligand exchange rate of 40.6(±4.3) s^{-1} at $9.3 \leq pH \leq 10.5$. As we mentioned above, the rates determined by Stout et al[23] were obtained using the Swift-Connick[24] formalism which measures the broadening in the spectral line width as a result of the ligand exchange, while the rates we report were determined using the saturation-transfer technique, which directly measures the rate of magnetization exchange between the bound and free carbonate. Szabo and Grenthe[37] demonstrated that saturation-transfer experiments gave more accurate rate values than the line-broadening technique when the exchange is slow on the NMR time scale, resulting into two well defined peaks, as is the case for the $[NpO_2(CO_3)_3]^{4-}$ system.

Banyai et al. determined that there are two pathways of carbonate ligand exchange on the $[UO_2(CO_3)_3]^{4-}$ ion.[35] The first pathway dominates at higher pH, is independent of pH, and is controlled by the unenhanced dissociation of the carbonate ligand from the complex, for which at pH> 8.7, they report, k_{ex}^{298} =13(±3) s^{-1}, and $\Delta H^{\ddagger}$ and $\Delta S^{\ddagger}$ of 82(±11) kJ mol^{-1} and 50(±30) J mol^{-1} K^{-1}, respectively[37]. The second pathway depends on proton concentration, for which at pH<8.6, they reported k_{ex}^{298} = 2.32(±0.03)□10^9 s^{-1} M^{-1}. They calculated this rate using the following equation (Eqn. 4.3):

$$k_2 = \frac{\left(k_{obs} - k_1\right)}{\left[\mathrm{H}^+\right]} \qquad (4.3)$$

We conducted experiments at pH<9 specifically to search for evidence of a proton-enhanced pathway in the $[NpO_2(CO_3)_3]^{4-}$ complex. Using the values we obtained for the experiments at pH=9.3 and pH=8.8 as indicated an unenhanced pathway, the presence of a proton-enhanced pathway would not be evident unless the rate coefficient, k_2, were greater than □1□10^{10} s^{-1} M^{-1}. Furthermore, one anticipates that the experimental activation enthalpy would be smaller to reflect a contribution from the enthalpy of protonation. Both of these phenomenon should be observed as the proton-enhanced pathway becomes evident in the raw experimental data. For samples 6 (pH=8.1) and 7 (pH=8.55) we calculate k_2 □1.9□10^{10} s^{-1} M^{-1} and □1.5□10^{10} s^{-1} M^{-1}, respectively, from Eqn. (4.3). For both samples, the experimental activation energies (and enthalpies) are significantly smaller than the values at pH>9. The values of $\Delta H^{\ddagger}$ for all samples pH ≥ 8.55 are 43.3(± 4) kJ mol^{-1}. The values for Samples 4.2 and 4.7 are indistinguishable from this average. However, our lowest pH sample, Sample 6, exhibited values $\Delta H^{\ddagger}$=25.7(± 9 kJ mol^{-1}), which is significantly distinct from the higher pH results. We therefore conclude that there is a proton-enhanced pathway for exchange of the carbonate, as Banyai et al.[35] observed for

$[UO_2(CO_3)_3]^{4-}$ complex, and that it is evident only at pH<8.6. The contribution of the proton-enhanced pathway is evident in **Figure 4.9 (a,b)**.

Table 4.3: Experimental activation parameters.

	$[NpO_2(CO_3)_3]^{4-}$ (mM)	pH	E_a (kJ mol^{-1})	k_{ex}^{298} (s^{-1})	$\Delta H^{\ddagger}$ (kJ mol^{-1})	$\Delta S^{\ddagger}$ (J mol^{-1} K^{-1})
Sample 4.1	12	10.5	49.8 ± 9.2	35.2 ± 5.4	47.3 ± 7.2	-57 ± 24
Sample 4.2	12	8.8	44.9 ± 11	53.1 ± 4.6	42.3 ± 8.7	-63 ± 17
Sample 4.3	10	9.3	44.1 ± 9.4	45.4 ± 5.3	41.6 ± 6.9	-74 ± 26
Sample 4.4	8	10.1	39.5 ± 11	37.5 ± 6.5	37.0 ± 8.9	-91 ± 30
Sample 4.5	7.2	10.1	46.8 ± 10	44.1 ± 5.9	44.3 ± 8.0	-64 ± 27
Sample 4.6	10	8.1	28.1 ± 12	157 ± 6.2	25.7 ± 9.1	-117 ± 30
Sample 4.7	10	8.55	50.0 ±8.9	93.3 ± 5.8	47.5 ± 6.4	-48 ± 22

There is understandable disagreement about the mechanisms of the carbonate ligand-exchange reaction, which must be at least a two-step process. Free carbonate (or bicarbonate) must associate with the ion and either exploit or induce a ring-opening of an existing ligated bidentate carbonate. Once the ring opens, the incoming carbonate could bond via a unidentate oxygen and collapse into a ring when the leaving carbonate is gone. What is not fully clear is whether there exists an intermediate state of aquated Np(VI) between the incoming and outgoing

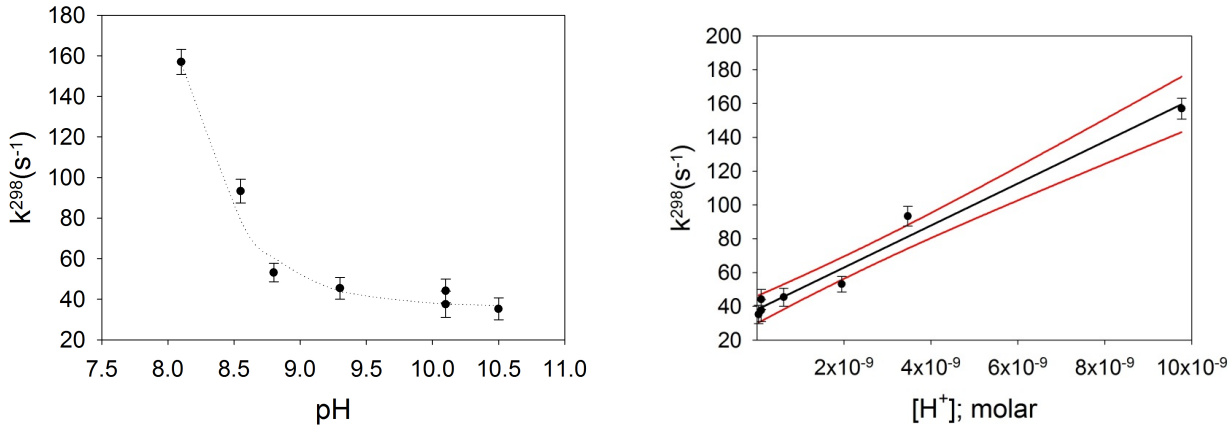

Figure 4.9: The experimental rate data plotted from Table 2 as a function of solution pH. The dotted line is the approximate location of a least-squares fit of Eqn. (3) to the data, yielding k_1=36.3 s^{-1} and k_2=1.23⊠10^{10} M^{-1} s^{-1}, using γ_{H^+} =0.81 to convert proton activities to concentrations. **Right:** The data regressed against hydrogen-ion concentration, yielding a slope of 1.243(±0.04)⊠10^{10} M^{-1} s^{-1} and an intercept of 38 s^{-1}(±3). The 95% confidence interval is shown as red lines.

carbonates. Elucidation of such detail is difficult because the evidence to constrain it consists of experimental entropies, which themselves must be composite parameters. Carbonate exchange in : $[UO_2(CO_3)_3]^{4-}$,$[UO_2(CO_3)_3]^{5-}$, $[PuO_2(CO_3)_3]^{4-}$ are reported as dissociative [34, 27, 36] while, Stout et al., as do we, reported negative activation entropies for both the U(VI) species the Np(VI) species.[23] Stout et al used these negative entropies to suggest a more associative mechanism between the complex and the incoming carbonate ligand.

To extend their work, we recently measured apparent activation volumes for both the proton-enhanced and pH-independent pathways using high-pressure NMR.[27] The net activation volumes for the $[UO_2(CO_3)_3]^{4-}$ proton-enhanced pathway and the pH-independent pathway were found to be positive, +6.6(±0.7) cm^3 mol^{-1} and +10.6(±0.7) cm^3 mol^{-1}, respectively.[27] These activation volumes correspond to a multi-step reaction pathway and cannot be uniquely interpreted to indicate mechanism of exchange, but an obvious question is whether these values are quantitatively similar for the nearly identical $[NpO_2(CO_3)_3]^{4-}$ ion. The addition of apparent activation volumes could couple to new methods of simulation of volume changes during the reaction and advance the field since the simulations would treat structurally very similar molecules.[38] Finally, we think that the overall similarity in reactivity between the Np(VI) and U(VI) complexes is important to geochemical efforts, since the reactivities of the transuranic elements are so poorly documented in natural systems.

Section 4.5- References

[1] Poinssot, C.; Geckeis, H. *Radionuclide Behavior in the Natural Environment; Science, Implications, and Lessons for the Nuclear Industry*; Woodhead Publishing Ltd.; Cambridge, U.K., 2012

[2] Szabó, Z.; Toraishi, T.; Vallet, V.; Grenthe, I., *Coord. Chem. Rev.* **2006,** *250*, 784-815.

[3] Dozol, M.; Hagemann, R., *Pure and Appl. Chem.* **1993,** *65*, 1081-1081.

[4] Novikov, A., *Geochem. Int.* **2010,** *48*, 1263-1387.

[5] Maher, K.; Bargar, J. R.; Brown Jr, G. E., *Inorg. Chem.* **2012,** *52*, 3510-3532.

[6] Clark, D. L.; Conradson, S. D.; Donohoe, R. J.; Keogh, D. W.; Morris, D. E.; Palmer, P. D.; Rogers, R. D.; Tait, C. D., *Inorg. Chem.* **1999,** *38*, 1456-1466.

[7] Ikeda-Ohno, A.; Hennig, C.; Rossberg, A.; Funke, H.; Scheinost, A. C.; Bernhard, G.; Yaita, T., *Inorg. Chem.* **2008,** *47*, 8294-305.

[8] V. P. Shilov, A. V. G., and A.M. Fedoseev, *Radiochemistry* **2012,** *54*, 212-227.

[9] Vasudeva Rao, P.; Gudi, N.; Bagawde, S.; Patil, S., *J. Inorg. Nucl. Chem.* **1979,** *41*, 235-239.

[10] Hindman, J. C.; Sullivan, J. C.; Cohen, D., *J. Am. Chem. Soc.* **1958,** *80*, 1812-1814.

[11] Rao, L.; Srinivasan, T. G.; Garnov, A. Y.; Zanonato, P.; Di Bernardo, P.; Bismondo, A., *Geochim. Cosmochim. Acta* **2004,** *68*, 4821-4830.

[12] Hindman, J.; Sullivan, J.; Cohen, D., *J. Am. Chem. Soc.* **1954,** *76*, 3278-3280.

[13] Rao, L.; Tian, G., *Symmetry* **2009,** *2*, 1-14.

[14] Clark, D. L.; Hobart, D. E.; Neu, M. P., *Chem. Rev.* **1995,** *95*, 25-48.

[15] Ikeda-Ohno, A.; Tsushima, S.; Takao, K.; Rossberg, A.; Funke, H.; Scheinost, A. C.; Bernhard, G.; Yaita, T.; Hennig, C., *Inorg. Chem.* **2009,** *48*, 11779-87.

[16] Maya, L., *Inorg. Chem.* **1983,** *22*, 2093-2095.

[17] Clark, D. L.; Hobart, D. E.; Palmer, P. D.; Sullivan, J. C.; Stout, B. E., *J. Alloys Compd.* **1993,** *193*, 94-97.

[18] Wester, D.; Sullivan, J., *J. Inorg. Nucl. Chem.* **1981,** *43*, 2919-2923.

[19] Grenthe, I.; Riglet, C.; Vitorge, P., *Inorg. Chem.* **1986,** *25*.

[20] Maya, L., *Inorg. Chem.* **1982,** *21*, 2895-2898.

[21] Madic, C.; Hobart, D.; Begun, G., *Inorg. Chem.* **1983,** *22*, 1494-1503.

[22] Tait, C.; Palmer, P.; Ekberg, S.; Clark, D. *Report on neptunium speciation by NMR and optical spectroscopies*; Los Alamos National Lab., NM (United States): 1995.

[23] Stout, B. E.; Choppin, G. R.; Sullivan, J. C.*Transuranium elements: a half century*; An American Chemical Society Publication: Washington D.C., 1992.

[24] Swift, T. J.; Connick, R. E., *J. Chem. Phys.* **1962,** *37*, 307-20.

[25] Harley, S. J.; Ohlin, C. A.; Casey, W. H., *Geochim. Cosmochim. Acta* **2011,** *75*, 3711-3725.

[26] Helm, L.; Nicolle, G. M.; Merbach, R. E., *Adv. Inorg. Chem.* **2005,** *57*, 327-379.

[27] Johnson, R. L.; Harley, S. J.; Ohlin, C. A.; Panasci, A. F.; Casey, W. H., *Chemphyschem* **2011,** *12*, 2903-2906.

[28] Snow, M. S.; Zhao, P.; Dai, Z.; Kersting, A. B.; Zavarin, M., *J. Colloid Interface Sci.* **2012**.

[29] Johnson, A.; Shepherd, G. *Spectrophotometry of neptunium in nitric acid solutions*; Dow Chemical Co., Golden, Colo. Rocky Flats Div.: 1967.

[30] Sjoblom, R.; Hindman, J., *J. Am. Chem. Soc.* **1951,** *73*, 1744-1751.

[31] Hagan, P.; Cleveland, J., *J. Inorg. Nucl. Chem.* **1966,** *28*, 2905-2909.

[32] Ammann, C.; Meier, P.; Merbach, A., *J. Magn. Reson. (1969)* **1982,** *46*, 319-321.

[33] Kaplan, M.; Bovey, F.; Cheng, H., *Anal. Chem.* **1975,** *47*, 1703-1705.

[34] Brucher, E.; Glaser, J.; Toth, I., *Inorg. Chem.* **1991,** *30*, 2239-2241.

[35] Banyai, I.; Glaser, J.; Micskei, K.; Toth, I.; Zekany, L., *Inorg. Chem.* **1995,** *34*, 3785-3796.

[36] Mizuoka, K.; Grenthe, I.; Ikeda, Y., *Inorg. Chem.* **2005,** *44*, 4472-4474.

[37] Szabó, Z. ; Grenthe, I., *Inorg. Chem.* **2010,** *49*, 4928-4933.

[38] Deglint, E.; Martens, H.; Edwards, E.; Boon, N.; Dance, P.; Weinberg, N., *Phys. Chem. Chem. Phys.* **2011,** *13*, 438-440.

Chapter 5:

Rate of oxygen-isotope-exchange of equatorial waters on the $[NpO_2(OH_2)_5]^+$ ion

Section 5.1- Introduction

Transport models that accurately predict the movement of contaminants, especially the actinides, through waste-barriers, soil, and groundwater are critical for the future of nuclear power and nuclear-waste storage[1]. The actinide species are stable in multiple different oxidation states in nature, form colloids, and interact with complexing ligands and mineral surfaces, leading to complex chemistry and increased difficulty in predicting their movements[2]. In order for these interactions to occur, an actinide must lose solvated waters, and to correctly incorporate that into models, an accurate rate of water exchange and oxygen exchange for actinide species is critical. Highly constrained experiments on fully hydrolyzed actinide species can determine water-exchange rates that can also be compared to *ab initio* molecular-dynamics calculations.

Neptunium, having a long half-life of 2.14 x 10^6 years, is problematic for long-term repositories. Aqueous neptunium can be found in oxidation states ranging from (III) to (VII), with the pentavalent state being the most stable. This ion contains two opposing axial 'yl' oxygens having a high bond order and five equatorial bound waters, $[NpO_2(H_2O)_5]^+$ (**Figure 5.1)** which will be referred to as NpO_2^+(aq). Although there has been some debate regarding the number of equatorial bound waters[3-8], more recent publications have continued to show the presence of five bound waters, and we assume this structure for this subsequent discussion. EXAFS studies show two oxygens at a distance of ~1.8 Å correlating to the two axial oxygens, and five oxygens at a distance of ~2.5 Å, which have been assigned to five equatorial waters[3-6]. Allen *et al.*[4] demonstrate the fully hydrated NpO_2^+(aq) EXAFS resulted in a structure similar to UO_2^{2+}(aq) differing in that the bond lengths between the metal center and the oxygens are longer due to a larger ion size of Np(V). However, the plutonyl(V) aqueous ion has been shown to have four bound waters in the equatorial plane Ikeda-Ohno *et al*[6] fixed the number of coordinated

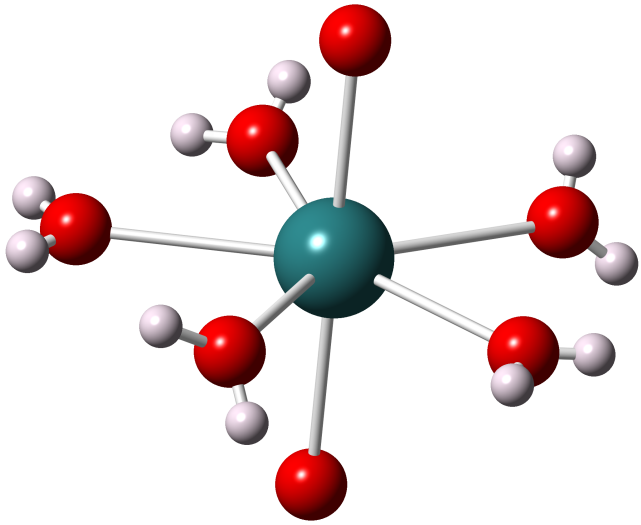

Figure 5.1: The $[NpO_2(H_2O)_5]^+$ ion. Np(V) is green, oxygen red, and hydrogen white. The two opposing "yl" oxygens are in the axial positions, while the five water ligands are in the equatorial plane.

waters to determine the best fit to the EXAFS data of the NpO_2^+(aq) ion. Using that, and the bond-valence model[9], they determined a hydration number near 5 for NpO_2^+, which is consistent with other EXAFS results[3,4]. Thus we assume this value in this paper.

Study of the pentavalent species has been heavily studied in acidic to neutral conditions, however, the rate at which water exchanges is still poorly known [10-17]. Rabideau measured water exchange by injecting isotopically labeled $Np^{18}O_2^+$(aq) into isotopically normal water and then tracking the evolution of ^{18}O in the bulk solution using an isotope-ratio mass spectrometer[18]. A water-exchange rate of 0.31 sec^{-1} was found for the NpO_2^+(aq)ion, but their experiments were carried out at only one pH and temperature. No uncertainty was reported. The chapter described here is an attempt to extend the earlier study by Rabideau. Our hypothesis is that modern ^{17}O-nuclear magnetic resonance (NMR) spectroscopy can measure the rates of water exchange if the solutions are heated to enhance the reaction rate by following the effect of the paramagnetic electrons on the ^{17}O-NMR signal for bulk water, since the paramagnetic species itself is probably not observable. This would be the first NMR-measure rate of water exchange at various pH values for NpO_2^+(aq) and will greatly enhance our understanding of transuranic chemistry.

The NpO_2^+(aq) ion has two *f* valence electrons that are predicted to be unpaired, resulting in a paramagnetic species. Magnetic-susceptibility experiments on the aqueous ions have been completed[19] on actinides in different acidic media that could coordinate to the neptunium metal center. Recent work published by Wall *et al*. used the Evans Method, an NMR technique, to experimentally determine the paramagnetism of fully hydrated actinides in perchloric acid[20]. The chemical shift of an NMR signal depends on the magnetic susceptibility of the bulk solution. A *tert*-butanol reference solution and a capillary containing *tert*-butanol and the paramagnetic ion are placed inside a NMR tube[21]. The difference in chemical shift between the *tert*-butanol

signal of the reference and in the presence of the Np(V) is related to the magnetic susceptibility difference of the two solutions. Completing these experiments at variable temperatures allows for detection of Curie behavior of the species. The authors found Np(V) to have an effective magnetic moment of 3.06 μ_b, where $\mu_b = 9.27 \times 10^{-27}$ J T^{-1} (T in this case is Tesla, the magnetic field strength, and not temperature), which is lower than 3.58 μ_b predicted using Hund's Rule[22], but still paramagnetic and a good candidate for kinetic exchange experiments in NMR using paramagnetic methods, like the Swift-Connick Formalism[23,34].

As a paramagnetic species, the NpO_2^+(aq) ion can potentially be used for ^{17}O NMR exchange-rate studies via the Swift-Connick formalism[23,24], since the rate determined by Rabideau[18], 0.31 sec^{-1}, falls within the timescale of which NMR can capture exchange, which is 10^{-2} to 10^2 sec^{-1} [25]. The rate of 0.31 s^{-1}, of course, would be accelerated by heating the solution. The Swift-Connick method compares the peak width and intensity of the free ^{17}O water signal with, and without, the presence of the paramagnetic metal, NpO_2^+(aq), in solution. The change in the unbound ^{17}O signal is used, because the signal of bound water is quenched due to the paramagnetic electrons of the ion. This method has been used extensively for paramagnetic monomer ions with ^{17}O in the hydration sphere [26-28]. NMR experiments to determine the rate of water exchange for the aqueous NpO_2^+(aq) at different pH values and temperatures are described below.

Section 5.2- Experimental

Caution. ^{237}Np is a radioactive isotope and an α-emitter. It should be handled in dedicated facilities with appropriate equipment for radioactive materials to avoid health risks caused by radiation exposure.

Section 5.2.1- Sample Preparation

A stock solution of Np(V) was prepared using the ^{237}Np column-purification method of Snow et al.[29] The solution was washed and dried in 18-Megaohm resistance water until the solid would no longer dissolve. The solid was heated to complete dryness and for initial experiments, Np concentrations of ~10 mM, the solid was dissolved in various acids including nitric acid, tetrafluoroacetic acid, perchloric acid, and phosphoric acid. For higher concentration experiments, ~30 mM, the solid was redissolved in 0.01 M perchloric acid so the counterion would be perchlorate. The total dissolved neptunium concentration was established using liquid-scintillation counting. The majority of this solution was Np(V), but to ensure a pure oxidation state of Np(V), the solution was electrolyzed using a Wavenow USB potentiostat. The potentiostat had a three-electrode array with a platinum wire-working electrode that was separated from a Pt-wire counter electrode by a Vycor frit, and the reference electrode was an Ag/AgCl microelectrode. Solutions were kept under electrolysis at +0.4 V until the characteristic peak of Np(VI) at 1230 nm disappeared and the Np(V) characteristic peak at 980 nm was predominant. The pure Np(V) solution was then used to make subsamples for the NMR experiments. The pH of the solution was measured using an Ingold microelectrode and adjusted using dilute perchloric acid and sodium hydroxide.

All experiments were performed within one week of solution preparation and we found no evidence of sample degradation during this time. The pH of the solutions was measured before and after experiments in order to verify that changes in temperature did not alter the pH of the solution.

Section 5.2.2- NMR Spectroscopy

Initial NMR measurements were carried out on the less concentrated Np(V) solutions using a Bruker Avance DRX 600 MHz (14.1 T, ^{17}O: 81.4 MHz) spectrometer equipped with a 5-mm broadband probe. The ^{17}O spectra were acquired using single-pulse excitations using an 18.5 μs π/2 pulses with 0.1 s recycle delay. The sweep width was set to 12210 Hz. 10 μL 40% $H_2{}^{17}O$ (Isotec Laboratories) was added to a 200 μL neptunyl solution sample, with a total dissolved concentration of Np of ~10 mM. Collection of 128 acquisitions established adequate signal-to-noise ratio in the spectrum. Temperature was controlled using the Bruker Avance system which was calibrated using neat ethylene glycol[30,31], and the uncertainty was determined to be ±0.2 K. Solutions of the same concentration of background acid spiked with 10 μL 40% $H_2{}^{17}O$ (Isotec Laboratories) was used as the diamagnetic standard.

Experiments carried out on solutions that contained higher concentrations of the NpO_2^+(aq) ion, 30.1 mM Np(V), were performed on a Bruker Avance DRX 500 MHz (11.7 T, ^{17}O: 67.7 MHz) spectrometer. A hand-made copper wire micro coil was attached to a 5 mm broadband probe that allowed for smaller sample size and could be tuned to ^{17}O frequency. The ^{17}O spectra were acquired using a single-pulse excitation using a 5.0 μs π/2 pulses with 0.2 s recycle delay. The sweep width was set to 6775 Hz, and 250 acquisitions established adequate signal-to-noise ratio. 10 μL 40% $H_2{}^{17}O$ (Isotec Laboratories) was added to a 200 μL neptunyl solution sample so that the final concentration of NpO_2^+(aq) was 32 mM. 5 μL of this solution was placed into a 1 mm capillary, which was then sealed into a Teflon EPR liner using epoxy. The temperature was controlled by placing copper tubing connected to a water bath above the sample in the magnet. The temperature was calibrated using a Type T thermocouple placed next

to the coil; the uncertainty was determined to be ±0.1 K. A perchloric acid solution spiked with ^{17}O was used as the diamagnetic standard.

The goal of the experiments was a rate estimate using a Swift-Connick formalism[19,20]. A two-site exchange mechanism in the dilute-solution limit allows for the peak widths to be interpreted using a simplified form of the steady-state Bloch-McConnell equations. The experimental line widths are adjusted for the presence of the diamagnetic standard: $\frac{1}{T_{2r}} = \frac{\pi}{P_m}(\Delta\nu_{obs} - \Delta\nu_{solvent})$. Equation 5.1 is derived from Swift-Connick line-broadening analysis where P_m is the mole fraction of bound waters divided by the mole fraction of solvent

$$\frac{1}{T_{2r}} = \frac{1}{\tau_m}\left[\frac{T_{2m}^{-2} + (T_{2m}\tau_m)^{-1} + \Delta\omega_m^2}{(T_{2m}^{-1}\tau_m^{-1})^2 + \Delta\omega_m^2}\right] \quad (5.1)$$

water and τ_m is the exchange time. The exchange time directly relates to the rate coefficient, $\tau_m = \frac{1}{k_{ex}}$. The changes in exchange rate as a function of time is described using the Eyring-Polanyi equation: $\frac{1}{\tau_m} = \left(\frac{k_B T}{h}\right) e^{\left(\frac{\Delta S^{\ddagger}}{R} - \frac{\Delta H^{\ddagger}}{RT}\right)}$. The temperature variation of $\frac{1}{T_{2r}}$ is exponential with $\frac{1}{T}$ and $\Delta\omega_m$ is linear with the inverse temperature, resulting in a system of nonlinear equations in $\frac{1}{T_{2r}}$ that could be minimized using a Levenberg-Marquardt algorithm with data collected over a wide range of temperatures. We have used this approach before, as discussed in earlier chapters of this thesis that treated oxygen-isotope exchange at the Fe(III) oligomer.

Section 5.2.3- Magnetic Susceptibility

Magnetic-susceptibility measurements were made using a Quantum Design SQUID Magnetometer. In order to prevent contamination to the instrument, 10 μL of the liquid

NpO_2^+(aq) solution was placed into an approximately 5 cm long 3 mm in diameter Teflon liner with openings at both ends. The openings were then closed using epoxy to ensure a sealed environment.

Section 5.2.4- Swift-Connick Simulations

All calculations were performed using a code in wxMaxima (*Appendix E*) that solves the full Bloch equations using the McConnell formalism for rates, and calculates spectra from the component of magnetization (v) that produces a Lorentzian peak shape as a function of frequency[24]. The solution to the Bloch-McConnell equations is approximated within the Swift-Connick treatment and magnetization is given by:

$$v = \frac{\omega M_0^w [T_{2,m}^{-1} + k_w(\frac{1/T_{2,m}^2 + k_m/T_{2,m} + \Delta\omega_m^2}{(1/T_{2,m} + k_m)^2 + \Delta\omega_m^2})]}{[T_{2,w}^{-1} + k_w(\frac{1/T_{2,m}^2 + k_m/T_{2,m} + \Delta\omega_m^2}{(1/T_{2,m} + k_m)^2 + \Delta\omega_m^2})]^2 + [\Delta\omega_m + \frac{\Delta\omega_m}{(1/k_w k_m)((1/T_{2,m} + k_m)^2 + \Delta\omega_m^2)}]^2} \qquad (5.2)$$

where, ω is the frequency, M_0^w is the magnetization of bulk water at time zero, $T_{2,m}$ and $T_{2,w}$ are the transverse relaxation for the bound and free oxygen, respectively, k_w is the rate of exchange for the free water, k_m is the rate of exchange for the bound water. Due to the Law of Detailed Balance, $k_w = k_m \frac{C_m}{C_w}$, C_m is the mole fractions of bound water and C_w is the mole fraction of bulk water. $\Delta\omega_m$ is the chemical shift difference between the bound and bulk water, which is not experimentally known since the bound water signal is quenched. The shift difference is determined using equation 5.3[32,33]:

$$\Delta\omega_m = \frac{g_L \mu_B J(J+1)B}{3k_B T}\frac{A}{\hbar} \qquad (5.3)$$

where g_L is the isotropic Landé g factor, μ_B is the Bohr magneton (9.274 x 10^{-24} J T^{-1}), J is the total angular momentum of the nuclei, k_B is Boltzmann's constant, T is temperature, B is the magnetic field (14.1 for the lower NpO_2^+(aq) concentration calculations and 11.7 for the higher NpO_2^+(aq) concentration), and A/h is the hyperfine coupling constant divided by Planck's constant divided by 2μ.

The following parameter values were used for the simulations. $T_{2,w}$ was set to 0.005 s (typical relaxation of bulk water[26]) and $T_{2,m}$ was 0.000001 s since this value is usually not measureable but small. Since NpO_2^+(aq) has a $5f^2$ configuration[34], its ground state is $^3H_4$ so the total angular momentum, J, is 4. The g_L was calculated using the following equation and the other quantum numbers for a $^3H_4$ ground state, L=5 and S=1[35]:

$$g_L = \frac{3}{2} + \frac{S(S+1) - L(L+1)}{2J(J+1)} \quad (5.4)$$

resulting in a value of 4/5. The hyperfine scalar coupling constant, A/h was set to 7.3 x 10^5 based on the work done by Farkas *et al.*[33]

Two simulations were carried out to compare the predicted peak width of the NpO_2^+(aq) system. The one simulation used an exchange rate so slow the signal is dependent only on the ^{17}O bulk water magnetization, and then compared to a simulation run with an exchange rate of 0.31 s^{-1}, the experimental value reported by Rabideau[18]. To determine whether the concentration of NpO_2^+(aq) in the system would have an effect, we estimated predicted peak widths using the NpO_2^+(aq) concentrations from the NMR experiments. A second set of simulations show the changes of peak width as a function of increasing exchange rate was also carried out.

Section 5.3- Results

UV-VIS-NIR spectroscopy is used to determine what oxidation state of the neptunium in solution. Figure 5.2 shows a UV-VIS-NIR spectrum showing the characteristic spectra of the NpO_2^+(aq) ion. Neptunium(V) has a strong absorbance peak at 980 nm, which is used to determine concentration and purity of sample. **Figure 5.2** is the UV-Vis-NIR spectra for the NpO_2^+(aq) solution used for NMR experiments. The strong peak at 980 nm demonstrates that the neptunium is in the fifth oxidation state. The absence of peaks at 1223 nm and 504 nm results due to the lack of neptunium in the six and four oxidation state, respectively.

NMR spectra were expected to show a broadening and shift in the bulk ^{17}O NMR water signal in a solution that also contains the paramagnetic NpO_2^+(aq) ion compared to a reference solution without the paramagnetic species. **Figure 5.3** shows an NMR spectra of the NpO_2^+(aq) ion dissolved in 1 M nitric acid compared to a nitric acid reference, while **Figure 5.4** shows the NpO_2^+(aq) ion dissolved in 0.1 M triflic acid compared to a triflic acid reference at two different temperature values. We varied the counterion to assure ourselves that the shifts were not due to changes in ligation. There is no difference in chemical shift or peak width between the reference solution and the solution containing the paramagnetic species, resulting in further investigation into the paramagnetism of Np(V) and NMR experiments with higher concentrations.

The magnetic-susceptibility measurements on the aqueous neptunyl ion in perchloric acid demonstrate paramagnetic behavior. A plot **[Figure 5.5]** of mass-magnetic-susceptibility multiplied times temperature ($\chi_m * T$) versus temperature in Kelvin yields a line with the y-intercept being the material specific Curie constant. In this case, the value was determined to be 2.16 emuK/mol.

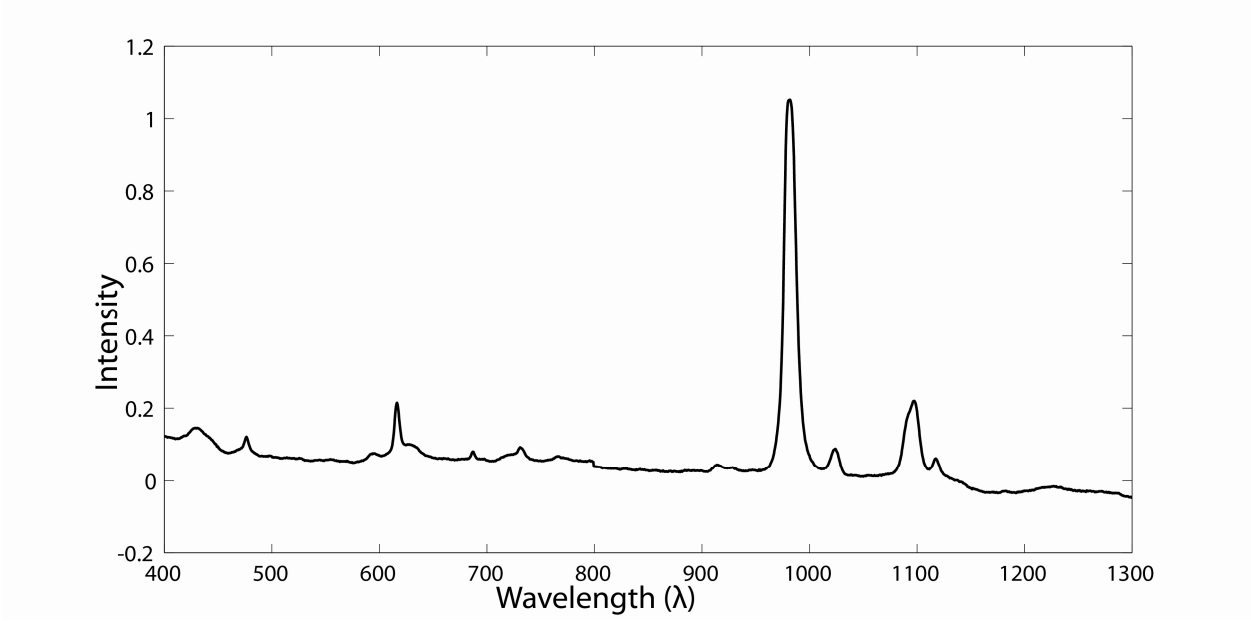

Figure 5.2 UV-Vis-NIR spectra of 5 mM neptunium stock solution after electrochemistry. The peak characteristic for Np(V) is at 980 nm. The solid line is after electrolysis when the solution is nearly pure in Np(V).

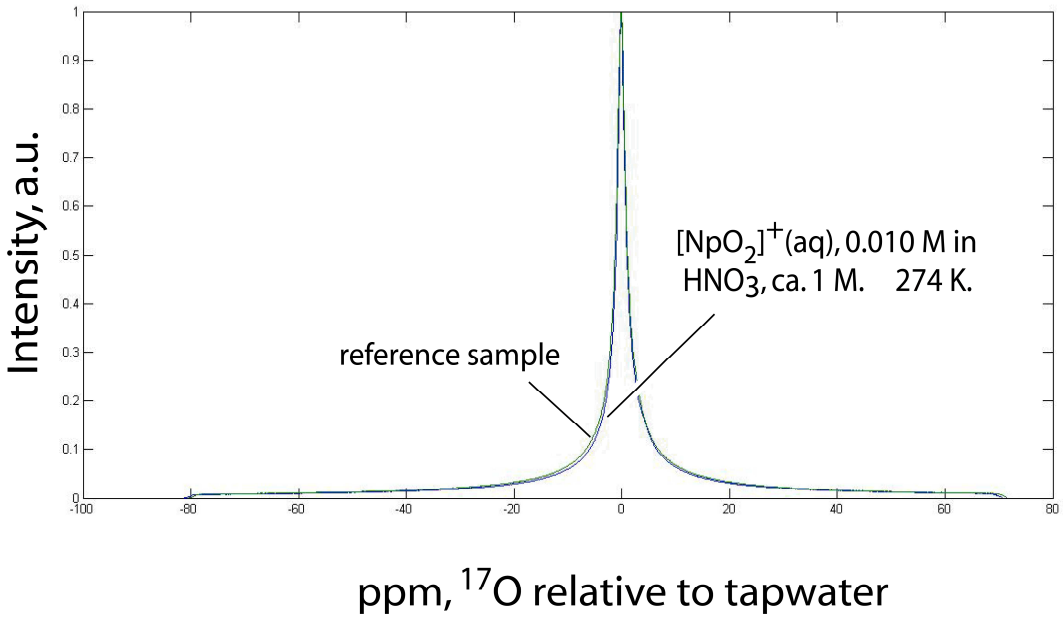

Figure 5.3 NMR spectra of aquated 10 mM NpO_2^+(aq) ion in 1 M nitric acid at 274 K. No difference in either chemical shift or peak width is observed.

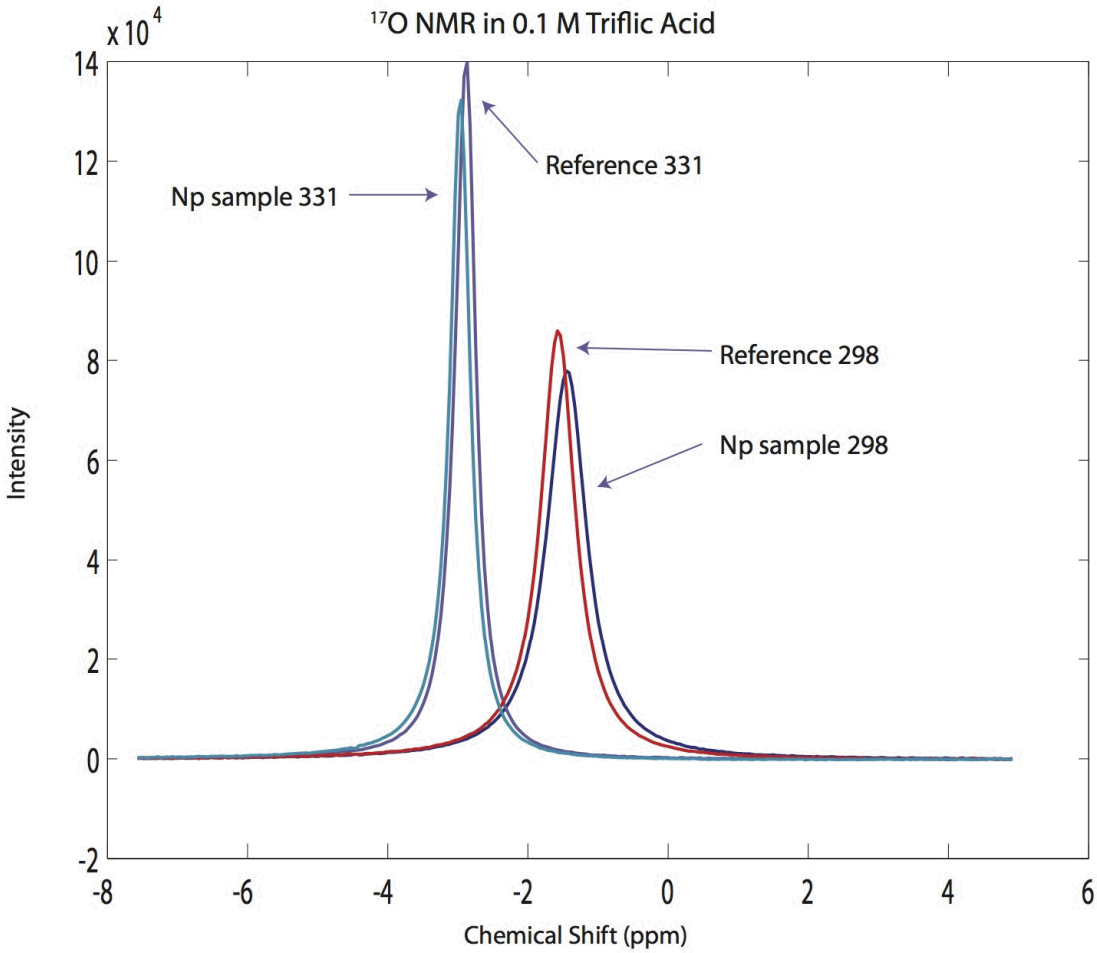

Figure 5.4 NMR spectra of 10 mM NpO_2^+(aq) in 0.1 M triflic acid compared to a triflic acid reference solution at two different temperatures, 298 K and 331 K.

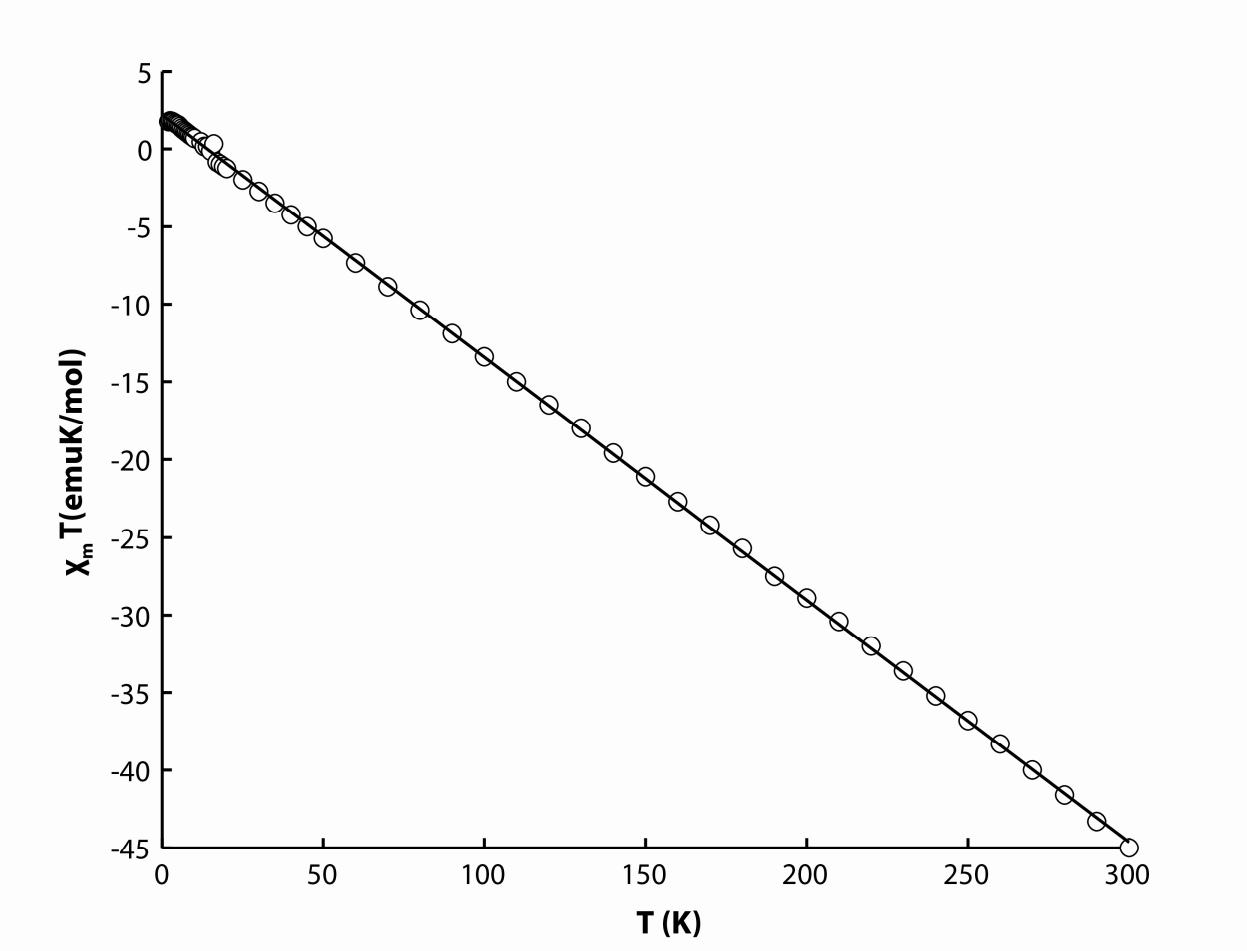

Figure 5.5 Magnetic-susceptibility results for aqueous 10 mM NpO_2^+(aq) in 0.1 perchloric acid. Unfilled circles are the collected data and the solid line is the linear-regression of the best fit with an equation $\chi_m * T$ = -0.16*T+2.16 and a R^2 value of 0.9997.

In contrast to studies of more dilute solutions, NMR experiments on higher concentrated NpO_2^+(aq) solutions show a shift and broadening of the ^{17}O bulk signal when the paramagnetic species is present, **Figure 5.6**. NMR spectra were collected at various temperatures to perform the Swift-Connick experiments. As temperature increases, the peak width is expected to broaden as rates of exchange becomes faster. Yet we find that, over a temperature range of 20 K, the bulk water signal did not shift or broaden as temperature increased, **Figure 5.7**. The increased the concentration of the paramagnetic neptunyl has caused a shift and broadening of the ^{17}O bulk water signal, but the shift and width of the peak is not affected by changes in temperature. This behavior is expected if the paramagnetic ion is affecting the bulk magnetic susceptiblity of the solution, but exchange with bulk waters is at a rate that falls outside the NMR timescale.

The simulations performed to predict the peak width of ^{17}O water signal produced **Figures 5.8** and **5.9**. **Figure 5.8** shows the predict spectra of both the low- and high-concentration experiments at two different exchange rates, one at an arbitrarily chosen extremely slow rate (3.1×10^{-100} s^{-1}) and one at 0.31 s^{-1} for the water exchange rate determined by Rabideau[18]. The result for both concentrations show that there is no change in peak shift or width when the exchange rate was change, predicting that the Swift-Connick experiments would not capture the rate of exchange under these conditions. To be clear, the simulations were solutions to the full Bloch-McConnell equations. Experimental results would have been treated using the Swift-Connick formalism, had they been suitable.

We then increased the rate numerically to identify the conditions where exchange-broadened spectra would be identifiable. **Figure 5.9** is a plot of predicted peak shape as a function of increasing rate of exchange by factor of ten; the peak width does not broaden until

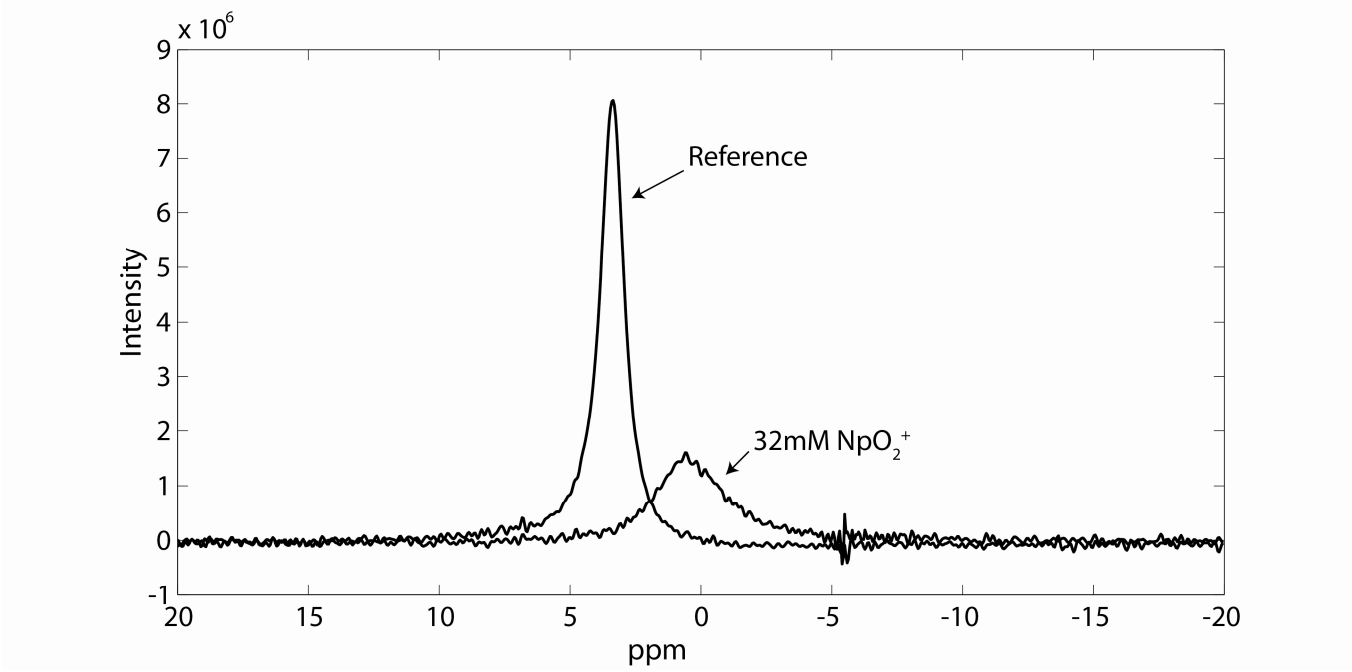

Figure 5.6 NMR spectra of 32 mM NpO_2^+(aq) in 0.1 M perchloric acid compared to perchloric acid reference at 291 K. Note the broadening and shifting of the NMR signal when NpO_2^+(aq) is added to the solution.

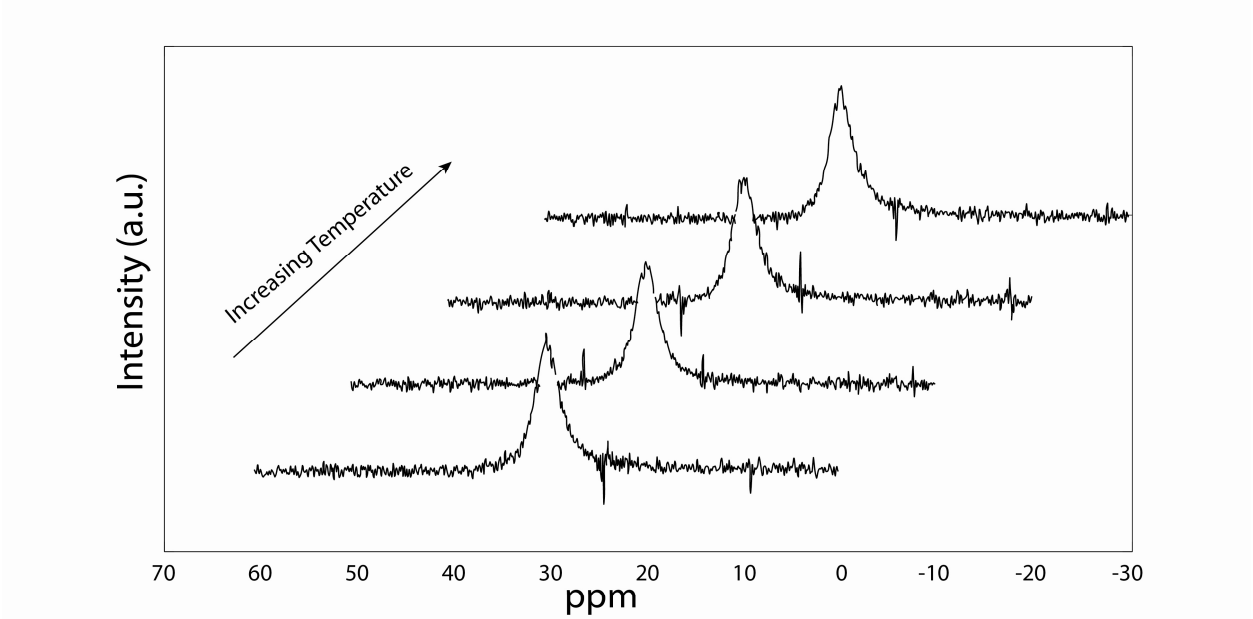

Figure 5.7 NMR spectra of the 32 mM NpO_2^+(aq) in 0.1 M perchloric acid at four different temperatures, 308 K, 303 K, 301 K, 291 K. Note the overall similarity of the spectra.

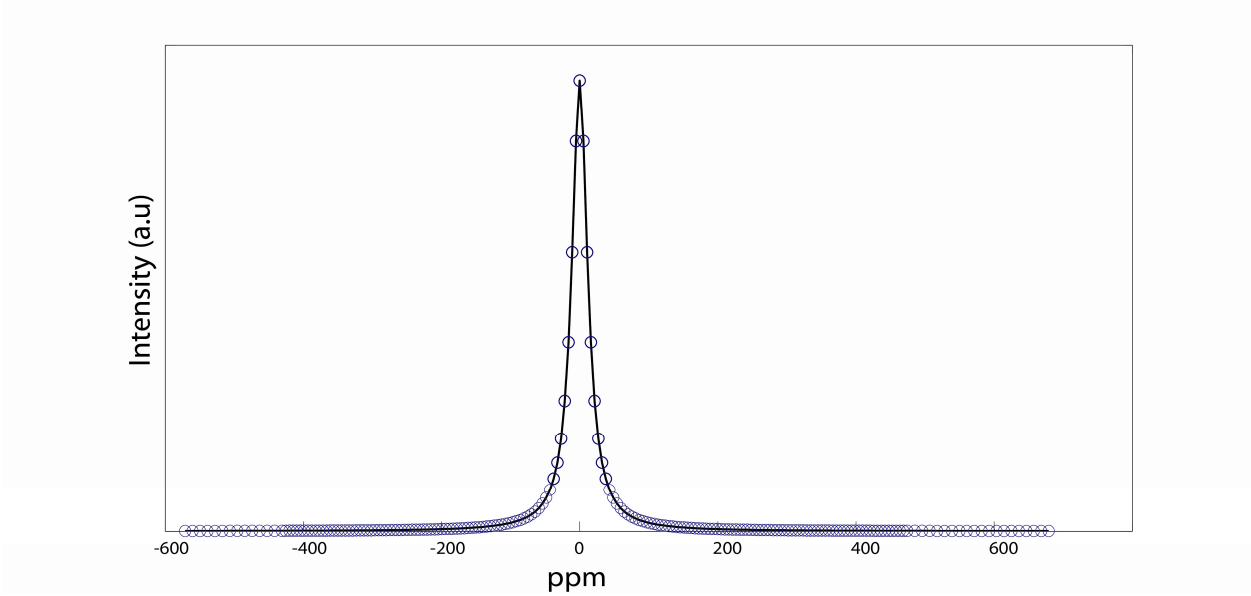

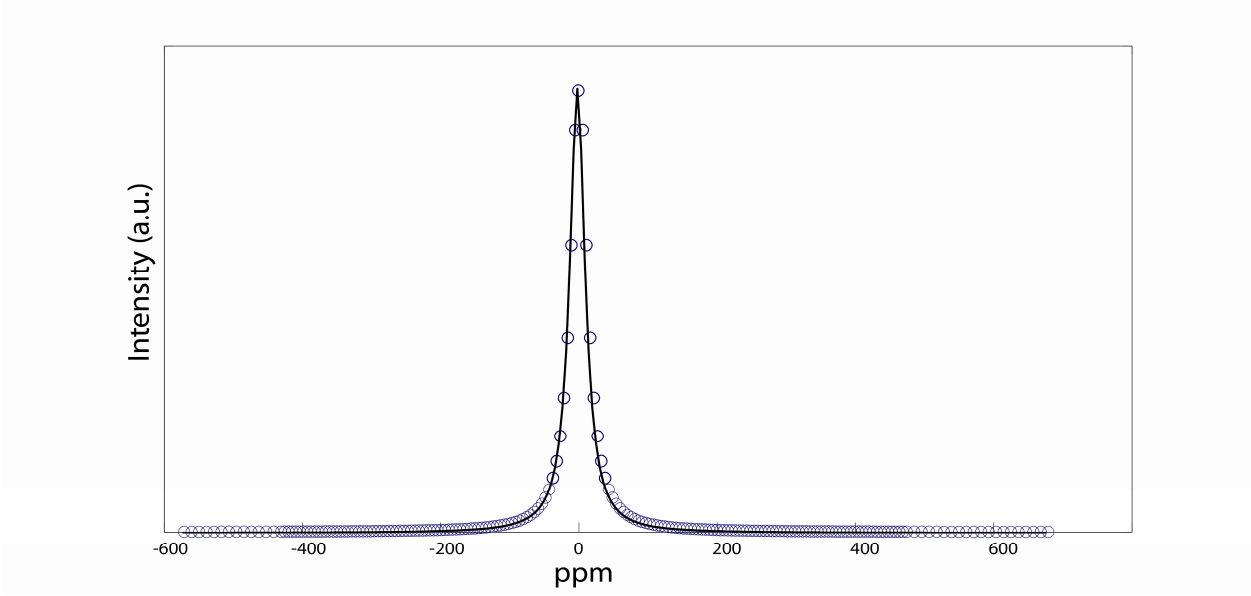

Figure 5.8 Top: Predicted NMR spectra of 10 mM NpO_2^+(aq) in 0.1 M perchloric acid with exchange rate ~0 (k_w= 3.1 x 10^{-100} ; circles) and k_w= 3.1 x 10^{-1}, the value reported by Rabideau[18] (solid line). **Bottom:** NMR spectra of 32 mM NpO_2^+(aq) in 0.1 M perchloric acid predicted for an exchange rate ~0 (circles) and k_w= 3.1 x 10^{-1} (solid line).

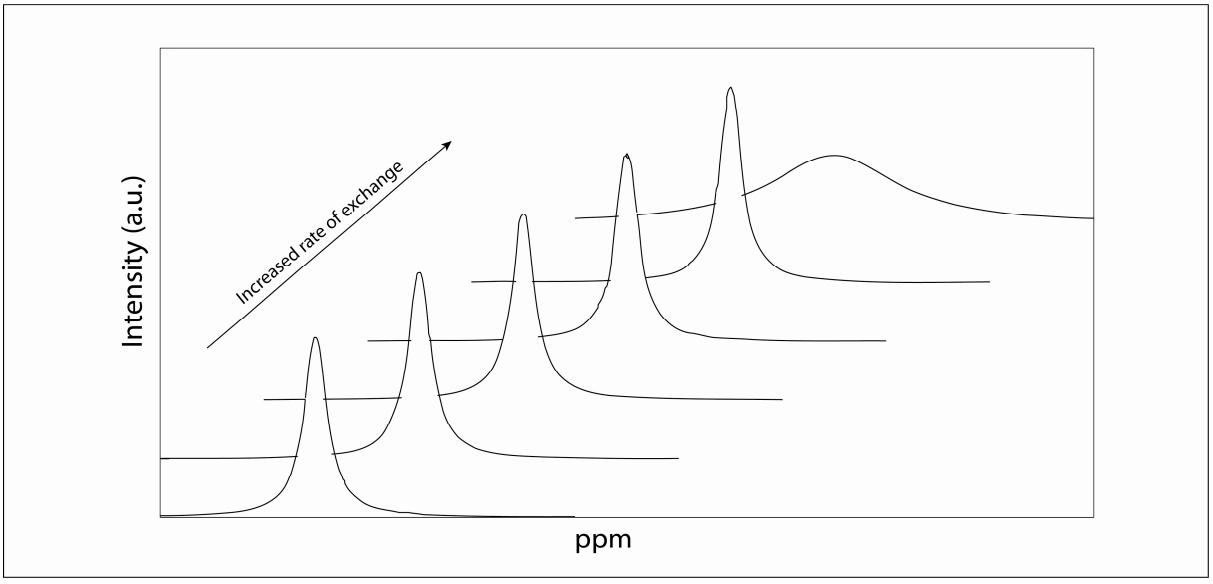

Figure 5.9 Predicted NMR spectra of 32 mM NpO_2^+(aq) in 0.1 M perchloric acid with increasing exchange rate.

the rate of exchange is 1.5 x 10^5 s^{-1}. The rate of water exchange would have to be extremely fast to be able to capture the exchange in the NMR experiments.

Section 5.4-Discussion

Due to a lack of evidence for peak broadening and no shift in the ppm of the peak, use of the Swift-Connick Formalism for paramagnetic species cannot be used to determine the rate of water exchange on the NpO_2^+(aq) ion. The lack of broadening could be explained by four ways: 1.) the neptunyl ion is diamagnetic, 2.) all waters have been displaced from the inner-sphere water by ligation, 3.) initial NMR experiments were performed on solutions there were too dilute in the neptunyl ion, or 4.) the ligand-exchange rate of water is slower than what can be captured via NMR.

The results from the magnetic susceptibility show that the NpO_2^+(aq) ion is paramagnetic. The experimentally determined Curie Constant, C=2.16 emuK/mol, was used to calculate the effective magnetic moment using the equation, $\mu_{eff} = \sqrt{\frac{3kC}{N\mu_B^2}}$, resulting in an effective magnetic moment of 4.16 μ_B, where k is Boltzmann's constant, N is Avogadro's number, and μ_B is the Bohr magneton[36]. Using Hund's Rule[37] the magnetic moment of an ion can be calculated using the quantum numbers (L, S, and J) of the stable electronic state. For the neptunium ion in the fifth oxidation state, a magnetic moment of 3.58 μ_B is calculated. The effective magnetic moment of 4.16 is higher than expected because the measurements from the magnetometer were not corrected for any magnetization from the sample holder or the Teflon liner and any diamagnetic contribution from the sample was not corrected for. With the corrections, it would be expected that the experimentally determined effective magnetic moment

were lower than that predict using Hund's Rule based on the results of Wall *et al.* [20], who determined an effective magnetic moment of 3.06 μ_B for the NpO_2^+(aq) ion in solution. Magnetic-susceptibility measurements of solid Np(V) have also resulted in smaller than expected magnetic moments[34,38]. The reason for this observation is still being investigated, but possible reasons to decreased magnetization are the first hydration sphere around the ion and the effect of the axial oxygens.

Ikeda-Ohno et al. demonstrated that with increased nitrate concentration, the hydrated water molecules are replaced by nitrate in the inner-coordination sphere. At 1 M nitric acid concentrations, the neptunium ion will exist as the hydrated species $[NpO_2(H_2O)]_5^+$, with increasing acid concentration, the nitrate coordinates to the neptunyl ion in a bidentate fashion. Since high nitric acid concentrations are used to clean and prepare Np(V) from the stock solutions, it was of thought that the hydrated waters were displaced during sample preparation, enabling water exchange, resulting in no broadening in the bulk water ^{17}O NMR signal. ^{15}N NMR spectra were collected on a neptunyl solution in 1 M nitric acid, made from ^{15}N tagged nitrate. No bound nitrate peak was observed and no broadening in the bulk nitrate peak occurred, suggesting that the nitrate was not displacing the waters, preventing water exchange.

In the Swift-Connick formalism, the parameter, P_m, is the ratio of bound waters to solvent waters and is inversely proportional to the width of the bulk water signal. Increasing the concentration of neptunyl in the solution, decreases P_m, which should enhance the affect of exchange on the bulk water signal. The NMR experiments using the microcoil probe and concentrated solutions resulted in a broadened and shifted NMR specta, **Figure 5.6**, but the peak did not change when temperature was varied, **Figure 5.7**, which causes more rapid exchange rates. This result hints that exchange between the bound and bulk water is not causing the peak

broadening, but that the broadening is a result of the two *f* orbital unpaired electrons reducing the T_1 relaxation of the bulk water.

That leaves us with the conclusion that the ligand-exchange rate of water on the neptunyl (V) ion is slower than what can be captured on the NMR time scale. Based on calculations, the slowest rate that would be seen in the line-broadening experiment is 1.5×10^5 s^{-1}. The water exchange rate value reported by Rabideau of 0.31 s^{-1} is well below that calculated value and cannot be sufficiently enhanced by increasing temperature in a resonable range. Based on the experiments and simulations, the water exchange for the NpO_2^+(aq) ion can not be experimentally determined using these NMR methods.

Section 5.5-Acknowledgements

The authors are grateful for advice from Dr. David Clark of LANL and to Professor Thomas Albrecht-Schmitt for loan of ^{237}Np that helped us begin experiments with neptunium. Authors would also like to thank Pihong Zhao for the advice on neptunium purification and Christopher Colla for his work on the figure of the neptunyl complex. This work was supported by the Subsurface Biogeochemical Research Program of the U.S. Department of Energy's Office of Biological and Environmental Research. Prepared by LLNL under Contract DE-AC52-07NA27344. It was also supported by the Office of Basic Energy Science of the U.S. Department of Energy as part of the Materials Science of Actinides Energy Frontier Research Center (DE-SC0001089). This work was supported by the Lawrence Livermore National Laboratory Lawrence Scholar Fellowship. The author thanks Prof. C. Andre Ohlin and Dr. Stephen J. Harley for help with the simulations.

Section 5.6- References

[1] Poinssot, C.; Geckeis, H. *Radionuclide Behavior in the Natural Environment; Science, Implications, and Lessons for the Nuclear Industry*; Woodhead Publishing Ltd.; Cambridge, U.K., 2012

[2] Szabó, Z.; Toraishi, T.; Vallet, V.; Grenthe, I., *Coord. Chem. Rev.* **2006,** *250*, 784-815.

[3] Skanthakumar, S.; Antonio, M. R.; Soderholm, L. *Inorg. Chem.* **2008**, *47*(11), 4591-4595.

[4] Combes, J. M.; Chrisholm-Brause, C. J.; Brown, G. E., Jr.; Parks, G. A.; Conradson, S. D.; Eller, P. G.; Triay, I. R.; Hobart, D. E.; Meijer, A. *Environ. Sci. Technol.* **1992**, *26*, 376-382.

[5] Allen, P. G.; Bucher, J. J.; Shuh, D, K.; Edelstein, N. M.; and Reich, T. *Inorg. Chem.* **1997**, *36*(21), 4676-4683.

[6] Ikeda-Ohno, A.; Henning, C.; Rossberg, A.; Funke, H.; Scheinost, A. C.; Bernhard, G.; Yaita, T. *Inorg. Chem.* **2008**. *47*(18), 8294-8305.

[7] Reich, T; Bernhard, G.; Giepel, G.; Funke, H.; Henning, C.; Rossberg, A.; Matz, W.; Schell, N.; Nitsche, H. *Radiochim. Acta*. **2000**, *123*, 4346-4347.

[8] Antonio, M. R.; Soderholm, L.; Williams, C. W.; Bluadeau, J.P.; Bursten, B. E. *Radiochim. Acta* **2001**, *89*, 17-25.

[9] Brown, I. D. *Chem. Soc. Rev.* **1978**, *7*, 359-376.

[10] Clark, D. L.; Conradson, S. D.; Donohoe, R. J.; Keogh, D. W.; Morris, D. E.; Palmer, P. D.; Rogers, R. D.; Tait, C. D., *Inorg. Chem.* **1999,** *38*, 1456-1466.

[11] Ikeda-Ohno, A.; Hennig, C.; Rossberg, A.; Funke, H.; Scheinost, A. C.; Bernhard, G.; Yaita, T., *Inorg. Chem.* **2008,** *47*, 8294-305.

[12] V. P. Shilov, A. V. G., and A.M. Fedoseev, *Radiochemistry* **2012,** *54*, 212-227.

[13] Vasudeva Rao, P.; Gudi, N.; Bagawde, S.; Patil, S., *J. Inorg. Nucl. Chem.* **1979,** *41*, 235-239.

[14] Hindman, J. C.; Sullivan, J. C.; Cohen, D., *J. Am. Chem. Soc.* **1958,** *80*, 1812-1814.

[15] Rao, L.; Srinivasan, T. G.; Garnov, A. Y.; Zanonato, P.; Di Bernardo, P.; Bismondo, A., *Geochim. Cosmochim. Acta* **2004,** *68*, 4821-4830.

[16] Hindman, J.; Sullivan, J.; Cohen, D., *J. Am. Chem. Soc.* **1954,** *76*, 3278-3280.

[17] Rao, L.; Tian, G., *Symmetry* **2009,** *2*, 1-14.

[18] Rabideau, S. W. *J. Phys. Chem.* **1963***, 67*, 12, 2655-2659.

[19] Howland, J. J. Jr.; Calvin, M. *J. Chem. Phys.* **1950**, *18*, 239-243.

[20] Wall, T. F.; Jan, S.; Autillo, M.; Nash, K. L.; Guerin, L.; Le Naour, C.; Moisy, P.; Berthon, C. *Inorg. Chem.* **2014**, *53*(3), 2450-2459.

[21] Evans, D. F. *J. Chem. Soc.* **1959**, 2003-2005.

[22] Hund, F. Z. *Phys.* **1925**, *33*, 855-859.

[23] Swift, T. J.; Connick, R. E.,*J.Chem. Phys.* **1962,** 37, 307-20.

[24] Harley, S. J.; Ohlin, C. A.; Casey, W. H., *Angew. Chem., Int. Ed.***2011,** 75, 3711-3725.

[25] Orrell, K. G., Vladimir, S., Stephenson, K. *Progress in NMR Spectroscopy*. **1990**. *22*, 141-208.

[26] Harley, S. J.; Ohlin, C. A.; Casey, W. H., *Geochim. Cosmochim. Acta* **2011,** *75*, 3711-3725.

[27] Helm, L.; Nicolle, G. M.; Merbach, R. E., *Adv. Inorg. Chem.* **2005,** *57*, 327-379.

[28] Clark, D. L.; Hobart, D. E.; Palmer, P. D.; Sullivan, J. C.; Stout, B. E., *J. Alloys Compd.* **1993,** *193*, 94-97.

[29] Snow, M. S.; Zhao, P.; Dai, Z.; Kersting, A. B.; Zavarin, M., *J. Colloid Interface Sci.* **2013**, *390*, 176-182.

[30] Ammann, C.; Meier, P.; Merbach, A., *J. Magn. Reson. (1969)* **1982,** *46*, 319-321.

[31] Kaplan, M.; Bovey, F.; Cheng, H., *Anal. Chem.* **1975,** *47*, 1703-1705.

[32] Balogh, E.; Todea, A. M.; Muller, A.; Casey, W. H. *Inorg. Chem.* **2007**, *46(17)*, 7087-7092 .

[33] Farkas, I.; Banyai, I.; Szabo, Z.; Wahlgren, U.; Grenthe, I. *Inorg. Chem.* **2000**, *39(4)*, 799-805.

[34] Karraker, D.G.; Stone, J. A. *Inorg. Chem.* **1972,** *11(8)*, 1742-1746.

[35] Couture, L.; Zitoun, R.; *Statistical Thermodynamics and Properties of Matter*. **2000**. Gordon and Breach Science Publishers.

[36] Forbes, T. Z.; Burns, P. C.; Soderholm, L.; Skanthakumar, S., *Chem. Mater.* **2006**, *18*, 1643-1649.

[37] Hund, F. Z., *Phys*. **1925**, *33*, 855-859.

[38] Almond, P. M.; Skanthakumar, S.; Soderholm, L.; Burns, P. C., *Chem. Mater.* **2007**, *19*, 280-285.

Appendix A:

The pressure dependence of oxygen-isotope-exchange rates between solution and apical oxygens on the $UO_2(OH)_4^{2-}$ ion

A key concern in the use of nuclear energy is the disposal and long-term storage of spent fuel. The aqueous chemistry of the uranyl(VI) ion under strongly alkaline conditions, such as those found in many aboveground waste storage tanks, remains poorly understood. To this effect, the oxygen exchange between the uranyl oxygens and bulk solvent water has been studied by ^{17}O NMR under acidic[1] and alkaline conditions[2-4] using line broadening by Clark *et al.* and recently saturation-transfer methods by Szabó, Grenthe *et al.*, but no determination of activation volumes has been attempted. Such data are invaluable in verifying *in silico* models for reaction pathways[5]. The activation volume probes the transition state and complements molecular-dynamic simulations. In this study the activation volume of the oxygen exchange of the uranyl oxygens with bulk water has been determined by experiments at 60˚C between 0.1 and 350 Mpa as a function of uranyl and hydroxide concentrations.

A common method for determining exchange involving coordinated oxygen species and bulk water is by line-broadening studies according to the method by Swift and Connick,[6,7] in which the broadening of a signal due to rapidly occurring dynamic processes is followed. While this is experimentally straightforward, the separation of contributing factors to the observed line width is often difficult. Such is particularly the case when there are several exchangeable oxygens, such as apical 'yl' and equatorial waters or hydroxo ligands. Saturation-transfer measurements provides an alternative approach which, assuming that certain conditions are met – such as well-separated NMR signals and slow longitudinal relaxation – offers a more direct and precise determination of exchange rates[4]. Here, one site, *e.g.* ^{17}O in bulk water, is selectively excited with a 180° pulse and magnetization is transferred through chemical exchange to another site, *e.g.*^{17}O in UO_2^{2+}:

$$\frac{dM_{z,a}}{dt} = -\frac{(M_{z,a}(t) - M_{z,a}^{\infty})}{T_{1,a}} + k_b M_{z,b}(t) - k_a M_{z,a}(t) \quad \text{(A.1)}$$

$$\frac{dM_{z,b}}{dt} = -\frac{(M_{z,b}(t) - M_{z,b}^{\infty})}{T_{1,b}} - k_b M_{z,b}(t) + k_a M_{z,a}(t) \quad \text{(A.2)}$$

With selective inversion, the *x* and *y* components of the magnetization may be omitted and the system may be completely described by the *z* component of the Bloch equations. We here adopt a McConnell formalism for exchange (see supporting information for derivation of model equation). M_i is the bulk magnetic moment, T_1 denotes the longitudinal relaxation for sites a and b, and *k* is the pseudo-first-order rate constant.[7] For a selective 180˚ pulse at t_0 on site *b*, the initial conditions in the ideal case become $M_{z,b}(t_0) = -M_{z,b}^{\infty}$ and $M_{z,a}(t_0) = M_{z,a}^{\infty}$ which allows for the analytical solution of the set of differential equations. In practice, long, shaped pulses are required to provide for a truly selective 180˚ pulse during the life-time of which some relaxation of *b* will occur, so that $M_{z,b}(t_0) \leq -M_{z,b}^{\infty}$. The system was thus solved for $M_{z,b}(t_0) = -M_{z,b}^{0}$ and $M_{z,a}(t_0) = M_{z,a}^{0}$.

The activation volume ($\Delta V^{\ddagger}$) is defined by equation A.3, and can be determined by measuring rates as a function of pressure.

$$\Delta V^{\ddagger} = RH\left(\frac{\delta \ln(k)}{\delta P}\right)_T \quad \text{(A.3)}$$

According to transition-state theory the activation volume can then be interpreted as the difference in molar volume between the transition state and the sum of the partial molar volumes of the reactants and thus offers a less ambiguous measure than activation entropy as to whether a reaction is associative or dissociative, in addition to giving an indication as to the species involved. The activation volume is one of a few properties of the transition state that can be

accurately probed and therefore it is an invaluable indicator towards the mechanism of exchange reactions.[10]

The speciation of U(VI) as a function of concentration and pH is complicated and partly unresolved. However, while a range of monomeric, dimeric and trimeric species have been observed at acidic conditions, at highly alkaline pH (3.5 M $N(CH_3)_4OH_{(aq)}$) monomeric uranyl-hydroxide species form. Clark *et al.* suggested the dominant species to be $[UO_2(OH)_5]^{3-}$ based on EXAFS and UV-VIS spectroscopy,[1] whereas Szabó, Grenthe *et al.* have suggested that $[UO_2(OH)_4]^{2-}$ is the main species.[5,4] While there is some disagreement as to which one is the major species, it is, however, clear that a rapid equilibrium between $[UO_2(OH)_4]^{2-}$ and $[UO_2(OH)_5]^{3-}$ is present. We here assign the stoichiometry to $[UO_2(OH)_4]^{2-}$ to simplify the discussion; we have no information about the relative accuracy of the tetra- or pentahydroxyl stoichioimetric assignment. There is certainly no evidence for polynuclear species under these conditions, such as would be evident in new peak appearances or peak broadenings with increases in concentration.

Clark et al.[2] determined ambient-pressure activation enthalpy and entropy of the exchange of the uranyl oxygens in $[UO_2(OH)_4]^{2-}$ to be 41±1.7 $kJ \cdot mol^{-1}$ and -75±25 $J \cdot K^{-1} \cdot mol^{-1}$, respectively, in 3.5 M $N(CH_3)_4OH$ through ^{17}O-NMR signal line-broadening. This is in good agreement with the values of 36.6±0.4 $kJ \cdot mol^{-1}$ and -75±17 $J \cdot K^{-1} \cdot mol^{-1}$ observed by Szabó *et al.* under the same conditions using the saturation-transfer method that we employ here. In addition, the detailed rate law was investigated and found to be first-order with respect to hydroxide concentration and second-order with respect to uranyl concentration. After ruling out the presence of binuclear complexes in solution the authors concluded that the first-order dependence on hydroxide is due to the equilibrium between the tetrahydroxy and the

pentahydroxy uranyl species, whereas the second-order dependence on uranium concentration is due to the formation of a binuclear $[UO_2(OH)_4]^{-}[UO_2(OH)_5]^{5-}$ transition state.

In this study we have investigated the pressure effects on the rates of oxygen exchange at the 'yl' oxygens at different total U(VI) and hydroxide concentrations. We first confirmed agreement with the rate law proposed by Grenthe and Szabo[4] at low pressure then extended the results to high pressure in order to probe the activated equilibria. Samples consisted of solutions of 16-73 mM uranyl nitrate in aqueous solutions of 2.0-3.5 M $N(CH_3)_4OH$ **[Table A.1]**. Using a custom-built high-pressure NMR probe, the samples were kept at 333 K and the pressure varied between 0.1 and 350 MPa. The peak corresponding to the 'yl' oxygen was put on resonance and was given a selective 180° tip angle using a 500-μs Gaussian-shaped pulse. The perturbed water magnetization was then allowed to mix with the equilibrium 'yl' magnetization via chemical exchange for some variable time (a mixing time). A 90° pulse was used to tip magnetization into the x-y plane for detection. Due to the large difference in

Table A.1: Activation volumes determined at 333.0±0.1 K.

C_{UO2} (10^{-3} mol·dm^{-3}) [a]	C_{OH} (mol·dm^{-3}) [b]	C_{OH} Free (mol·dm^{-3}) [c]	$\Delta V^{\ddagger} \pm \sigma$ (cm^3·mol^{-1})
22.4	1.99	1.9	-9.8 ± 0.8
45	2.07	1.89	-9.2 ±0.5
56.6	2.12	1.89	-9.0 ± 0.7
24.3	1.48	1.38	-9.8 ± 1.3
21.5	1.98	1.89	-10.4 ± 1
16.1	2.96	2.9	-9.8 ± 1.1
73	1.9	1.61	-9.06 ± 0.63

[a] Total concentration of uranyl nitrate. [b] Total concentration of added $[N(CH_3)_4]OH$. [c] Free hydroxide concentration assuming complete reaction with uranyl nitrate to form tetrahydroxy species.

chemical shift between the two sites, the spectrometer frequency was alternated between the 'yl' frequency, or the bulk-water frequency, in order to digitize either with sufficient resolution. The

time-domain signals were fitted to decaying exponential functions and the amplitude values were compiled as a function of mixing time.

The resulting data array was then fit to the model described above using a least-squares fitting routine that employed an interior-reflective Newton search method. A value for exchange rate and associated uncertainty are obtained for each pressure. The uncertainty in the fitting of the saturation-transfer model was always larger than the uncertainty in the linear curve fit of the pressure dependence, thus it became necessary to propagate this larger error through the calculations to the reported activation volume. To accomplish this, a random, normally distributed array of 1000 points having a mean value of the regressed rate and a standard deviation of regression was generated for each pressure. Then a single point from each array was randomly chosen and linearly regressed to obtain a value for slope. This process of picking points from the normally distributed array was repeated 1000 times and the average slope was obtained. The standard deviation of this process is the reported uncertainty. Thus the values and uncertainties are conservative and reasonable.

Activation volumes were obtained by equation A.4, where k^0 is the rate at P^0 (~5 MPa). An attractive feature of this equation is that the activation volume is independent of the absolute magnitude of the measured rates, and depends only on the relative change in rate with pressure. Thus, as long as the only variable being changed is pressure, any reaction can be treated as if exhibiting first-order kinetics. As a consequence, the activation volume should not change with either reactant concentrations or temperature, but remain constant for a given reaction as long as the reaction mechanism is unchanged. Any significant deviation can be interpreted as an indication of a change in reaction mechanism.

$$\ln\left(\frac{k}{k^0}\right) = \frac{-\Delta V^{\ddagger}}{RT} P - \frac{P^0}{RT} \qquad \text{(A.4)}$$

The activation volumes were measured at conditions given in **Table A.1**; Σ[U(VI)] = 16-73 mM and Σ[OH^-] from 1.5-3.0 M and 333 K. All reaction rate coefficients are consistent with the ambient- pressure studies of Szabo and Grenthe.[4] The rate coefficients used to yield activation volumes in Table 1 via equation A.4 were not corrected for the dependence on Σ[U(VI)] or on Σ[TMAOH], but these dependencies do not affect the derivatives with respect to pressure and thus the values of $\Delta V^{\ddagger}$.

We were motivated in this study to alleviate the absence of high-pressure studies on actinide elements that could yield information about reaction mechanisms.[10] Although we here report large negative activation volumes, it would be a mistake to interpret these values via careless application of the Langford-Gray formalism relating $\Delta V^{\ddagger}$ to involvement of second-shell hydration waters in the activated state.[11] We find, as did Szabó and Grenthe[4], that the rates depend on total dissolved uranium concentrations and thus probably involves a yet-undetected dimeric intermediate or dimeric activated complex. We see no spectroscopic evidence that such an intermediate is stable, but we cannot rule out the possibility that the volume change to form this intermediate is folded into our $\Delta V^{\ddagger}$ measurements, since the putative intermediate may be at concentrations too low for us to detect. The interpretation may also be complicated by the possibility that the isotope-exchanging moiety is a hydroxide ion at these high pH conditions, although we consider this to be unlikely.

The large negative activation volume is consistent with molecular association in the transition state. We certainly find no trends that might suggest reaction pathways that change with pressure or variations in concentration. The large negative activation volume, however, argues strongly against a rate-controlling step where a rapidly exchanging equatorial hydroxyl rotates upward internally to form the new axial 'yl' oxygen. Such internal shuffling of oxygens

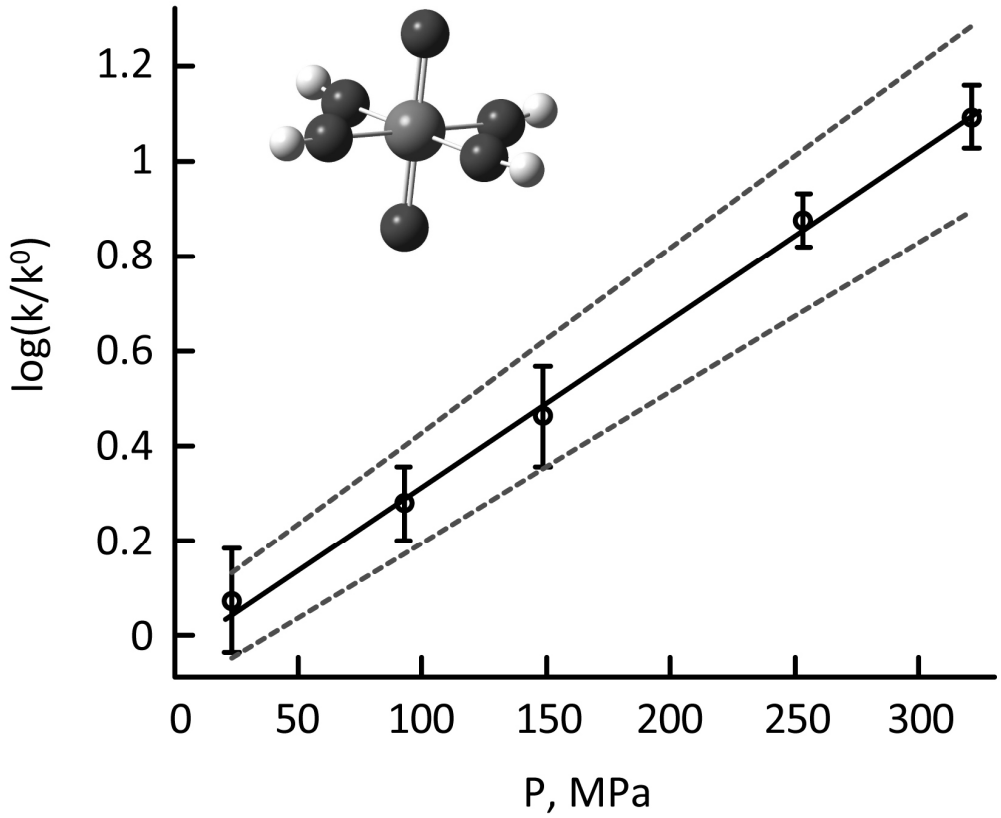

Figure A.1: ln(k/k_0) as a function of pressure. Σ[U(VI)] = 22.4 mM, T=333 K. The slope of these data indicates an activation volume, which in this case was: $\Delta V^{\ddagger}$ = -9.8(±0.8) cm^3 mol^{-1}, and the dashed lines indicate the standard error of the slope. The error bars indicate the standard error of each rate datum.

would not require such a large and negative activation volume, except for the caveat that our measurement may include the reaction volume for equilibrium between $[UO_2(OH)_4]^{2-}$ and a yet-undetected precursor to the activated complex.

Experimental Section

Samples were prepared by dissolving uranyl nitrate into 40% ^{17}O enriched water that had been degassed by vacuum distillation. This resulting solution was acidic and was combined with a pre-weighed amount of TMAOH (TMA=$N(CH_3)_4^+$) and then double-sealed in a high pressure NMR tube. The TMAOH was used as received from Acros. The high-pressure sample assembly was completely isolated from the atmosphere. The samples were submerged in a hexane fluid during the NMR measurements, thereby further preventing air leakage into the sample during the measurements. All NMR measurements were conducted on the day of sample preparation. There was no visual evidence of precipitation, which would have been uranyl carbonate, nor any NMR evidence of additional solutes.

^{17}O-NMR experiments were carried out on a wide-bore Bruker Avance (11.7 T) spectrometer using a high-pressure probe system similar to that described by Jonas et al.[12] The probe pressure was generated with a high-pressure syringe pump coupled to a valve system to maintain and regulate pressures throughout the experiment. *iso*-Hexane was used as the pressure conduit and pressures were continuously monitored and were never allowed to fluctuate more than 0.5% during data acquisition. Temperature was kept constant via a circulating water bath and was monitored with a type-T thermocouple situated in the probe body near the probe head and at pressure. Thermal equilibrium was established after each pressure jump before data was acquired.

Derivation of Model Equations

The Bloch equations describe the relaxation of longitudal magnetization via:

$$\frac{dM_z(t)}{dt} = -\frac{M_z(t) - M_z^{\infty}}{T_1} \qquad \text{(A. 5)}$$

where M_z^{∞} is the equilibrium magnetization.

Using McConnell formalism, a two-nuclei system comprising nuclei a and b in which there is magnetization transfer via chemical exchange between the two nuclei can be accounted for by including the appropriate transfer terms for pseudo-first-order kinetics

$$\begin{aligned} \frac{dM_{z,a}(t)}{dt} &= -\frac{(M_{z,a}(t) - M_{z,a}^{\infty})}{T_{1,a}} + k_b M_{z,b}(t) - k_a M_{z,a}(t) \\ \frac{dM_{z,b}(t)}{dt} &= -\frac{(M_{z,b}(t) - M_{z,b}^{\infty})}{T_{1,b}} - k_b M_{z,b}(t) + k_a M_{z,a}(t) \end{aligned} \qquad \text{(A.6)}$$

where $k_a = \frac{1}{\tau_{a\to b}}$ and $k_b = \frac{1}{\tau_{b\to a}}$. The law of detailed balance states that $k_a C_a = k_b C_b$ - where C_a and C_b denote the concentrations of a and b, respectively – so that

$$\begin{aligned} \frac{dM_{z,a}(t)}{dt} &= -\frac{(M_{z,a}(t) - M_{z,a}^{\infty}}{T_{1,a}} + \frac{K_a C_a}{C_b} M_{z,b}(t) - k_a M_{z,a}(t) \\ \frac{dM_{z,b}(t)}{dt} &= -\frac{(M_{z,b}(t) - M_{z,b}^{\infty}}{T_{1,b}} + \frac{K_a C_a}{C_b} M_{z,b}(t) + k_a M_{z,a}(t) \end{aligned} \qquad \text{(A.7)}$$

In the ideal case the initial conditions are

$$\begin{aligned} M_{z,a}(t_0) &= M_{z,a}^{\infty} \\ M_{z,b}(t_0) &= M_{z,b}^{\infty} \end{aligned} \qquad \text{(A.8)}$$

However, as the 180° pulse typically is long, some magnetization and relaxation has taken place during the lifetime of the pulse and as such the equilibrium magnetizations were modified to

$$\begin{aligned} M_{z,a}(t_0) &= M^0_{z,a} \\ M_{z,b}(t_0) &= M^0_{z,b} \end{aligned} \qquad \text{(A.9)}$$

and where left as new fit parameters.

The set of coupled differential equations can be solved analytically using a suitable software package such as Maxima or Matlab. The resulting functions for $M_{z,a}(t)$ and $M_{z,b}(t)$ model the transient nature of longitudal magnetization for two sites under chemical exchange where one site has received an inversion in magnetization.

References

[1] I. Farkas, I. Banyai, Z. Szabo, U. Wahlgren, I. Grenthe, *Inorg. Chem.* **2000**, *39*, 799.

[2] D. L. Clark, S. D. Conradson, R. J. Donohoe, D. W. Keogh, D. E. Morris, P. D. Palmer, et al., *Inorg. Chem.* **1999**, *38*, 1456.

[3] Z. Szabo, I. Grenthe, *Inorg. Chem.* **2007**, *46*, 9372.

[4] Z. Szabo, I. Grenthe, *Inorg. Chem.* **2010**, *49*, 4928

[5] a) M. A. Lee, N. W. Winter, and W. H. Casey, *J. Phys. Chem.* **1994**, *98* 8641; b) F. P. Rotzinger, *J. Am. Chem. Soc.* **1996**, *118*, 6760; c) Th. Kowall, P. Caravan, H. Bourgeois, L. Helm, F. P. Rotzinger and A. E. Merbach, *J. Am. Chem. Soc.* **1998**, 6569;

[6] a) T. J. Swift, G. M. Anderson, R. E. Connick, M. Yoshimine, *J. Chem. Phys.* **1964**, *41*, 2553; b)T. J. Swift, R. E. Connick, *J. Chem. Phys.* **1962**, *37*, 307.

[7] H. M. McConnell, *J. Chem. Phys.* **1958**, *28*, 430.

[8] H. Moll, T. Reich, Z. Szabo, *Radiochim. Acta* **2000**, *88*, 411.

[9] U. Wahlgren, H. Moll, I. Grenthe, B. Schimmelpfennig, L. Maron, V. Vallet, et al., *J. Chem. Phys. A* **1999**, *103*, 8257.

[10] Richens, D. T. *The Chemistry of Aqua Ions.* Wiley, Chichester, 1997, pp. 10-20; Asano, T.; Le Noble, W. J. *Chem. Rev.* **1978**, *78* 407.

[11] a) Langford, C.H. and H.B. Gray, *Ligand Substitution Processes. 2nd Ed*. 1974, New York: Benjamin. 120 pp; b) Swaddle, T. W. *Inorg. Chem.* **1983**, *29*, 2663-2665.

[12] Jonas, J. W.; Koziol, P.; Peng, X.; Reiner, C.; Campbell, D. *J. Magn. Reson. B* **1993**, *102*, 299-309.

Appendix B:

Multinuclear NMR Study of the Pressure Dependence for Carbonate Exchange in the $UO_2(CO_3)_3^{4-}$(aq) Ion

Predicting the reactivity of actinide elements in nature is among the most pressing concerns in environmental geochemistry, yet even some basic measures of reactivity are not well known. Included among these are the mechanisms of ligand exchange in simple complexes. These data are important because the reaction dynamics can be compared to computer simulations to gain confidence for cases where experiments are impossible. Among the key parameters used to describe ligand-exchange mechanisms are activation volumes, which derive from the pressure dependence of the reaction rates. These activation volumes are interpreted to indicate the extents to which the incoming ligand can influence the activated state and, in this sense, the $UO_2(CO_3)_3^{4-}$(aq) ion is a particularly compelling system because rates of carbonate exchange are apparently independent of free carbonate concentrations.[1]

Here we report high-pressure rate data for the mononuclear uranyl carbonate ion, $UO_2(CO_3)_3^{4-}$(aq), which is a dominant species in uranyl-rich, near-neutral pH solutions that are open to atmospheric CO_2.[1b-d, 2] Bányai et al. presented rate equations for two pathways for carbonate exchange[1d] in the mononuclear $UO_2(CO_3)_3^{4-}$(aq) species, which have been combined into the overall rate equation below:

$$\text{Rate} = (k_1 + k_2[H^+])[\ UO_2(CO_3)_3^{4-}] \qquad \text{(B.1)}$$

where k_1 and k_2 are the rate coefficients, $[H^+]$ is the proton concentration, and $[UO_2(CO_3)_3^{4-}]$ is the concentration of the target ion. Pathway 1 (k_1) is independent of pH and dominates at high pH (~9.50), while the proton-enhanced pathway 2 (k_2) dominates at low pH (~7.00). The ^{13}C chemical shifts of bound and free carbonate are less than 1 kHz apart, which presents a unique challenge for high-pressure saturation-transfer experiments. The long, soft, Gaussian-shaped pulses used in previous studies[3] were not adequately selective. Others have employed the DANTE[4] pulse sequence to better shape excitation bandwidth[1d]. However, the inherently long

90° durations that are characteristic of high-pressure probes make optimization of the DANTE sequence excessively long. Instead, we used the pulse sequence, described below and illustrated in **Figure B.1**, which exploits the principles of null points obtained via the DANTE sequence, and is similar to the pulse sequence used by Bodor et al.[5]

Magnetization for both sites is tipped into the xy-plane using a hard 90° pulse. A calibrated time, τ_{Prec}, is allowed to pass where, in the rotating frame, the off-resonance signal is allowed to precess until it is exactly 180° out of phase with the on-resonance peak. Here another hard 90° pulse is used to achieve inversion of magnetization for one site and, by varying the phase of the second pulse, one can manipulate which peak achieves the inversion. We then allow a delay so the two spin states are allowed to mix via chemical exchange. As magnetization between the two sites transfers, intensity decreases for the positive site, and increases for the inverted (negative) site (see **Figure B.2**). Eventually T_1 relaxation dominates the magnitude of both peaks as they relax towards equilibrium. A third 90° pulse is used to tip magnetization in the xy-plane for detection.

The Bloch equations[6] adopting a McConnell formalism for exchange[7] allow modelling of this magnetically perturbed system:

$$\frac{dM_{z,a}}{dt} = -\frac{(M_{z,a}(t) - M_{z,a}^{\infty})}{T_{1,a}} + k_b M_{z,b}(t) - k_a M_{z,a}(t) \quad \text{(B.1)}$$

$$\frac{dM_{z,b}}{dt} = -\frac{(M_{z,b}(t) - M_{z,b}^{\infty})}{T_{1,b}} - k_b M_{z,b}(t) + k_a M_{z,a}(t) \quad \text{(B.2)}$$

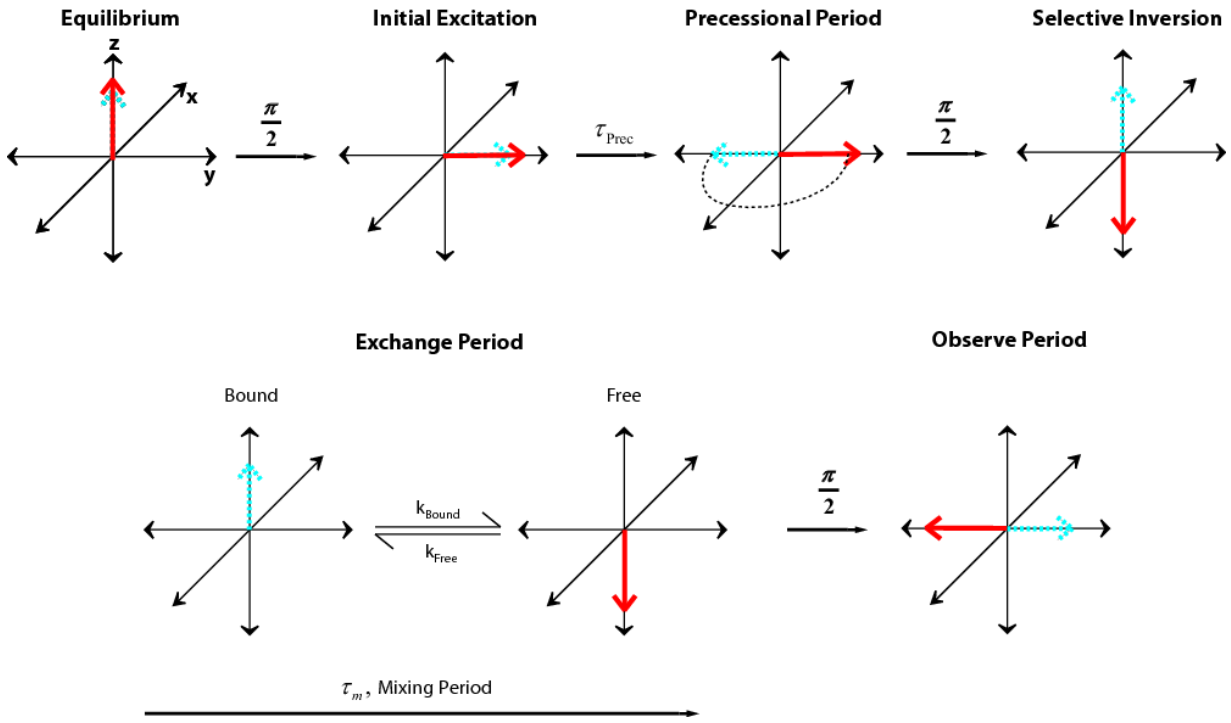

Figure B.1: A saturation-transfer pulse sequence, making use of the differences in precessional rates to achieve selective inversion. The solid arrow represents the magnetization for the species that is kept on resonance, while the dotted arrow represents the magnetization for the species that is off resonance. A 90° pulse tips magnetization for both sites into the xy-plane. The difference in precessional frequency between the two sites determines the time necessary for the off-resonance signal (dotted arrow) to be 180° from its original position. Another 90° pulse is applied to invert one peak (solid arrow). During the exchange period, a variable waiting time allows magnetization between both sites to mix. A final 90° pulse is applied to observe the net magnetization of each site.

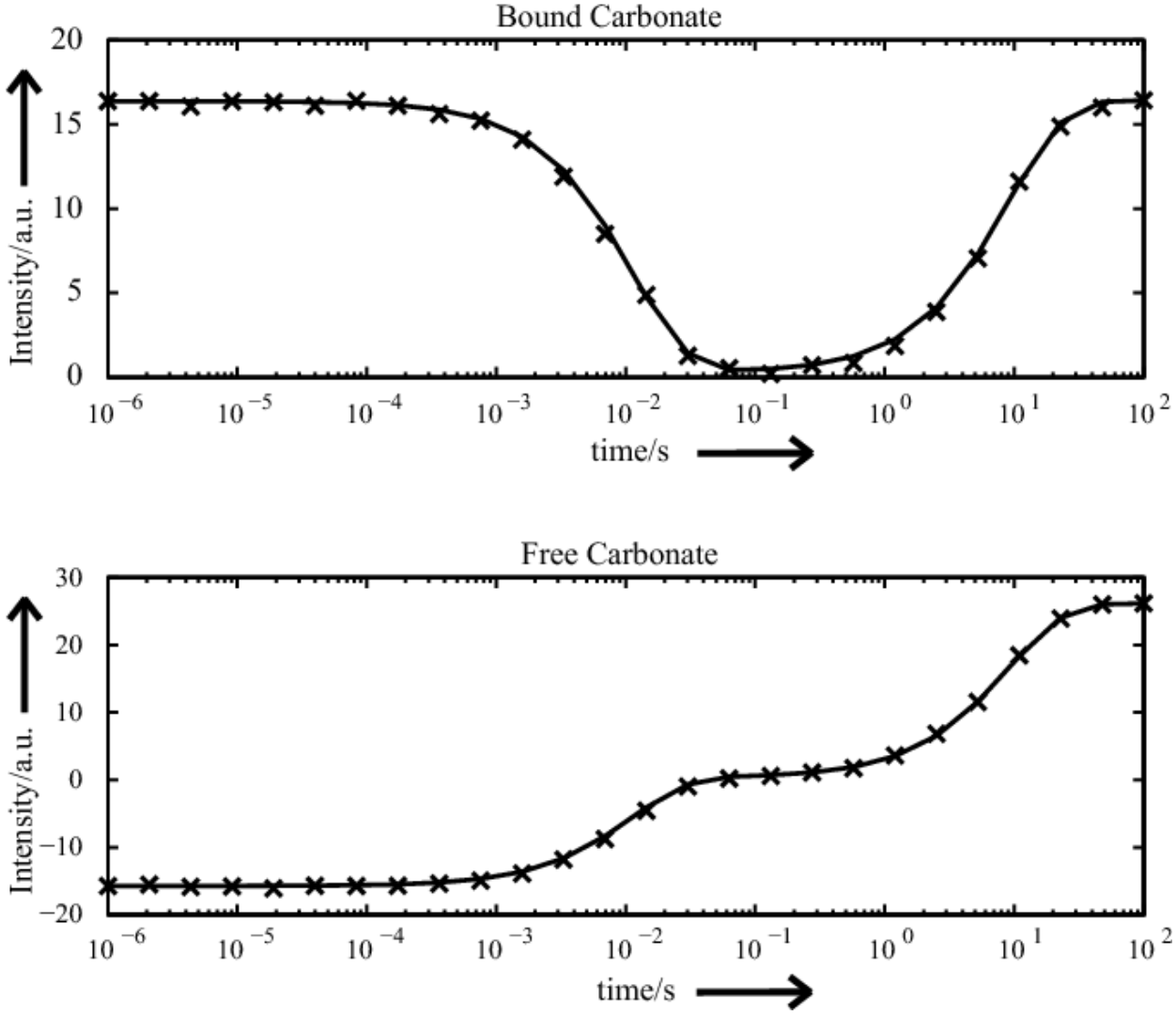

Figure B.2: A magnetization-transfer experiment on the $UO_2(CO_3)_3^{4-}$(aq) at 150 MPa. The x's represent the sample data, and the solid line represents the corresponding best fit.

where $M_{z,i}(t)$ and $M_{z,i}^{eq}$ denote the magnitude of z magnetization for species *i* as a function of time and at equilibrium respectively. $T_{1,i}$ is the rate of longitudinal relaxation for species *i*, and *k* is the rate constant for chemical exchange between the free and bound states. An analytical solution was obtained using MATLAB. [8]

The pH conditions were chosen to isolate contributions from each of the two pathways to the net rate of exchange. At a temperature of 47.0°C and a pH of 9.50 the contribution of pathway 2 to 1 is only 4% of the total measured rate. Similarly, reducing the temperature to 25.0°C and lowering the pH to 7.07 reduces the contribution of pathway 1 to the net rate to less than 3%, making it possible to isolate the two pathways cleanly. However, the Brønsted acidities of both water and carbonate ions vary considerably with temperature and pressure[9] and these variations greatly affect the interpretation of the rate data for pathway 2. Previous studies used the the ^{13}C chemical shift of cyanide as an internal pH reference.[1d] Although cyanide does show a large variation in chemical shift as a function of its protonated state[10], the pH investigated for pathway 2 is more than two pH units away from the pK_a of cyanide. Instead we used 1-methylimidazole to monitor pH *in situ* in the high-pressure experiments. The ^{14}N chemical shift exhibits more than a 60 ppm shift between its protonated and unprotonated states[11] and has a pK_a of ~7.2.[12] The relationship between chemical shift and pH is given by[13]

$$pH = pK_a - Log\left(\frac{\left(\delta_{MI} - \delta_{obs}\right)}{\left(\delta_{MI} - \delta_{HMI}\right)}\right) \qquad \text{(B.4)}$$

where δ_{MI} and δ_{HMI} are the chemical shifts for unprotonated and protonated 1-methylimidazole, respectively, and δ_{obs} is the observed chemical shift for the population-weighted average between the protonation states in solution. No data exist for the pressure dependence of the chemical shift of 1-methylimidazole, so we performed a high-pressure experiment on a 10 mM 1-

methylimidazole solution in 1 M $NaNO_3$ at pH 7.20. The pressure was varied from ~5 to 350 MPa and changes in chemical shift were recorded. While a small change in chemical shift was observed, the change was accurately predicted by the pressure change for K_w. Therefore, no significant variation in the pK_a of 1-methylimidazole is expected. The pH values of $UO_2(CO_3)_3^{4-}$ (aq) solutions, however, were quite sensitive to pressure. A typical experimental result is shown in **Figure B.3** where the pH at ambient conditions, measured with a glass electrode, is pH = 7.07 but that pH varies with pressure, yielding an empirical relation from Equation (B.4) of:

$$pH = 1.789 * 10^{-6} P^2 - 0.00253P + 7.075 \qquad \text{(B.5)}$$

with an intercept that recovers the ambient value at 0.1 MPa. The pH conditions were similarly adjusted for changes in temperature. A UV-vis spectrum taken before, and after, addition of 1-methylimidazole indicates no coordination of 1-methylimidazole to $UO_2(CO_3)_3^{4-}$(aq). Furthermore, there was no change in rates observed for samples with or without 1-methylimidazole.

To measure the rates at pressure, the NMR signal for free carbonate ion was put on resonance and was selectively inverted via the method described above. Each peak was phased independently and then fit to a Lorentzian function. The amplitude values were compiled as a function of mixing time. The activation volume ($\Delta V^{\ddagger}$) for the overall exchange process was obtained by fitting rate data to:

$$\ln(k(P)) = -\frac{\Delta V^{\ddagger}}{RT} P - \ln(k(0)) \qquad \text{(B.6)}$$

where k is the pressure dependent rate constant, P is pressure, R the gas constant, and T the temperature **[Figure B.4]**. Thus defined, the activation volume for pathway 1 was found to be 6.6±0.7 $cm^3 \cdot mol^{-1}$, while for pathway 2, when corrected for the pressure dependence of the pH, was found to be 10.6±0.7 $cm^3 \cdot mol^{-1}$. Taken at face value, both $\Delta V^{\ddagger}$ values seem to indicate a

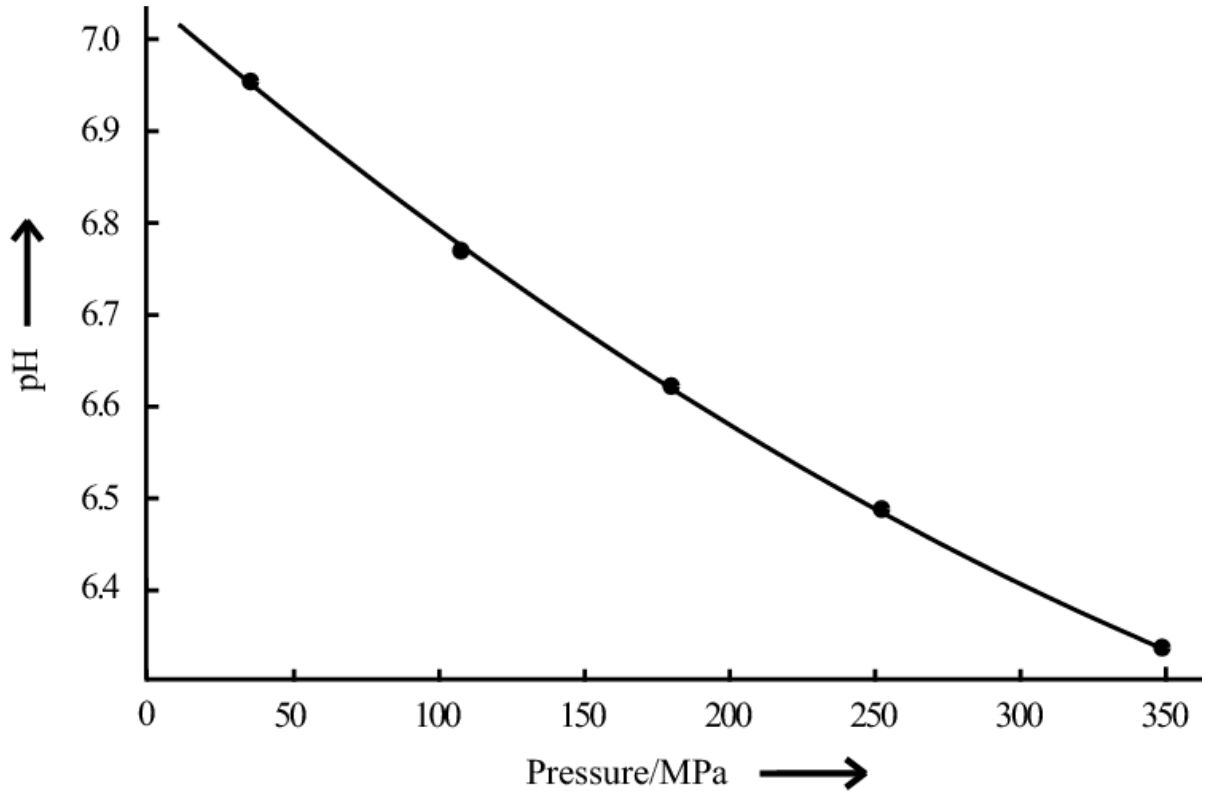

Figure B.3: The pressure dependence of pH of the $UO_2(CO_3)_3^{4-}$(aq) system. The chemical shifts of the protonated and unprotonated 1-methylimidazole species were used to calculate pH.

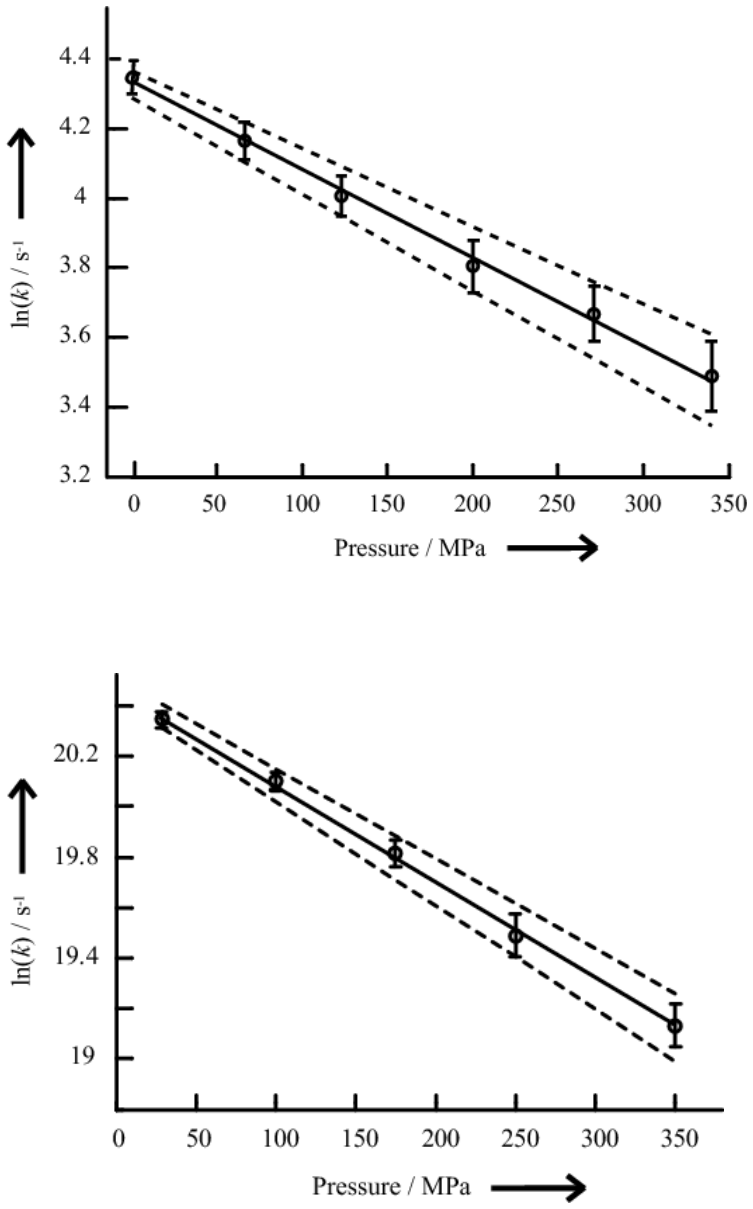

Figure B.4: The activation volumes for the proton-independent pathway 1 (**top**), and proton-enhanced pathway 2 (**bottom**), for exchange of the carbonate ligand in the $UO_2(CO_3)_3^{4-}(aq)$ complex are: $\Delta V^{\ddagger}$ = 6.6±0.7 $cm^3 \cdot mol^{-1}$ and $\Delta V^{\ddagger}$ = 10.6±0.7 $cm^3 \cdot mol^{-1}$, respectively, both indicating dissociative mechanisms for exchange[1d]. The error bars signify the standard error in each datum point, while the dashed line signifies error of the slope.

dissociative mechanism mechanism **[Figure B.4]**, with the caveat that exchange may not be a one-step reaction for either pathway.

Both values also agree with the earlier temperature studies in which Bányai et al. reported an activation entropy that suggested a dissociative mechanism for both pathways.[1d] These data provide an excellent foundation for dynamic simulation of the process.

And there is a pressing need for high-pressure experimental data describing rates of ligand exchange for actinide elements. More common are mechanisms of ligand exchange deduced through temperature or computational studies, or both. Farkas et al..[14] conducted temperature and computational studies of water exchange on the uranyl aqua ion, $UO_2(H_2O)_5^{2+}(aq)$, and concluded that the mechanism was dissociative although the authors pointed out that their conclusions were tentative, as they did not have the means by which to measure activation volume.[14] Vallet et al. [15] studied the uranyl aqua ion via quantum chemical methods and concluded that a dissociative pathway for exchange was not a possibility, although they were unable to distinguish between an associative and interchange pathway. Rotzinger[16] and Tsushima[17] also separately treated the uranyl aqua ion in computational studies that concluded an associative mechanism for exchange. The calculated activation parameters for an associative mechanism better agreed with the experimental parameters.[16] Evans et al.[18] caution about using static ab initio simulations, particularly of small scale, for interpreting mechanisms of aqueous ligand-exchange reactions. Their point is that hydrogen-bonding networks dramatically affect the pathways as identified by DFT and are best sampled dynamically.

Our data on activation volumes thus add to this discussion, but we caution to interpret them carefully. The standard model for interpreting activation volumes derived from water exchanges in octahedral metal ions, not ligands around multimers. However, changes in

solvation that accompany the ligand exchanges, and thus understanding of activation volumes for ligand exchange around actinide complexes, is a subject that is particularly well posed for simulation. The high-pressure experiments are also delicate--ignorance of the pressure variation of pH could have led to incorrect assignment of exchange mechanisms (**Figure B.5** activation volume ignoring the pressure dependence of pH). Here, we estimate activation volumes for the $UO_2(CO_3)_3^{4-}$(aq) complex only after taking care to account for variations of the solution pH *in situ*. Uncompensated, these pH variations would have conflated the activation parameters for the proton-dependent and proton-independent pathways.

Experimental Section

Samples were prepared by dissolving $UO_2(NO_3)_2$ (0.151 g, 0.3 mmol) in 3 mL of 18 MΩ water followed by the addition of a excess of $Na_2{}^{13}CO_3$ (0.223 g, 2.1 mmol) into 1 M $NaNO_3$ background electrolyte. The pH was then adjusted by the addition of small amounts of 6 M nitric acid, causing CO_2 loss. The final ratio of free-carbonate ion to carbonate in the $UO_2(CO_3)_3^{4-}$(aq) ion could be determined by the ^{13}C NMR peak integration and was close to 1:1. In these experiments, the final $UO_2(CO_3)_3^{4-}$(aq) concentration was 0.1 M and the free carbonate concentration is 0.3 M.

All NMR experiments were performed in a wide-bore Bruker Avance 400 MHz (9.4 T) spectrometer using a home-built high-pressure probe similar to that used in previous experiments.[3, 19] The sample was sealed in a custom high-pressure quartz NMR tube with a dual viton o-ring plunger and the probe pressure was set with a high-pressure syringe pump in combination with a valve system. Isohexane was used as the pressure-transfer medium and the pressure exhibited less than 0.5% variation during an experiment. Temperature was set to

47.0°C for experiments to probe pathway 1, and 25.0°C for experiments to probe pathway 2. Thermal equilibrium was controlled by a circulating water bath and closely controlled to ±0.1°C using an in situ thermocouple.

To monitor pH *in situ,* we used 1-methylimidazole as an internal pH reference. The probe circuit was modified when switching from ^{14}N to ^{13}C but 90° pulse times never exceeded 40 μs for ^{14}N and 20 μs for ^{13}C. To create a homogeneous magnetic field over the sample, a coarse shim was obtained using the ^{23}Na signal from the electrolyte and a fine shim was obtained by pulsing ^{13}C at a small 12° Ernst angle[20] allow for a faster repetition rate, as ^{13}C has a long T_1 relaxation time. Ground shielding was physically adhered to the NMR tube to maximize RF homogeneity with Rabi cycling experiments used to determine the optimum shielding position. We employed an adaptation of NMR inversion-transfer[21] to monitor the rates of exchange between free carbonate ion in solution and carbonate in $UO_2(CO_3)_3^{4-}(aq)$.

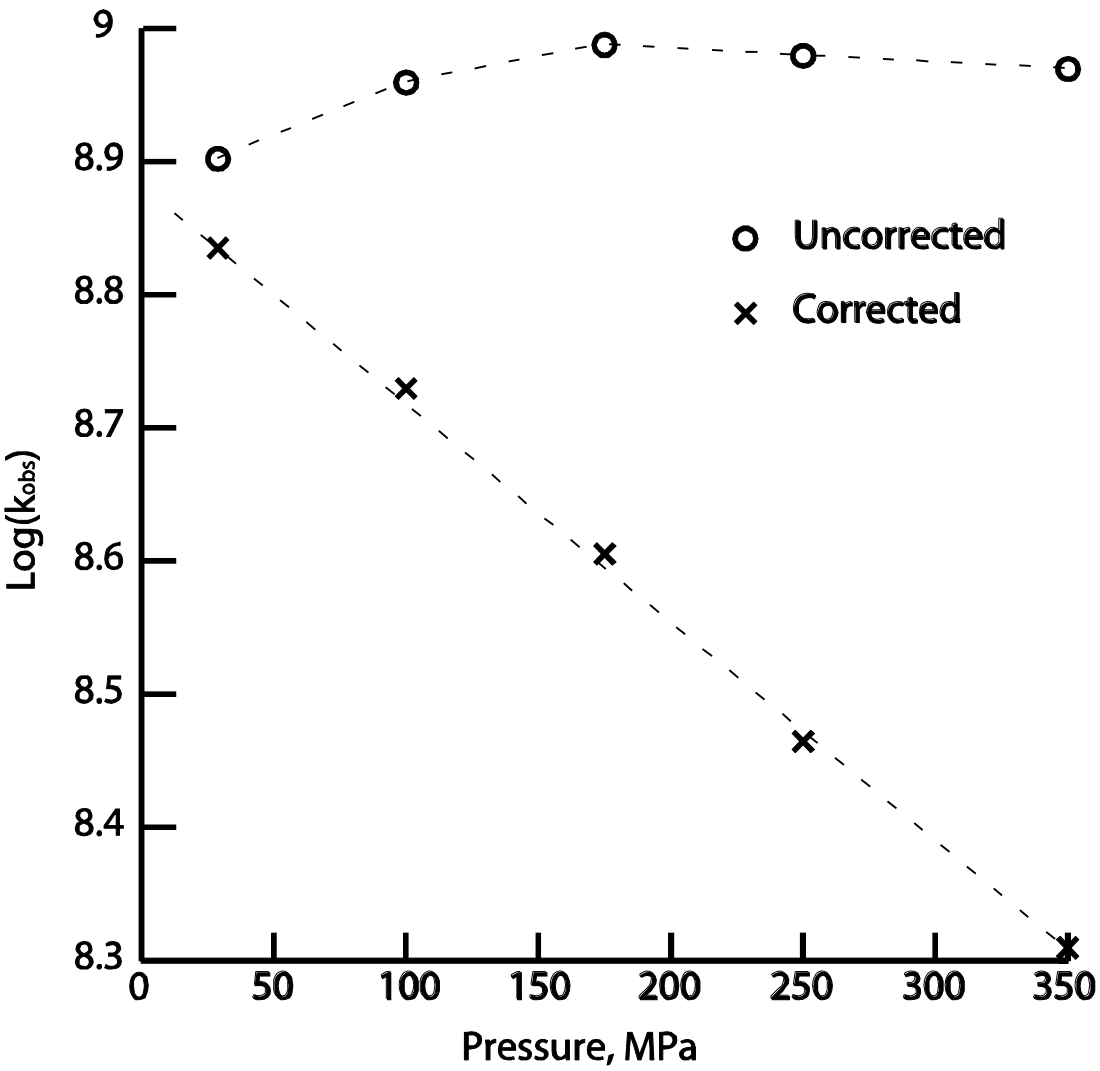

Figure B.5: The importance of correcting for the pressure dependence of pH of a system for determination of activation volume. Using uncorrected values can lead to large misinterpretation of data.

Pathway Contribution

Contributions from each pathway were calculated using the activation parameters published by Bányai et al.[1d]

Pathway 1: □H‡ = 82 kJ·mol-1; □S‡ = 50 J·mol-1·K-1

Pathway 2: □H‡ = 52 kJ·mol-1; □S‡ = 110 J·mol-1·K-1

Plots were made by inputting the above information into the Eyring-Polanyi equation (below) and solving for k at different temperatures, for each pathway.

$$k = \left(\frac{k_B T}{h}\right) e^{\left(\frac{\Delta S^{\ddagger}}{R}\right)} e^{\left(-\frac{\Delta H^{\ddagger}}{RT}\right)} \qquad \text{(B.7)}$$

The value of k was then plugged into the rate law for each respective pathway, also provide by Bányai et al.[1d], and the rate was plotted as a function of temperature.

Pathway 1: rate = k1[UO2CO3-4(aq)]

Pathway 2: rate = k2[UO2CO3-4(aq)]·[H+]

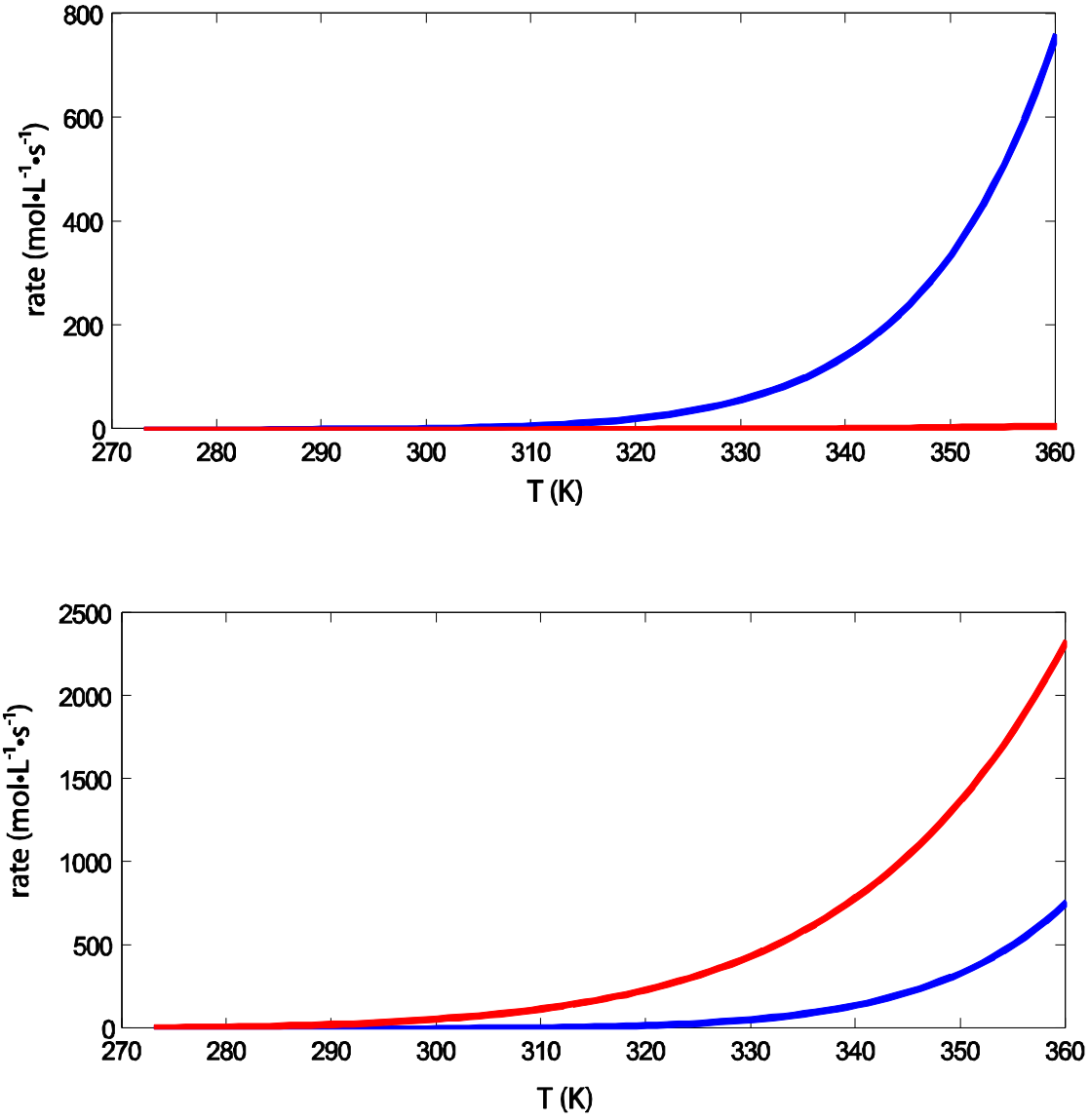

Figure B.6: (top) Contributions of pathway 1 (blue) and pathway 2 (red) to the overall rate of carbonate exchange as a function of temperature at pH 9.50. (bottom) Contributions of pathway 1 (blue) and pathway 2 (red) to the overall rate of carbonate exchange as a function of temperature at pH 7.07.

Carbonate system

The temperature dependence for the ionization constant of water and carbonate used the following model[9c]

$$\ln(K_i) = A_i + \frac{B_i}{T} + C_i \ln(T) \quad \text{(B.8)}$$

where:

Acid	A	-B	-C
H_2O	148.9802	13847.26	23.6521
H_2CO_3	290.9097	14554.21	45.0575
HCO_3^-	207.6548	11843.79	33.6485

T has units of Kelvin

The pressure dependencies are given by[9c]

$$K_i(P) = K_i T e^{-(\frac{V_i}{RT})(P-1)+0.5(\frac{\kappa_i}{RT})(P-1)^2}$$

$$Vi = A_{v,i} + B_{v,i}t + C_{V,i}t^2 \quad \text{(B.8)}$$

$$\kappa_i = (A_{\kappa,i} + B_{\kappa,i}t + C_{\kappa,i}t^2) * 10^{-3}$$

where t has units of °C and:

Acid	A_V	B_V	C_V	A_κ	B_κ	C_κ
H_2O	-25.6	0.2324	$-3.625*10^{-3}$	-7.33	0.1368	$-1.233*10^{-3}$
H_2CO_3	-30.54	0.1849	$-2.3366*10^{-3}$	-6.22	0.1368	$-1.233*10^{-3}$
HCO_3^-	-29.81	0.1150	$-1.816*10^{-3}$	-5.74	0.093	$-1.896*10^{-3}$

The values obtained using these equations were in good agreement with experimentally reported values.[9b]

1-Methylimidazole pressure variance

The Ka for each pressure was determined by solving the following system of equations: Equilibrium Relations:

$$K_w=[H^+][OH^-]$$
$$K_a=\frac{[HMI]}{[H^+][MI^-]} \quad \text{(B.10)}$$

Species Balance:

$$MI_{total}=[MI^-]+[HMI] \quad \text{(B.11)}$$

Charge Balance:

$$[OH^-]+[NO_3^-]=[H^+][HA] \quad \text{(B.12)}$$

Shift Dependence:

$$pH = pK_a - \log(\frac{(\delta_{MI^-} - \delta_{obs})}{(\delta_{obs} - \delta_{HMI})}) \quad \text{(B.13)}$$

In this system of equations we have a total of 11 variables. The known variables are δ_{MI}, δ_{HMI}, δ_{obs}, $[NO_3]$, and MI_{Total}, leaving 5 unknowns, indicating the above 5 equations are well constrained. At each pressure a Kw is calculated using the above pressure dependence of the Kw and a Ka is solved for. Then these pressure dependent values were fit to

$$K_a(P) = K_{a_T} e^{-(\frac{V_a}{RT})(P-1)+0.5(\frac{\kappa_a}{RT})(P-1)^2} \quad \text{(B.14)}$$

The nitrate concentration corresponds to the amount on nitric acid used to set the solution to the desired pH.

Pressure Dependence of pH for UO2(CO3)4-3 system

The pressure dependence of the pH for the UO2(CO3)4-3 was monitored via the 14N chemical shift of 1-methylimidazole via:

$$pH = pK_a - \log(\frac{(\delta_{MI^-} - \delta_{obs})}{(\delta_{obs} - \delta_{HMI})}) \qquad \text{(B.15)}$$

Where δMI = -137.4 and δHMI = -205 relative to the nitrate peak.

Which resulted in:

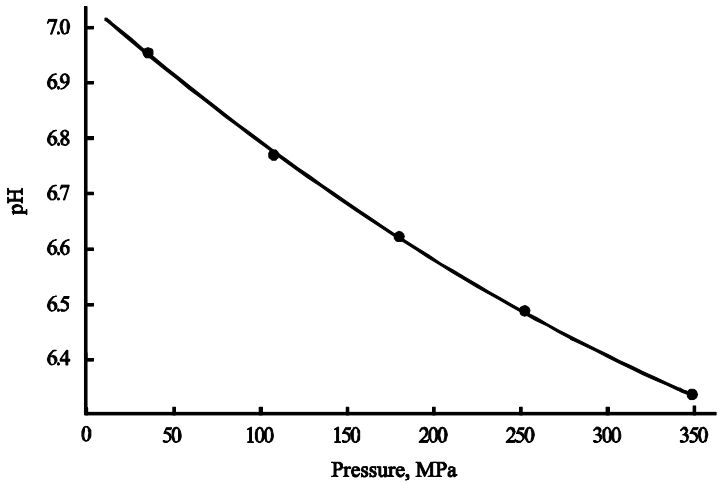

The curvature was fit to a generic quadratic equation:

$$p\text{H} \square a\text{P}2\underline{\ } b\underline{P}c \qquad \text{(B.16)}$$

where a = 1.789x10-6, b = -0.00253, and c = 7.075.

Example of variation of pH with changes in pressure and temperature□

A 0.5 M solution of sodium carbonate set to pH = 7.10 at 0.1 MPa and 25.0°C would reach pH = 6.25 at 47.0°C and 200 MPa (see Supporting Information) and the exchange rate of pathway 2 would increase by a factor of ~8.

Treatment of raw data

To measure the rates at pressure, the NMR signal for free carbonate ion was put on resonance and was selectively inverted via the method described above. Each peak was phased independently and then fit to a Lorentzian function. The amplitude values were compiled as a function of mixing time. This data array was then fit to the model derived above using a least-squares fitting routine employing an interior-reflective Newton search method to solve the equations simultaneously. The resulting analytical solutions, too, are coupled and thus simultaneous fitting of the two data arrays to the two expressions is required. A value for exchange rate and associated uncertainty was obtained for each pressure. The uncertainty in the fitting of the saturation transfer model was always larger than the linear curve fit of the pressure dependence; thus, it became necessary to propagate this larger error to the reported activation volume. To accomplish this, a random, normally distributed, array of 1000 points having a mean value of the regressed rate and a standard deviation of regression standard deviation was generated for each pressure. A single point from each array was randomly chosen and linearly regressed to obtain a value for the slope. This process of picking points from the normally distributed array is repeated 1000 times and the average slope is obtained and the standard deviation of this process is the reported uncertainty.

References

[1] a) E. Brucher, J. Glaser, I. Toth, *Inorg. Chem.* **1991**, *30*, 2239-2241; b) L. Ciavatta, D. Ferri, I. Grenthe, *Inorg. Chem.* **1981**, *20*, 463-467; c) D. Ferri, I. Grenthe, F. Salvatore, *Acta Chem. Scand., Ser. A*, **1981**, *35a*, 165-168; d) I. Bányai, J. Glaser, K. Micskei, I. Tóth, L. Zekany, *Inorg. Chem.* **1995**, *34*, 3785-3796.

[2] a) E. T. Strom, D. E. Woessner, *J. Am. Chem. Soc.* **1981**, *103*, 1255-1256; b) P. G. Allen, J. J. Bucher, D. L. Clark, N. M. Edelstein, S. A. Ekberg, J. W. Gohdes, E. A. Hudson, N. Kaltsoyannis, W. W. Lukens, M. P. Neu, P. D. Palmer, T. Reich, D. K. Shuh, C. D. Tait, B. D. Zwick, *Inorg. Chem.* **1995**, *34*, 4797-4807.

[3] S. J. Harley, C. A. Ohlin, R. L. Johnson, A. F. Panasci, W. H. Casey, *Angew. Chem.* **2011**, *123*, 4559-4561; *Angew. Chem., Int. Ed.* **2011**, *50*, 4467-4469.

[4] G. A. Morris, R. Freeman, *J. Magn. Reson.* **1978**, *29*, 433-462.

[5] A. Bodor, I. Bányai, L. Zékány, I. Tóth, *Coord. Chem. Rev.* **2002**, *228*, 163-173.

[6] F. Bloch, W. W. Hansen, M. Packard, *Phys. Rev.* **1946**, *70*, 474.

[7] H. M. McConnell, *J. Chem. Phys.* **1958**, *28*, 430-431.

[8] 7.9.0.529 ed., Mathworks, Inc., Natick, MA, **2009**.

[9] a) Chapman and Hall/CRCnetBASE, Boca Raton, FL, **1999**; b) A. V. Bandura, S. N. Lvov, *J. Phys. Chem. Ref. Data* **2006**, *35*, 15-30; c) F. J. Millero, *Geochim. Cosmochim. Acta* **1979**, *43*, 1651-1661.

[10] a) I. Bányai, J. Blixt, J. Glaser, I. Tóth, *Acta Chim. Scand.* **1992**, *46*, 138-141; b) I. Bányai, J. Blixt, J. Glaser, I. Tóth, *Acta Chim. Scand.* **1992**, *46*, 142-146.

[11] H. I. A. Phillips, L. Ronconi, P. J. Sadler, *Chem.—Eur. J.* **2009**, *15*, 1588-1596.

[12] a) B. Lenarcik, P. Ojczenasz, *J. Heterocyclc. Chem.* **2002**, *39*, 287-290; b) N. C. Li, J. M. White, E. Doody, *J. Am. Chem. Soc.* **1954**, *76*, 6219-6223.

[13] J. Blixt, B. Gyori, J. Glaser, *J. Am. Chem. Soc.* **1989**, *111*, 7784-7791.

[14] I. Farkas, I. Banyai, Z. Szabo, U. Wahlgren, I. Grenthe, *Inorg. Chem.* **2000**, *39*, 799-805.

[15] V. Vallet, U. Wahlgren, B. Schimmelpfennig, Z. Szabó, I. Grenthe, *J. Am. Chem. Soc.* **2001**, *123*, 11999-12008.

[16] F. P. Rotzinger, *Chem.—Eur. J.* **2007**, *13*, 800-811.

[17] S. Tsushima, *J. Phys. Chem. A* **2007**, *111*, 3613-3617.

[18] R. J. Evans, J. R. Rustad, W. H. Casey, *J. Phys. Chem.A* **2008**, *112*, 4125-4140.

[19] C. A. Ohlin, S. J. Harley, J. G. McAlpin, R. K. Hocking, B. Q. Mercado, R. L. Johnson, E. M. Villa, M. K. Fidler, M. M. Olmstead, L. Spiccia, R. D. Britt, W. H. Casey, *Chem.—Eur. J.* **2011**, *17*, 4408-4417.

[20] R. R. Ernst, W. A. Anderson, *Rev. Sci. Instrum.* **1966**, *37*, 93-102.

[21] a) J. J. Led, H. Gesmar, *J. Magn. Reson.* **1982**, *49*, 444-463; b) K. G. Orrell, V. Sik, D. Stephenson, *Prog. Nucl. Magn. Reson. Spectrosc.* **1990**, *22*, 141-208; c) Z. Szabo, I. Grenthe, *Inorg. Chem.* **2010**, *49*, 4928-4933; d) J. Sandström, *Dyn. NMR Spectrosc.*, Academic Press, London, **1982**; e) S. Forsen, R. A. Hoffman, *J. Chem. Phys.* **1963**, *39*, 2892-2901.

Appendix C:

Supplemental Information for $[Fe_4(OH)_2(hpdta)_2(H_2O)_4]^o(aq)$

Figure C.1: Temperature dependence of the magnetic susceptibility of $[Fe_4(OH)_2(hpdta)_2(H_2O)_4]^o(aq)$. Here two complete sets of data are plotted corresponding to reversed measurements.

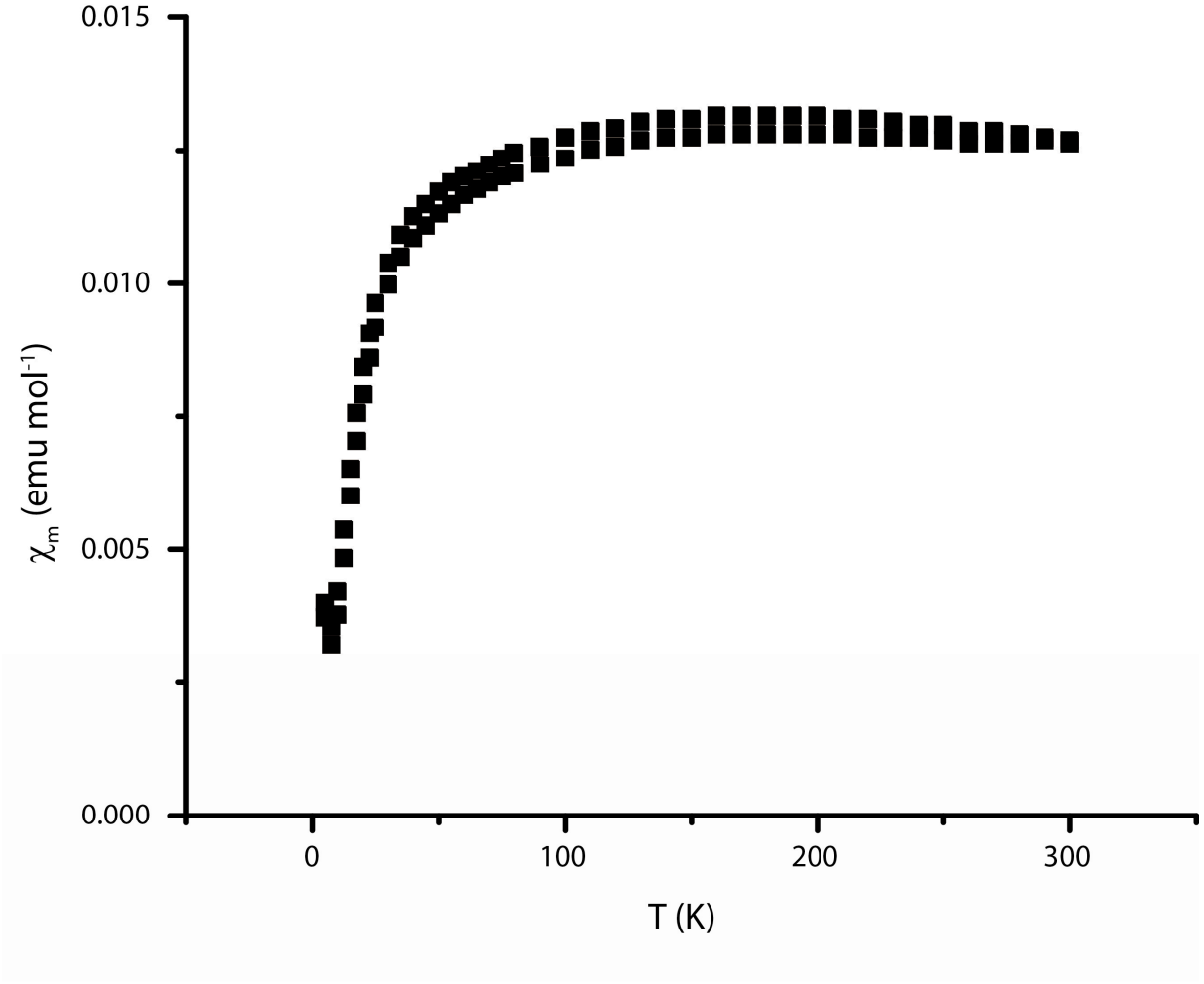

Table C.1: Titration data and calculations of excess charge density for $[Fe_4(OH)_2(hpdta)_2(H_2O)_4]^o(aq)$, leading to Here acidward and baseward titrations are compiled, along with calculations of charge.

Base Conc	0.105 M	
Acid Conc	0.09 M	
Compound Start Conc	0.003746423 M	2.1E-05 moles
Cation Start Conc	0.002816524 M	
Anion Start Conc	0.007113734	
Starting Volume	0.005592 L	

Volume[Added]	Volume added L	Moles Added	pH	[H+]	[OH-]	[Compound]	[Cation]	[Anion]	Free Charge
0	0	0	3.46837	0.00034	2.94E-11	0.003746423	0.002817	0.007114	1.056231915
0.1	0.0001	0.0000105	5.00807	9.82E-06	1.02E-09	0.003680604	0.004612	0.006989	0.64315674
0.15	0.00015	0.00001575	5.25027	5.62E-06	1.78E-09	0.003648555	0.005486	0.006928	0.393686904
0.175	0.000175	0.000018375	5.36445	4.32E-06	2.31E-09	0.003632738	0.005917	0.006898	0.268739671
0.2	0.0002	0.000021	5.49593	3.19E-06	3.13E-09	0.003617058	0.006345	0.006868	0.143748438
0.225	0.000225	0.000023625	5.63087	2.34E-06	4.27E-09	0.003601513	0.006769	0.006839	0.018683331
0.25	0.00025	0.00002625	5.79176	1.62E-06	6.19E-09	0.003586101	0.007189	0.006809	-0.106415281
0.275	0.000275	0.000028875	6.03396	9.25E-07	1.08E-08	0.00357082	0.007606	0.00678	-0.231520872
0.288	0.000288	0.00003024	6.16544	6.83E-07	1.46E-08	0.003562925	0.007821	0.006765	-0.296607698
0.301	0.000301	0.000031605	6.42667	3.74E-07	2.67E-08	0.003555065	0.008036	0.00675	-0.361672979
0.314	0.000314	0.00003297	6.66887	2.14E-07	4.67E-08	0.00354724	0.008249	0.006736	-0.426777587
0.327	0.000327	0.000034335	6.92491	1.19E-07	8.41E-08	0.003539449	0.008462	0.006721	-0.49189526
0.34	0.00034	0.0000357	7.21555	6.09E-08	1.64E-07	0.003531693	0.008673	0.006706	-0.557011298
0.353	0.000353	0.000037065	7.31589	4.83E-08	2.07E-07	0.00352397	0.008884	0.006691	-0.622150686
0.366	0.000366	0.00003843	7.4664	3.42E-08	2.93E-07	0.003516281	0.009094	0.006677	-0.687277315
0.379	0.000379	0.000039795	7.59615	2.53E-08	3.95E-07	0.003508625	0.009302	0.006662	-0.752400726
0.392	0.000392	0.00004116	7.69822	2E-08	4.99E-07	0.003501003	0.00951	0.006648	-0.817524251
0.405	0.000405	0.000042525	7.78645	1.64E-08	6.12E-07	0.003493413	0.009717	0.006633	-0.882645844
0.418	0.000418	0.00004389	7.8989	1.26E-08	7.92E-07	0.003485857	0.009923	0.006619	-0.947747686
0.431	0.000431	0.000045255	8.00789	9.82E-09	1.02E-06	0.003478333	0.010129	0.006605	-1.01283655

Base Conc	0.105	M	
Acid Conc	0.09	M	
Compound Start Conc	0.003478333	M	2.1E-05 moles
Cation Start Conc	0.010128673	M	
Anion Start Conc	0.006604682	M	
Starting Volume	0.006023	L	

Volume[Added]	Volume added L	Moles Added	pH	[H+]	[OH-]	[Compound]	[Cation]	[Anion]	Free Charge
0	0	0	8.5522	2.8E-09	3.57E-06	0.003478333	0.010129	0.006605	-1.01210205
0.05	0.00005	0.0000045	8.176	6.67E-09	1.5E-06	0.003449695	0.010045	0.007291	-0.797896559
0.075	0.000075	0.00000675	7.96738	1.08E-08	9.28E-07	0.003435553	0.010004	0.00763	-0.690663913
0.088	0.000088	0.00000792	7.86991	1.35E-08	7.41E-07	0.003428244	0.009983	0.007806	-0.634871277
0.101	0.000101	0.00000909	7.75876	1.74E-08	5.74E-07	0.003420967	0.009962	0.00798	-0.579073641
0.114	0.000114	0.00001026	7.62538	2.37E-08	4.22E-07	0.00341372	0.009941	0.008154	-0.523272324
0.127	0.000127	0.00001143	7.49371	3.21E-08	3.12E-07	0.003406504	0.00992	0.008327	-0.467459689
0.14	0.00014	0.0000126	7.34323	4.54E-08	2.2E-07	0.003399319	0.009899	0.008499	-0.411643018
0.153	0.000153	0.00001377	7.19275	6.42E-08	1.56E-07	0.003392163	0.009878	0.008671	-0.35582022
0.166	0.000166	0.00001494	7.0132	9.7E-08	1.03E-07	0.003385038	0.009857	0.008841	-0.299998204
0.179	0.000179	0.00001611	6.81313	1.54E-07	6.5E-08	0.003377943	0.009836	0.009012	-0.244179014
0.192	0.000192	0.00001728	6.61819	2.41E-07	4.15E-08	0.003370877	0.009816	0.009181	-0.188364635
0.205	0.000205	0.00001845	6.43009	3.71E-07	2.69E-08	0.003363841	0.009795	0.00935	-0.132560658
0.218	0.000218	0.00001962	6.23686	5.8E-07	1.73E-08	0.003356834	0.009775	0.009518	-0.076778506
0.231	0.000231	0.00002079	6.07954	8.33E-07	1.2E-08	0.003349856	0.009755	0.009685	-0.021008699
0.244	0.000244	0.00002196	5.94445	1.14E-06	8.8E-09	0.003342907	0.009734	0.009852	0.034746206
0.257	0.000257	0.00002313	5.81962	1.51E-06	6.6E-09	0.003335987	0.009714	0.010018	0.090478662
0.27	0.00027	0.0000243	5.72386	1.89E-06	5.29E-09	0.003329096	0.009694	0.010183	0.146212332
0.283	0.000283	0.00002547	5.64349	2.27E-06	4.4E-09	0.003322233	0.009674	0.010347	0.201942585
0.308	0.000308	0.00002772	5.50498	3.13E-06	3.2E-09	0.003309114	0.009636	0.010662	0.309080102
0.333	0.000333	0.00002997	5.3887	4.09E-06	2.45E-09	0.003296098	0.009598	0.010974	0.416183525
0.358	0.000358	0.00003222	5.27755	5.28E-06	1.89E-09	0.003283184	0.00956	0.011283	0.523214066
0.383	0.000383	0.00003447	5.16298	6.87E-06	1.46E-09	0.003270372	0.009523	0.011591	0.630119031
0.408	0.000408	0.00003672	5.03473	9.23E-06	1.08E-09	0.003257658	0.009486	0.011896	0.736784702
0.433	0.000433	0.00003897	4.86373	1.37E-05	7.31E-10	0.003245043	0.009449	0.012198	0.842799486
0.446	0.000446	0.00004014	4.72351	1.89E-05	5.29E-10	0.003238522	0.00943	0.012354	0.897027751
0.459	0.000459	0.00004131	4.52857	2.96E-05	3.38E-10	0.003232027	0.009411	0.01251	0.949550066
0.472	0.000472	0.00004248	4.21735	6.06E-05	1.65E-10	0.003225558	0.009393	0.012665	0.995763403
0.485	0.000485	0.00004365	3.87877	0.000132	7.56E-11	0.003219115	0.009374	0.01282	1.0293387
0.498	0.000498	0.00004482	3.6445	0.000227	4.41E-11	0.003212697	0.009355	0.012973	1.055681363

Figure C.2: An annotated figure of $[Fe_4(OH)_2(hpdta)_2(H_2O)_4]^o(aq)$ with some bond lengths identified. The blue proton is disordered over the two μ_2-O(H). The full structure, from Schmitt *et al.* [20], is available free of charge from the Cambridge Crystallographic Data Center (www.ccdc.cam.ac.uk) as file=MUKNIP.

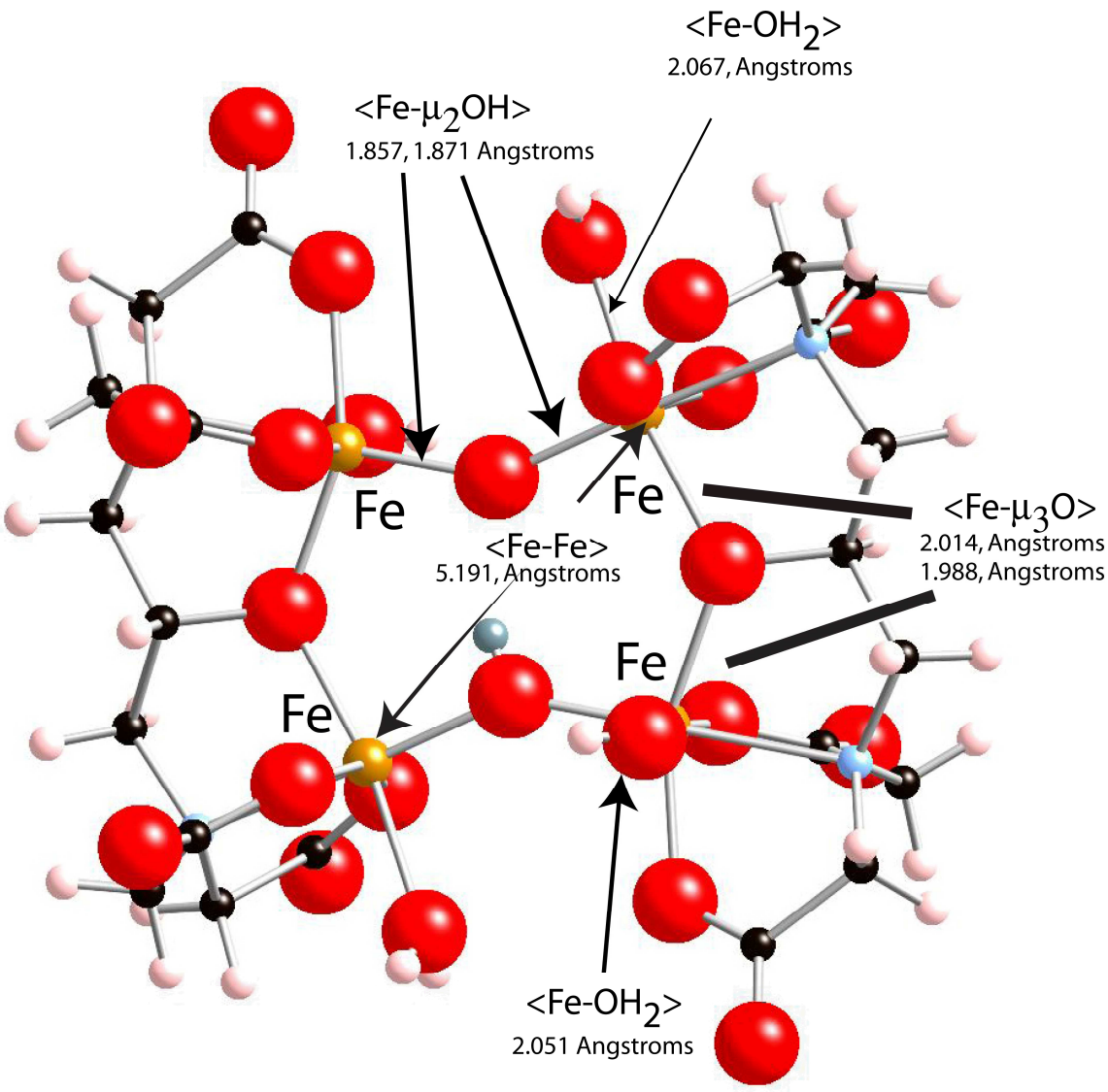

Table C.2: Data used to establish the rate coefficients. Estimates of k^{298} are reported using both the full fit to the nonlinear Swift-Connick equations, as discussed and presented in the text, and the rate coefficient that would be achieved by only a linear fit near the 298 K region. In this table, 'obs' refers to the paramagnetic sample and 'ref' identifies the diamagnetic standard. Extra digits are included to minimize round-off errors.

pH=3.79

T	obs	ref	calc. conc	calc. Pm		
288	202.78	71.07	0.012685	0.000913411		
291	229.71	65.59				
294	258.10	61.19		ln(T2r)	k298 Single s-1	
297	290.20	57.22		13.59	800903.19	
300	338.37	52.31				
303	364.38	48.98		H (kJ/mole)	S (J/mole/K)	k298 nonlin
306	398.02	46.33		49.2	34.6	9.7*10^5 per s.
309	425.41	44.63	stdev	0.2	4.2	1.2
312	440.13	42.25				
315	438.36	41.58				

pH=4.7

T	obs	ref	calc. conc	calc. Pm		
286.4	154.68	69.53	0.012586	0.000906283		
288.4	164.12	65.42				
290.5	172.64	61.81				
292.5	184.17	58.15				
294.5	195.40	55.19				
296.5	207.47	51.97		ln(T2r)	k298 Single s-1	
298.6	220.90	49.31		13.30	594491.04	
300.6	236.37	46.99				
302.6	249.60	44.77				
304.7	260.12	42.80		H (kJ/mole)	S (J/mole/K)	k298 nonlin
306.7	274.85	39.99		43.36	11.8	6.44*10^5 per sec.
308.7	285.84	38.53	st. dev.	0.8	2.70	1.5
311.8	295.59	36.32				
314.8	298.74	33.85				
318.9	289.77	31.29				

pH=4.9

T	obs	ref	calc. conc	calc. Pm			
286	128.6	62	0.010511	0.000756868			
288	136.85	58.85					
290	144.37	55.4					
292	150.7	52.2					
294	157.89	49.19					
296	166.59	46.69		ln(T2r)	k298 Single s-1		
298	175.13	43.83		13.21	544721.37		
300	182.89	41.46					
302	194.37	39.36					
304	201.24	37.13		H (kJ/mole)	S (J/mole/K)	k298 nonlinear	
306	210.37	40		42.3	7.8	5.9*10^5 per s	
308	219.62	32.67	stdev	0.1	2.3	1.8	
311	223.37	35.03					
314	223.33	30.54					
318	214.99	28.2					

pH=5.2 7.2 mM

T	obs	ref	calc. conc	calc. Pm		
288	132.99	72.52	0.007267	0.000523276		
291	136.14	66.27				
294	140.18	61.11		ln(T2r)	k298 Single s-1	
297	144.46	56.31		13.18	528929.12	
300	149.30	52.27				
303	155.80	48.63		H (kJ/mole)	S (J/mole/K)	k298 nonlin
306	158.33	45.25		34.4	-18.4	6.3*10^5 per s.
309	162.80	42.56	stdev	0.15	5.4	1.9
312	161.00	40.04				
315	156.38	37.57				

pH=5.2 14.1 mM

T	obs	ref	calc. conc	Pm		
288	175.09	72.52	0.014091	0.001014653		
291	188.89	66.27				
294	200.39	61.11		ln(T2r)	k298 Single s-1	
297	213.04	56.31		13.01	445882.57	
300	225.69	52.27				
303	238.34	48.49		H (kJ/mole)	S (J/mole/K)	k298 nonlin
306	246.39	45.28		37.8	-7.4	6.05*10^5 per s.
309	252.14	42.53	stdev	0.4	14	1.1
312	255.59	39.95				
315	250.99	37.69				

pH=5.4

T	obs	ref	calc. conc	Pm		
287.6	115.77	72.53	0.010673	0.000768533		
290.7	116.87	67.52				
293.8	119.02	63.62		ln(T2r)	k298 Single s-1	
296.9	123.78	59.41		12.48	262996.95	
300.0	126.31	56.42				
303.1	129.39	53.82				
306.3	135.85	51.42		H (kJ/mole)	S (J/mole/K)	k298 nonlin
309.4	137.44	49.12		34.2	-22.3	4.5*10^5 per s.
317.7	130.53	43.93	stdev	0.3	11	1.8

pH=5.83

T	obs	ref	calc. conc	Pm		
287.6	95.6	72.53	0.010673	0.000768533		
290.7	91.29	67.52				
293.8	88.02	63.62				
296.9	85.49	59.41				
300.0	84.13	56.42				
303.1	82.91	53.82				
306.3	82.19	51.42		ln(T2r)	k298 Single s-1	
309.4	80.87	49.12		11.77	129721.19	
313.5	79.25	46.81				
317.7	75.6	43.93		H (kJ/mole)	S (J/mole/K)	k298 nonlin
				18.9	-80.6	1.86*10^5 per s.
			st. dev.	2.0	7.40	0.17

pH=4.47

T	obs	ref	calc. conc	calc. Pm		
288	207.08	72.53	0.011635	0.000837804		
291	235.35	67.52				
294	270.95	63.62		ln(T2r)	k298 Single s-1	
297	302.40	59.41		13.72	910704.58	
300	349.01	56.42				
303	374.57	53.82		H (kJ/mole)	S (J/mole/K)	k298 nonlin
306	422.56	51.42		52.7	48.3	12*10^5 per sec
309	437.19	49.12	stdev	0.4	12	3
312	447.70	46.81				
315	456.26	43.93				

pH=4.9

T	obs	ref	calc. conc	calc. Pm		
287.9	166.15	72.53	0.011723	0.00084414		
290.9	181.63	67.52				
293.9	199.8	63.62		ln(T2r)	k298 Single s-1	
296.9	221.52	59.41		13.31	603010.34	
299.9	240.22	56.42				
302.9	262.55	53.82		H (kJ/mole)	S (J/mole/K)	k298 nonlin
305.9	287.21	51.42		42.9	10.8	6.9*10^5 per s.
308.9	303.81	49.12	stdev	0.2	5.8	3
311.9	315.88	46.81				
314.9	325.89	43.93				

pH=5.2

T	obs	ref	calc conc	calc. Pm		
285	152.3	72.53	0.012075	0.000869487		
288	163.58	67.52				
291	174.2	63.62				
294	185.19	59.41		ln(T2r)	k298 Single s-1	
297	196.29	56.42		13.13	505116.03	
300	207.18	53.82				
303	214.43	51.42		H (kJ/mole)	S (J/mole/K)	k298 nonlinear
306	218.54	49.12		38.6	-4	6.6*10^5 per s.
309	222.03	46.81	stdev	0.1	3.9	6.5
312	217.76	43.93				

pH=5.2 11.7 mM

T	obs	ref	calc. conc	calc. Pm		
288	131	72.5	0.011708	0.00084306		
291	134	66.3				
294	137	61.1		ln(T2r)	k298 Single s-1	
297	140	56.3		12.65	311701.85	
300	155	52.3				
303	152	48.5		H (kJ/mole)	S (J/mole/K)	k298 nonlin
306	158	45.3		36.5	-14.2	4.5*10^5 per s.
309	156	42.5	stdev	0.35	9.6	3
312	160	40.0				
315	155	37.7				

pH=5.2 19.2 mM

T	obs	ref	calc. conc	Pm		
288	196.6	72.5	0.019178	0.001380954		
291	213.2	66.3				
294	224.2	61.1		ln(T2r)	k298 Single s-1	
297	240.5	56.3		12.95	418807.16	
300	254.8	52.3				
303	268.1	48.5		H (kJ/mole)	S (J/mole/K)	k298 nonlin
306	278.2	45.3		36	-14.5	5.3*10^5 per s
309	284.7	42.5	stdev	0.2	4	1.4
312	287.6	40.0				
315	283.4	37.7				

pH=5.5

T	obs	ref	calc. conc	Pm		
286.4	97.77	69.53	0.010074	0.000725401		
288.4	95.04	65.42				
290.5	93.38	61.81				
292.5	92.66	58.15				
294.5	90.86	55.19				
296.5	90.98	51.97		ln(T2r)	k298 Single s-1	
298.6	91.19	49.31		12.11	181283.57	
300.6	91.47	46.99				
304.7	92.22	42.80	stdev	H (kJ/mole)	S (J/mole/K)	k298 nonlin
306.7	92.67	39.99		25	-60.9	1.7*10^5 per s.
308.7	92.70	38.53		1.3	4.4	0.1
311.8	91.49	36.32				
314.8	89.81	33.85				
318.9	95.27	31.29				

Figure C.3: pK_{a1} versus 1/T (K) to get the enthalpy change of the deprotonation reaction affecting $[Fe_4(OH)_2(hpdta)_2(H_2O)_4]^o(aq)$**.** The uncertainty is reported as one standard deviation of the regression. The background electrolyte was 0.1 M $NaNO_3$ and the concentration of $[Fe_4(OH)_2(hpdta)_2(H_2O)_4]^o(aq)$ was 5 mM.

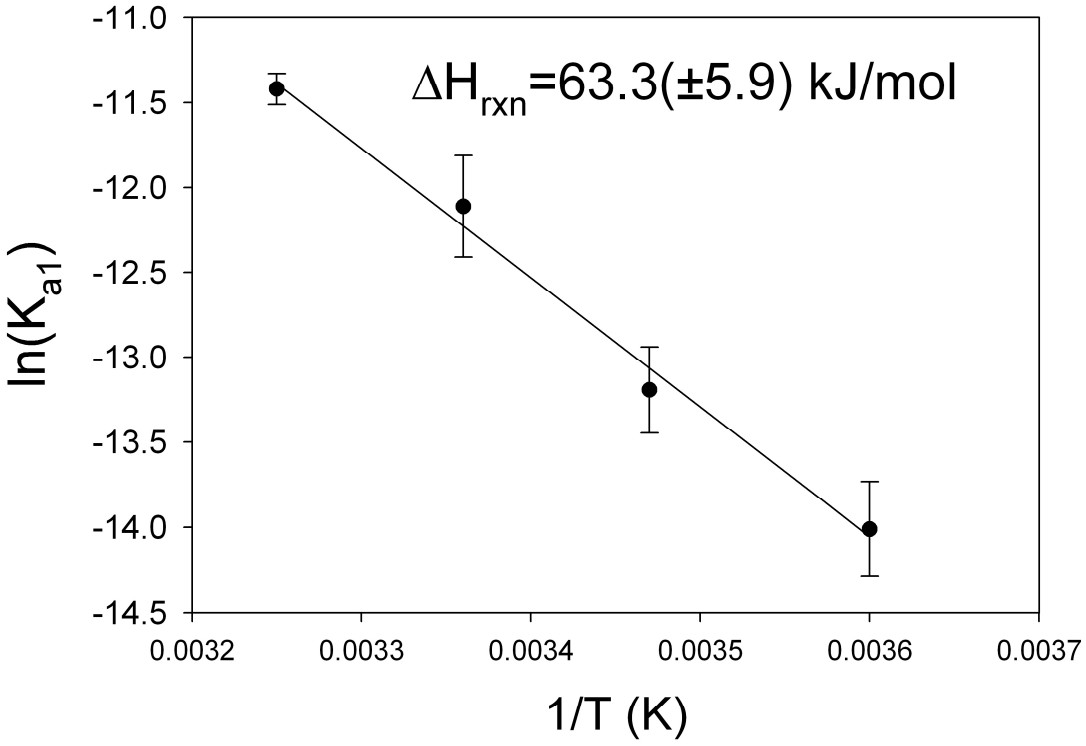

Table C.3: Linewidths for the paramagnetic sample and diamagnetic reference as a function of pressure. Extra significant digits are included in order to minimize round-off errors.

pH=5.1		298 K		
P MPa	obs (Hz)	ref (Hz)	conc M	Pm
19.85	222.9	62.6	0.014961	0.001077
77.15	216.7	61.4		
148.3	208.9	59.8		
260.76	193.4	57.4		
311.71	187.0	56.3		
150.9	208.5	59.8		

pH=4.6		291 K		
P MPa	obs (Hz)	ref (Hz)	conc M	Pm
4.24	236.5	64.6	0.014961	0.001077
53.4	223.4	62.6		
105.69	215.5	60.5		
187.41	205.8	57.3		
244.66	196.2	55.0		
100.37	219.8	60.8		

Appendix D:

Supplemental information for $[NpO_2(CO_3)_3]^{4-}$ (aq) ion

Figure D.1: Sample 4.1 (12mM $[NpO_2(CO)_3]^{4-}$ solution at pH 10.5 at 298 K). The black line is the least-squares fit to the data, which are shown as the red crosses. The top box shows the peak intensity of the bound carbonate peak and the bottom box is the intensity of the free carbonate peak.

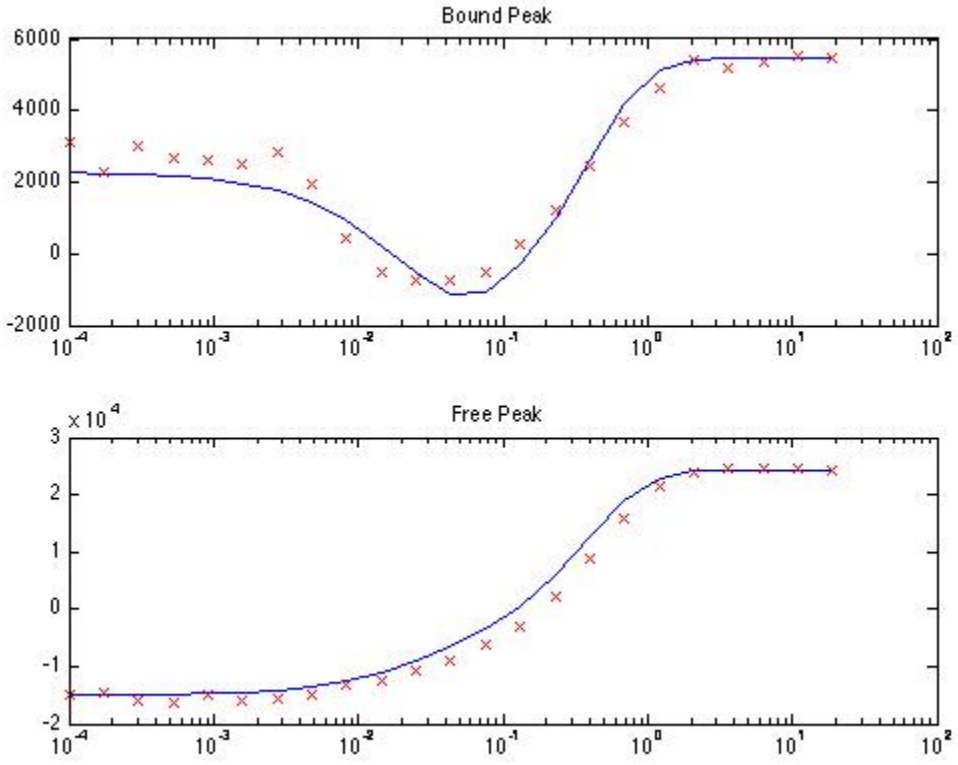

Figure D.2: Sample 4.1 (12mM $[NpO_2(CO)_3]^{4-}$ solution at pH 10.5 at 310 K). The black line is the least-squares fit to the data, which are shown as the red crosses. The top box shows the peak intensity of the bound carbonate peak and the bottom box is the intensity of the free carbonate peak.

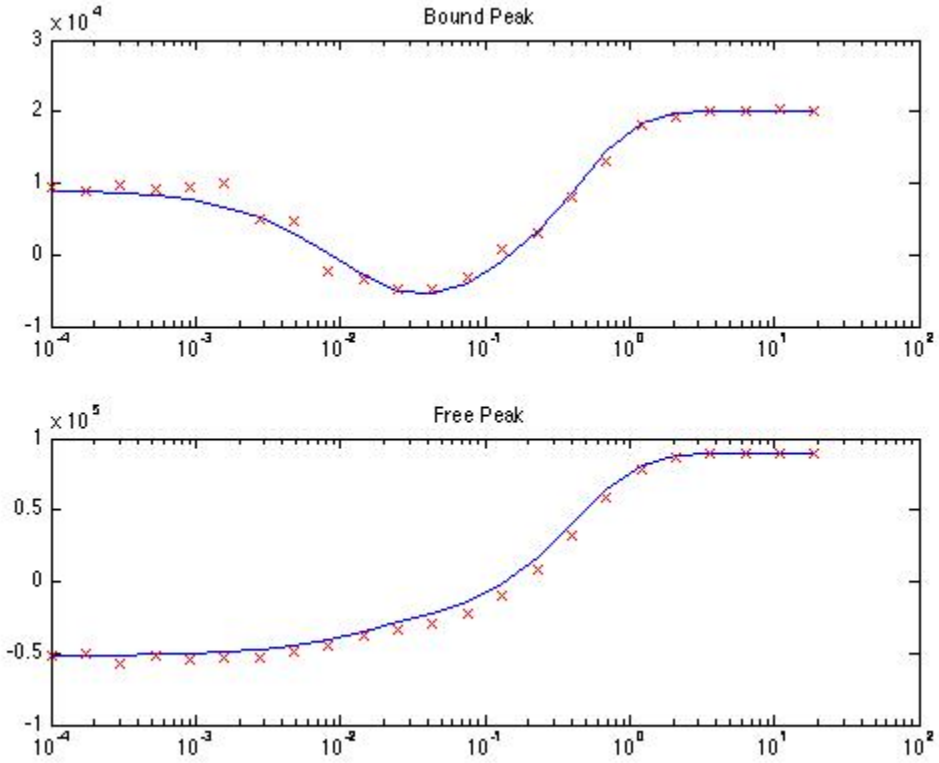

Figure D.3:Sample 4.1 (12mM $[NpO_2(CO)_3]^{4-}$ solution at pH 10.5 at 325 K). The black line is the least-squares fit to the data, which are shown as the red crosses. The top box shows the peak intensity of the bound carbonate peak and the bottom box is the intensity of the free carbonate peak.

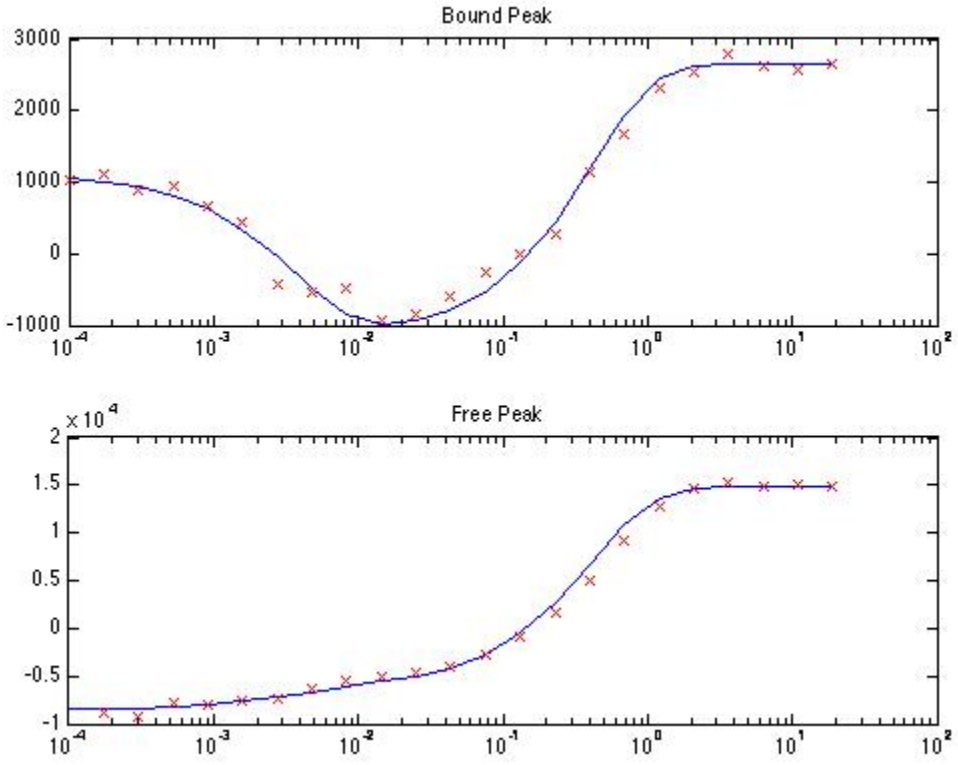

Figure D. 4: Sample 4.1 (12mM $[NpO_2(CO)_3]^{4-}$ solution at pH 10.5 at 340 K). The black line is the least-squares fit to the data, which are shown as the red crosses. The top box shows the peak intensity of the bound carbonate peak and the bottom box is the intensity of the free carbonate peak.

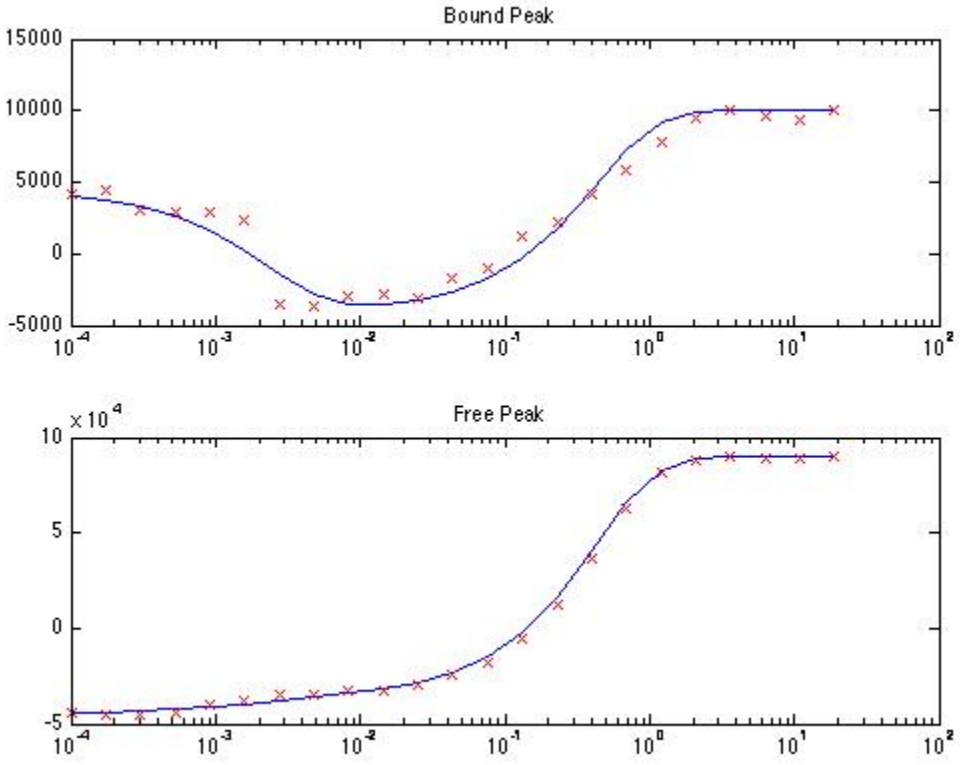

Figure D.5: Sample 4.2 (12mM $[NpO_2(CO)_3]^{4-}$ solution at pH 8.8 at 305 K). The black line is the least-squares fit to the data, which are shown as the red crosses. The top box shows the peak intensity of the bound carbonate peak and the bottom box is the intensity of the free carbonate peak.

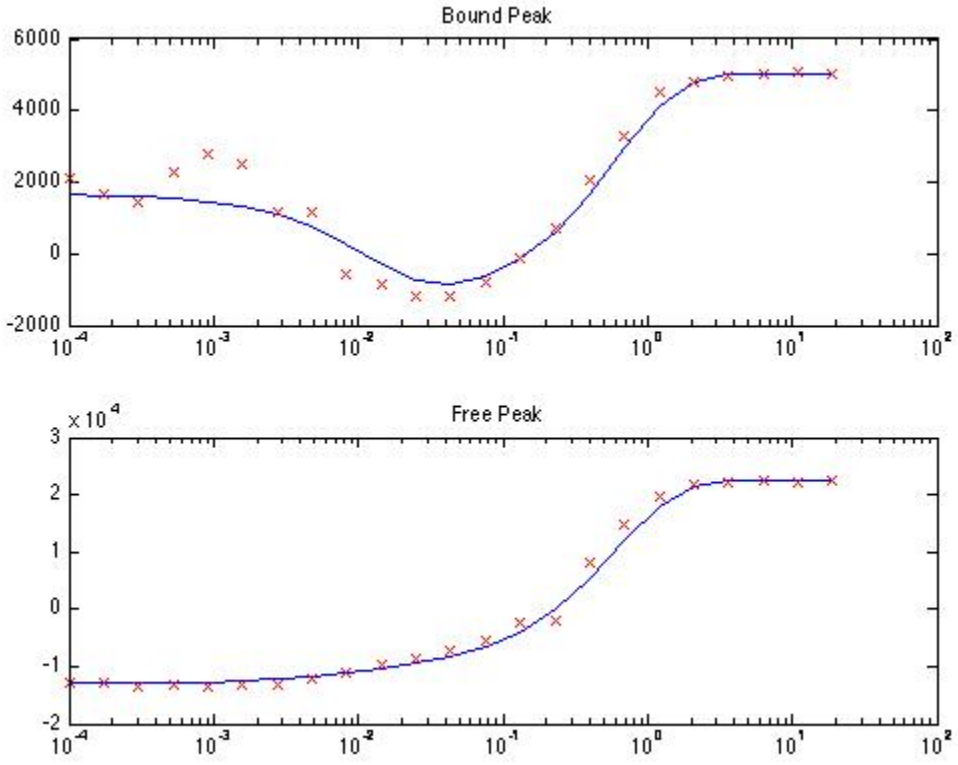

Figure D.6: Sample 4.2 (12mM $[NpO_2(CO)_3]^{4-}$ solution at pH 8.8 at 310 K). The black line is the least-squares fit to the data, which are shown as the red crosses. The top box shows the peak intensity of the bound carbonate peak and the bottom box is the intensity of the free carbonate peak.

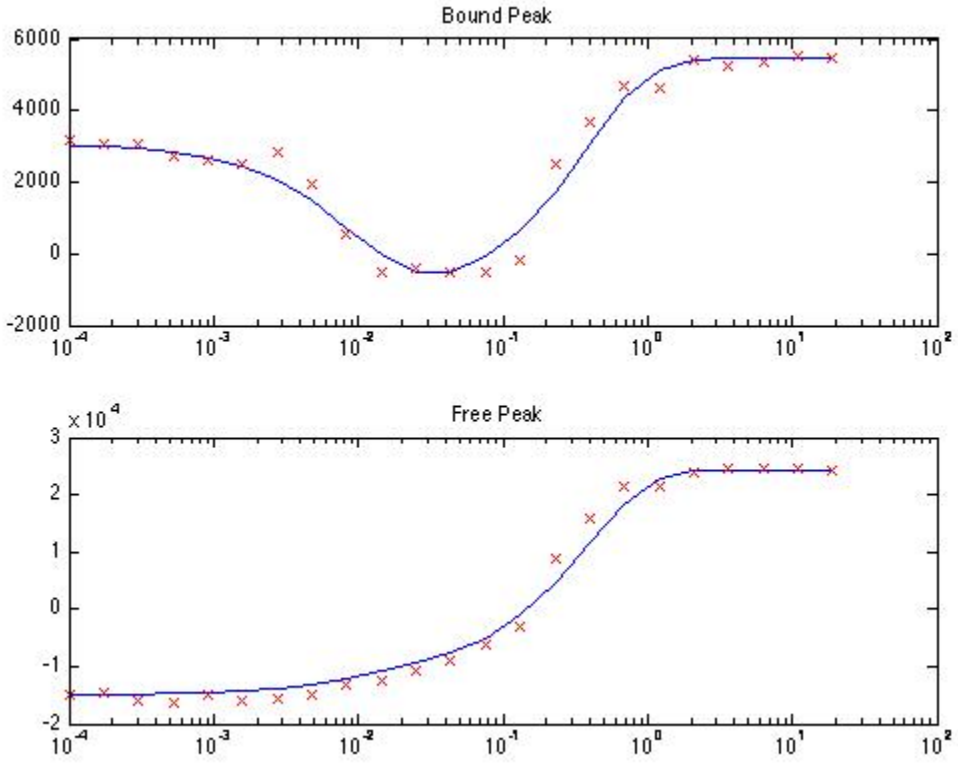

Figure D.7: Sample 4.2 (12mM $[NpO_2(CO)_3]^{4-}$ solution at pH 8.8 at 325 K). The black line is the least-squares fit to the data, which are shown as the red crosses. The top box shows the peak intensity of the bound carbonate peak and the bottom box is the intensity of the free carbonate peak.

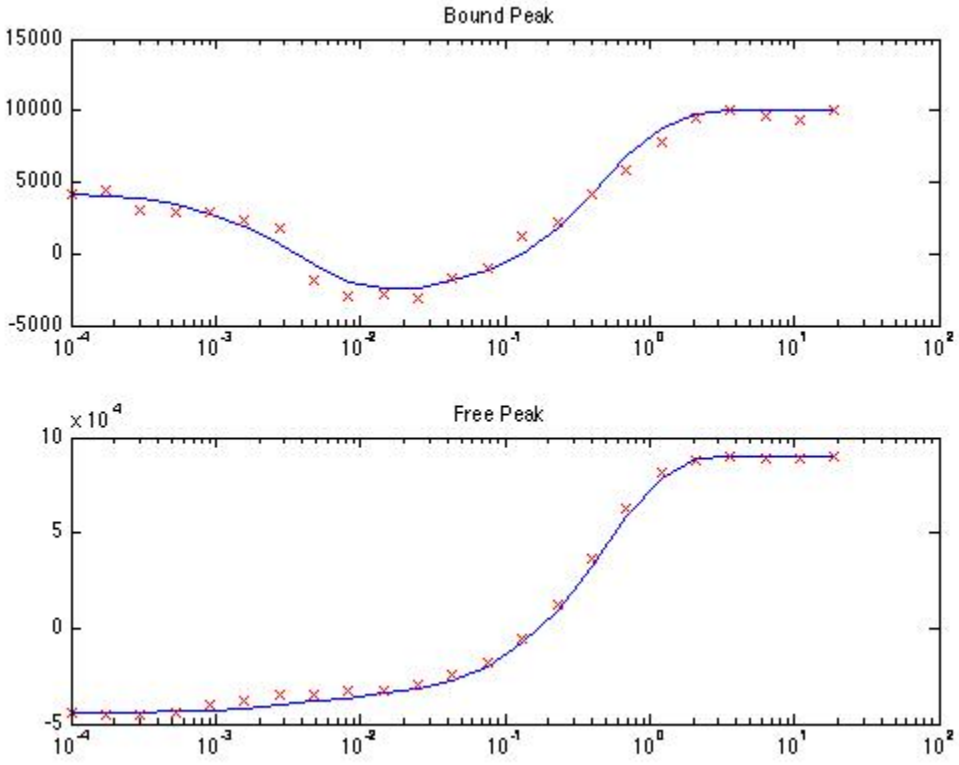

Figure D.8: Sample 4.2 (12mM $[NpO_2(CO)_3]^{4-}$ solution at pH 8.8 at 340 K). The black line is the least-squares fit to the data, which are shown as the red crosses. The top box shows the peak intensity of the bound carbonate peak and the bottom box is the intensity of the free carbonate peak.

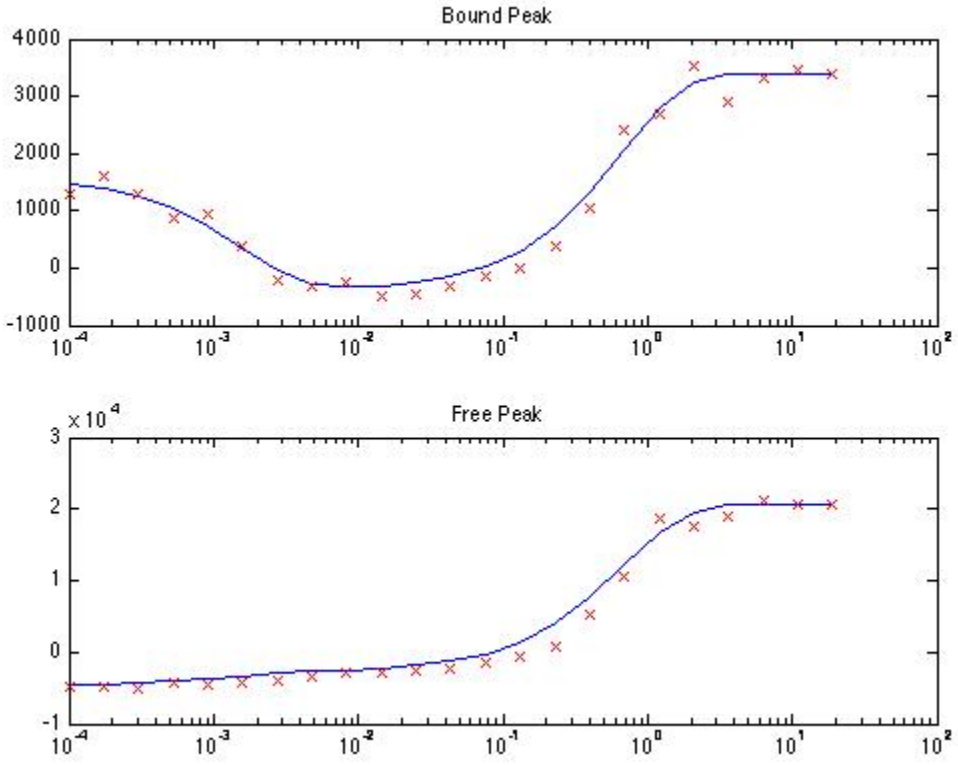

Figure D.9: Sample 4.3 (10mM $[NpO_2(CO)_3]^{4-}$ solution at pH 9.3 at 293 K). The black line is the least-squares fit to the data, which are shown as the red crosses. The top box shows the peak intensity of the bound carbonate peak and the bottom box is the intensity of the free carbonate peak.

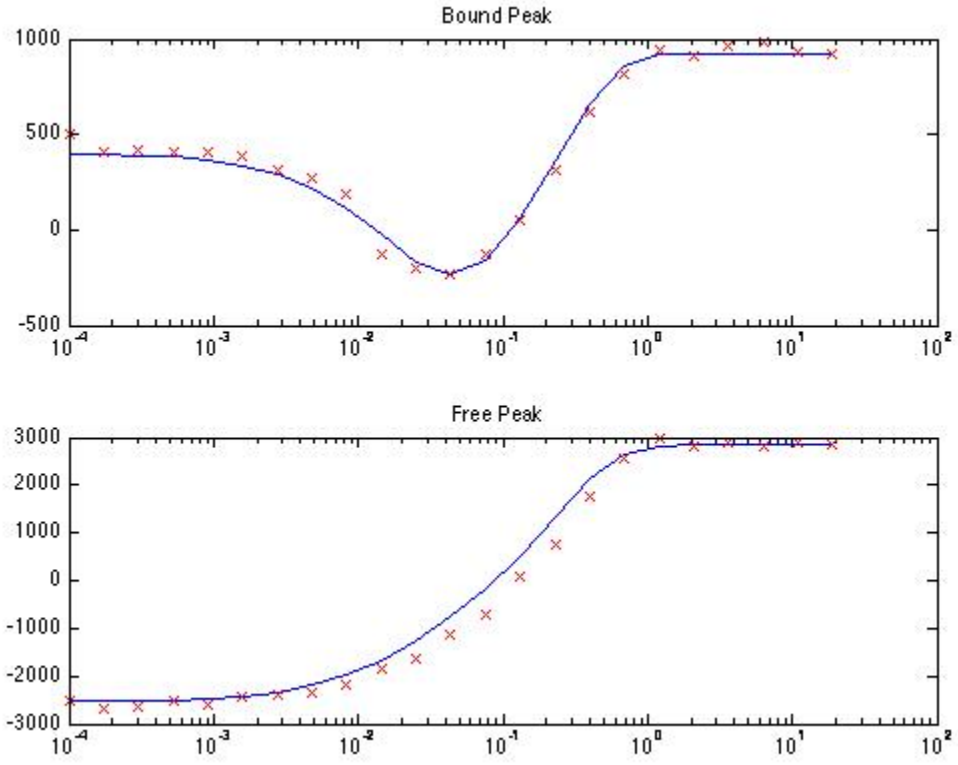

Figure D.10: Sample 4.3 (10mM $[NpO_2(CO)_3]^{4-}$ solution at pH 9.3 at 306 K). The black line is the least-squares fit to the data, which are shown as the red crosses. The top box shows the peak intensity of the bound carbonate peak and the bottom box is the intensity of the free carbonate peak.

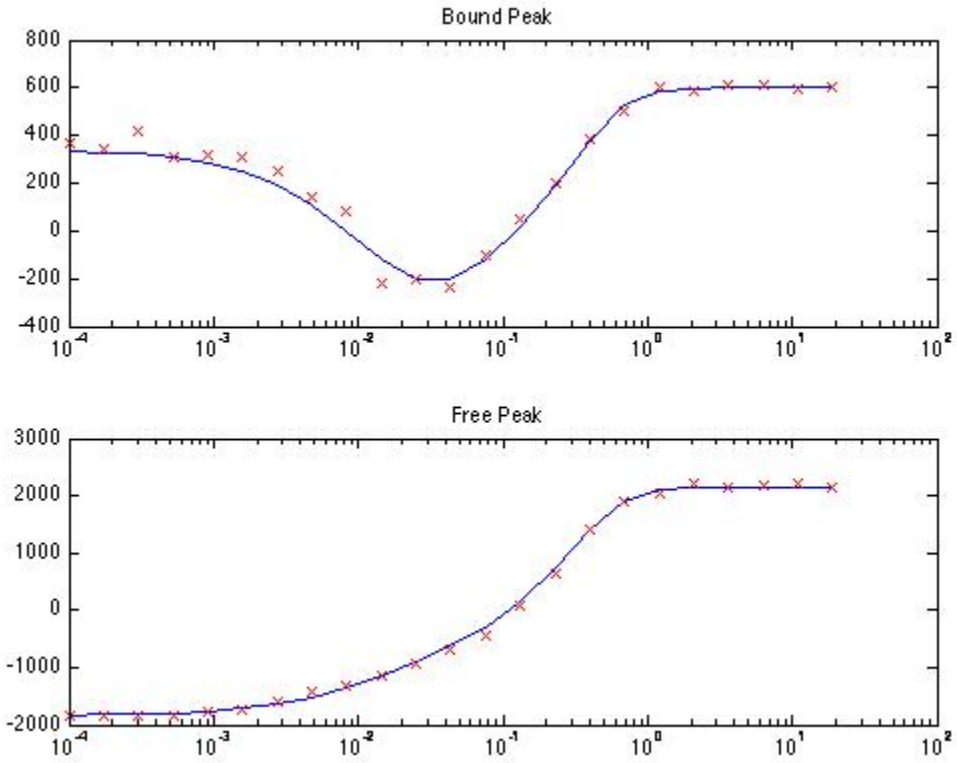

Figure D.11: Sample 4.3 (10mM $[NpO_2(CO)_3]^{4-}$ solution at pH 9.3 at 318 K). The black line is the least-squares fit to the data, which are shown as the red crosses. The top box shows the peak intensity of the bound carbonate peak and the bottom box is the intensity of the free carbonate peak.

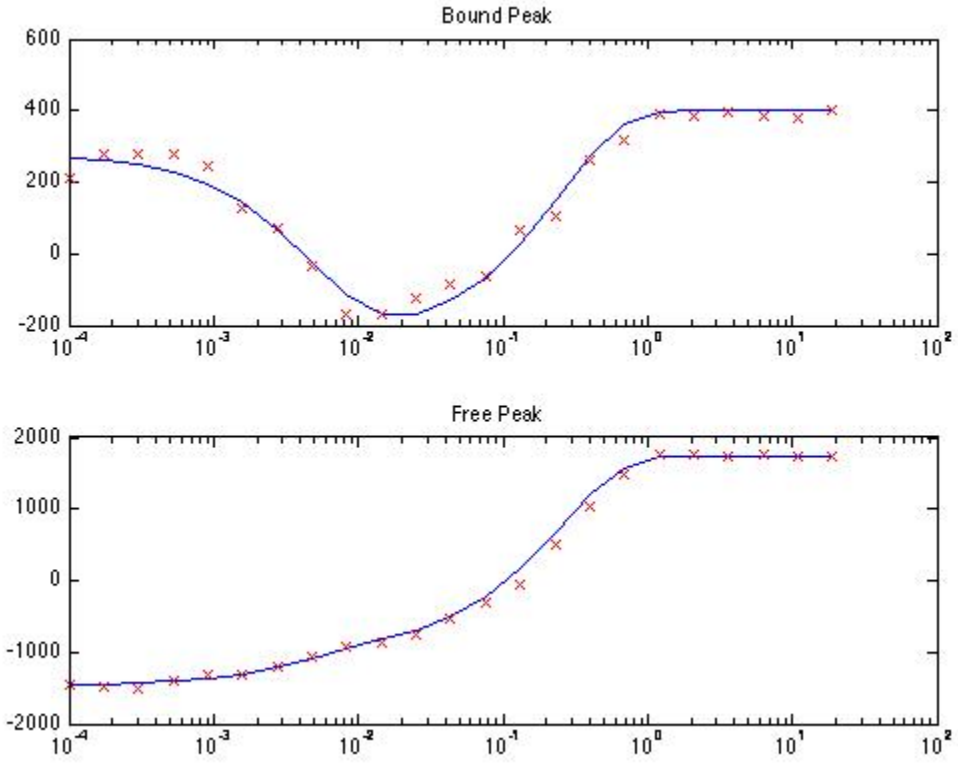

Figure D.12: Sample 4.3 (10mM $[NpO_2(CO)_3]^{4-}$ solution at pH 9.3 at 330 K). The black line is the least-squares fit to the data, which are shown as the red crosses. The top box shows the peak intensity of the bound carbonate peak and the bottom box is the intensity of the free carbonate peak.

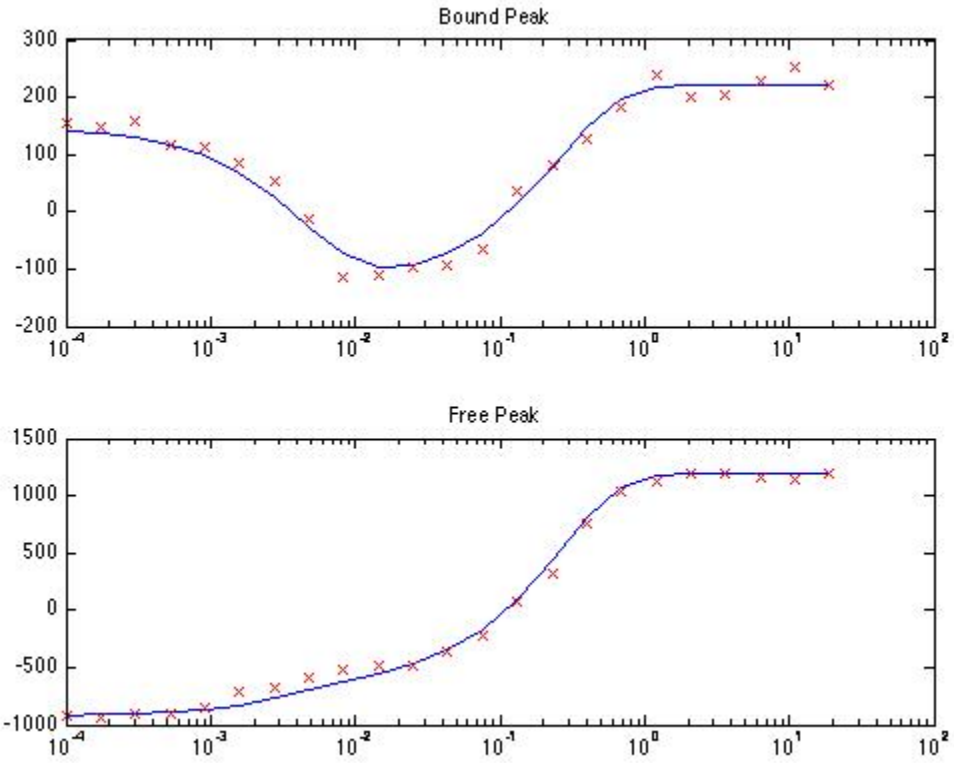

Figure D.13: Sample 4.4 (8 mM $[NpO_2(CO)_3]^{4-}$ solution at pH 10.1 at 298 K). The black line is the least-squares fit to the data, which are shown as the red crosses. The top box shows the peak intensity of the bound carbonate peak and the bottom box is the intensity of the free carbonate peak.

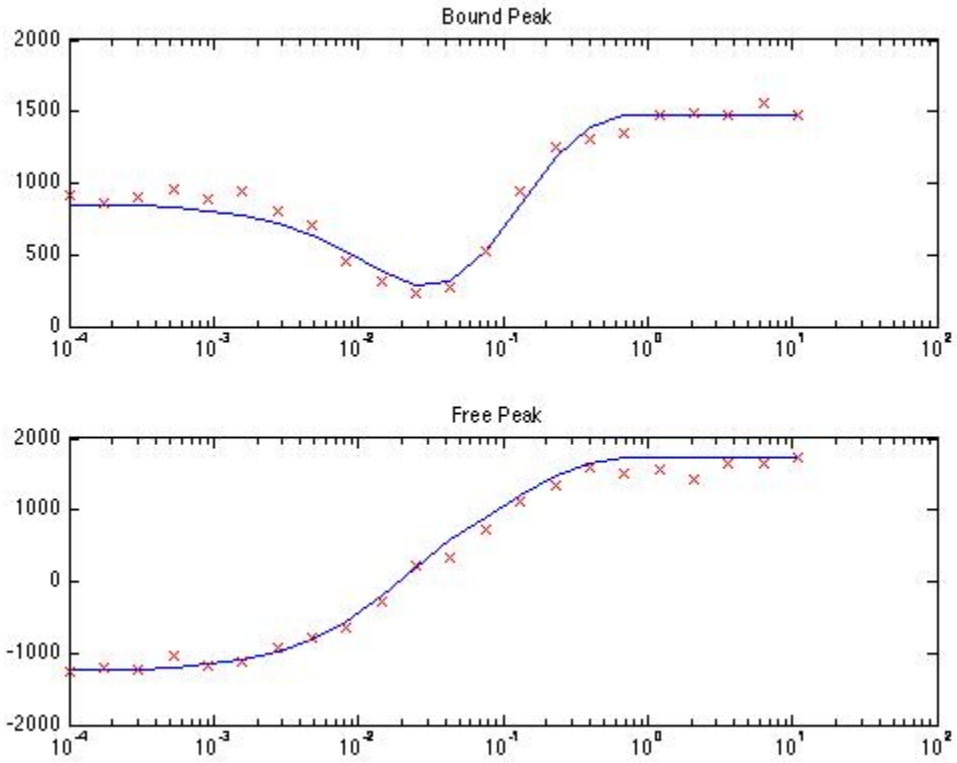

Figure D.14: Sample 4.4 (10mM $[NpO_2(CO)_3]^{4-}$ solution at pH 10.1 at 310 K). The black line is the least-squares fit to the data, which are shown as the red crosses. The top box shows the peak intensity of the bound carbonate peak and the bottom box is the intensity of the free carbonate peak.

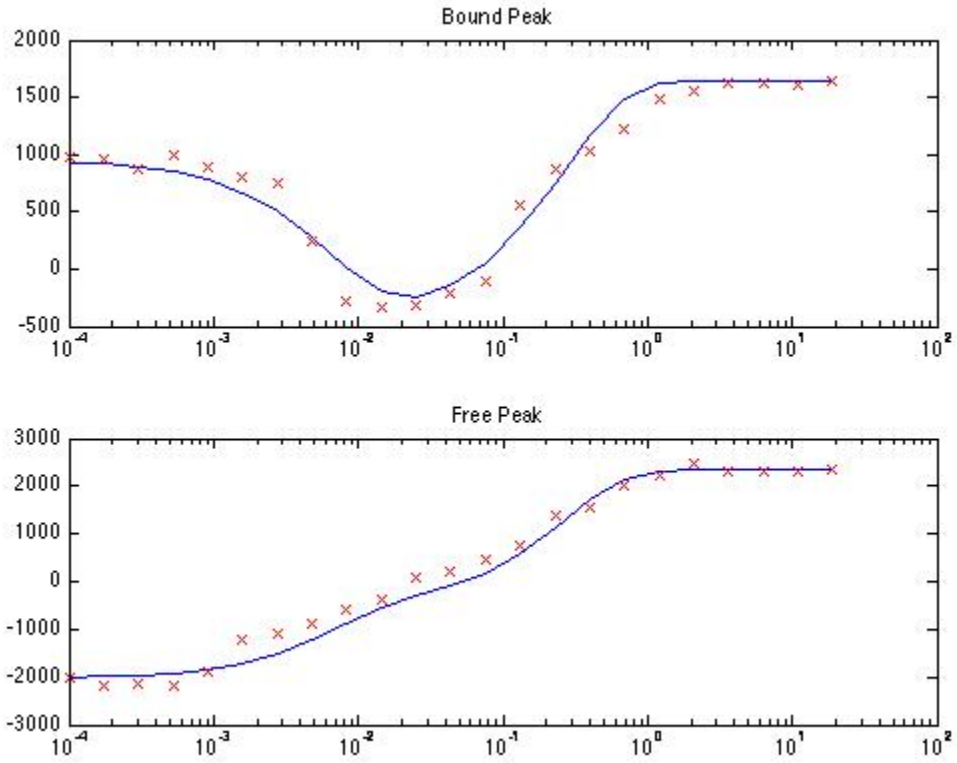

Figure D.15: Sample 4.4 (10mM $[NpO_2(CO)_3]^{4-}$ solution at pH 10.1 at 325 K). The black line is the least-squares fit to the data, which are shown as the red crosses. The top box shows the peak intensity of the bound carbonate peak and the bottom box is the intensity of the free carbonate peak.

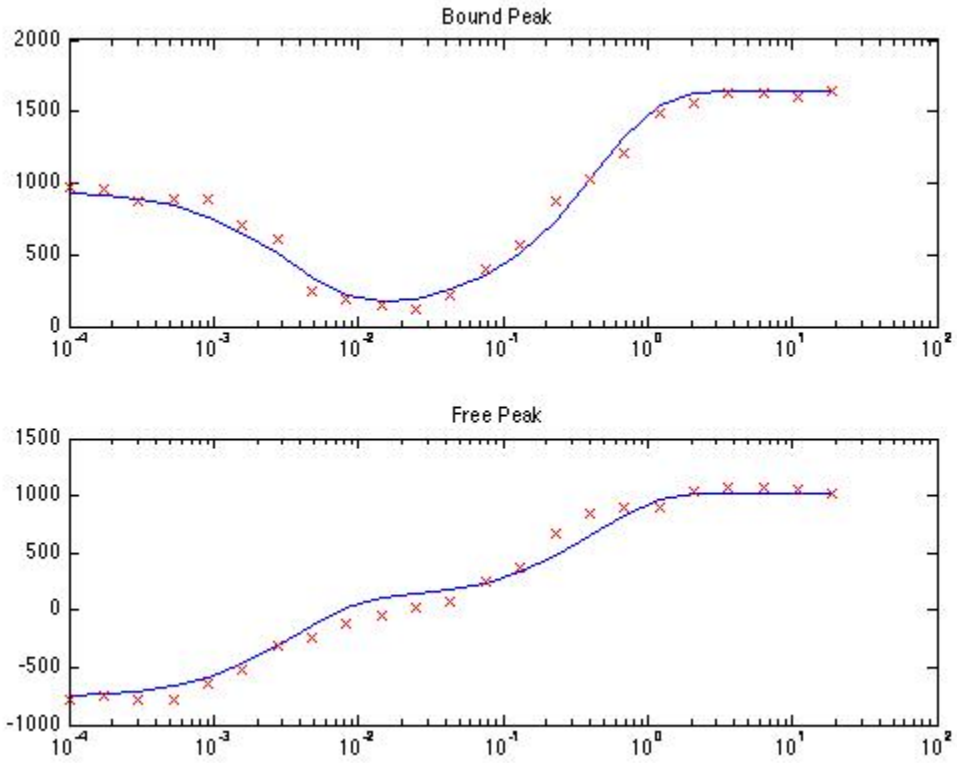

Figure D.16: Sample 4.4 (10mM $[NpO_2(CO)_3]^{4-}$ solution at pH 10.1 at 340 K). The black line is the least-squares fit to the data, which are shown as the red crosses. The top box shows the peak intensity of the bound carbonate peak and the bottom box is the intensity of the free carbonate peak.

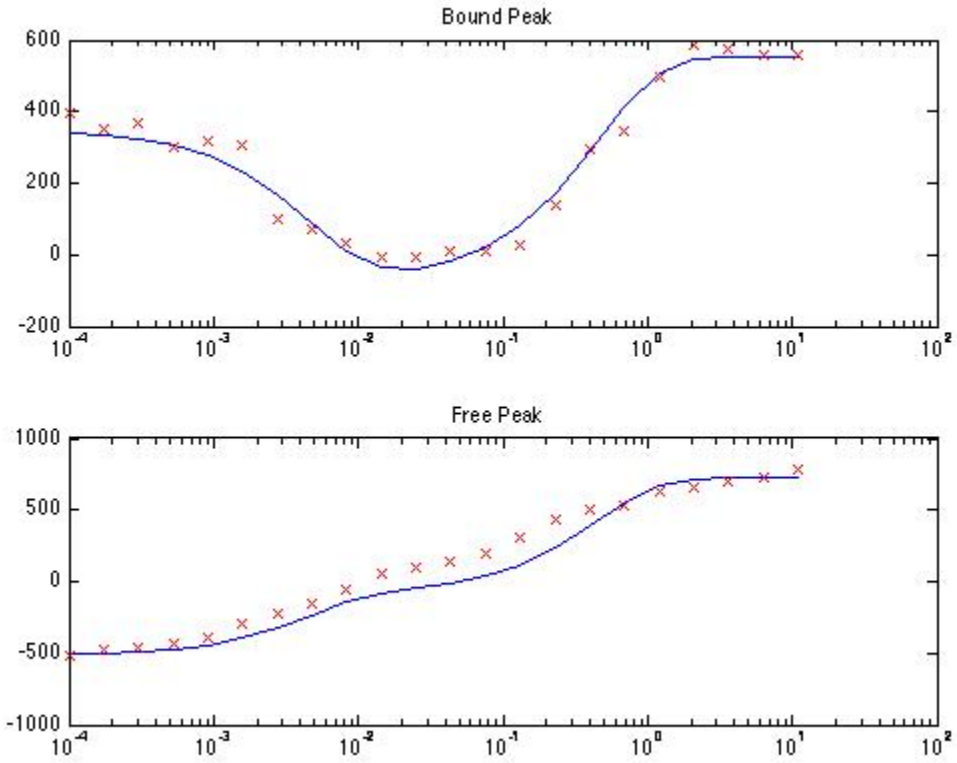

Figure D.17: Sample 4.5 (7.2mM $[NpO_2(CO)_3]^{4-}$ solution at pH 10.1 at 294 K). The black line is the least-squares fit to the data, which are shown as the red crosses. The top box shows the peak intensity of the bound carbonate peak and the bottom box is the intensity of the free carbonate peak.

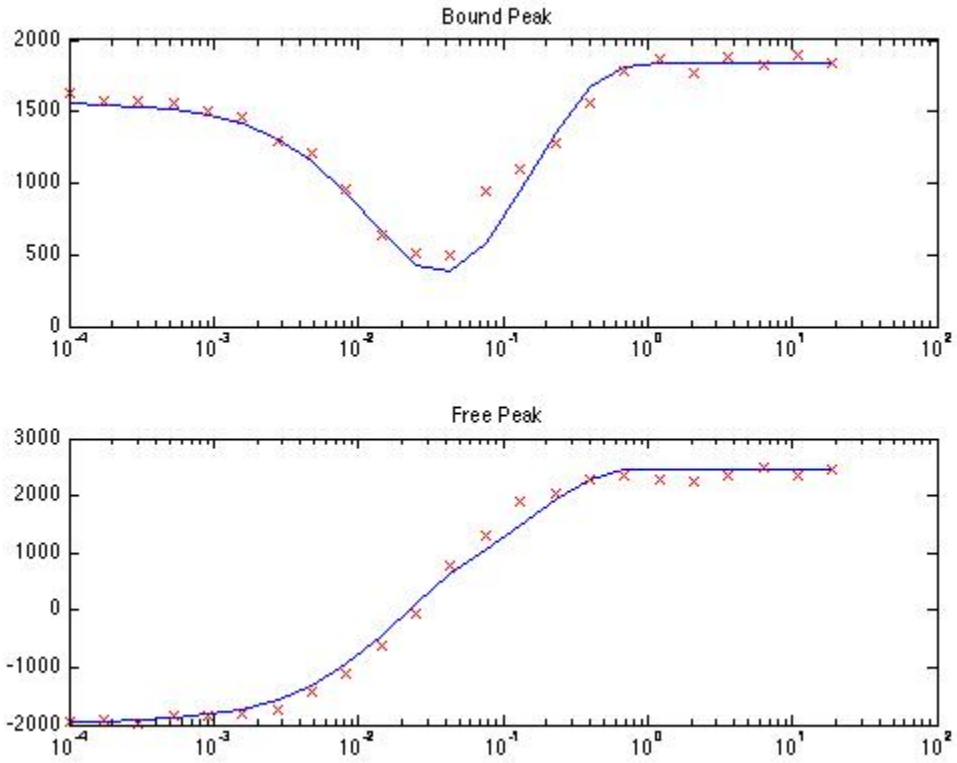

Figure D.18: Sample 4.5 (7.2mM $[NpO_2(CO)_3]^{4-}$ solution at pH 10.1 at 306 K). The black line is the least-squares fit to the data, which are shown as the red crosses. The top box shows the peak intensity of the bound carbonate peak and the bottom box is the intensity of the free carbonate peak.

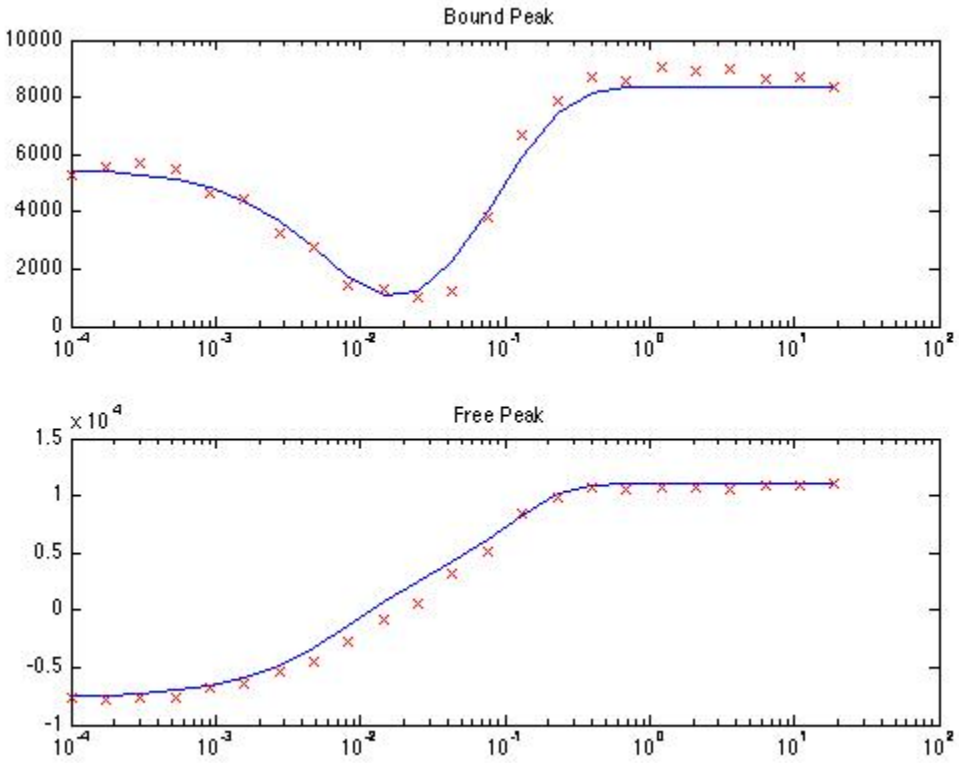

Figure D.19: Sample 4.5 (7.2mM $[NpO_2(CO)_3]^{4-}$ solution at pH 10.1 at 318 K). The black line is the least-squares fit to the data, which are shown as the red crosses. The top box shows the peak intensity of the bound carbonate peak and the bottom box is the intensity of the free carbonate peak.

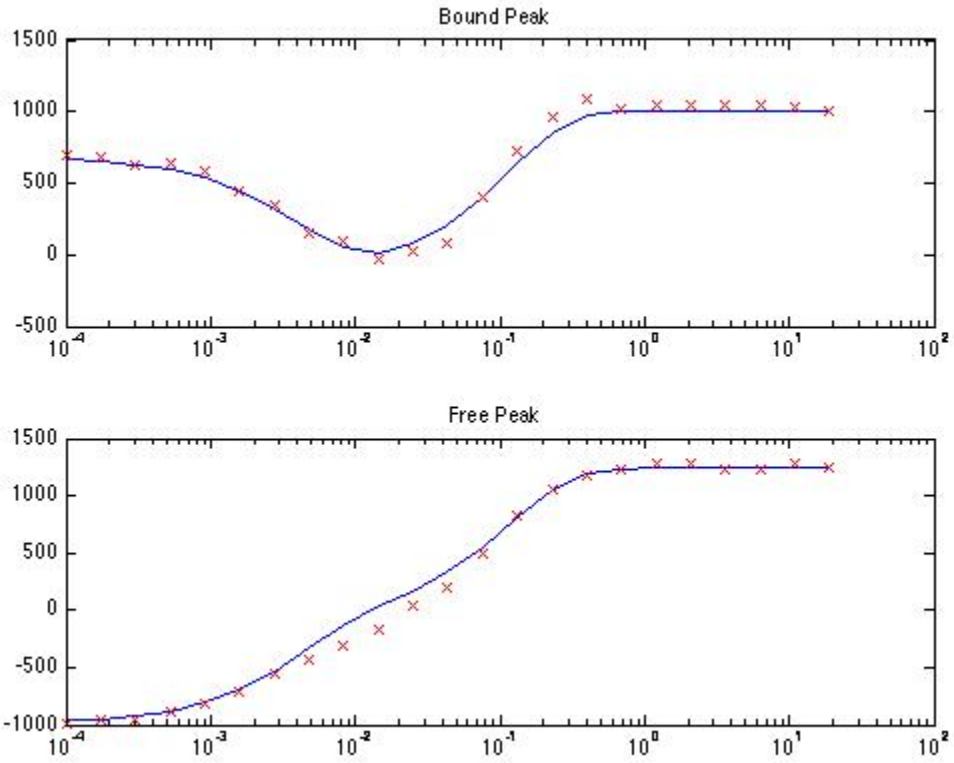

Figure D.20: Sample 4.5 (7.2mM $[NpO_2(CO)_3]^{4-}$ solution at pH 10.1 at 330 K). The black line is the least-squares fit to the data, which are shown as the red crosses. The top box shows the peak intensity of the bound carbonate peak and the bottom box is the intensity of the free carbonate peak.

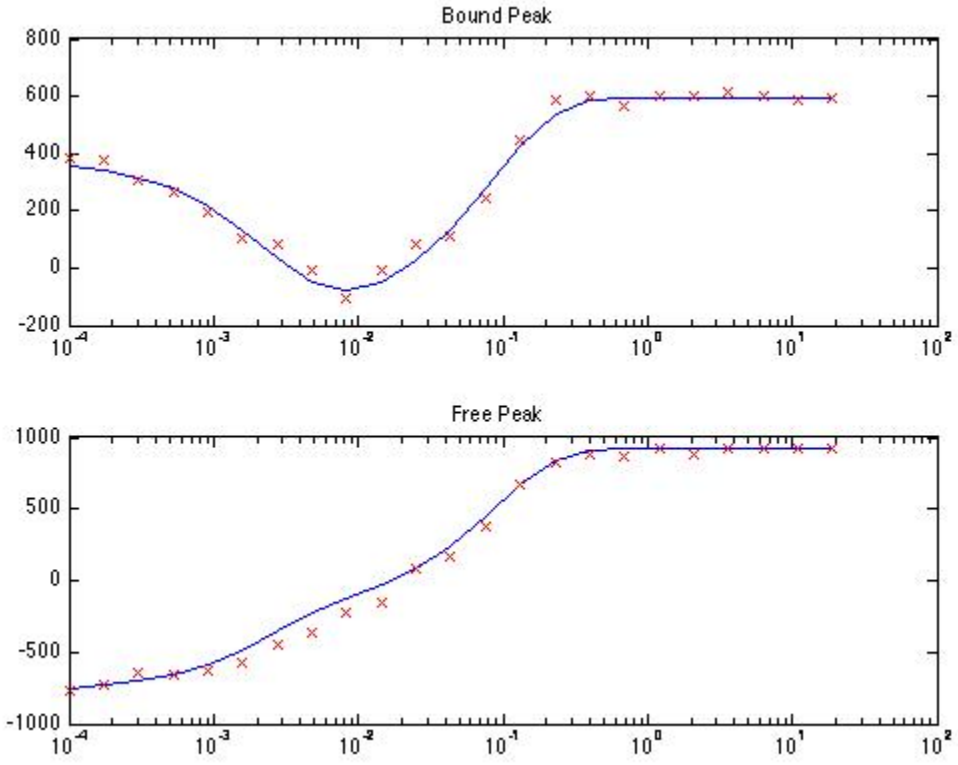

Figure D.21: Sample 4.6 (7.2mM $[NpO_2(CO)_3]^{4-}$ solution at pH 8.1 at 293 K). The black line is the least- squares fit to the data, which are shown as the red crosses. The top box shows the peak intensity of the bound carbonate peak and the bottom box is the intensity of the free carbonate peak.

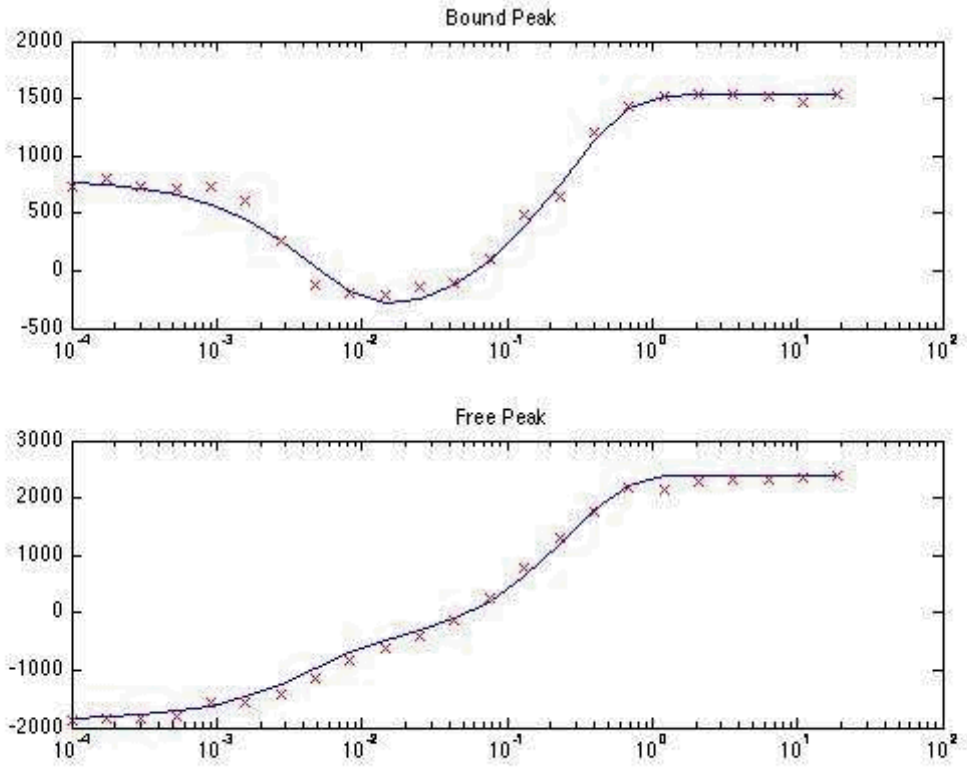

Figure D.22: Sample 4.6 (7.2mM $[NpO_2(CO)_3]^{4-}$ solution at pH 8.1 at 306 K). The black line is the least- squares fit to the data, which are shown as the red crosses. The top box shows the peak intensity of the bound carbonate peak and the bottom box is the intensity of the free carbonate peak.

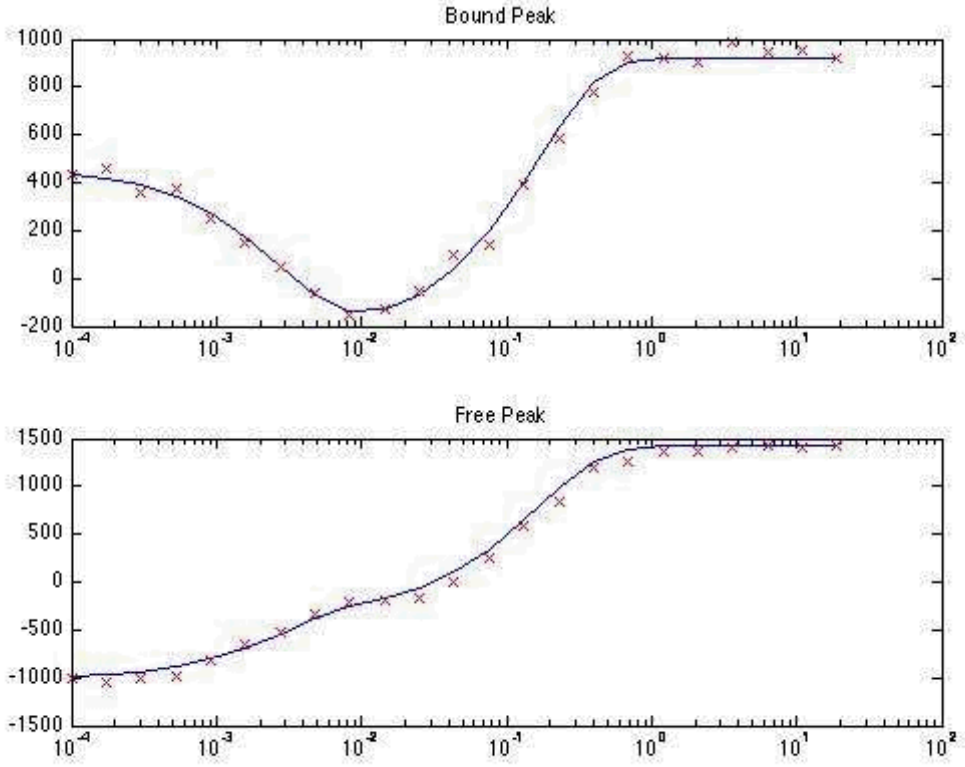

Figure D.23: Sample 4.6 (7.2mM $[NpO_2(CO)_3]^{4-}$ solution at pH 8.1 at 318 K). The black line is the least- squares fit to the data, which are shown as the red crosses. The top box shows the peak intensity of the bound carbonate peak and the bottom box is the intensity of the free carbonate peak.

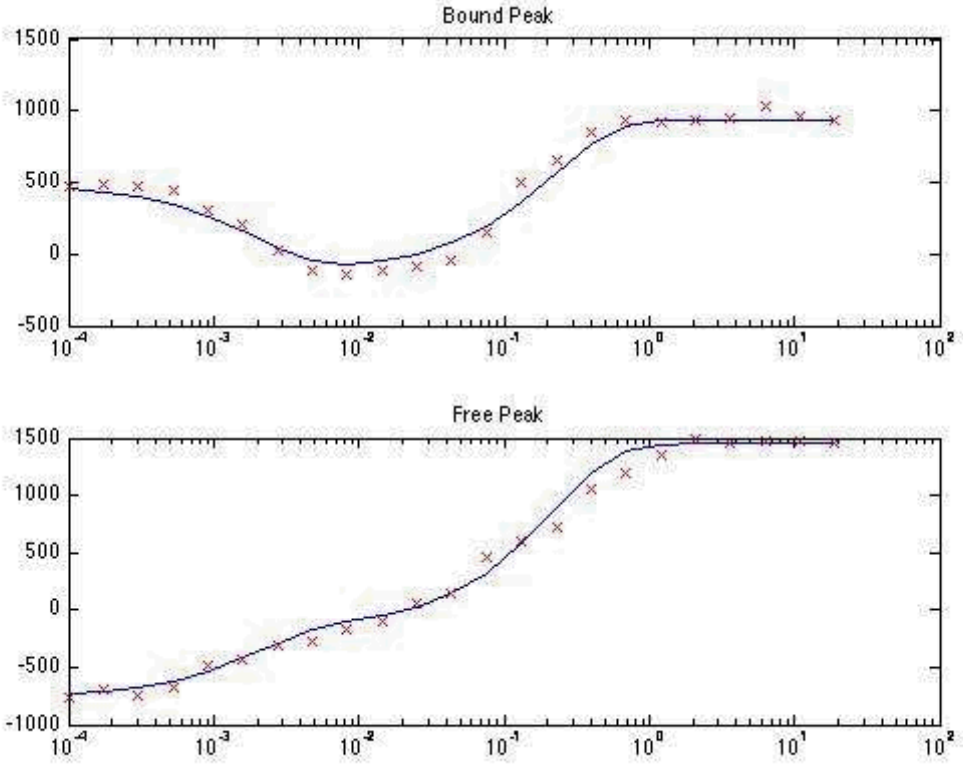

Figure D.24: Sample 4.6 (7.2mM $[NpO_2(CO)_3]^{4-}$ solution at pH 8.1 at 330 K). The black line is the least- squares fit to the data, which are shown as the red crosses. The top box shows the peak intensity of the bound carbonate peak and the bottom box is the intensity of the free carbonate peak.

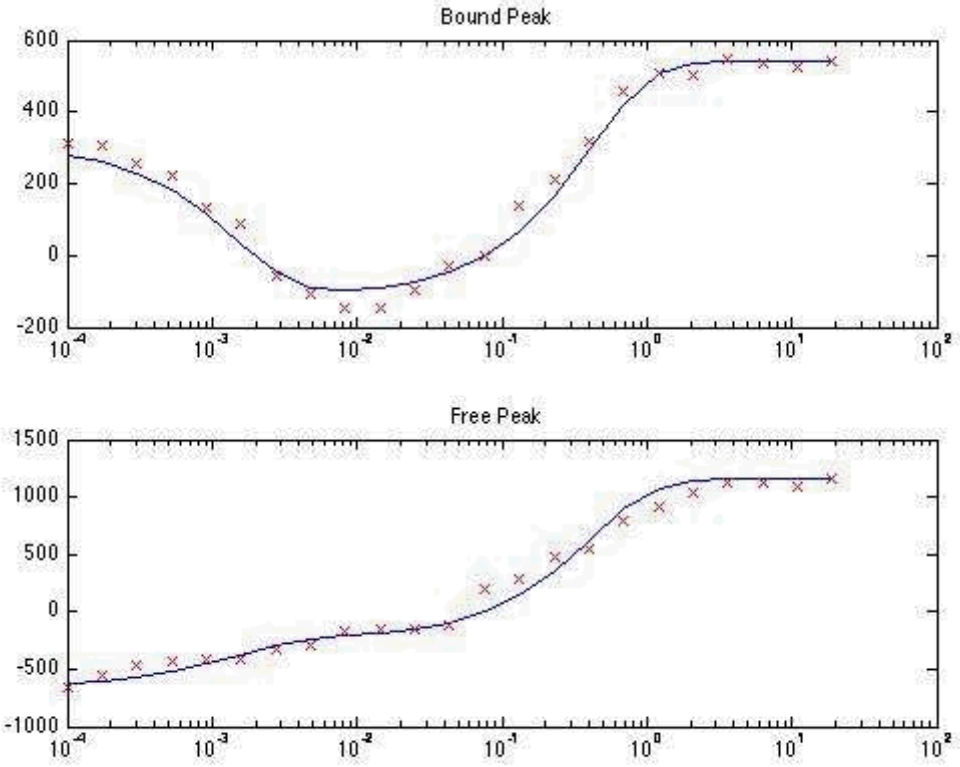

Figure D.25: Sample 4.7 (7.2mM $[NpO_2(CO)_3]^{4-}$ solution at pH 8.55 at 293 K). The black line is the least-squares fit to the data, which are shown as the red crosses. The top box shows the peak intensity of the bound carbonate peak and the bottom box is the intensity of the free carbonate peak.

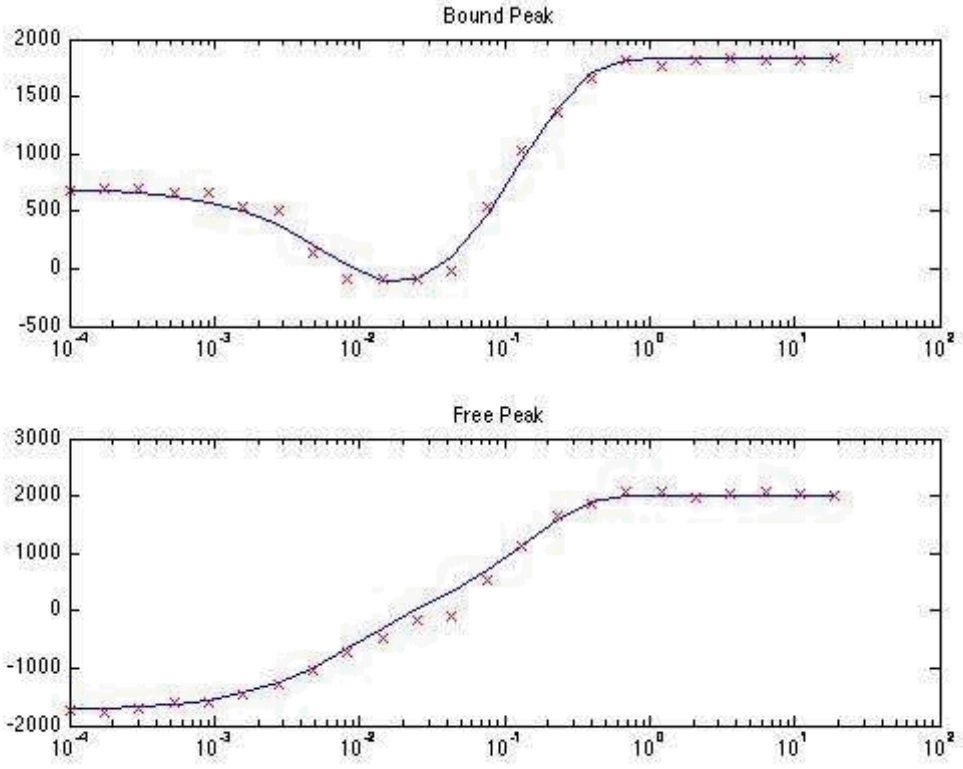

Figure D.26: Sample 4.7 (7.2mM $[NpO_2(CO)_3]^{4-}$ solution at pH 8.55 at 306 K). The black line is the least-squares fit to the data, which are shown as the red crosses. The top box shows the peak intensity of the bound carbonate peak and the bottom box is the intensity of the free carbonate peak.

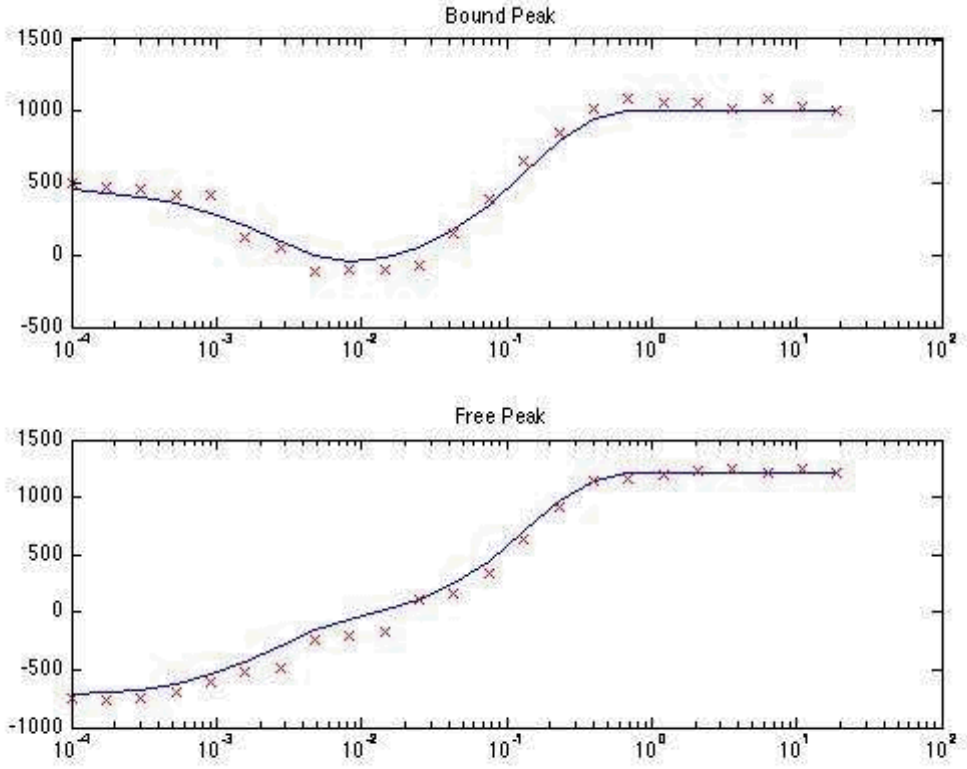

Figure D.27: Sample 7 (7.2mM $[NpO_2(CO)_3]^{4-}$ solution at pH 8.55 at 318 K). The black line is the least-squares fit to the data, which are shown as the red crosses. The top box shows the peak intensity of the bound carbonate peak and the bottom box is the intensity of the free carbonate peak.

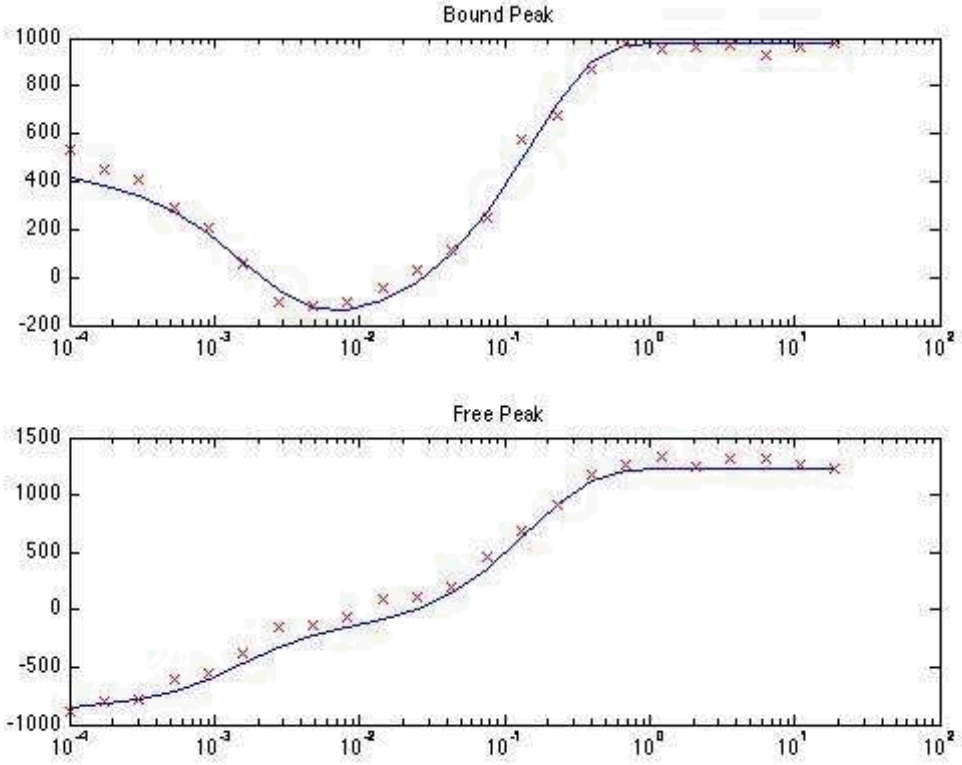

Figure D.28: Sample 7 (7.2mM $[NpO_2(CO)_3]^{4-}$ solution at pH 8.55 at 330 K). The black line is the least-squares fit to the data, which are shown as the red crosses. The top box shows the peak intensity of the bound carbonate peak and the bottom box is the intensity of the free carbonate peak.

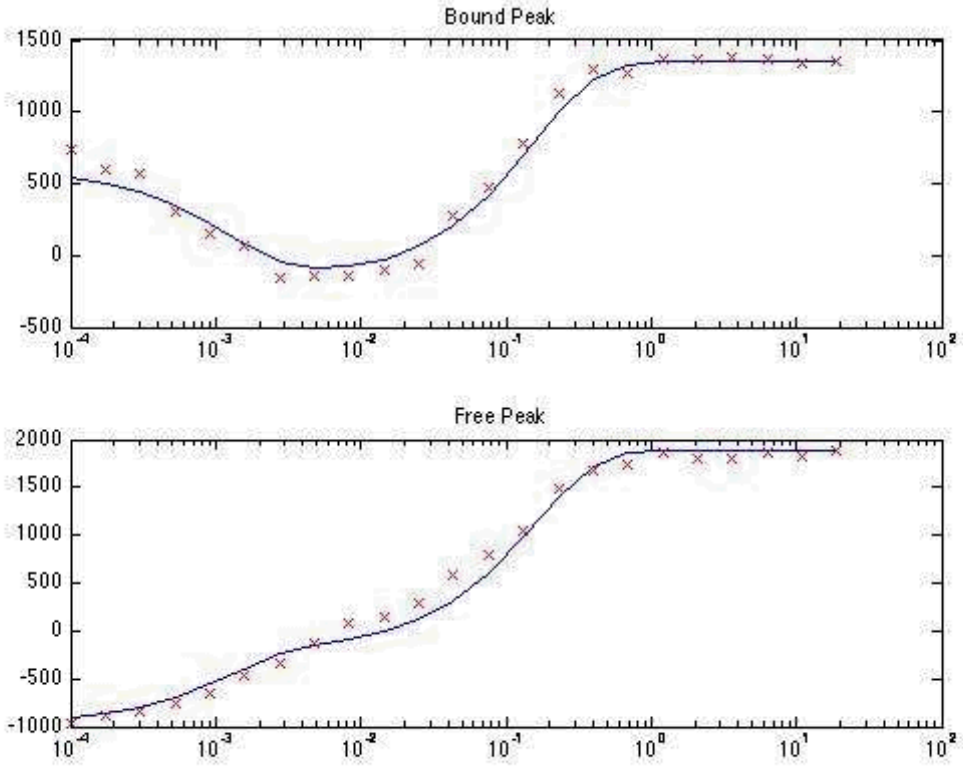

Treatment of raw data

The rates at different temperatures were measured by putting the free carbonate ion NMR signal on resonance and then selectively inverting the signal using the previously mentioned pulse program. Each peak was individually phased and fit using a Lorentzian function to determine their amplitude. The compiled amplitudes as a function of time were fit to the derived model using a least-squares fitting routine employed with a Levenberg-Marquardt algorithm to solve the equations simultaneously. A value for the exchange rate and associated uncertainty was obtained for each temperature.

The uncertainty in the fitting of the saturation transfer model was larger than the linear fit of the temperature dependence; therefore, the large error was propagated to report the uncertainty in the activation parameters. This was done by generating a random, normally distributed, array of 1000 points having a mean value of the regressed rate and a standard deviation of regression standard deviation. A single point from each array was chosen at random and linearly regressed to obtain a value of the slope. The random single point picking process was repeated 1000 times. The average and standard deviation of the slope that resulted was used to report the uncertainty in the activation energy. The uncertainty in the rate was then propagated through to determine the uncertainty in enthalpy, rate, and entropy.

Model Equations: The Bloch equations describe the relaxation of longitudal magnetization via:

$$\frac{dM_z(t)}{dt} = -\frac{M_z(t) - M_z^{\infty}}{T_1} \tag{D.1}$$

where M_z^{∞} is the equilibrium magnetization.

Using McConnell formalism, a two-nuclei system comprising nuclei a and b in which there is magnetization transfer via chemical exchange between the two nuclei can be accounted for by including the appropriate transfer terms for pseudo-first-order kinetics

$$\begin{aligned}\frac{dM_{z,a}(t)}{dt} &= -\frac{(M_{z,a}(t) - M_{z,a}^{\infty})}{T_{1,a}} + k_b M_{z,b}(t) - k_a M_{z,a}(t) \\ \frac{dM_{z,b}(t)}{dt} &= -\frac{(M_{z,b}(t) - M_{z,b}^{\infty})}{T_{1,b}} - k_b M_{z,b}(t) + k_a M_{z,a}(t)\end{aligned} \tag{D.2}$$

where $k_a = \frac{1}{t_{a\to b}}$ and $k_b = \frac{1}{t_{b\to a}}$. The law of detailed balance states that $k_a C_a = k_b C_b$ - where C_a and C_b denote the concentrations of a and b, respectively – so that

$$\begin{aligned}\frac{dM_{z,a}(t)}{dt} &= -\frac{(M_{z,a}(t) - M_{z,a}^{\infty}}{T_{1,a}} + \frac{K_a C_a}{C_b} M_{z,b}(t) - k_a M_{z,a}(t) \\ \frac{dM_{z,b}(t)}{dt} &= -\frac{(M_{z,b}(t) - M_{z,b}^{\infty}}{T_{1,b}} + \frac{K_a C_a}{C_b} M_{z,b}(t) + k_a M_{z,a}(t)\end{aligned} \tag{D.3}$$

In the ideal case the initial conditions are

$$\begin{aligned}M_{z,a}(t_0) &= M_{z,a}^{\infty} \\ M_{z,b}(t_0) &= M_{z,b}^{\infty}\end{aligned} \tag{D.4}$$

However, as the 180° pulse typically is long, some magnetization and relaxation has taken place during the lifetime of the pulse and as such the equilibrium magnetizations were modified to

$$\begin{aligned}M_{z,a}(t_0) &= M_{z,a}^{0} \\ M_{z,b}(t_0) &= M_{z,b}^{0}\end{aligned} \tag{D.5}$$

and where left as new fit parameters.

The set of coupled differential equations can be solved analytically using a suitable software package such as Maxima or Matlab. The resulting functions for $M_{z,a}(t)$ and $M_{z,b}(t)$ model the transient nature of longitudinal magnetization for two sites under chemical exchange where one site has received an inversion in magnetization.

Table D.1: Exchange-rate values obtained through the non-linear least squares fittings at different temperatures for each sample, along with the fitted T_1 value for free carbonate. The results are not sensitive to this fitted T_1 value.

Sample Number	Temperature (K)	Rate (s^{-1})	T_1 (uncertainty)	Sample Number	Temperature (K)	Rate (s^{-1})	T_1 (uncertainty)
1	299	35.2	0.089 (0.016)	4	324	145	0.091 (0.029)
1	310	74.8	0.083 (0.009)	4	339	229	0.075 (0.017)
1	324	211	0.077 (0.013)	5	295	34.3	0.074 (0.019)
1	339	353	0.074 (0.032)	5	306	74.1	0.052 (0.007)
2	305	88.5	0.085 (0.026)	5	318	157	0.063 (0.008)
2	310	97.1	0.088 (0.016)	5	329	242	0.052 (0.005)
2	324	226	0.093 (0.006)	6	294	134	0.094 (0.014)
2	339	475	0.097 (0.016)	6	306	213	0.089 (0.012)
3	294	33.8	0.093 (0.023)	6	318	310	0.094 (0.021)
3	306	70.8	0.099 (0.031)	6	329	463	0.099 (0.022)
3	318	163	0.097 (0.020)	7	294	62.1	0.066 (0.007)
3	329	216	0.088 (0.019)	7	306	191	0.065 (0.011)
4	295	28.1	0.060 (0.008)	7	318	332	0.081 (0.012)
4	310	80.5	0.095 (0.018)	7	329	574	0.064 (0.020)

Figure D.29: Plot of ln(k) vs 1/T for the exchange of carbonate in $[NpO_2(CO_3)_3]^{4-}$ for Sample 4.2 (12mM $[NpO_2(CO)_3]^{4-}$ solution at pH 8.8). Experimental results are shown by the dots and the dashed line is the best fit. The equation to the line is y = -8004.7x + 29.9 and the R^2 value is 0.99735.

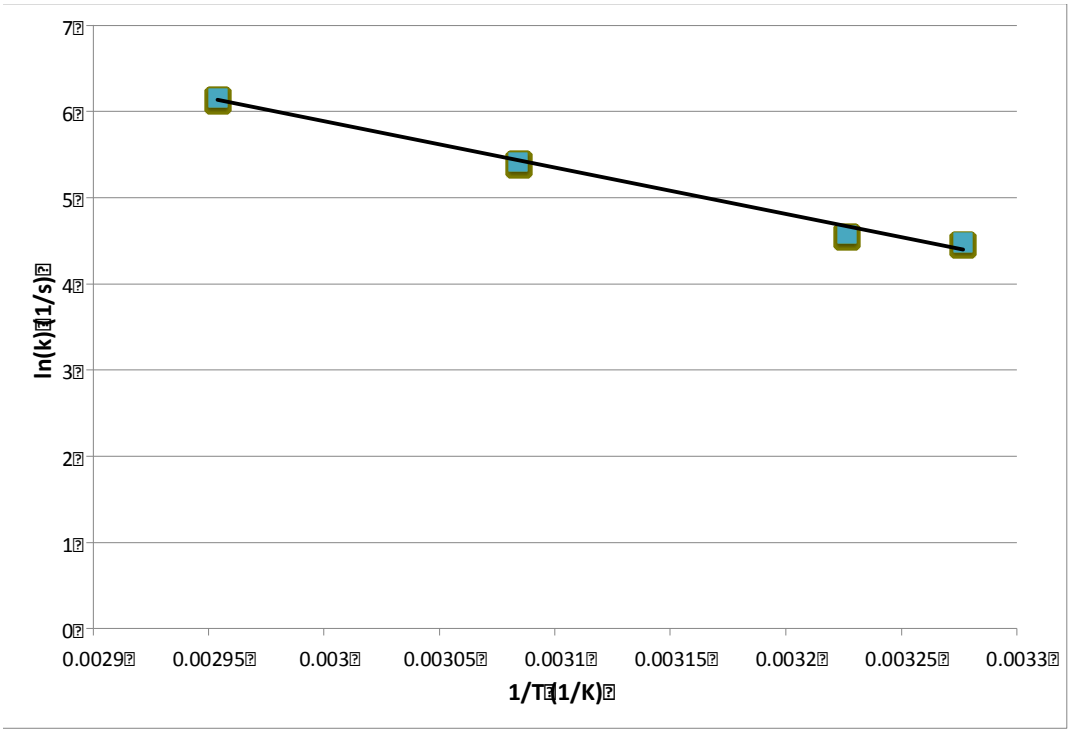

Figure D.30: Plot of ln(k) vs 1/T for the exchange of carbonate in $[NpO_2(CO_3)_3]^{4-}$ for Sample 4.3 (10mM $[NpO_2(CO)_3]^{4-}$ solution at pH 9.3). Experimental results are shown by the dots and the dashed line is the best fit. The equation to the line is y = -5303.9x + 21.6 and the R^2 value is 0.97721.

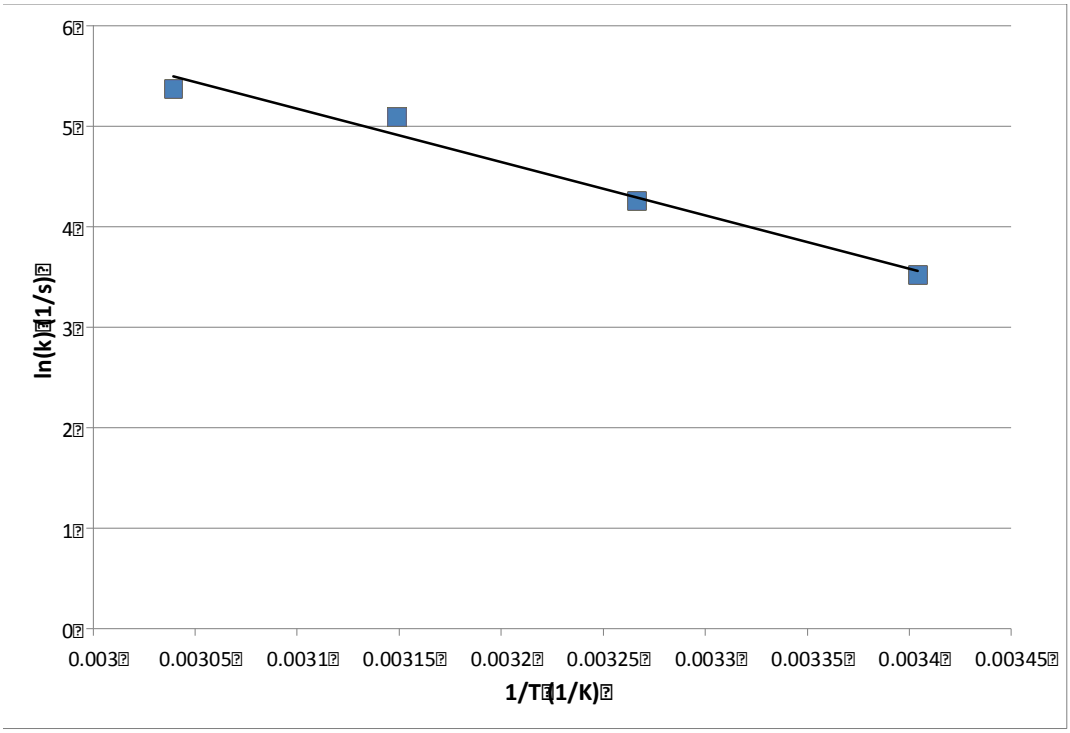

Figure D.31: Plot of ln(k) vs 1/T for the exchange of carbonate in $[NpO_2(CO_3)_3]^{4-}$ for Sample 4.4 (8mM $[NpO_2(CO)_3]^{4-}$ solution at pH 10.1). Experimental results are shown by the dots and the dashed line is the best fit. The equation to the line is y = -4752.6x + 19.6 and the R^2 value is 0.9804.

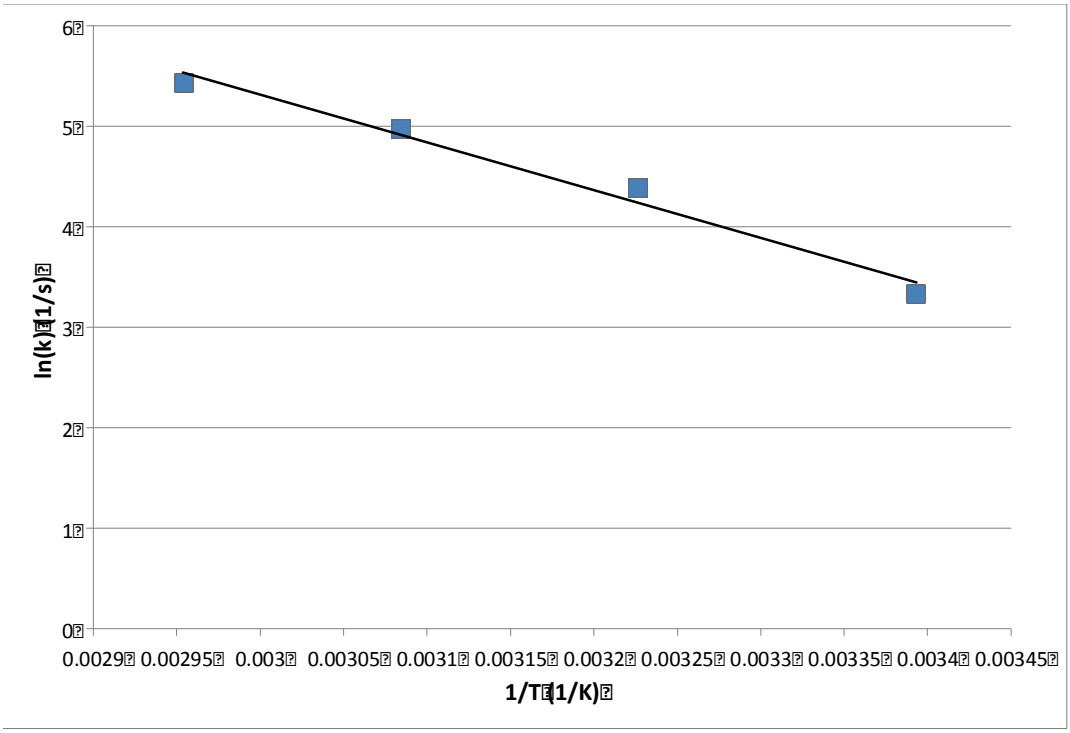

Figure D.32: Plot of ln(k) vs 1/T for the exchange of carbonate in $[NpO_2(CO_3)_3]^{4-}$ for Sample 4.5 (7.2 mM $[NpO_2(CO)_3]^{4-}$ solution at pH 10.1). Experimental results are shown by the dots and the dashed line is the best fit. The equation to the line is y = -5622.8x + 22.7 and the R^2 value is 0.9915.

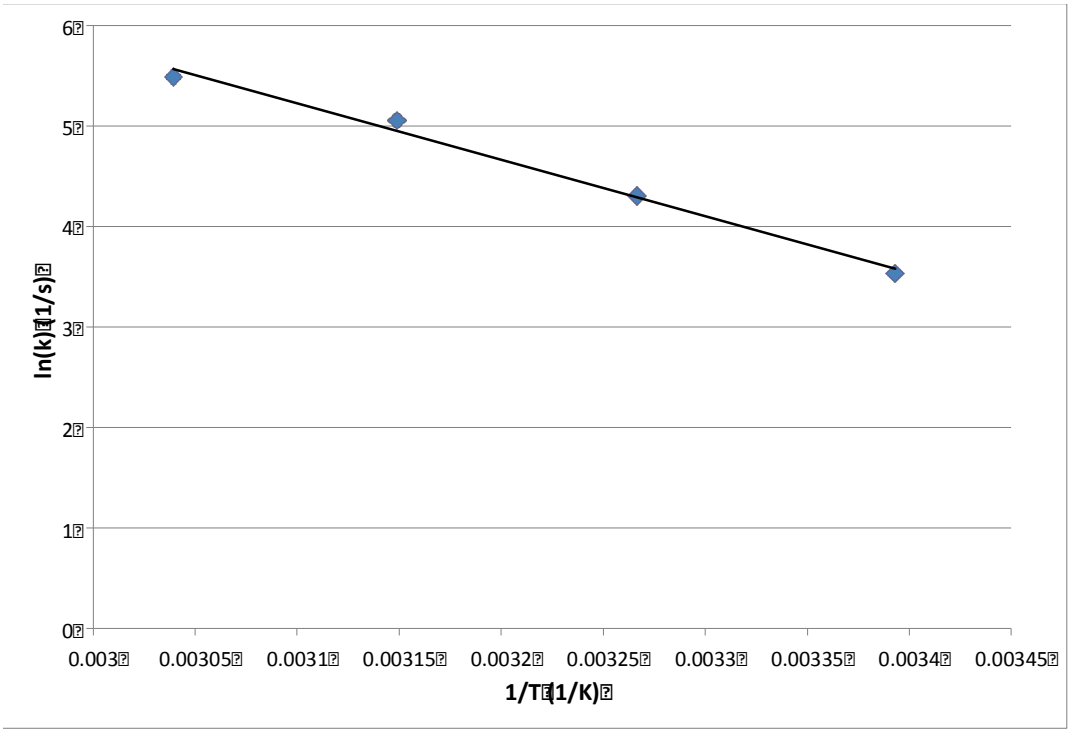

Figure D.33: Plot of ln(k) vs 1/T for the exchange of carbonate in $[NpO_2(CO_3)_3]^{4-}$ for Sample 4.6 (7.2 mM $[NpO_2(CO)_3]^{4-}$ solution at pH 8.1). Experimental results are shown by the dots and the dashed line is the best fit. The equation to the line is y = -3384.6x + 16.4 and the R^2 value is 0.9994.

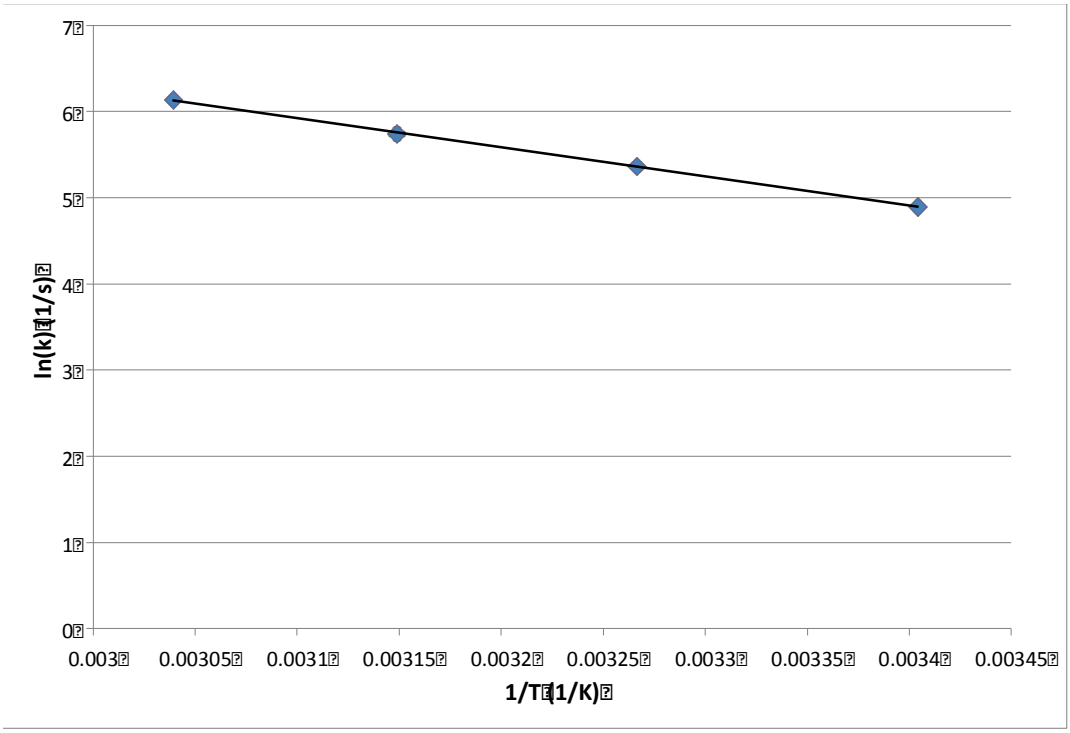

Figure D.34: Plot of ln(k) vs 1/T for the exchange of carbonate in $[NpO_2(CO_3)_3]^{4-}$ for Sample 4.7 at pH 8.55). Experimental results are shown by the dots and the dashed line is the best fit. The equation to the line is y = -6010.3x + 24.7 and the R^2 value is 0.981.

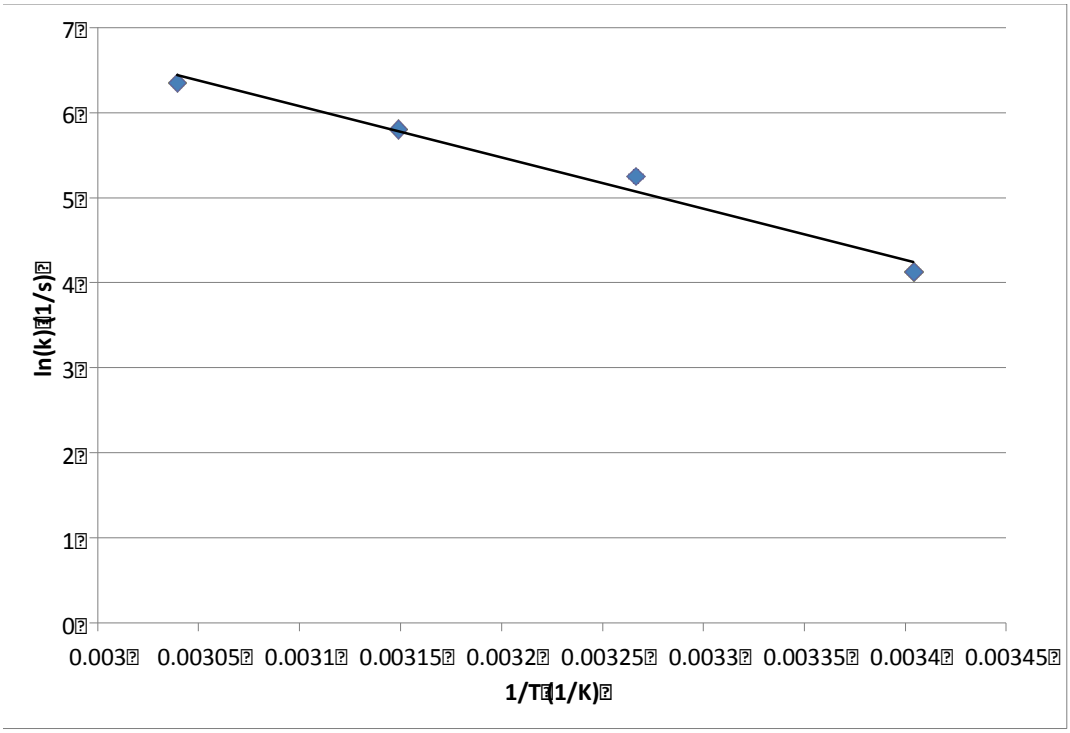

Inorganic Chemistry
including bioinorganic chemistry
June 16, 2014
Volume 53, Number 12
pubs.acs.org/IC

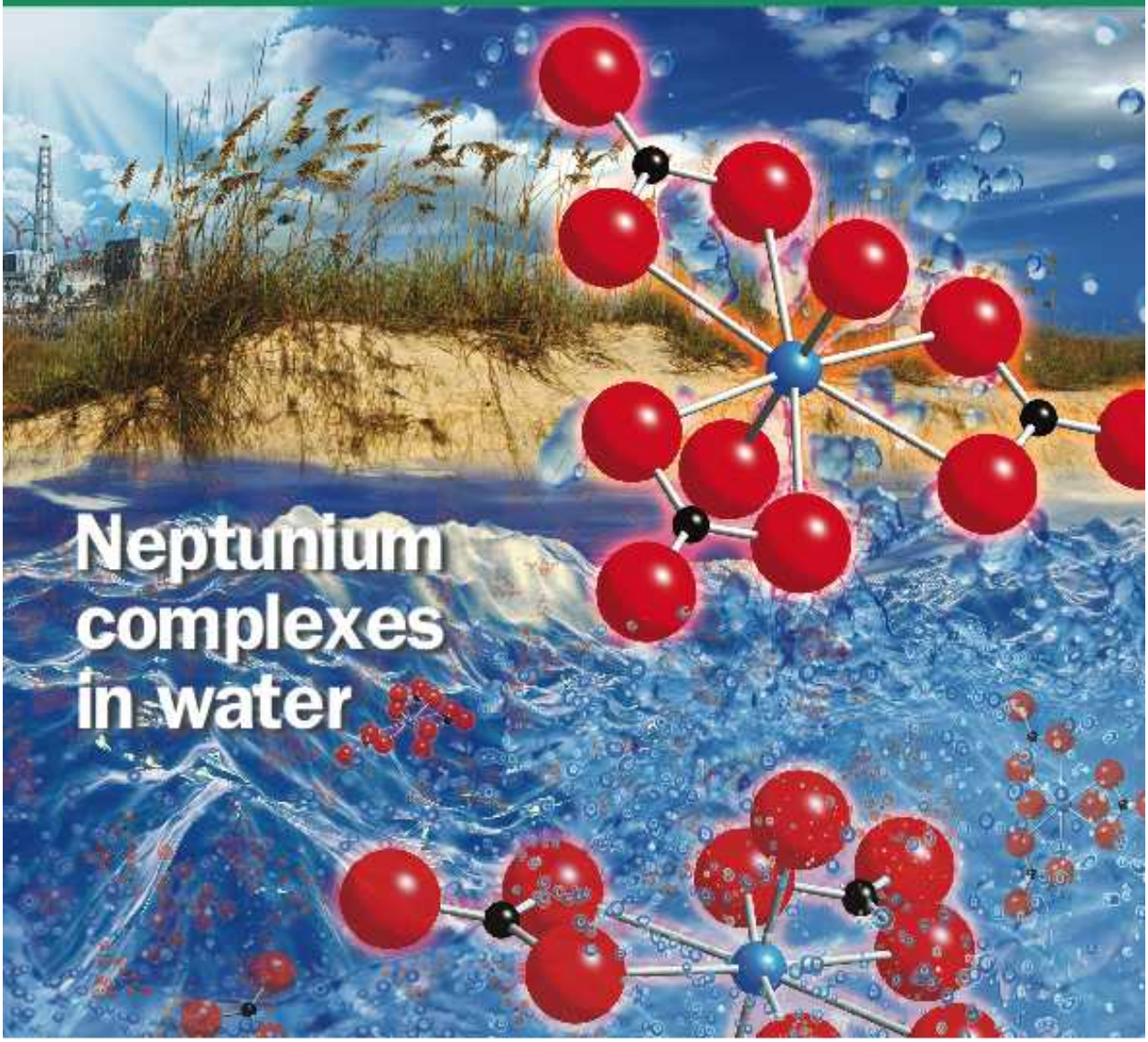

ACS Publications
Most Trusted. Most Cited. Most Read.
www.acs.org

Appendix E:

Script for $[NpO_2(OH_2)_5]^+$(aq) ion Swift-Connick Simulations

E.1 wxMaxima script by Prof. C. Andre Ohlin, Chemistry, Monash University and previously from U. C. Davis, California:

```
/* We need to load vect to do vector multiplication */

load("vect");

/* The standard Bloch equation is written */

diff(M(t),t,1)=gamma*(M(t)~B(t)); /*This line does nothing*/

/*where */

M(t):= [Mx,My,Mz];
B(t):= [Bx,By,Bz];

/* and */

Bx: B1*cos(omegarf*t);
By: -B1*sin(omegarf*t);
Bz: B0;

/* We introduce the relation 3x3 matrix, T */

T: matrix([-cos(omegarf*t),sin(omegarf*t),0],

[-sin(omegarf*t),-cos(omegarf*t),0],[0,0,1]);

/*By multiplying T with M(t)(labframe) we get M(t)(rotating frame) */

rot:T . M(t);

/* We need to define Mx, My and Mz in terms of u, v and w, where mz=Mz(rot) */

*sol: rot[1,1];

solu:trigsimp(linsolve([u=rot[1,1],v=rot[2,1],mz=rot[3,1]],[Mx,My,Mz]));

Mx: rhs(solu[1]);

My: rhs(solu[2]);

Mz: rhs(solu[3]);


/*Everything is plugged into the Bloch equation */

dM: express(gamma*(M(t)~B(t)))

/* we reuse solu to define Mx, My and Mz as functions so that we can generate
the derivatives and turn u,v and mz into functions*/

solu[1] : subst(u(t),u,solu[1]);
solu[1] : subst(v(t),v,solu[1]);
solu[1] : subst(mz(t),mz,solu[1]);
Mx(t):= rhs(solu[1]);
```

```
solu[2] : subst(u(t)=u.solu[2]);
solu[2] : subst(v(t)=v.solu[2]);
solu[2] : subst(mz(t)=mz.solu[2]);
My(t):= rhs(solu[2]);

solu[3] : subst(u(t)=u.solu[3]);
solu[3] : subst(v(t)=v.solu[3]);
solu[3] : subst(mz(t)=mz.solu[3]);
Mz(t):= rhs(solu[3]);

/*calculate the derivatives. then replace du/dt with du and dv/dt with dv */
eq1b: "dM[1];
eq2b: "dM[2];
eq3b: "dM[3];

dMxlh: diff(Mx(t),t,1);
dMxlh: subst([du.diff(u(t),t,1)],dMxlh);
dMxlh: subst(dmz.diff(mz(t),t,1),dMxlh);
eq1: subst(dv.diff(v(t),t,1),dMxlh);

dMylh: diff(My(t),t,1);
dMylh: subst([du.diff(u(t),t,1)],dMylh);
dMylh: subst(dmz.diff(mz(t),t,1),dMylh);
eq2: subst(dv.diff(v(t),t,1),dMylh);

dMzlh: diff(Mz(t),t,1);
dMzlh: subst([du.diff(u(t),t,1)],dMzlh);
dMzlh: subst(dmz.diff(mz(t),t,1),dMzlh);
eq3: subst(dv.diff(v(t),t,1),dMzlh);

/* derive du/dt, dv/dt and dMz/dt */

solu: triginsm1(linsolve([eq1=eq1b,eq2=eq2b,eq3=eq3b],[du,dv,dmz]));
solu: subst(u.u(t),solu);
solu: subst(v.v(t),solu);
du:rhs(solu[1]);
dv:rhs(solu[2]);
dmz:rhs(solu[3]);

/*Demonstrate a 2 site exchange system with magnetisation transfer and T1,T2 relaxation*/

uRxy: u/T2-u1/tau1+u2/tau2;
vRxy: v/T2+v1/tau1-v2/tau2;


/*For water*/

uwRxy: subst(T2w,T2,subst(tauw,tau1,subst(taum,tau2,subst(um,u2,subst(-
uw,u1,subst(uw,u,uRxy))))));
vwRxy: subst(T2w,T2,subst(tauw,tau1,subst(taum,tau2,subst(vm,v2,subst(-
vw,v1,subst(vw,v,vRxy))))));

/*For m */
```

```
umRxy: subst(T2m,T2,subst(lau,mlau1,subst(lauw,lau2,subst(uw,u2,subst(-
um,u1,subst(um,u,uRxy))))));
vmRxy: subst(T2m,T2,subst(laum,lau1,subst(lauw,lau2,subst(vw,v2,subst(-
vm,v1,subst(vm,v,vRxy))))));

/*next we rename all instances of u,v, and mz to uw,vw and mzw where w stands for water*/

duw: subst(mzw,mz,subst(vw,v,subst(uw,u,du)));
dvw: subst(mzw,mz,subst(vw,v,subst(uw,u,dv)));

/*We do the same thing for m*/

dum: subst(mzm,mz,subst(vm,v,subst(um,u,du)));
dvm: subst(mzm,mz,subst(vm,v,subst(um,u,dv)));

/*We reveal that omegarl=vw-v and vm-v */

duw: subst(vw-v,omegarl,duw);
dvw: subst(vw-v,omegarl,dvw);
dum: subst(vm-v,omegarl,dum);
dvm: subst(vm-v,omegarl,dvm);

/* We introduce the relaxation/exchange terms */

duw: duw+uwRxy;
dvw: dvw+vwRxy;

dum: dum-umRxy;
dvm: dvm+vmRxy;

/* And then we look at Mxy*/
uw: Mw-%i*vw;
dMw: duw-%i*dvw;
dMm: dum-%i*dvm;

/*We replace all instances of lau */
dVw: subst(1/km,laum,subst(1/kw,lauw,dMw));

/*uw: Mw-%i*vw;*/
dVw: subst(Vm-%i*um,subst(Mw-%i*vw,uw,dMw));
dVm: subst(1/km,laum,subst(1/kw,lauw,dVm));

/*um: Mm-%i*vm;*/
dVm: subst(Vw-%i*uw,subst(Mm-%i*vm,um,dMm));

/*then replace kw with km*Pm/Pw */
dVw: subst(km*Pm/Pw,kw,subst(1/kw,lauw,dMw));
dVm: subst(km*Pm/Pw,kw,subst(1/kw,lauw,dVm));


/*Prettify the expression */
dVw: fullratsimp(dMw);
dVm: fullratsimp(dVm);
```

```
/*Time to start plotting */

/*We'll use the following values for the variables*/

gL: 4/3;
J: 4;
kB: 1.3806503*10^(-23);
T: 298;
B: 14.1;
A1: -3.6*10^6;
uB: 9.274*10^(-24);
vw: 0;
vm: A1*(gL*(gL-1)*J*(J+1)*uB*B)/(3*kB*T);
T2w: 0.005;
T2m: 0.000001;
km: 3.1*10-200;
Pm: 0.01*5;
Pw: 55.55;
H1: 1;
M0:1;
gamma:1;
B1:gamma*H1;B0:2*%pi*v;
mzm: Pm*M0;mzw:Pw*M0;

solu: solve([dMw,dVm],[Mw,Mm]);
sol: solu[1];
M: rectform(imagpart(rhs(sol[1]))+rhs(sol[2]));
plot2d([abs(M)],[v,-150,150]);
```